APPLICATIONS OF MAGNETICS TO PROBLEMS IN SWITCHED-MODE POWER CONVERSION

Thesis by

William M. Polivka

In Partial Fulfillment of the Requirements

for the Degree of

Doctor of Philosophy

California Institute of Technology

Pasadena, California

1984

(Submitted February 7, 1984)

ACKNOWLEDGMENTS

I am deeply indebted to my advisors, Professor R. D. Middlebrook and Professor Slobodan Ćuk, for permitting me to work and to grow with the Power Electronics Group during the five years I have spent at Caltech. I am grateful for having had the opportunity to make a small contribution to the Group, and I realize that I have received much more than I have given.

I also wish to acknowledge the support and encouragement of Professor J. K. Watson of the University of Florida, Visiting Professor of Electrical Engineering at Caltech 1980-81, for the many enlightening discussions which inspired the work in the first part of this thesis.

I very much appreciate the financial support of the California Institute of Technology by way of several Graduate Teaching Assistantships and a Silicon-Hewlett Packard Fellowship. In addition, I thank the Office of Naval Research, the Naval Ocean Systems Center and the International Business Machines Corporation for their financial support through several Graduate Research Assistantships.

The first part of this thesis would not have been possible without the technical support and dedicated assistance of Alan Cocconi, who discovered the effect of orthogonal flux in power transformers and first used it to detect impending saturation while working with the Power Electronics Group at Caltech. The design and construction of the experimental converters described in Part I are the products of his insight and ingenuity.

The work on the high-power photovoltaic converter discussed in Part I was done at TESLAco–Optimum Power Conversion, Pasadena, California, under a subcontract from Sandia National Laboratories, Albuquerque, New Mexico, and their cooperation is gratefully acknowledged.

Finally, I wish to express my thanks and appreciation to the present and former members of the Power Electronics Group for the enrichment of their help and support and for the pleasure of their company.

ABSTRACT

Two topics are presented which advance the use of magnetic devices in switched-mode power converters. Part I discusses a novel method of detecting impending saturation of magnetic materials. The technique exploits the interaction of perpendicular magnetic fields to provide a simple, direct and continuous measure of the increasing nonlinearity of the material without any elaborate unconventional devices or complex electronic circuitry. Theoretical foundations and applications to ferrite cores in switching converters are given. Specific practical hardware examples are described including magnetics for a 4-kilowatt push-pull buck converter. Part II presents a discussion of the analysis of zero ripple integrated magnetic structures. These complex devices are of great interest in the field of switched mode power conversion because they have the ability to exclude ac currents from some of their windings when they are excited by ac voltages. A thorough analysis is carried out to establish which of the many characteristic parameters of these devices are responsible for the unusual zero ripple behavior. Practical methods of modelling and analysis are developed by which a designer can quickly determine the conditions required for zero ripple. Equivalent electric circuit models are given to aid in the electrical design of converters and to support the simple physical explanations of the observed phenomena including the effects of parasitic quantities. A number of experiments confirm the validity of the models.

TABLE OF CONTENTS

INTRODUCTION

This thesis is divided into two parts, each one a self-contained treatment of an interesting problem in the rapidly expanding field of Power Electronics. Part I describes a novel way to detect impending magnetic saturation in power converters. This very simple and easy-to-use technique effectively uses the magnetic device as its own magnetometer to assess the amount of flux in the material. The chief application of the technique is to protect semiconductor devices from the damaging currents which result when a power transformer saturates rapidly and unexpectedly. Part II addresses the curious phenomenon of *zero ripple* which is a property of certain properly-designed magnetic structures. Several years ago it had been discovered that some multi-winding magnetic devices have the remarkable ability to exclude ac currents from some of their windings despite their being driven by ac voltages, and this has been of great interest to power processing engineers who desire pure dc currents on the input and output ports of their power converters. This long-awaited analysis shows which of the many characteristic parameters of the device are chiefly responsible for the zero current ripple effect and illustrates simple techniques for analysis and design of these special structures.

In keeping with the tradition and purpose of earlier theses that have come from the Caltech Power Electronics Group, the discussions presented here are not esoteric treatments written for academic experts, but rather are presentations of practical solutions intended to be understood and used by

practicing engineers in industry. Therefore, to ensure that the intended beneficiary is adequately familiar with these topics, each discussion contains a substantial review of basics and background material. Although the presentation of some of the fundamentals may appear to be trivial and unnecessary, one should consider that both topics addressed here were discovered by accident, and for a long time those unanticipated results were quite mysterious, even to the experts.

This presentation breaks tradition in that it is the first thesis from the Power Electronics Group to be written entirely about magnetic devices. Although rapid advances have been made in the field of switched mode power conversion over the last decade, the development of magnetic devices has not kept pace with the progress made in other important areas of power electronics such as electronic devices, circuit topologies, modelling, analysis, measurement and control. As explained in the introductory chapters which follow, a major deterrent to progress in this area has been the intimidation which comes from a general unfamiliarity with the tools of analysis and an overestimation of the complexity of the problem. This thesis will demonstrate that just as magnetic and electronic devices are equally important to switched mode power conversion, they are also equal in complexity and facility of analysis. The following chapters will show that analogous to the more familiar electronic devices, very simple models can be found which give good engineering solutions to some very complicated magnetic problems.

PART I

USE OF ORTHOGONAL FLUX TO DETECT IMPENDING MAGNETIC SATURATION IN SWITCHING CONVERTERS

CHAPTER 1

INTRODUCTION

Electrical engineers who become involved in the design of electronic equipment for power conversion find themselves working in the often unfamiliar world of magnetic devices. The topic of magnetics design is not extensively covered in textbooks, and, although it is based on uncomplicated fundamental principles, its application to modern power conversion is often considered to be black magic. This reputation, however, is undeserved. Design with magnetic components is no more difficult than design with electrical components, for both classes of elements suffer from the same problems and limitations as all physical devices, which include nonlinearity and saturation.

The first part of this thesis addresses the problem of magnetic saturation and discusses a novel method [1] by which one may easily detect impending saturation to avoid its undesirable effects. The importance of finding a solution to this problem has become more acute with the advent of switched-mode power conversion, because unexpected saturation of a high-frequency power transformer not only degrades the performance of the converter, but often triggers spectacular catastrophic failures.

The new method uses the interaction of two perpendicular magnetic fields in the core of a transformer to produce a voltage signal which is related to the magnitude of the total flux in the magnetic structure. This

signal can be used directly by the control circuitry of a power converter to prevent saturation of the transformer.

The mechanism by which the perpendicular magnetic fields interact is an exploitation of the nonlinearity of the magnetic material of the transformer's core. Although the principles of nonlinear interactions in magnetic media have been well-known for quite some time [2], they are not yet *widely known*, and are certainly not widely used in the field of switched-mode power processing.

Because the field of Power Electronics is still a relatively new and unfamiliar discipline to most electrical engineers, the treatment of this topic has a tutorial tone for the benefit of new practitioners in this growing area. The purpose is two-fold: (1) to provide a simple but complete explanation of the principles of the phenomenon to give the practicing engineer a good understanding of *why the technique works*, and (2) to supply sufficient information and practical examples to illustrate *how to use it*.

CHAPTER 2

USE OF MAGNETIC DEVICES IN SWITCHING CONVERTERS

Part I of this thesis describes a simple and novel way to detect impending saturation of magnetic devices. Although the idea may be applied to practically any area of electronics where magnetic materials are used, it is of particular interest to engineers in the field of *Power Electronics*. This chapter establishes the motivation not only for the topics discussed in both parts of this thesis, but also for further work in magnetics from the point of view of the Power Electronics Specialist. It will be seen that unlike most other areas of Electrical Engineering, where the use of magnetic devices may be only casual at best, the field of modern Power Electronics depends on the magnetic component as one of the basic elements *essential* for lossless power conversion.

2.1 The Importance of L's

Electrical Engineering, as an academic discipline, has come to be synonymous with *Signal Processing* -- the electronic manipulation of information. Most electrical engineers are very much at home in the domain of Signal Processing Engineering, where amplification of analog signals, analog-to-digital and digital-to-analog conversions, frequency conversions, and so on, are to be accomplished with a minimum amount of power. In contrast to this point of view is the emerging discipline of *Power Processing* [3], in

which the goal is to process *power* with 100 per cent efficiency, rather than information with minimum power.

The differences between Signal Processing Systems and Power Processing Systems begin at the most basic level of engineering design, the components available for use by the engineer. All electronic systems are constructed from components which may be simply classified according to only five categories: resistors, inductors, capacitors, linear-mode semiconductor devices and switched-mode semiconductor devices. The designer of a signal processing system has at his disposal all these elements with the possible exception of the inductors. He tries to avoid magnetic elements because they are bulky, heavy, and are difficult to fabricate on silicon chips. Often the designer chooses to develop elaborate circuits to simulate inductor properties over the painful alternative of using a real magnetic device.

The designer of a power processing system, on the other hand, is much more restricted in the types of components he can use. Because he cannot afford losses of power (just as the signal processing engineer cannot afford loss of information) he must avoid both resistors and linear-mode operation of semiconductors. Therefore, there are only three types of elements available for use in power processing circuits: L's, C's and Switches.

2.2 Isolation and Energy Storage

A power processing system converts power of one voltage, current, and frequency combination to another voltage, current, and frequency combination. The power processing engineer must accomplish the conversion by means of suitable connections of the available elements. The "suitable connections" involve periodic topological switching of energy storage elements (inductors and capacitors) under the constraint that all voltages and currents remain finite. One can see immediately that inductors are very important because they are one of the two elements available for energy storage. Furthermore, magnetic devices are valuable for *energy transfer* in the capacity of transformers. The ability to transfer energy via a magnetic field is an attribute of transformers which makes them indispensable for satisfaction of the often mandatory requirement that input and output ports of the power system be electrically isolated.

CHAPTER 3

SATURATION OF PHYSICAL DEVICES

The undesirable saturation of electronic and magnetic devices has always been a troublesome problem for circuit designers because the boundaries of saturation impose limitations on the performance of almost any design. Saturation of most *electronic* devices is generally easy to avoid because the physical quantities which are responsible for the saturation (voltages and currents) are nearly always quite accurately known, and are therefore are easily controlled. The problem of *magnetic* saturation, on the other hand, has been much more difficult to overcome owing to the lack of a good practical way to measure the quantity which saturates the magnetic material, the flux density. This chapter describes some of the problems peculiar to the magnetic devices used in power processing systems and discusses a number of proposed solutions.

3.1 Special Problems with Transformers

The preceding chapter established the importance of magnetic devices to electronic power conversion as components for both energy storage and energy transfer. In some applications a single device is used for energy storage only, as an ordinary inductor. When used as a transformer, only energy transfer is desired and the device is designed and optimized for that purpose. Part II of this thesis will show that sophisticated devices can

be designed to perform *both* functions in a single integrated physical structure. However, all these components are limited in their capacity, whatever that might be, by the maximum flux density the magnetic material can sustain and still retain its desirable properties. Although one must protect all these devices against unwanted saturation, the most difficult problem in practice is associated with the pure transformer.

The isolation transformer of a dc-dc power converter, in order to take full advantage of the available magnetic material and simultaneously meet minimum size and weight constraints, is required to be designed to handle only ac currents. For a compact, efficient, and otherwise high-performance design, no net dc magnetization current can be permitted in the transformer windings. If a net dc current were present, the resultant dc flux, which cannot transfer energy, would consume part of the maximum flux density available for energy transfer. Furthermore, if the device is properly designed for use as a transformer, any attempt to store energy or otherwise introduce more than the expected flux density in the magnetic material will ultimately lead to magnetic saturation. Whole or partial saturation of a power transformer is undesirable for many reasons, but the most significant one is that it causes excessive and often destructive stresses on the power semiconductor devices in the converter.

Unfortunately, unless one takes definite measures to prevent it, it is possible for a well-designed transformer to saturate as a result of transient excitations or naturally occurring nonidealities of components.

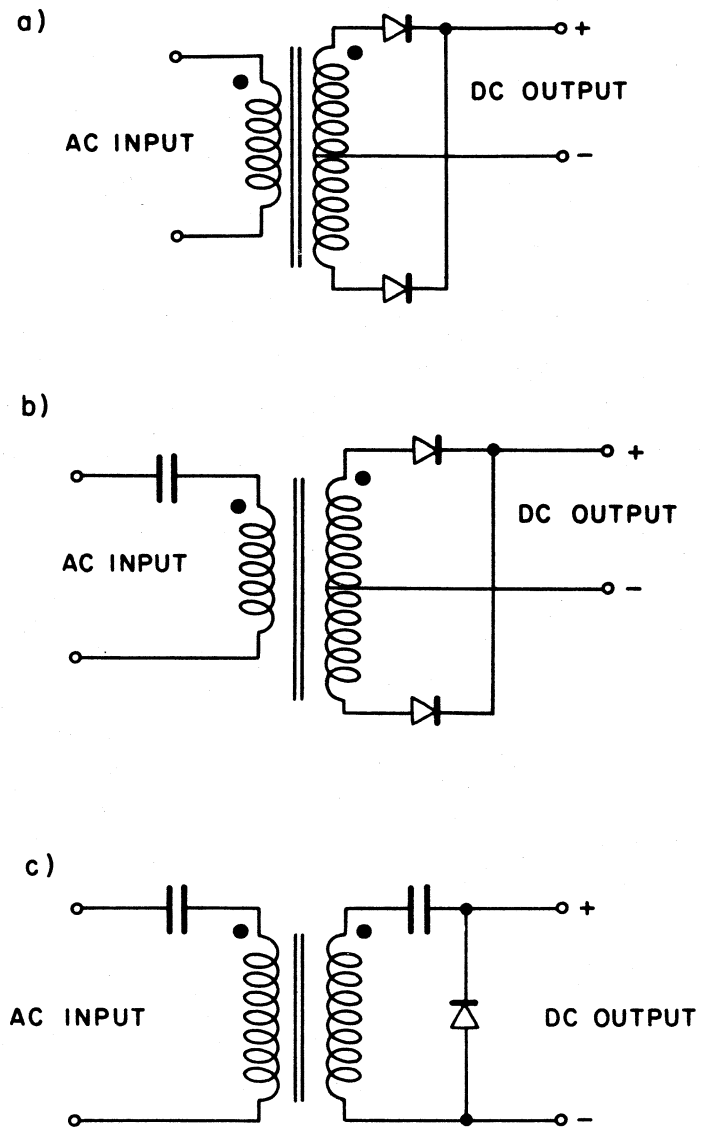

Fig. 3.1 Some transformers for power converters. Addition of a dc-blocking capacitor to the primary of (a) guarantees steady-state volt-second balance, (b), but does not prevent steady-state dc magnetization current. Series capacitors on both primary and secondary, (c), guarantee zero dc magnetization current, but the transformer can still saturate in response to transients.

Subsequent chapters of this thesis will describe and demonstrate a new and interesting way to sense impending saturation of the power transformer so that one may be able to take proper measures to avoid this common problem. Several other methods have been proposed and used to detect or to prevent saturation of power transformers, and these are described in the following sections.

3.2 Passive Solutions

Consider the particular transformer of Fig. 3.1a. The ac input at the primary is a periodic rectangular voltage waveform which could come from a common full-bridge or equivalent push-pull pulse width modulated dc-to-dc converter. If the time average of the primary voltage is not zero, then a dc magnetization current will rise in the transformer and the magnetic core will eventually saturate. One technique to counter this cause of saturation is shown in Fig. 3.1b. The primary is ac-coupled to the input voltage by means of a dc-blocking capacitor. Thus any average input voltage will appear across the capacitor and not across the primary. A steady-state volt-second balance will be maintained and therefore no net dc current can exist in the primary circuit.

The insertion of a capacitor in series with the input, however, is *not sufficient* to prevent a dc flux component from saturating the core. A net dc current may still be introduced from the *output*. This will happen if the output diodes and winding resistances are not perfectly matched, or if there is an asymmetry in the timing of the voltage waveform at the primary. The latter condition always exists to some degree when bipolar transistors are

used as switches owing to natural differences in storage time between individual devices. Although the possibility of dc saturation exists when the primary is ac-coupled as in Fig. 3.1a, it does not usually occur in practice because the important parameters are usually reasonably well-matched and sufficient margin is usually designed into the transformer [4, 5].

The only passive way to guarantee that there will be no steady-state dc magnetization current is to ac-couple *both* input and output as shown in Fig. 3.1c. If there is more than one output, then they all must be dc-blocked.

Even with ac coupling of the input and all the outputs, however, the possibility of saturating the transformer still exists. This can occur if there is a sudden increase in input voltage, for example. A transient on the power line can produce a large magnetization current which can last for several switching periods -- ample time to saturate the transformer and damage the components.

The semiconductor devices can be protected by means of active current limiting on each transistor, but this safeguard does not eliminate the need for the dc-blocking capacitors. The capacitors are required to prevent a steady-state dc magnetization current, which, if permitted, would force half of the switches to operate at the current limit level all the time.

Clearly some sort of active compensation is needed to correct for these naturally occurring mismatches and imbalances [4, 5]. This

necessity becomes especially apparent at high power levels, where the magnetics have to be optimized for efficient power transfer, and thus can tolerate very little dc current.

3.3 Active Solutions

Several methods are available by which one may avoid saturation of the transformer without the need of a dc-blocking capacitor at each port. Some are quite obvious (with equally obvious disadvantages):

(1) Integrate the voltage on the transformer and maintain a volt-second balance by control of the drive symmetry. This very straightforward approach requires an accurate integrator with its associated sensitive analog circuitry. In addition, a knowledge of the dc flux level is required, since integration yields only the ac flux excursion.

(2) Sum all the winding currents in the proper ratios to find the magnetization current and then have the control circuit work to minimize the average. Users of this very basic technique have to work against the fundamental problem of the resolution of small differences between large numbers. This is especially difficult to do for typical situations in which the winding currents are very much greater than the magnetization current.

(3) Build a Hall device into the structure to sense the flux

in the transformer core. Although this would provide a means to sense the peak flux density, the use of such a sensor would amount to the introduction of a low permeability gap in the flux path. The accompanying reduction of the magnetization inductance would lead to higher current stresses on the transistors and reduced efficiency of the converter.

In addition to these, however, there are several novel and diverse solutions reported in the literature:

(4) In [6] and [7] Schwarz uses a two-core transformer of uncut square-loop material. The two toroidal cores are pre-biased by a dc current in auxiliary windings such that one of the two cores saturates first. In so doing, it generates a signal pulse which is used to turn off the transistors while the remaining unsaturated core supports the primary voltage.

(5) Hirschberg in [8] demonstrates a "Twin Pulse Circuit" which desensitizes a converter against transformer saturation by virtue of an unconventional pulse-width modulation system.

(6) Patel describes a method in [9] in which one can detect impending saturation by the use of an

unsymmetrically gapped EE core.

(7) Kuttner in [10] senses the switch currents and uses a tuned circuit to detect the presence of the fundamental component of the switching frequency in the primary circuit. If the magnetization current is zero, then the lowest frequency present is twice the switching frequency. The presence of a fundamental component indicates an unbalance -- a manifestation of a dc magnetization current. The control circuit works to minimize this fundamental component.

(8) In [11] Wilson uses both the primary voltage and primary current as inputs to a new pulse-width modulation circuit which maintains flux balance by the allotment of equal V-I areas to alternate pulses.

The technique to be described in the following chapters is yet another way to detect impending saturation in magnetic materials. The method exploits the interaction of perpendicular magnetic fields to provide a simple, direct, and continuous measure of the increasing nonlinearity of the magnetic material of the transformer without any elaborate devices or complex electronic circuitry.

It should be noted that all the techniques described above, including the one presented in this thesis, can be supplanted by the use of a sophisticated method of control commonly known as *current*

programming [12, 13, 14], in which the output voltage of the power converter is regulated indirectly by precise control of the currents in the switches. This method of control can provide protection if (1) the currents can be measured with sufficient precision and (2) the transistors can be turned off in time to avoid destruction. Because of transistor storage time and delays in digital circuits, the latter requirement is often very difficult to meet when the transformer saturates without warning. In any case, since the conventional method of *voltage programmed control* is still highly desirable and widely used in many applications, the focus here will be on that scheme. The new sensing technique described here is not devalued by the use of more sophisticated methods of control, but, on the contrary, offers yet another very attractive alternative to the circuit designer. In addition, the new method is not limited to transformers for power converters, but may be extended for applications to magnetic devices in other circuits as well.

CHAPTER 4

REVIEW OF FUNDAMENTALS

This thesis presents a discussion of some first-order magnetic effects which occur in practical circuits for electronic power processing. Although the circuits involve some rather unconventional magnetic structures, the analysis is not difficult, amounting to straightforward applications of well-established fundamental ideas. While Part II solves a *linear* problem with techniques familiar to most engineers, Part I deals with a topic which involves a strictly *nonlinear* phenomenon. With constant exposure to linearized engineering problems one may tend to forget the true nature of the working materials. It is easy to be led astray by the natural temptation to take relationships which were derived from *linear models* and to apply them incorrectly to phenomena which are governed exclusively by *nonlinear processes*. For this reason the foundations for the treatment of the topic of Part I should begin from first principles, with all assumptions and approximations explicitly stated and justified as they arise.

4.1 Maxwell's Equations

The foundations of all descriptions of classical electromagnetic phenomena are contained in Maxwell's equations, written here in integral form.

$$\int\int_{closed} \mathbf{D}\cdot d\mathbf{A} = Q_{free} \tag{4.1}$$

$$\int_{closed} \mathbf{E}\cdot d\mathbf{l} = -\frac{\partial}{\partial t}\int\int_{A} \mathbf{B}\cdot d\mathbf{A} \tag{4.2}$$

$$\int_{closed} \mathbf{H}\cdot d\mathbf{l} = \int\int_{A} \mathbf{J}\cdot d\mathbf{A} + \frac{\partial}{\partial t}\int\int_{A} \mathbf{D}\cdot d\mathbf{A} \tag{4.3}$$

$$= I_{conduction} + I_{displacement}$$

$$\int\int_{closed} \mathbf{B}\cdot d\mathbf{A} = 0 \tag{4.4}$$

where the boldface quantities are *vectors* having both magnitude and direction. Quantitities which are not emboldened are scalars with magnitude only.

It is appropriate to write these equations in this way rather than in the alternative point form because the objective of this analysis is to describe *macroscopic* rather than *microscopic* effects. The plan is to model observed electrical phenomena from bulk material properties which can be obtained from the electrical terminals of the magnetic device and the geometry of its structure.

Equation (4.1) will not be required for this analysis. The remaining equations, however, will be applied under the following assumptions which are reasonable for the study of first-order effects in practical situations.

1. Displacement currents are negligible compared to conduction currents. That is, $I_{conduction} \gg I_{displacement}$, and Eq. (4.3) becomes

$$\int_{closed} \mathbf{H} \cdot d\boldsymbol{l} = I \qquad (4.5)$$

where $I \equiv I_{conduction}$, the total conduction current which passes through the the area defined by the closed path of integration $\boldsymbol{l}$.

2. The frequencies of the time-varying quantities are low enough such that the wave-nature of the fields can be ignored. In other words, traditional quasi-static approximations and lumped parameter models apply.

3. All the flux outside the volume of the magnetic material is negligible compared to the flux inside.

4. The geometry of the structure is such that the magnitude of the flux density **B** can be assumed to be uniform throughout.

5. There are no currents within the magnetic material. This is a very reasonable assumption for materials of high resistivity such as ferrites.

6. The structure is homogeneous. That is, the material is the same throughout; it does not change in composition and has the same properties everywhere within the structure.

7. The material is isotropic. That is, it has the same

properties in every direction. Given a block of material, a structure carved from the block would behave the same regardless of the original orientation of the block. Ferrite is generally considered to be isotropic for quasi-static fields. Some magnetic materials, however, are highly *anisotropic* owing to their having a single crystal structure or because of heating and mechanical treatment.

4.2 Ampere's Law

Equations (4.3) and (4.5) are known as forms of Ampere's Circuital Law. Under certain common conditions this law reduces to a very simple form. If the magnetic field intensity H is both uniform on and parallel to some path l, and if this path encloses N turns of wire each carrying a current I, then one can write from Eq. (4.5),

$$Hl = NI \tag{4.6}$$

which is arranged into the familiar form

$$H = \frac{NI}{l}$$

Note that this relationship is valid only if H is uniform on the path l. In other words, there must not be any discrete gaps in the material along the path, as this would introduce boundary conditions which would force H to take on different values along the path of integration. The absence of gaps

is the common situation for analysis of transfomers, which will be addressed here. A similar treatment for gapped structures is straightforward. Although slightly more *complicated* because one must then consider fields of the gap as well as those of the material, it is conceptually no more *difficult*.

4.3 Faraday's Law

If one can find a situation where a component of flux density of magnitude B_0 is uniform and perpendicular to a path l which defines an area A he can write from Eq. (4.2)

$$\int_{closed} \mathbf{E} \cdot d\boldsymbol{l} = -\frac{\partial}{\partial t} B_0 A \tag{4.7}$$

The product of flux density and area is just the flux Φ. If the area does not change with time and is always perpendicular to $\mathbf{B}_0$ one can replace the partial derivative with an ordinary derivative and write

$$\int_{closed} \mathbf{E} \cdot d\boldsymbol{l} = -\frac{d\Phi}{dt} \tag{4.8}$$

The potential difference v is related to the electric field $\mathbf{E}$ by the relation

$$v_{ab} = -\int_a^b \mathbf{E} \cdot d\boldsymbol{l} \tag{4.9}$$

Using (4.8) and the standard mathematical conventions for integration around the path l one finds that if one were to traverse the path N times, the potential at the start would be higher than that at the finish by the amount

$$v = N\frac{d\Phi}{dt} \tag{4.10}$$

This is commonly known as Faraday's Law.

4.4 The Relationship of B to H

In addition to Maxwell's equations there remains one other rule to be established, and that is the relationship of **B** to **H**. This relation is of paramount importance, for it is the only one which depends on the medium. The success of any analysis of magnetic phenomena depends on one's ability to model the relationship between these two magnetic vectors.

Units

In this thesis all dimensions will be measured according to the MKSA rationalized system which is now widely accepted, as it is part of the international standard (SI) system. In this system the two field quantities have the the following unit dimensions:

$$H\ (=)\ \frac{\text{A}}{\text{m}}\ \left[\frac{\text{ampere}}{\text{meter}}\right]$$

$$B\ (=)\ \text{T}\ \ (\text{tesla})$$

where the symbol *(=)* designates dimensional unit.

Unfortunately, the old CGS or Gaussian system is still widely used in the United States. In the Gaussian system the unit for magnetic field intensity H is oersted (Oe) while the unit for flux density B is gauss (G). There is, however, a simple conversion between the units of the two systems:

$$1 \text{ gauss} = 10^{-4} \text{ tesla}$$

$$1 \text{ oersted} = \frac{1000}{4\pi} \frac{\text{A}}{\text{m}}$$

That is, to convert to gauss multiply tesla by 10000; to convert to oersted divide A/m by $1000/4\pi \approx 79.6$.

Free Space

In free space the relationship between **B** and **H** is simple and linear:

$$\mathbf{B} = \mu_0 \mathbf{H} \tag{4.11}$$

The two vectors are *colinear* and their magnitudes are related by the scalar constant μ_0, the permeability of free space, which has the value

$$\mu_0 \equiv 4\pi \times 10^{-7} \frac{\text{henry}}{\text{meter}}$$

Linear Materials

For the case of linear *isotropic* media other than free space the relationship is like (4.11) but with a different value for the scalar constant:

$$\mathbf{B} = \mu \mathbf{H} \tag{4.12}$$

Since the two vectors are colinear it is sufficient to write only the relationship between the *magnitudes* of the vectors if the direction is known. Thus,

$$B = \mu H \tag{4.13}$$

is the simplified expression which will be used here. Figure 4.1a illustrates this relationship for some arbitrary direction in a linear isotropic material.

If the material happens to be linear and *anisotropic* the relationship between **B** and **H** depends on the direction, and Eq. (4.12) must be generalized to

$$\mathbf{B} = \boldsymbol{\mu}\mathbf{H} \tag{4.14}$$

where the bold $\boldsymbol{\mu}$ is a *tensor* of second rank in three dimensions. As mentioned previously, this case will not be considered here.

Nonlinear Materials

For nonlinear isotropic materials the **B** and **H** vectors, although colinear and independent of orientation, do not have their magnitudes related by a scalar constant as in (4.13). Instead, the relationship is described by some nonlinear operation. This idea can be written in a compact form as

$$B = M(H) \tag{4.15}$$

where the operation M, whose argument is the magnitude H, is whatever may be required to model the desired nonlinearities. Figure 4.1b shows a fictitious nonlinear $B-H$ characteristic without any hysteretic effects. For this case M is a single-valued function. It could be chosen to be a

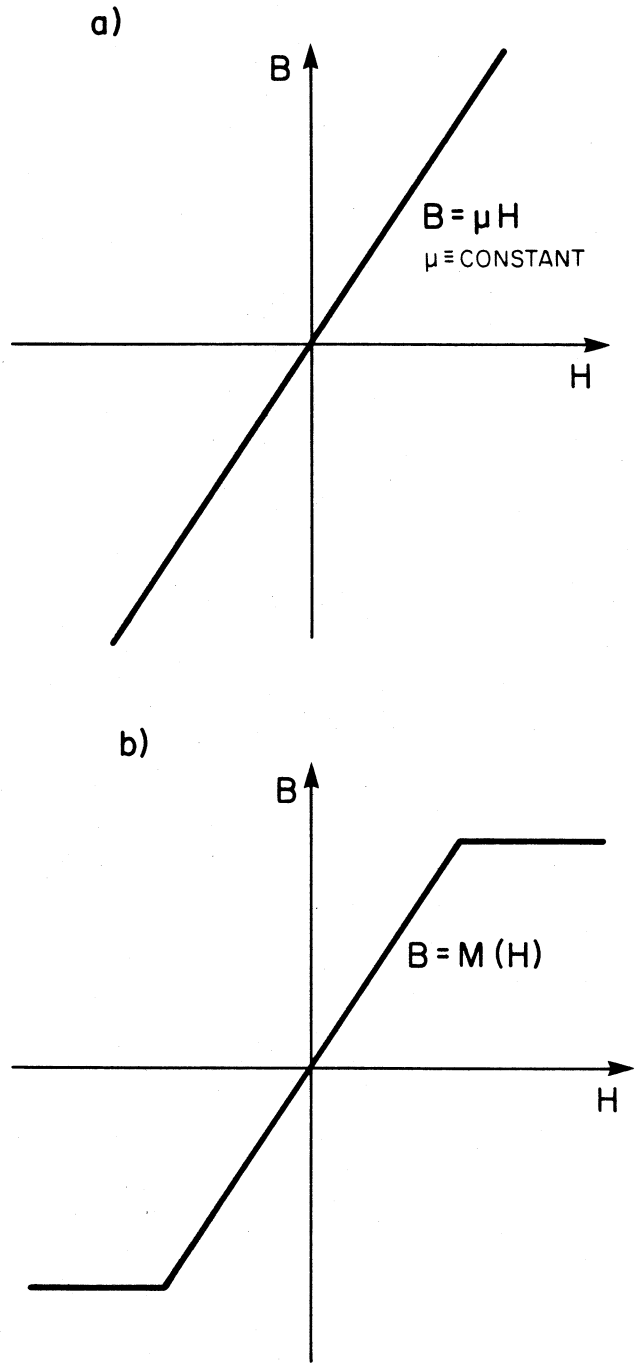

Fig. 4.1 The relationship between B and H for ideal isotropic magnetic materials: (a) linear material; (b) nonlinear material.

piecewise linear representation or a continuous representation such as an infinite series -- whatever is suitable for the situation. Equation (4.15) may of course be used to model the effects of hysteresis also, but at the hidden expense of a much more complicated M.

CHAPTER 5

ORTHOGONAL FIELDS IN NONLINEAR MEDIA

As a result of extensive use in the early literature, the word "orthogonal" has come to be used as a common synonym for "perpendicular." Although it is used here in the same way, the term is perhaps inappropriate to this discussion because orthogonality implies independence, at least in the strict mathematical sense. This chapter addresses the phenomenon of interactions between perpendicular magnetic fields in nonlinear media. The nonlinear coupling is shown in contrast to the independence expected from similar fields in ideal linear devices.

5.1 The Notion of Cause and Effect

In working with magnetic materials it is sometimes beneficial to think in terms of a cause-and-effect relationship. For the purpose of understanding the interactions of perpendicular fields in nonlinear media it is helpful to think of H as the cause and B as the effect.

Suppose there is a magnetic structure with two separate windings arranged to produce magnetic fields in two mutually perpendicular directions. Call one direction the *principal* direction and the other the *transverse* direction. A current I_P in the principal winding will produce an H-vector, $\mathbf{H}_P$, in the principal direction. Likewise, a current I_T in the transverse winding will give rise to another field $\mathbf{H}_T$ in the transverse

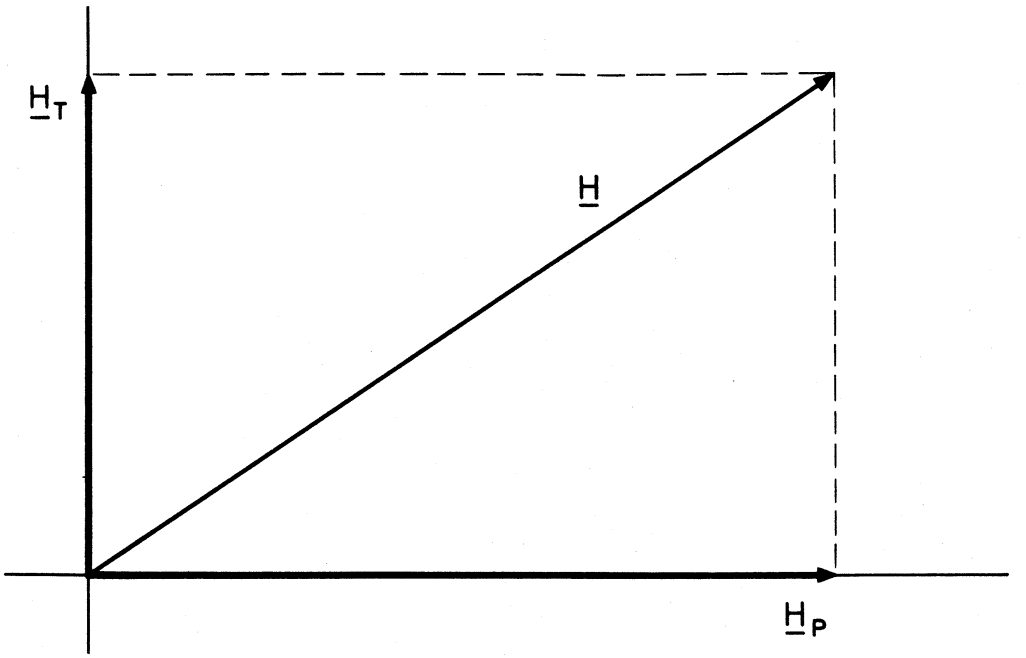

Fig. 5.1 Vector addition of two perpendicular magnetic fields $\mathbf{H}_T$ *and* $\mathbf{H}_P$ *to form the equivalent total field* **H**.

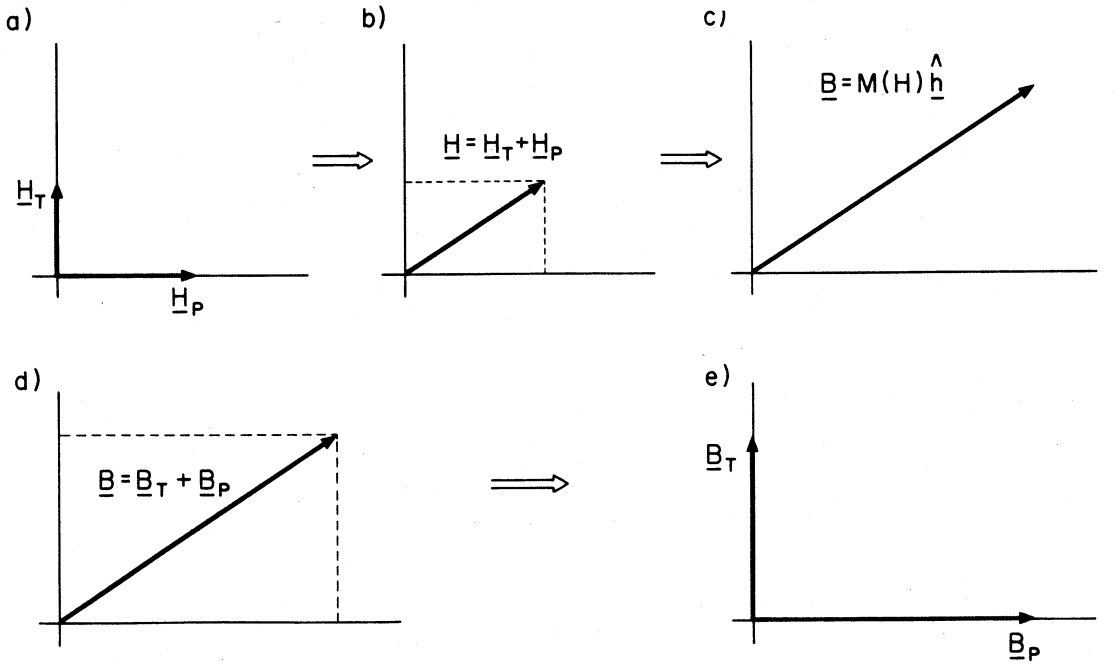

Fig. 5.2 Illustration of cause and effect. Perpendicular fields $\mathbf{H}_T$ *and* $\mathbf{H}_P$ *produce the corresponding flux densities* $\mathbf{B}_T$ *and* $\mathbf{B}_P$ *according to a relationship which depends on the characteristics of the medium.*

direction. The two magnetic field vectors, $\mathbf{H}_P$ and $\mathbf{H}_T$, will sum as vectors to form the resultant vector $\mathbf{H}$, which is the total magnetic intensity in the material. Figure 5.1 illustrates this straightforward vector addition. Vector quantities are indicated by underlines in the figures.

Figure 5.2 shows how the idea of cause and effect can be used to deduce two orthogonal B fields from the two orthogonal H fields. In Fig. 5.2a are the principal and transverse H fields. Figure 5.2b shows how the original individual fields are replaced by the equivalent resultant field H. This in turn leads to the total resultant B field of Fig. 5.2c where $\hat{\mathbf{h}}$ is a unit vector in the $\mathbf{H}$ direction. The notation in the figure emphasizes that the vector $\mathbf{B}$ is of magnitude $M(H)$ and is in the direction of $\mathbf{H}$. Figure 5.2d then shows how the total flux density vector $\mathbf{B}$ can be resolved into the sum of two orthogonal component vectors, $\mathbf{B}_T$ and $\mathbf{B}_P$. The equivalent resolution of $\mathbf{B}$ is shown in Fig. 5.2e.

A key point to be made here is that, owing to the nonlinearity of M, one must write for the general case:

$$B_T \neq M(H_T) \tag{5.1a}$$

$$B_P \neq M(H_P) \tag{5.1b}$$

The next paragraph demonstrates that Eqs. (5.1) are true for nonlinear M.

One can easily derive the following relations from the geometry of Fig. 5.2.

$$H = \sqrt{H_T^2 + H_P^2} \tag{5.2}$$

$$B = M(H) = \sqrt{B_T^2 + B_P^2} \tag{5.3}$$

$$B_T = \frac{M(H)}{H} H_T \tag{5.4}$$

$$B_P = \frac{M(H)}{H} H_P \tag{5.5}$$

If the material happens to be linear such that $M(H) \rightarrow \mu H$ then from (5.4) and (5.5)

$$B_T = \mu H_T \tag{5.6a}$$

$$B_P = \mu H_P \tag{5.6b}$$

But if the material is nonlinear, say for example $M(H) \rightarrow H^2$, then from Eqs. (5.2) through (5.5)

$$B_T = H_T \sqrt{H_T^2 + H_P^2} \neq H_T^2 \tag{5.7a}$$

$$B_P = H_P \sqrt{H_T^2 + H_P^2} \neq H_P^2 \tag{5.7b}$$

Thus the inequalities of (5.1) are true except for the special case of linear materials.

5.2 Time-varying Fields

Suppose now that the transverse current I_T is constant such that H_T is held constant. Let the principal current I_P change with time. As the principal current changes, H_P will also change because of Ampere's Law (4.6). Figure 5.3a shows the effect of a changing H_P on the resultant total **H**. As H_P takes on the magnitudes H_{P1}, H_{P2}, H_{P3}, and H_{P4}, the magnitude and direction of **H** changes respectively to $\mathbf{H}_1$, $\mathbf{H}_2$, $\mathbf{H}_3$, and $\mathbf{H}_4$. This straightforward vector addition can go on without limit as long as the material remains homogeneous. This restriction precludes any non-uniform saturation of the material which would have the effect of introducing air gaps in the magnetic path. Some non-uniform saturation is unavoidable in practice, but it is nearly always negligible for ferrites when they are operated within practical limits.

If the material were linear, such as the one characterized by Fig. 4.1a, then the application of the method of cause-and-effect would yield the **B** vectors with the components B_T and B_P as shown in Fig. 5.3b. The **B**'s are in the same directions as their respective **H**'s and the $\mathbf{B}_T$'s are all of the same magnitude. One would naturally expect this result from (5.6) since the material is assumed linear and H_T is constant by design.

Now consider the *nonlinear* material of Fig. 4.1b. As H_P increases while H_T remains constant, the magnitude of **B** increases in exactly the same way as for the linear material until it is limited by the abrupt nonlinearity of hard saturation. This situation is illustrated in Fig 5.3c. Note that the **B**'s are all in the same directions as their respective **H**'s, but

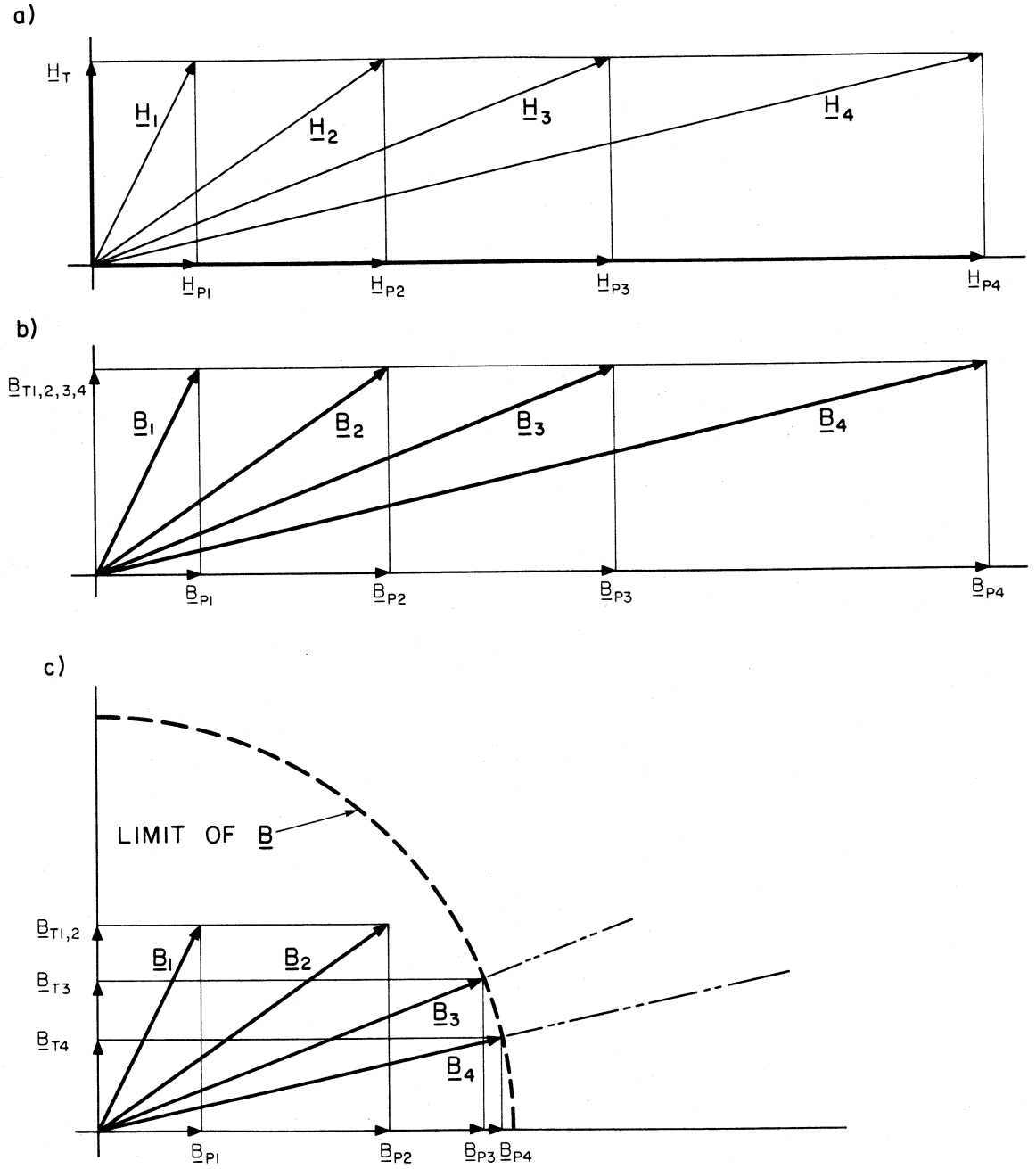

Fig. 5.3 If $\mathbf{H}_T$ *is constant and* $\mathbf{H}_P$ *changes (a), a linear material will maintain a constant* $\mathbf{B}_T$ *(b); but in a nonlinear material* $\mathbf{B}_T$ *will eventually be forced to change (c).*

as the magnitude of **B** becomes restricted, both B_P and B_T must change accordingly. Thus it is easy to see from the figure that, although H_T is constant, B_T must change with H_P and B_P. This is how orthogonal (perpendicular) magnetic fields can interact. *They are coupled not in the conventional manner by sharing of a common flux path, but rather by sharing the constraints imposed by the nonlinearity of the medium.* The B_T and B_P are no longer independent. In the nonlinear region, where B is at its limit in Fig. 5.3c, any change in B_P must be accompanied by a change in B_T. This requires, of course, that **B** change directions, and that occurs because H_P changes with B_P according to (5.5).

5.3 Exploitation of Nonlinear Effects

If there are N_T turns on the transverse winding, then a transverse voltage v_T will be produced according to Faraday's Law (4.10) as

$$v_T = N_T A_T \frac{dB_T}{dt} \tag{5.8}$$

Hence the transverse voltage v_T is a measure of the rate of change of B_T, which is in turn a measure of the increasing nonlinearity of the material. This suggests the possibility of the use of the transverse voltage to detect the impending saturation of a transformer. Real-life materials (even the so-called square-loop ones) do not saturate as abruptly as the fictitious material characteristic illustrated in Fig. 4.1b; there is always a gradual increase of nonlinearity as the material comes closer to saturation. This is illustrated in Fig. 5.4, which shows the characteristic of a typical ferrite

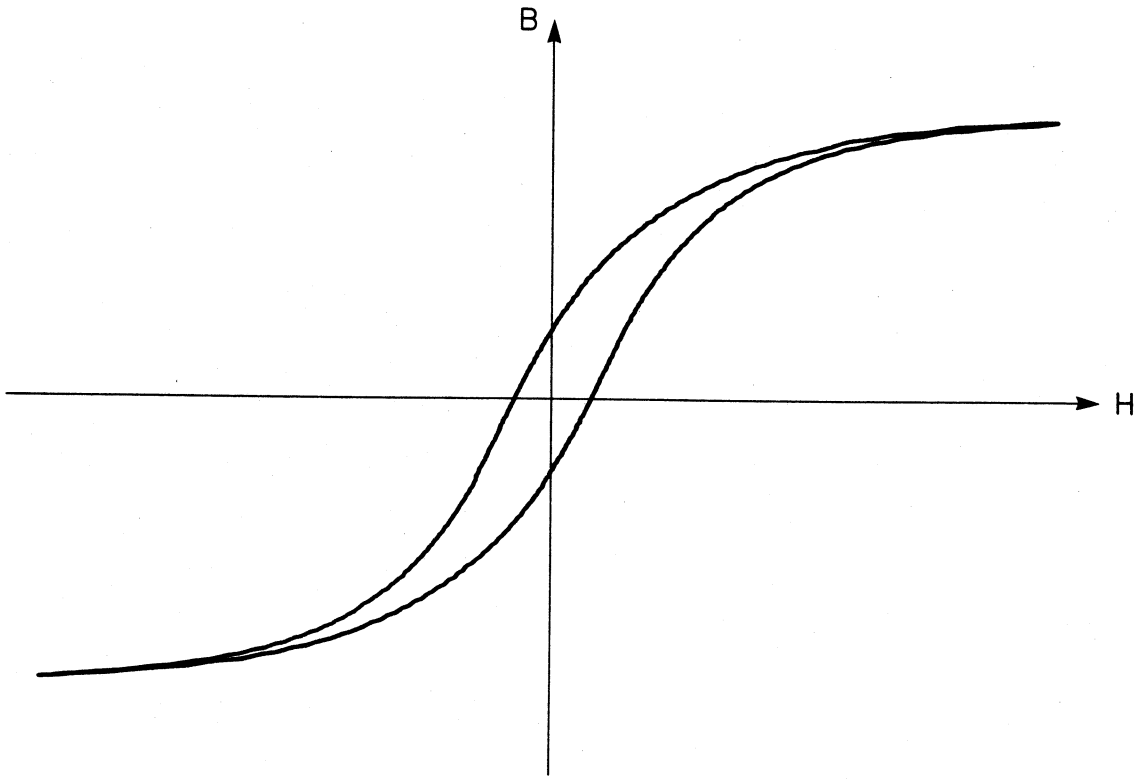

Fig. 5.4 The measured magnetic characteristic of a typical ferrite material under the assumption of uniform fields. The small amount of waviness in the curve is an artifact of digital acquisition and processing of real-time data.

material, for which this technique seems best suited.

When produced by a constant transverse field H_T, the magnitude of the resulting transverse flux density B_T indicates the degree of nonlinearity of the magnetic material, and hence is a measure of the instantaneous state of the medium as a position on the characteristic $B-H$ loop. In practice, however, the absolute flux density is not measured directly, but only its rate of change is known, being directly proportional to the transverse voltage v_T (5.8). Fortuitously, this restriction is not a drawback, but rather an advantage, simply by virtue of the way transformers are commonly used. In practice it is the principal *voltage* (primary or secondary voltage) and *not* the principal *current* (magnetization current) which is the more accurately known and controlled quantity. After all, if it were easy to measure the magnetization current accurately, one would merely use that signal to limit the $B-H$ excursion and the problem of saturation would be solved. The principal voltage v_P is related to the rate of change of B_P by Faraday's Law just as v_T is related to the rate of change of B_T. Thus, the increasing nonlinearity of the material can be deduced just as well from the ratio of v_T/v_P as it could from the ratio of B_T/B_P or from B_T alone. For example, if the material happened to be linear in some region, then B_T should not change and v_T would be zero, which would indicate no nonlinearity. Moreover, since in most applications of switching converters v_P is constant during the time that the transformer is being energized, the ratio v_T/v_P is just v_T scaled by a

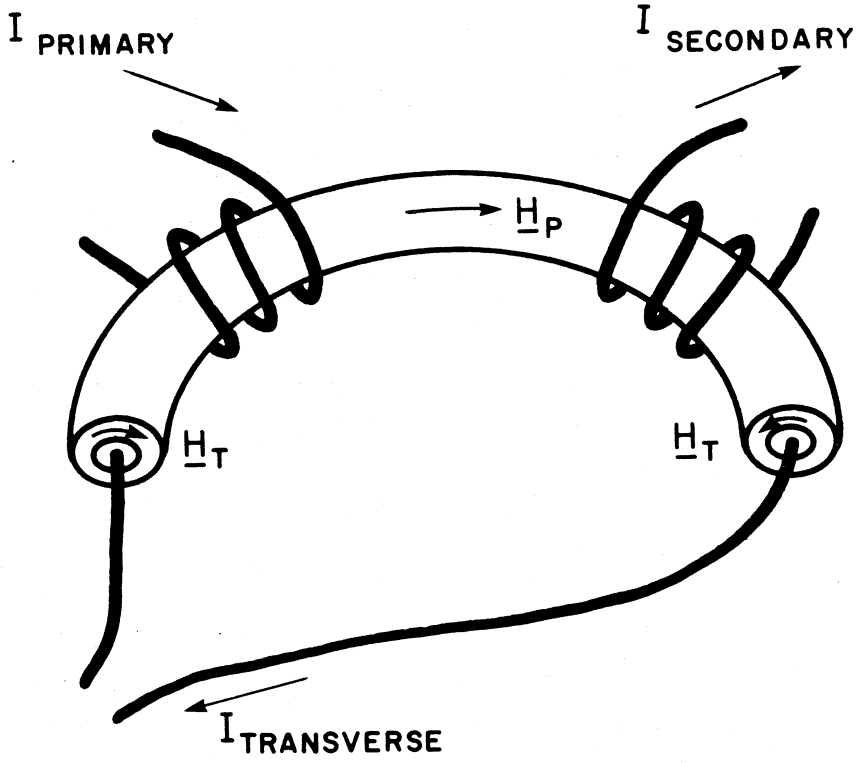

Fig. 5.5 Cutaway view of a hypothetical hollow toroid with principal and transverse windings. The two magnetic fields H_T *and* H_P *are perpendicular everywhere within the structure.*

known constant determined by the input voltage of the power converter. Thus the degree of nonlinearity can be deduced from observation of just the transverse voltage v_T.

5.4 Application to Conventional Transformer Structures

The problem to be addressed now is how to easily introduce a transverse field into the core material of a transformer. Figure 5.5 is a cut-away view of a fictitious transformer wound on an idealized hollow toroidal core with a transverse winding. Here the principal current is the familiar magnetization current, which, according to the directions assigned in the figure, is just

$$I_P = N_1 I_{PRIMARY} - N_2 I_{SECONDARY} \tag{5.9}$$

where N_1 and N_2 are the number of primary and secondary turns, respectively. This is the quantity NI used in Ampere's Law (4.6). It is clear from the cylindrical geometry of this structure that the principal and transverse fields are everywhere mutually perpendicular. (This idealization is slightly flawed for an actual physical structure of this type, because the wires of the transverse winding must somewhere penetrate the wall in order to be accessible.) Cores of this type have actually been built by others [15, 16, 17] for a variety of different purposes related to the use of orthogonal fields. This is the first time, however, that orthogonal fields have been exploited to detect impending saturation in power converters.

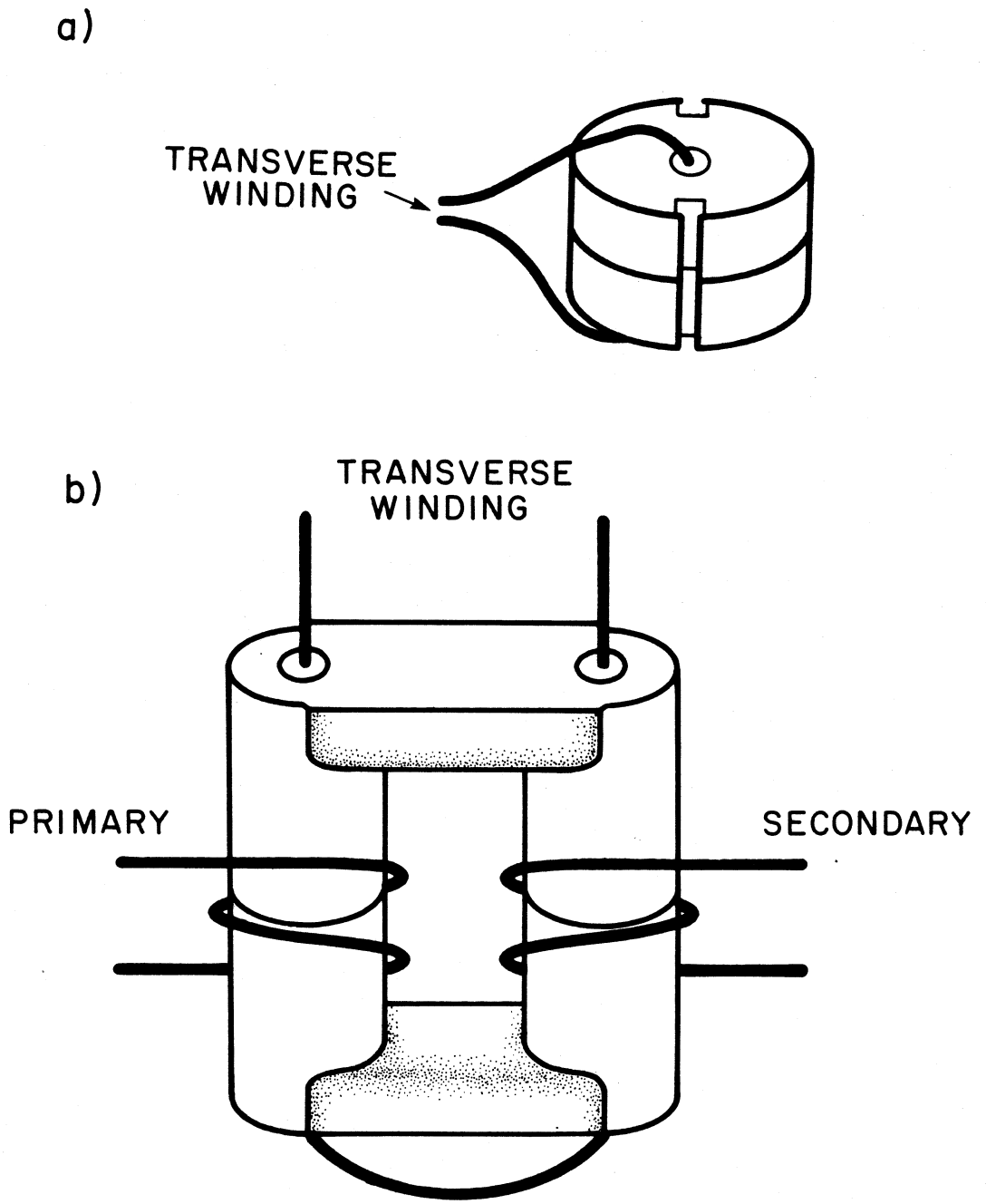

Fig. 5.6 Implementation of a transverse winding on a standard pot core (a) and a pair of U64 cores (b). The transverse winding is threaded through holes normally intended for mounting hardware.

In a more practical vein, it is relatively easy to find standard off-the-shelf ferrite parts with holes already in the right places to accommodate transverse windings. Figure 5.6a shows the implementation of a transverse winding on a standard pot core, and Fig. 5.6b shows how it may be used with a set of Ferroxcube U64 cores.

CHAPTER 6

GENERAL MATHEMATICAL TREATMENT

It has been established that perpendicular magnetic fields can indeed interact. Furthermore, a motivation and a philosophy are in place to exploit this phenomenon as a saturation detector for transformers. The next step, then, is to analyze this interaction to better understand how it may be used effectively to avoid undesirable saturation in real-life power transformers.

6.1 Qualitative Description

As a first approach to any mathematical treatment, it is useful to obtain a qualitative picture of the expected results. Assume that a pure, *symmetrical* ac voltage (dc-blocked) is applied to the primary of a transformer, and that any effects of hysteresis are negligible. Under these assumptions and with a constant H_T, Fig. 6.1 illustrates the relationship between B_P and B_T for specific instants of time for the simple nonlinear characteristic of Fig. 4.1b.

Several salient features of the response to be observed on the transverse winding are now apparent. As B_P swings positively and negatively along the horizontal axis, the symmetry of the geometry gives the same B_T for both positive and negative excursions of B_P. Thus it is easy to see that the fundamental frequency of the signal on the transverse winding is exactly

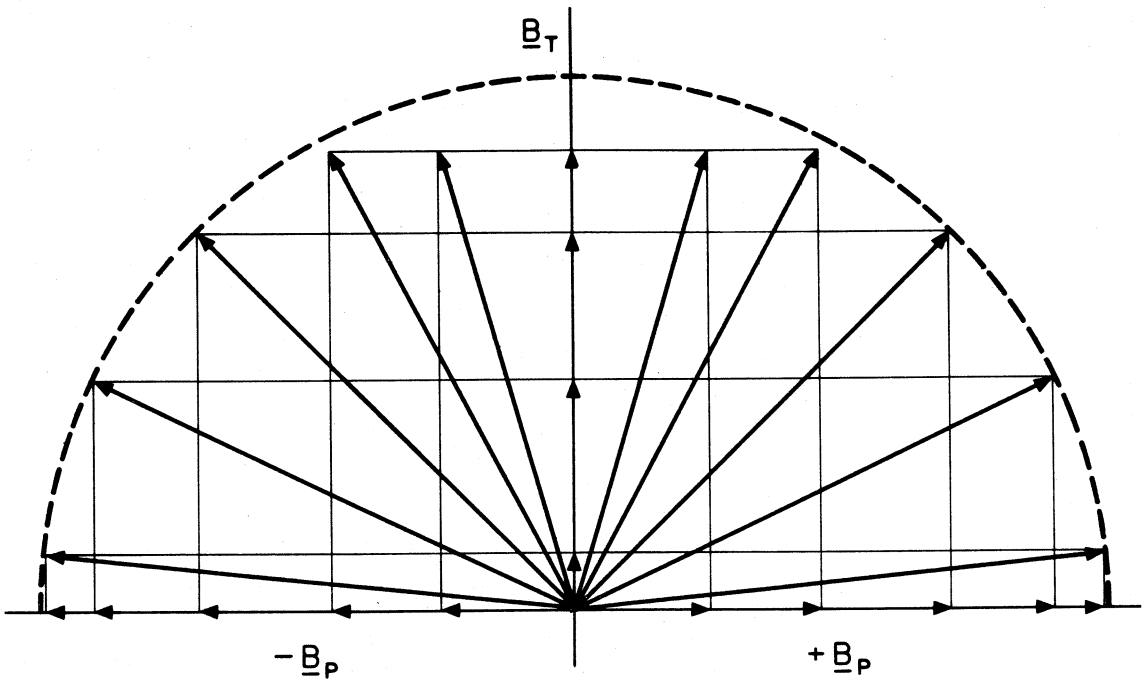

Fig. 6.1 Illustration of the locus of the total **B** *vector for the ideal nonlinear material characteristic of Fig. 4.1b. As the principal flux density* $\mathbf{B}_P$ *varies positively and negatively along the principal axis, the vector* **B** *swings back and forth, its magnitude being limited at the heavy dashed line. Symmetric periodic positive and negative variations of* $\mathbf{B}_P$ *cause the* $\mathbf{B}_T$ *to vary periodically at twice the frequency of* B_P.

twice that of the ac voltage on the primary (principal) winding. This same sort of frequency-doubling is observed when a signal is full-wave rectified (another nonlinear process). Note, however, that nothing has been said yet about the relative ***shapes*** of the waveforms of the voltages v_P and v_T.

It can also be seen from the figure that B_T ***decreases*** in the positive transverse direction as B_P ***increases*** in magnitude. If the direction of the transverse current were reversed to change the direction of H_T and B_T, then B_T would ***decrease*** in the ***negative direction***, which is equivalent to an ***increase*** in the ***positive direction***. Thus the polarity of v_T would change if the transverse current were reversed.

One more important attribute can be predicted from Fig. 6.1. If B_P changes at a constant rate, the B_T changes more rapidly as B_P gets closer to the saturation limit. Thus, one should expect the voltage on the transverse winding to increase monotonically in magnitude if B_P varies linearly with time.

As a prelude to the general mathematical treatment and in support of the qualitative understanding described above for an ideal material, a ferrite pot core (Fig. 5.6a) made from the material described by the characteristic of Fig. 5.4 was excited by perpendicular fields. Observations for two different principal voltage waveforms, square and sinusoidal, are shown in Fig. 6.2. The photographs on the left are of principal and transverse voltages; their respective flux densities (obtained by integration of the voltages) are on the right. All the voltage

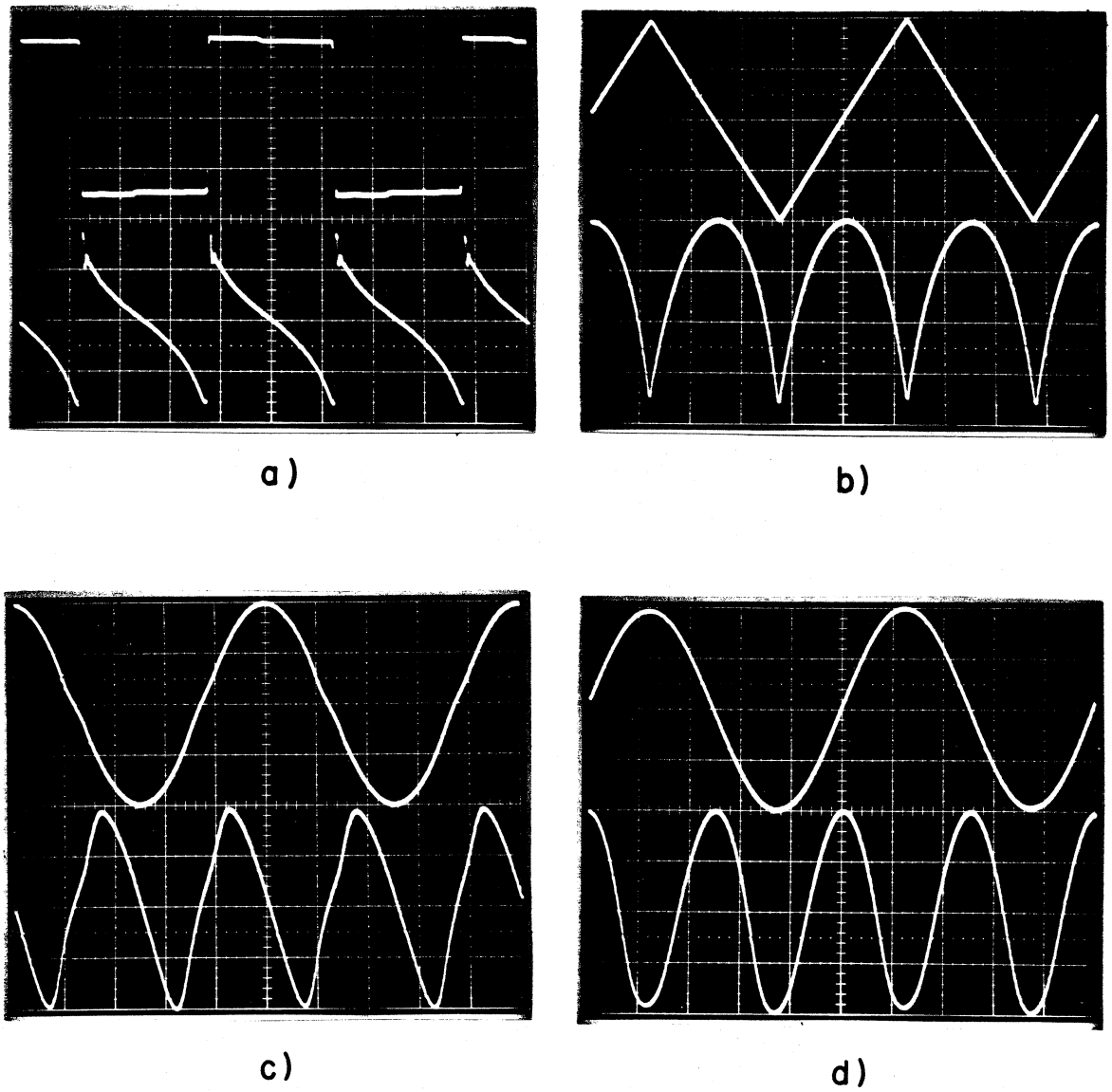

Fig. 6.2 Principal and transverse voltages and flux densities for two different excitations. Voltages are on the left and flux densities are on the right. Upper traces are principal quantities and lower traces are transverse quantities. Note the frequency doubling caused by the nonlinear process.

waveforms and the principal flux densities (top traces) are centered around zero, but the transverse flux densities are always positive, owing to the presence of the constant bias of the dc transverse current. Scale factors are immaterial at this point because only the qualitative features are of interest here.

Photographs (a) and (b) are illuminating because the principal flux density varies at a linear rate owing to the (nearly) square-wave drive. Thus the time axis of (b) is directly proportional to B_P, and hence the transverse flux density at the bottom of the photograph traces the relationship of B_T to B_P. If the material had the ideal piecewise-linear characteristic of Fig. 4.1b, then the locus of B_T would consist of repetitions of parts of semicircles with flat tops, as suggested by Fig. 6.1. Because the actual material is not piecewise-linear, however, it is not necessary to drive the core to its limits in order to see the nonlinear effects. In fact, these observations were made with rather small flux excursions to illustrate the presence of nonlinearity far from the obvious regions of saturation. In addition it should be pointed out that, commensurate with the levels of excitation, the principal and transverse quantities are not shown at the same scale factor -- the bottom traces are much smaller in absolute magnitude than their principal counterparts.

Photographs (c) and (d) show the results for a sinusoidal voltage drive. Although the shapes of the waveforms are quite different from those in (a) and (b), the observations are consistent with our qualitative

understanding of the phenomenon. That is, the transverse quantities repeat at twice the frequency of the principal excitation, and the transverse flux decreases as the principal flux increases in magnitude.

6.2 Derivation of Practical Expressions

Now that the qualitative examination is complete, one may attempt a more quantitative analysis. One possibility is to find an expression for B in terms of v_T and v_P. With such a relationship one should be able to compute the magnitude of B in the material from observation of v_T and knowledge of v_P. A more practical design-oriented approach, however, is to find an expression for v_T in terms of B and v_P. With the latter form of expression, a designer would first choose a maximum B to which he wishes to drive the transformer's core. Then, because he would know the v_P at which his transformer would operate, he would be able to calculate the magnitude of v_T which would appear on the transverse winding when that B is reached. Upon detection of this voltage level, the circuit would take appropriate action to prevent a further increase in B to keep the transformer out of saturation. The goal, then is to find an expression of the form

$$v_T = f(B, v_P) \tag{6.1}$$

At this early stage of the analysis there is no assurance that it is possible to find such an expression in a closed form. And even if an expression is found, it may not be useful to the designer owing to excessive complexity, limited accuracy, or a strong dependence on unquantified

characteristics of the material. Nevertheless, it will be beneficial to undertake this analysis to acquire a better understanding of the phenomena and to test and refine the rather crude qualitative predictions made in the previous discussion.

The starting point is to look for a general expression whose only time-varying quantities are B_T and B_P. One could then differentiate this expression with respect to time to obtain another expression which relates v_T to v_P and B.

From (5.2), (5.3), and (5.4) one can write the general relation

$$B_T = H_T \frac{\sqrt{B_T^2 + B_P^2}}{\sqrt{H_T^2 + H_P^2}} \tag{6.2}$$

This is almost what is required. The only difficulty is that H_P is an unknown function of B_P. The two are linked in a very complicated fashion through the material property $M(H)$ as shown previously in (5.5). It is absolutely essential that the characteristic of the material be included somewhere in the expression, because that is the very mechanism responsible for the variations in B_T. The easiest way to incorporate the material properties into (6.2) is to use the inverse of the customary form. Traditionally the B-H relationship has been given as a function of H; but there is no reason whatsoever why it cannot be presented as a function of B! That is, for a given material one may write either

$$B = M(H) \tag{4.15}$$

or the equivalent

$$H = W(B) \tag{6.3}$$

This defines W to be the inverse operation of M. Now one can rewrite (6.2) as

$$B_T = H_T \frac{\sqrt{B_T^2 + B_P^2}}{W\left(\sqrt{B_T^2 + B_P^2}\right)} \tag{6.4}$$

This relationship is the foundation upon which the general analysis is constructed, and some difficulties are already apparent. The fact that it is not possible to solve (6.4) explicitly for B_T (except for the linear case where $W = B/\mu$) means that any useful result obtained from this analysis will not be exact. Since the resulting expressions will necessarily be only approximate, care must be taken when they are used to see that the underlying assumptions of their derivations are valid.

Implicit differentiation of (6.4) with respect to B_P gives

$$\frac{dB_T}{dB_P} = - \frac{\frac{H_T}{W(B)}\left[\frac{B_P}{W(B)}\frac{dW(B)}{dB} - \frac{B_P}{B}\right]}{1 + \frac{H_T}{W(B)}\left[\frac{B_T}{W(B)}\frac{dW(B)}{dB} - \frac{B_T}{B_P}\right]} \tag{6.5}$$

where $B \equiv \sqrt{B_T^2 + B_P^2}$.

Although this expression is exact, it is quite useless owing to the presence of the unknown variable B_T on the right-hand side. Clearly

some judicious approximations are in order.

For practical applications, the transverse field H_T will be much less than the principal field H_P in the region of interest. This is reasonable since the only purpose of the transverse field is to sense the state of the core. An excessively large H_T would mean that a significant portion of the total H available in the core would be devoted to the sensing function, and this would indicate that the magnetic structure is being used ineffectively for power processing.

From (5.4) and (5.5) one gets the relationship

$$B_T = \frac{H_T}{H_P} B_P \tag{6.6}$$

From this it is clear that if $H_T \ll H_P$ then

$$B_T \ll B_P \tag{6.7}$$

The inequality is reinforced when both sides are squared:

$$B_T^2 \ll B_P^2 \tag{6.8}$$

Now one can use (6.8) to make the simplifying approximation

$$B_T^2 + B_P^2 = B^2 \approx B_P^2 \tag{6.9}$$

which, when substituted in (6.4), yields the approximate relation

$$B_T \approx H_T \frac{B_P}{W(B_P)} \tag{6.10}$$

This expression, when differentiated with respect to B_P gives

$$\frac{dB_T}{dB_P} \approx - \frac{H_T}{W(B_P)} \left[\frac{B_P}{W(B_P)} \frac{dW(B_P)}{dB_P} - 1 \right] \tag{6.11}$$

A comparison of this approximate relation with the exact expression (6.5) shows that the validity of (6.11) is subject to the satisfaction of an additional inequality, namely,

$$\frac{B_T}{B_P} \frac{H_T}{W(B_P)} \left[\frac{B_P}{W(B_P)} \frac{dW(B_P)}{dB_P} - 1 \right] \ll 1 \tag{6.12}$$

Thus, although the inequality of (6.8) is ***necessary*** for (6.11) to be valid, it is not ***sufficient***. The validity of (6.11) depends also on the material characteristic according to the second inequality, (6.12), which usually can be easily estimated with knowledge of the $W(H)$ of the magnetic material and the chosen region of operation. Note that a knowledge of B_T is not required for this computation since from (6.6)

$$\frac{B_T}{B_P} = \frac{H_T}{H_P} \tag{6.13}$$

The general analysis is now nearly complete, for all that remains is to produce an expression in v_T and v_P from (6.11). This is accomplished by application of the chain rule of calculus and Faraday's Law (4.10):

$$\text{chain rule:} \qquad \frac{dB_T}{dt} = \frac{dB_T}{dB_P}\,\frac{dB_P}{dt} \tag{6.14}$$

$$\text{Faraday's Law:} \qquad v_T = N_T\,\frac{d}{dt}\,(B_T A_T) = N_T A_T\,\frac{dB_T}{dt} \tag{6.15}$$

$$v_P = N_P\,\frac{d}{dt}\,(B_P A_P) = N_P A_P\,\frac{dB_P}{dt} \tag{6.16}$$

In (6.15) N_T and A_T are respectively the number of turns and the cross-sectional area in the transverse direction. In (6.16) A_P is the cross-sectional area in the principal direction and N_P is the number of turns on whatever winding (primary or secondary) happens to be associated with the voltage v_P.

Use of (6.14) with (6.15) and (6.16) yields the desired transformation:

$$v_T = v_P\,\frac{N_T A_T}{N_P A_P}\,\frac{dB_T}{dB_P} \tag{6.17}$$

A useful dimensionless quantity by which models and designs may be easily compared is obtained by normalization of (6.17) with respect to the principal voltage v_P. The normalized expression, here called the Magnetic Transfer Ratio (MTR), is defined to be

$$\text{MTR} \equiv \frac{v_T}{v_P} = \frac{N_T A_T}{N_P A_P}\,\frac{dB_T}{dB_P} \tag{6.18}$$

The material properties are included by substitution of (6.11) into (6.18):

$$\frac{v_T}{v_P} \approx - \frac{N_T A_T}{N_P A_P} \frac{H_T}{W(B_P)} \left[\frac{B_P}{W(B_P)} \frac{dW(B_P)}{dB_P} - 1 \right] \tag{6.19}$$

The transverse field H_T may be related to external parameters by Ampere's Law (4.6)

$$H_T = \frac{N_T I_T}{l_T} \tag{6.20}$$

In this last expression, I_T is the constant current in the transverse winding and l_T is the effective path length of the transverse magnetic field.

Substitution of (6.20) into (6.19) is the final step, which yields the MTR in terms of known quantities:

$$\frac{v_T}{v_P} \approx - I_T \frac{N_T{}^2 A_T}{N_P A_P l_T} \frac{1}{W(B_P)} \left[\frac{B_P}{W(B_P)} \frac{dW(B_P)}{dB_P} - 1 \right] \tag{6.21}$$

This result comes very close to the desired goal, which was to obtain a general expression that relates v_T to v_P and B in the form suggested by (6.1). Recall that here $B_P = B$ by virtue of the approximation (6.6). This form of the expression isolates the three factors which are of greatest interest to the designer: the sensing current, the geometrical factor, and the material factor. The MTR is written with a minus sign in front to emphasize that in the region of interest (B increasing toward saturation) the signal is negative, as was predicted in the qualitative analysis.

It will be demonstrated later that for common ferrites the expression in brackets is positive for positive v_p and negative for negative v_p as the material approaches saturation. Note that, for an ideal linear material whose characteristic may be described as $W(B_p) = \frac{B_p}{\mu}$, the term in brackets is identically zero as one should expect.

CHAPTER 7

PREDICTIONS OF PERFORMANCE

This chapter addresses the problem of finding suitable mathematical models for the intrinsic properties of magnetic materials. Several "W" functions of increasing complexity are used to approximate the dynamic magnetic characteristics of common ferrites. It is not the intent of this modelling to be able to give an accurate quantitative prediction of the observed performance, for that would require a model of such great detail that it would be much too complicated to be useful. Rather, simple models are sought to help understand the first-order effects of variations in the characteristics of practical materials to provide guidance for a good engineering design. The models will ultimately be evaluated on the basis of their ability to predict the Magnetic Transfer Ratio observed for typical ferrite compositions used for switched-mode power transformers.

7.1 Models for Practical Materials

Because of their low-loss properties and other favorable qualities, ferrite materials are widely used for high frequency switched-mode power processing. Despite their popularity in this and other areas, however, very little information is available to explain or to model the behavior of ferrites under various environmental and large-signal conditions. The intrinsic material properties depend not only on external parameters such as

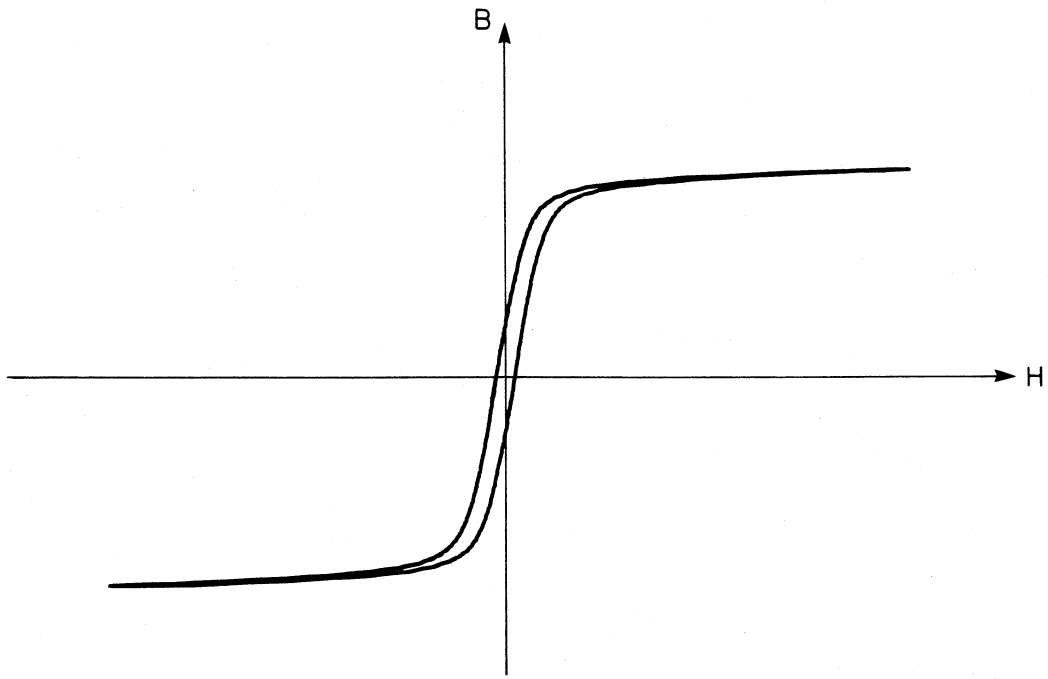

Fig. 7.1 B-H characteristic of an RM10 core of H7C1 material. The curve is computed from measurements of voltage and current under the assumption of uniform fields in the core.

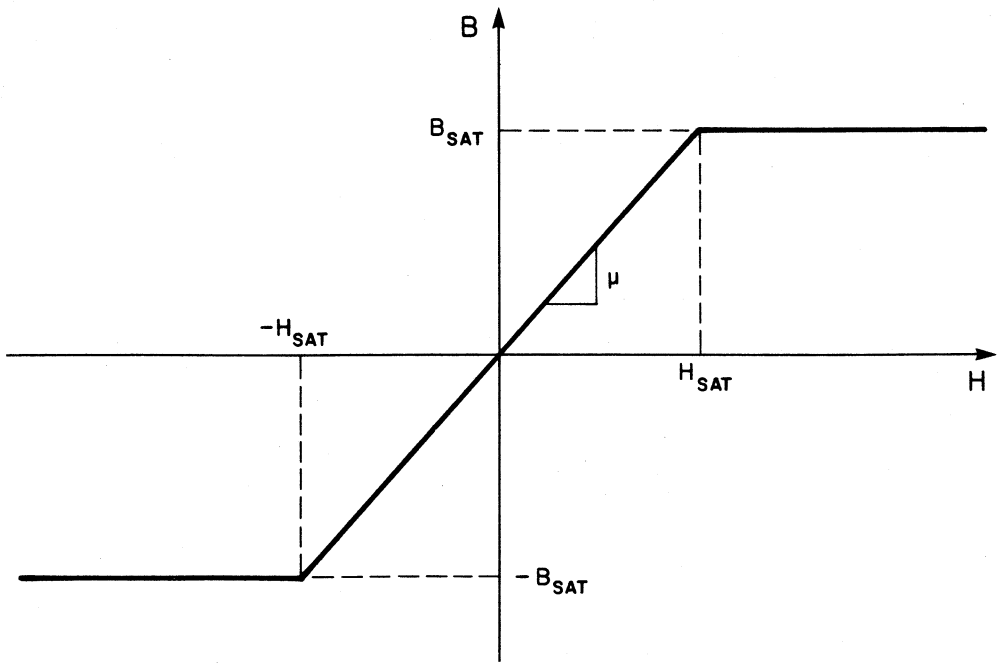

Fig. 7.2 B-H characteristic for the piecewise hard saturation model.

temperature, but also on the electrically induced excitations to which they are exposed. For example, the results of recent work on such characterizations [18] show that measurements of inductance made on ferrite toroids with signals of different magnitudes and shapes agree only at low signal levels. This being the case, one should expect at best to be able to find a model which gives only a good *qualitative* description of the MTR, since that ratio depends strongly on the nonlinear characteristics of the material and is interesting only for large flux excursions.

7.2 Piecewise Model for Hard Saturation

Figure 7.1 shows the material characteristic of a typical ferrite when it is driven far into saturation. The simplest model for this behavior is the familiar straight-line approximation introduced in Fig. 4.1b and reproduced with appropriate labels in Fig. 7.2. The approximate expression (6.21) is not very useful for this special case because the oversimplified model in combination with the analytic approximations hides all the interesting information behind singularities. Although the original expression of (6.5) can be used, its evaluation would be quite painful. But luckily, since this is such a special case, the extra mathematical labor can be avoided and at the same time an *exact* expression can be found from the geometry of Fig. 5.3c. This is possible only because B is a constant for $H > H_{SAT}$, and hence, the locus of the **B** vector is known to lie on a circle of radius B_{SAT}.

Since the model is linear for $B < B_{SAT}$ we know that the MTR must be zero in that region:

$$\frac{v_T}{v_P} \equiv 0 \quad \text{for} \quad B < B_{SAT} \tag{7.1}$$

When $B = B_{SAT}$ one can write

$$B_T = \sqrt{B_{SAT}^2 + B_P^2} \tag{7.2}$$

where $B_{SAT} \equiv$ CONSTANT.

Differentiation with respect to B_P gives

$$\frac{dB_T}{dB_P} = - \frac{B_P}{\sqrt{B_{SAT}^2 - B_P^2}} \tag{7.3}$$

Since the ratio $\frac{v_T}{v_P}$ is directly proportional to $\frac{dB_T}{dB_P}$ the scale factors are immaterial to our interest in the shape of the MTR, and they therefore may be set to unity.

The MTR changes from the description of (7.1) to (7.3) at the point where $B = B_{SAT}$; that is, where $H_T = B_T/\mu$ and $H_P = B_P/\mu$. It is easily shown, after a line or two of algebra, that at this point the value of B_P is

$$B_{P0} = \sqrt{B_{SAT}^2 - \mu^2 H_T^2} \tag{7.4}$$

at which place

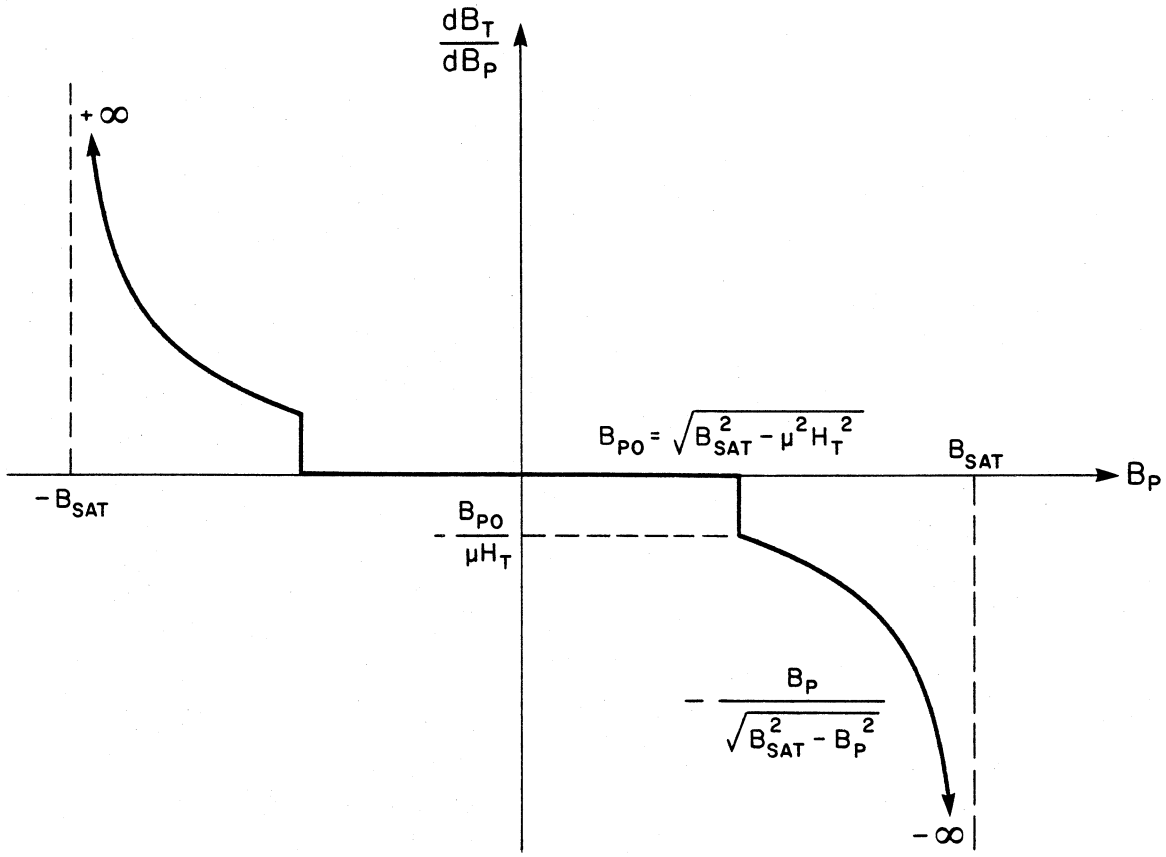

Fig. 7.3 General shape of the MTR as predicted by the piecewise hard saturation model.

$$\left.\frac{dB_T}{dB_P}\right|_{B_P = B_{P0}} = -\left[\frac{B_{SAT}^2}{\mu^2 H_T^2} - 1\right]^{\frac{1}{2}} = -\frac{B_{P0}}{\mu H_T} \qquad (7.5)$$

In these last two expressions positive square roots are to be taken for B_P in the positive direction. The results of this analysis are shown in Fig. 7.3.

The figure shows a discontinuity in $\frac{dB_T}{dB_P}$ at $B_P = B_{P0}$ which occurs at the point where the **B** vector reaches its maximum magnitude, and, consequently, forces B_T to begin to change. There is no violation of fundamentals here, for the discontinuity is not a step change in *flux*, but rather a change in the *rate of change of flux*. There is nothing wrong with an instantaneous change of voltage across an inductance, and that is just what happens in this model at B_{P0}.

According to this model, the response is independent of H_T for $B_P > B_{P0}$. The only role played by H_T is to determine the point of discontinuity at B_{P0}. The result that the magnitude of the MTR tends to infinity as B_P approaches B_{SAT} is predictable by inspection of Fig. 5.3c, which shows that the circle of maximum B has a vertical tangent at $B_P = \pm B_{SAT}$.

7.3 Piecewise Model for Soft Saturation

It was shown in the last section that the piecewise model for hard saturation predicts an unbounded MTR, independent of H_T as B_P approaches B_{SAT}. Both these results are caused by the vertical tangent of the limit of

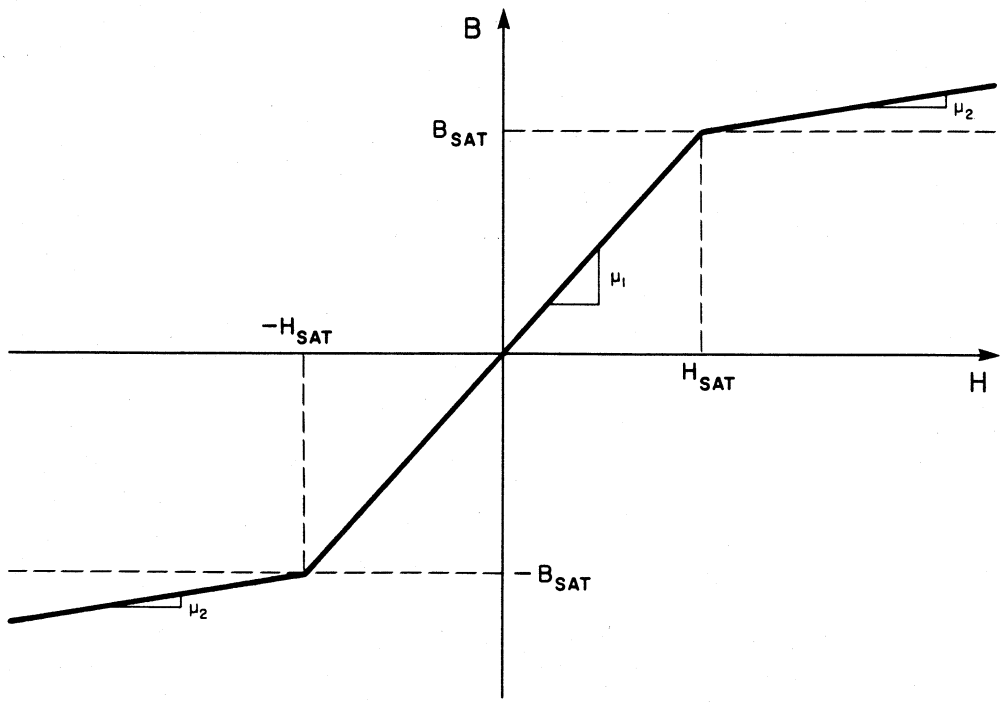

Fig. 7.4 B-H characteristic for the piecewise soft saturation model.

B in the principal-transverse plane. A closer look at the material characteristic measured for Fig. 7.1 reveals that, contrary to the description of the hard saturation model, the flux density is not asymptotic to a line that is parallel to the H-axis, but rather approaches a line with non-zero slope. This observation motivates the proposal of the piecewise model for soft saturation illustrated in Fig. 7.4.

There are several important differences between this model and the previous one. The major distinction between the two is that the soft saturation model permits B to exceed B_{SAT}. The locus of the tip of the **B** vector in the principal-transverse plane is not limited by the boundary of a circle at B_{MAX}, but is now described by the relation

$$B = \mu_2 \left[\sqrt{H_T^2 + H_P^2} - H_{SAT}\right] + B_{SAT} \qquad (7.6)$$

for $\sqrt{H_T^2 + H_P^2} \geq H_{SAT}$

The curve described by (7.6), unlike the circular boundary, does not have a vertical tangent in the principal-transverse plane because the total B is not limited, but rather increases as a function of H_P and H_T. The shape of this locus is not precisely known because it is not possible to solve the equation explicitly for B_T in this region. This additional complexity is another major difference between the two models. The nonzero value for the slope μ_2 is a mathematical complication which obviates the possibility of one's finding an exact general expression for the MTR. It is beneficial, however, to look at an approximate expression.

As in the hard saturation model, we know that the MTR must be zero in the linear region where $B < B_{SAT}$. For $B \geq B_{SAT}$ the characteristic model of Fig 7.4 is easily inverted to give

$$W(B) = \frac{(B - B_{SAT})}{\mu_2} + \frac{B_{SAT}}{\mu_1} \tag{7.7}$$

which may be used either with (6.5) or with (6.11) and (6.12) to find an approximate expression for the MTR. Either way, it turns out that an approximate expression can be found for the general case only under the assumptions that $B_T \ll B_P$ and $H_T \ll H_P$. Under those circumstances the general approximate expressions are valid only for values of B_P equal to or greater than B_{SAT}. For a *particular* characteristic model, where the actual numerical values for the parameters are known, one may write approximate expressions that are valid for a wider range of B_P. In the absence of such details, however, it is not possible to make such claims in general.

Use of (6.11) under the constraints of (6.12) gives the approximate relation

$$\frac{dB_T}{dB_P} \approx - H_T \frac{\mu_2 B_{SAT}\left[1 - \frac{\mu_2}{\mu_1}\right]}{\left[B_P - B_{SAT}\left[1 - \frac{\mu_2}{\mu_1}\right]\right]^2} \tag{7.8}$$

where it is understood that $\mu_2 < \mu_1$. This expression is valid for $B_P \geq B_{SAT}$ (where the hard saturation model is not defined) if H_T is sufficiently small. Although this model is of little practical use, it does

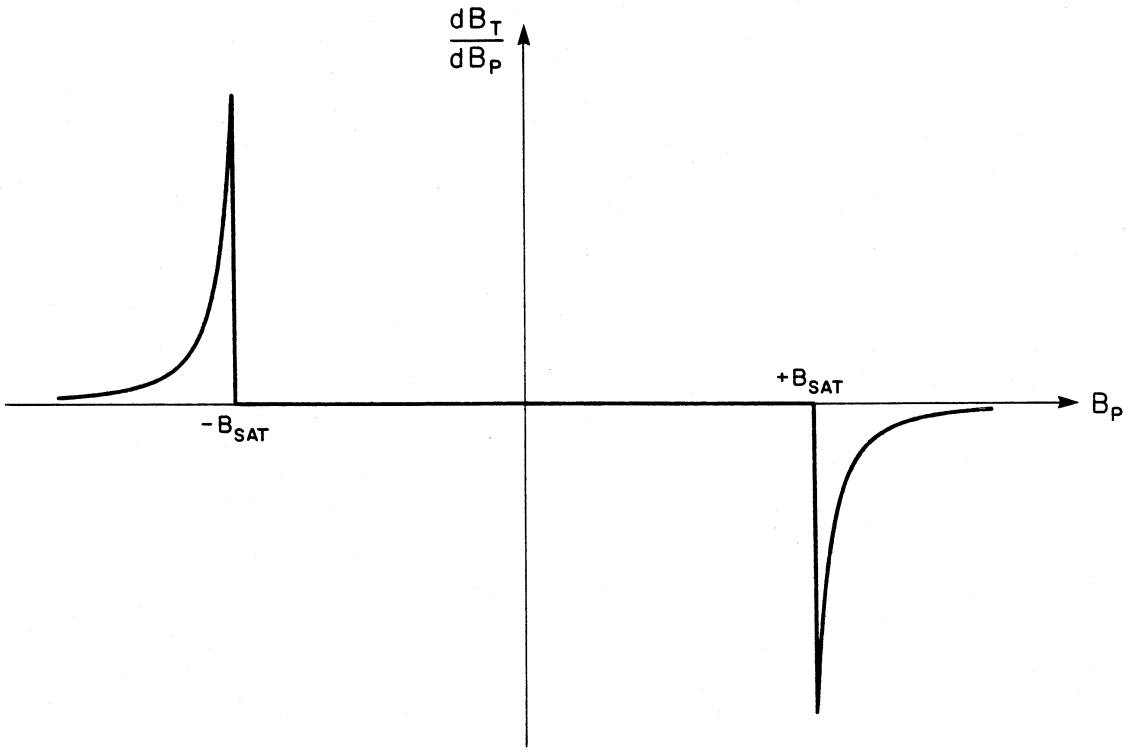

Fig. 7.5 General shape of the MTR as predicted by the piecewise soft saturation model for the conditions of $B_P > B_{SAT}$ and $H_T \ll H_P$. The model, of course, does not predict discontinuities at $B_P = \pm B_{SAT}$, but, since good general approximations cannot be made in the region between $\pm B_{SAT}$, nothing is plotted there.

show the two important theoretical results, that the MTR is proportional to H_T and that it *tends to zero as* $B_P \rightarrow \infty$. Figure 7.5 shows the general shape of the MTR predicted by (7.8) for $B_P \geq B_{SAT}$, $H_T \ll H_P$, and $\mu_2 \ll \mu_1$ for one arbitrary value of H_T. Although the MTR for this model is in general not strictly zero for $|\mathbf{B}| < B_{SAT}$ nothing is shown for that region in the figure because good approximations cannot be made without the consideration of numerical values.

7.4 Continuous Model for Hard Saturation

The second piecewise model predicted two important features of the MTR that were not predicted by the first model. The range over which the second model is valid, however, is rather restricted owing to a lack of detailed information about the general characteristics of the material. In each of the piecewise models just discussed, there were only two distinct slopes associated with the material characteristic and only a single point of intersection which formed the knee at $B = B_{SAT}$. If the number of slopes and the number of intersections could be increased, more detailed information about the general shape of the material characteristic could be incorporated into the model. Consequently, the range of validity would be increased and the general accuracy of the model would be improved. The necessary details are held in one's *a priori* knowledge of the general properties of the material.

A generalization of the idea of piecewise modelling is to find a *continuous function* which more closely approximates the known shape of the B-H characteristic of the material than the piecewise approximation.

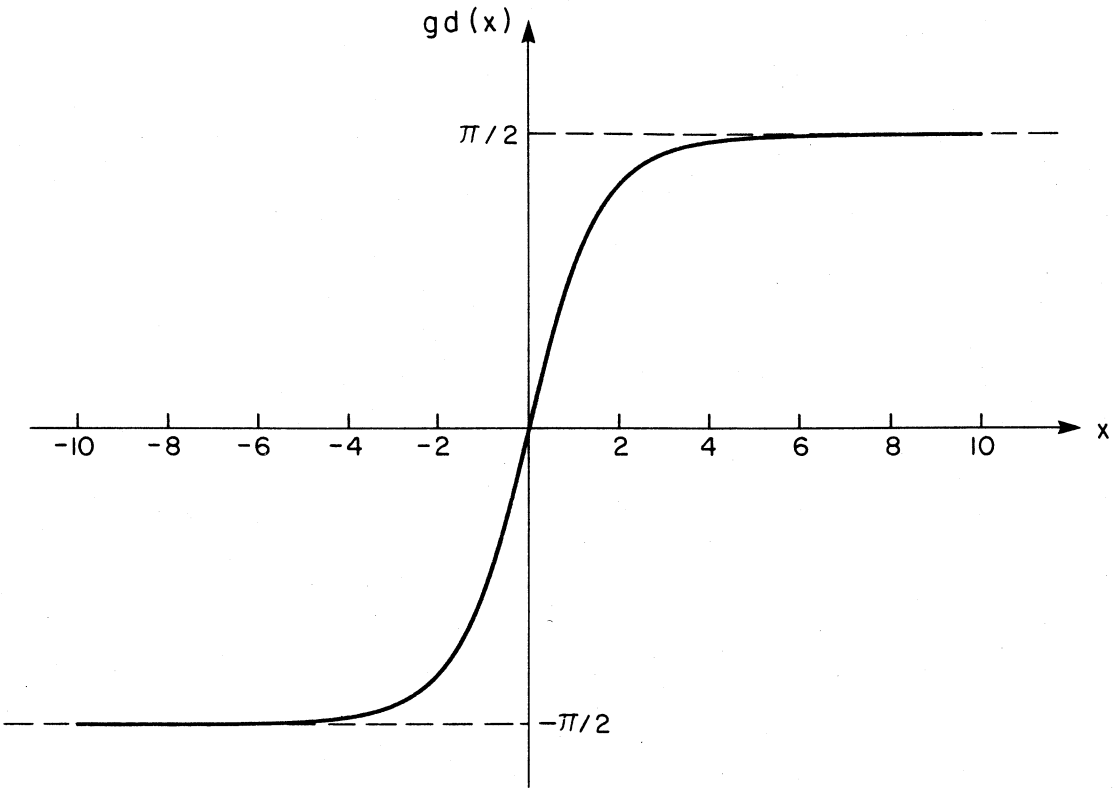

Fig. 7.6 Plot of the gudermannian.

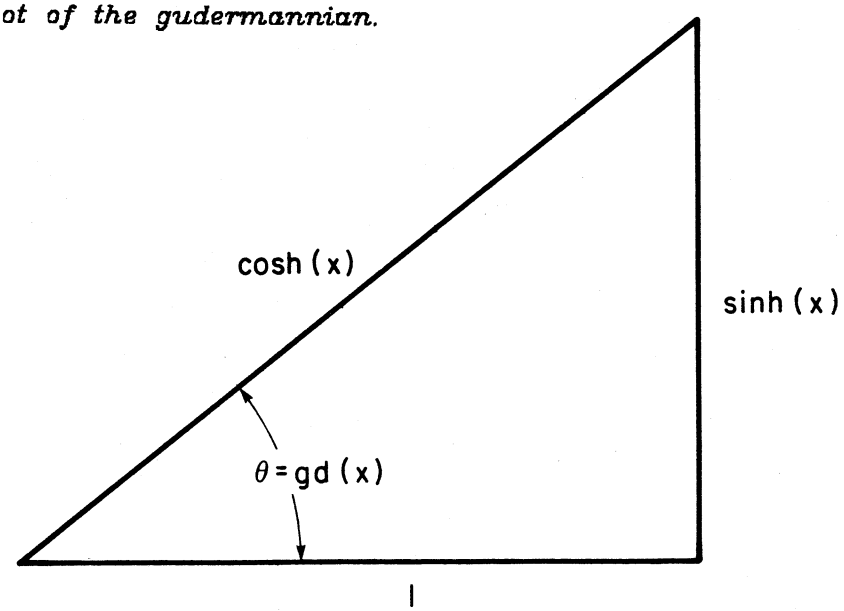

Fig. 7.7 Geometrical representation of the gudermannian, which relates the circular (trigonometric) functions to the hyperbolic (exponential) functions.

Such a function, if it matched the actual magnetization curve fairly closely, would be able to predict the behavior of the MTR in the vicinity of the knee of the B-H curve, which is the region of greatest interest.

For nearly one hundred years there have been attempts to develop equations to fit magnetization curves [19]. One of the most attractive continuous functions, first proposed for this purpose by J. D. Ryder [20], is the *gudermannian* [21]. Named for the German mathematician Guderman, who first investigated these functions, the gudermannian relates the circular functions to the hyperbolic functions according to the definition

$$\mathrm{gd}(x) \equiv \tan^{-1} \sinh(x) \tag{7.9}$$

The gudermannian is plotted in Fig. 7.6 and a geometric interpretation is given in Fig. 7.7. Notice the remarkable resemblance of the curve in Fig. 7.6 to the measured B-H characteristic of Fig. 7.1.

The first step to continuous modelling is to adapt Eq. (7.9) to the familiar format of $B = M(H)$ from which one obtains the relation

$$B = \frac{2}{\pi} B_{SAT} \, \mathrm{gd}(\alpha H) \tag{7.10}$$

where α is a constant scale factor having the units of meters/ampere and B_{SAT} is the limit of B at an infinite H, analogous to the hard saturation model of Fig. 7.2. Since this model does possess the hard saturation characteristic of a horizontal asymptote, one should expect that the MTR predicted by this model would become infinite as B_P

approaches B_{SAT}. This may not be a serious limitation, however, for in order for B_P to approach B_{SAT} in this model the H_P has to approach infinity, which requires infinite principal current. Since the ultimate practical purpose of this entire effort is to prevent an infinite principal current by limiting the B_P, the unbounded MTR may not be a serious defect in the model if in the region of interest B_P is not too close to B_{SAT}.

The inverse of (7.10), in the form of $H = W(B)$ is

$$W(B) = \frac{1}{\alpha} \ln \tan\frac{\pi}{4}\left[1 + \frac{B}{B_{SAT}}\right] \tag{7.11}$$

Use of (6.8) through (6.12) gives

$$\frac{dB_T}{dB_P} = -\alpha H_T \frac{\frac{\pi}{2} F \sec(\frac{\pi}{2} F) - \ln \tan \frac{\pi}{4}(1 + F)}{\left[\ln \tan \frac{\pi}{4}(1 + F)\right]^2} \tag{7.12}$$

where F is a normalized saturation factor defined as

$$F \equiv \frac{B_P}{B_{SAT}} \qquad \text{where} \quad 0 \leq F < 1 \tag{7.13}$$

The first point to note in (7.12) is that the function is directly proportional to H_T. That is, the magnitude of the MTR should increase with transverse current. Also, the magnitude is directly proportional to α, which means it is greater for curves with sharper knees.

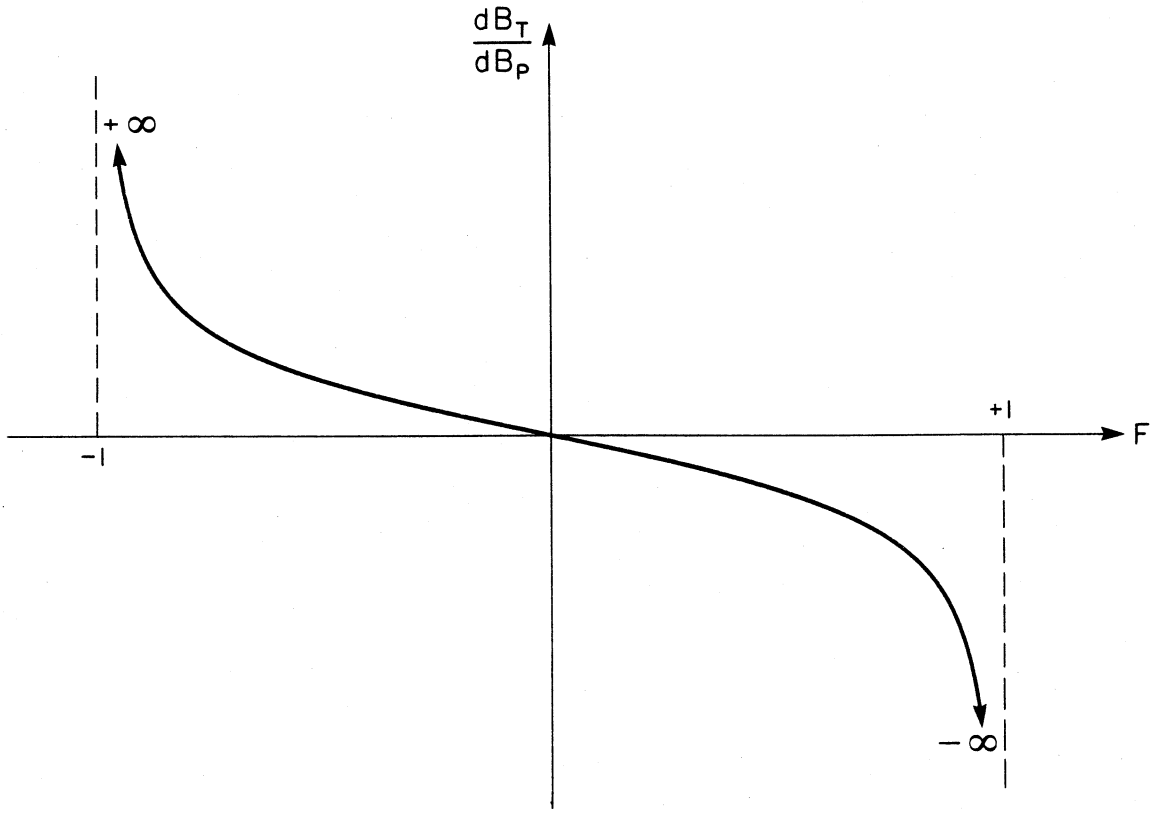

Fig. 7.8 General shape of the MTR as predicted by the continuous hard saturation model represented by the gudermannian.

An accurately scaled plot of the properties of the gudermannian, such as Fig. 7.6, permits one to easily verify that Eq. (7.12) is valid for all practical regions of interest on the B-H curve. That is, for practical cases the condition of (6.12) is well satisfied. Repeated applications of L'Hospital's Rule enable one to verify that Eq. (7.12) is indeed unbounded as B_P approaches B_{SAT} and that the limit is zero as B_P goes to zero.

The result of a numerical evaluation of (7.12) for arbitrary α and H_T is plotted in Fig. 7.8 to show the general shape of the predicted MTR.

7.5 Continuous Model for Soft Saturation

The next and final level of sophistication is to introduce a finite slope to the asymptotes of the gudermannian to more closely approximate the characteristic of the real device. A model can be formulated in principle simply by adding a linear term to the previous description of (7.10). This gives a relation of the form

$$B = \frac{2}{\pi} B_{SAT} \operatorname{gd}(\alpha H) + cH \tag{7.14}$$

where c is a positive constant. The addition of this linear term corresponds to an effective counterclockwise rotation of the curve in Fig. 7.6 about the origin of the B-H axes. This modification is easy enough, but it introduces the complication that the inversion of (7.14) to the form $H = W(B)$ is quite hopeless. An alternative way to approach the problem is to modify (7.11) such that it retains its original characteristics for small values of H, but

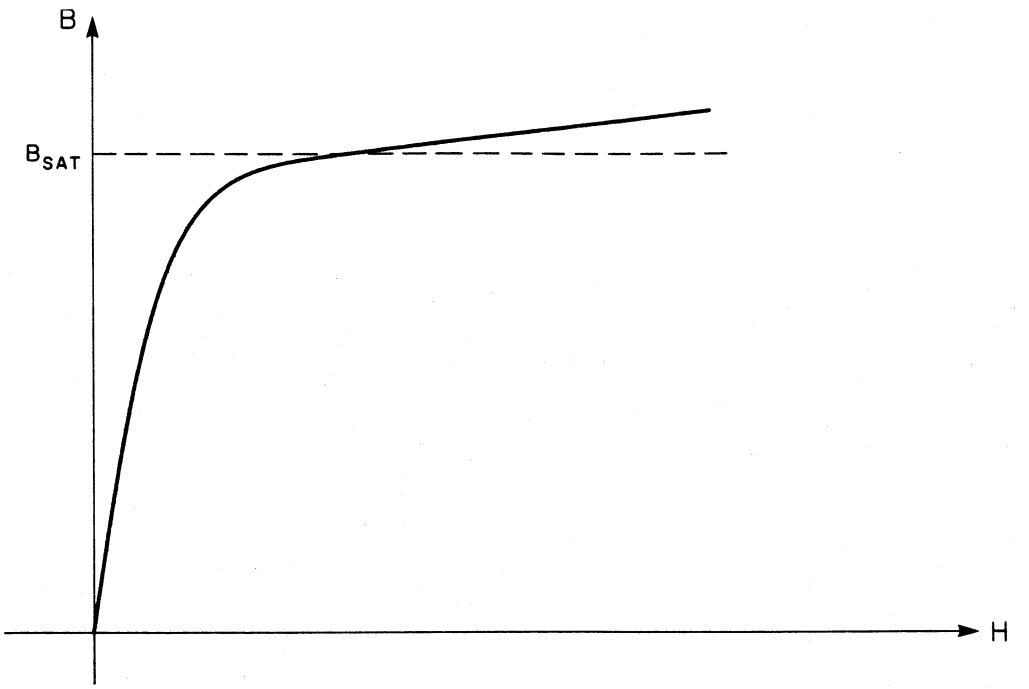

Fig. 7.9 Modified gudermannian function for the continuous soft saturation model. The particular modification used in this analysis is valid only in the first quadrant.

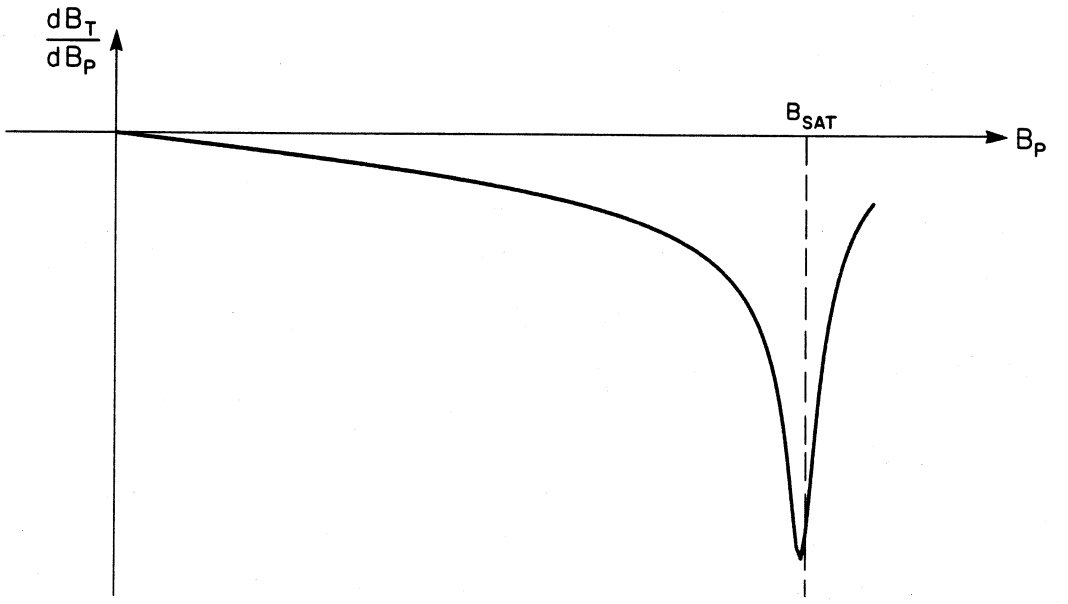

Fig. 7.10 General shape of the MTR as predicted by the continuous soft saturation model. The results of the analysis are valid only in the fourth quadrant owing to the limitations of the modified characteristic of Fig. 7.9.

has a *finite slope* for large values. The procedure is first to take the derivative of (7.11), then multiply the result by a suitable function to prevent the slope from blowing up at $B = B_{SAT}$, and finally integrate to obtain the properly modified $W(B)$. This modified function can be quite complicated, and reversion to the form of $B = M(H)$ is usually not possible. Also, the modified functions may not have the desired characteristics for all values of B or H, since the range of validity depends on the choice of the multiplier for the derivative, for which many functions are possible.

A soft saturation model has been derived by application of the above procedure and the results are given in Figs. 7.9 and 7.10. Figure 7.9 is actually a rotated plot of the modified $W(B)$ expression and Fig. 7.10 is a plot of a very large expression resulting from substitution of $W(B)$ into (6.11). The details are not important, and presentation of the messy derivation here would only show that the resulting expressions are too complicated to be of much practical use. The figures portray only a single quadrant because the particular modification presented here does not work for negative values of B and H. As one would expect, a soft saturation model predicts a bounded MTR, and the portion of the curve to the right of B_{SAT} in Fig. 7.10 is similar in shape to that of the piecewise soft saturation model of Fig. 7.5.

7.6 The Inductance Analogy

The interaction of orthogonal magnetic fields is a first-order nonlinear phenomenon -- it works solely because of *nonlinear* effects. For this reason the treatment of the subject thus far has avoided the use of terms and ideas which have been developed exclusively for *linear* problems. Although this approach leads to an explanation of the effect that is correct on fundamental physical grounds, it unfortunately lacks a close tie to the more familiar "intuitive" principles of linear magnetism with which an engineer may feel more comfortable. This section offers an alternative explanation of the phenomenon in terms of more familiar linear models.

From Eqs. (5.2) and (5.4) we can write the exact relation

$$B_T = H_T \frac{M\left(\sqrt{H_T^2 + H_P^2}\right)}{\sqrt{H_T^2 + H_P^2}} \tag{7.15}$$

Now, if $H_T < H_P$ we can make the approximation

$$B_T \approx H_T \left[\frac{M(H_P)}{H_P}\right] \tag{7.16}$$

Suppose that H_P were held constant and H_T were varied by an infinitesimal amount. Then the variation in B_T with respect to H_T would be

$$\frac{dB_T}{dH_T} \approx \frac{M(H_P)}{H_P} \tag{7.17}$$

Substitution of (7.17) back into (7.16) results in the approximation

$$B_T \approx H_T \left[\frac{dB_T}{dH_T} \right] \tag{7.18}$$

Use of the chain rule of calculus and Ampere's Law gives

$$\frac{dB_T}{dH_T} = \frac{dB_T}{dI_T} \frac{dI_T}{dH_T} = \frac{dB_T}{dI_T} \left[\frac{l_T}{N_T} \right] \tag{7.19}$$

Since $B_T = \Phi_T / A_T$, Eq. (7.19) can be written as

$$\frac{dB_T}{dH_T} = \frac{d\Phi_T}{dI_T} \left[\frac{l_T}{N_T A_T} \right] \tag{7.20}$$

Now, if we *define* the *incremental transverse inductance* to be

$$L_T \equiv N_T \frac{d\Phi_T}{dI_T} \tag{7.21}$$

then from (7.18) and (7.20) we get

$$B_T \approx H_T L_T \frac{l_T}{N_T{}^2 A_T} \tag{7.22}$$

But by Ampere's Law this can be written as

$$B_T \approx \frac{I_T}{N_T A_T} L_T \tag{7.23}$$

Finally, from (5.8), since I_T, N_T, and A_T are all constants, we arrive at

the desired result for the transverse voltage:

$$v_T \approx I_T \frac{dL_T}{dt} \tag{7.24}$$

Equation (7.24) says that the transverse voltage is approximately equal to the transverse current (which is constant) multiplied by the rate of change of the incremental inductance measured in the transverse direction. Most working engineers should find some degree of comfort in this explanation, for it relates a foreign idea of the nonlinearity of a magnetic material to the familiar notion of a rate of change of the value of a linear circuit quantity. A similar idea has been used historically in discussions of electric machinery, where, for different reasons and definitions of V, L, and I, it has been useful to think in terms of the relationship

$$V = \frac{d}{dt}(LI) = L\frac{dI}{dt} + I\frac{dL}{dt} \tag{7.25}$$

The change of inductance in (7.24) might also be interpreted as a variance in the slope of the B-H curve, if that slope may be thought of as an "incremental permeability," μ_i. This can be seen by substitution of $\Phi_T = B_T A_T = \mu_i H_T A_T$ in (7.21).

There are several cautions which should be heeded regarding the use of the inductance analogy (7.24). The foremost caveat is that even though the inequality $H_T \ll H_P$ may be very well satisfied, (7.24) is fundamentally incorrect. This is because the above derivation relies on the validity of the differential equation of (7.18), whose only solution is

$B_T = \mu H_T$, the linear case in which the transverse voltage must be identically zero. Therefore, one should not expect the the approximation of (7.24) to be meaningful where the material is highly nonlinear.

A further caution should be made with regard to attempts to make numerical predictions of v_T from measurements of incremental inductance in the transverse direction. The major difficulty here is with the definition of the inductance term, L_T. Equation (7.21) defines the incremental inductance in a strictly mathematical sense, and no easy way has been found to relate this definition, based on the large signal B-H characteristic, to any measurable small-signal quantity [18, 22].

Although the inductance analogy of (7.24) is not completely correct in a rigorous sense, the idea is nevertheless an extremely useful one. It will be seen in the remaining sections that the application of the idea of the rate of change of the slope of the B-H characteristic enables one to make reasonable qualitative predictions about the shape of the MTR.

CHAPTER 8

MEASUREMENT OF THE TRANSFER RATIO

The two previous chapters have introduced theoretical tools and mathematical models to describe and to exploit the phenomenon of nonlinear interactions of perpendicular fields. In Chapter 6 the Magnetic Transfer Ratio (MTR) was introduced as a dimensionless quantity which could be useful for modelling and design. Chapter 7 developed four models to describe typical B-H characteristics of ferrite materials and used the expressions which were developed in Chapter 6 to predict the MTR from those models. Now, in this chapter, the Transfer Ratio will be measured on a ferrite transformer core to examine the true nature of the phenomenon and to evaluate the models.

8.1 Instrumentation

The measurements given in this section were taken on an RM10 core of H7C1 material manufactured by TDK. This is similar in structure to the pot core pictured in Fig. 5.7a. The core was excited with an ac-coupled square-wave voltage at a frequency of 30 kHz on a principal winding of five turns. The transverse field was applied with a 100 mA constant current source on a single-turn transverse winding. An ac clip-on current probe measured the principal current and a dc ammeter monitored the transverse current.

A Tektronix 7854 digital oscilloscope was used to acquire the analog information and process the data numerically. The MTR was obtained by division of the digitized waveforms of v_T and v_P. Flux densities were obtained by integration of the voltage on a single turn and division by the appropriate cross-sectional area. The areas and mean path lengths were computed from measured dimensions of the particular core. Because the structure is rather oddly shaped, one must take care to obtain values for the areas and path lengths which are *effectively* those which would be used to characterize the imaginary hollow toroid of Fig. 5.6. To check the validity of the values obtained, B-H characteristics were measured separately in both the principal and transverse directions and the results compared to the manufacturer's curves for that material, which were measured on a standard toroid. The digitized waveforms were then stored on the floppy disc of a Hewlett-Packard 9826 desktop computer for subsequent plotting, comparison, and for archival storage.

Although these instruments offer obvious advantages over other more conventional means of measurement, the use of such highly sophisticated equipment is by no means *required* for the study and characterization of the MTR. The same information may be obtained in real time with conventional analog instrumentation. In fact, this simpler method may actually be preferable for use in the design process. The designer is most interested in the transverse voltage v_T, which is just the MTR multiplied by v_P as defined in Eq. (6.18). If v_P is a rectangular pulse-like waveform (nearly always true in dc-dc power converters), then

the transformer will be energized by a v_P of constant magnitude but alternating polarity. During the intervals where v_P is constant, the flux density B_P is directly proportional to time. Consequently, $\frac{dB_T}{dB_P}$ will have the same shape as $\frac{dB_T}{dt}$. This being the case, it is clear from Eq. (6.19) that the transverse voltage as a function of time is an exact replica of the MTR repeated at twice the frequency of v_P. Therefore, the necessary information is easily obtained with conventional instruments, and the data can be taken on transformers under actual operating conditions *in situ* on a power supply breadboard. The transverse voltage shown in the oscilloscope photograph of Fig. 6.2a is then actually a measurement of the MTR.

8.2 Salient Features

Figure 8.1 is the B-H characteristic of the RM10 core as measured on the principal winding. Strictly speaking, this is really a Φ versus I plot scaled by effective linear dimensions of the structure to arrive at an effective B and H. Although this is not precisely the actual intrinsic characteristic of the material owing to the presence of nonuniform fields within the structure, it is assumed to be adequate for the purposes of this study. One should be aware of the effects of nonuniform fields on such measurements, and further discussions of this topic can be found in [23].

Figure 8.2 shows the MTR measured for the same excitation used to produce Fig. 8.1. Since both v_T and v_P were measured with respect to a single turn, the MTR given here is normalized to the equivalent of a single

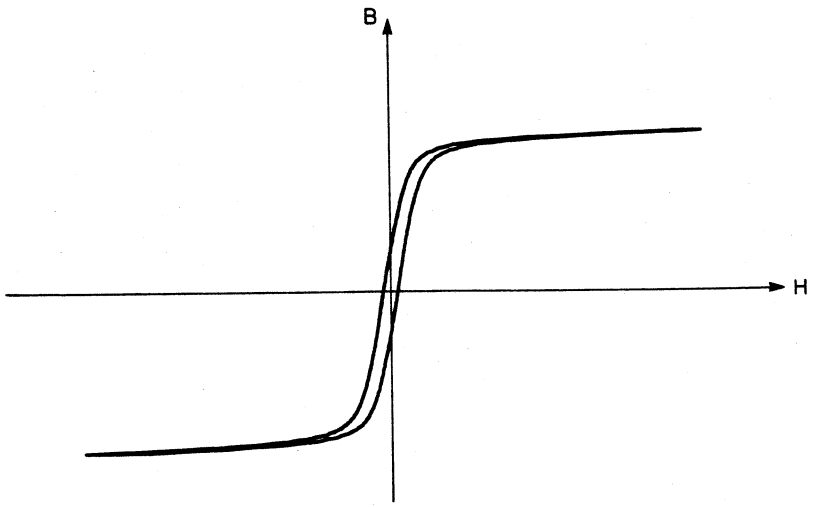

Fig. 8.1 Repeat of Fig. 7.1, measured B-H characteristic of an RM10 core of H7C1 material.

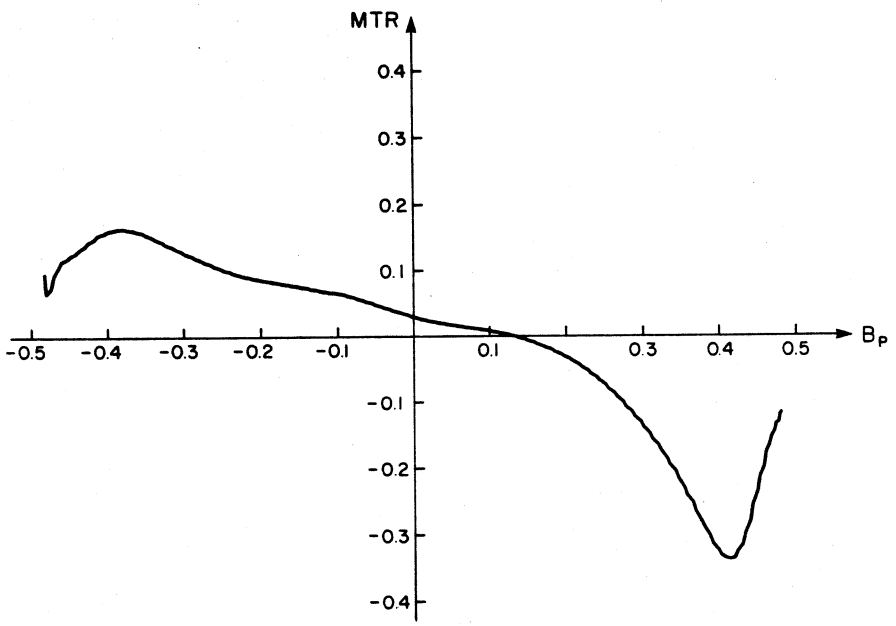

Fig. 8.2 Magnetic transfer ratio (MTR) for the characteristic of Fig. 8.1. Transverse current is 100mA in a single turn. The measurement was made as the material went from a region of negative saturation to positive saturation. The MTR is not symmetric because the curvature of the B-H characteristic as the material leaves saturation is different from when it enters saturation.

turn on both the principal and transverse windings.

Owing to magnetic hysteresis, the material has different dynamic properties for increasing and decreasing fields. This effect can be seen as differences in curvature at the knees of the B-H curve for increasing and decreasing B and is manifested in the asymmetry of the MTR. Another effect of hysteresis is that the MTR does not cross zero at $B_P = 0$. This shows that the actual **B** vector in the material lags the position inferred from integration of the terminal voltages. Hysteresis in the transverse direction can leave a remanent flux bias such that a small transverse voltage can appear on the transverse winding even after the transverse current is brought to zero. However, if the core is driven into hard saturation from the principal winding so that nearly all the magnetic domains are aligned in the principal direction, the residual transverse bias disappears.

Probably the most notable feature of Fig. 8.2 is that the magnitude of the MTR, and hence the transverse voltage, does not increase without bound as B_P gets larger, but rather has a definite limit. Recall that this is contrary to the qualitative picture given by the simple hard-saturation models but is predicted by the soft-saturation models developed in Chapter 6.

An interesting and informative illustration is given in Fig. 8.3, which shows the ac variation in transverse flux density B_T plotted against the variation in principal flux density B_P over an entire period of v_P. The arrows show how the trajectory is traced out in time. Since these

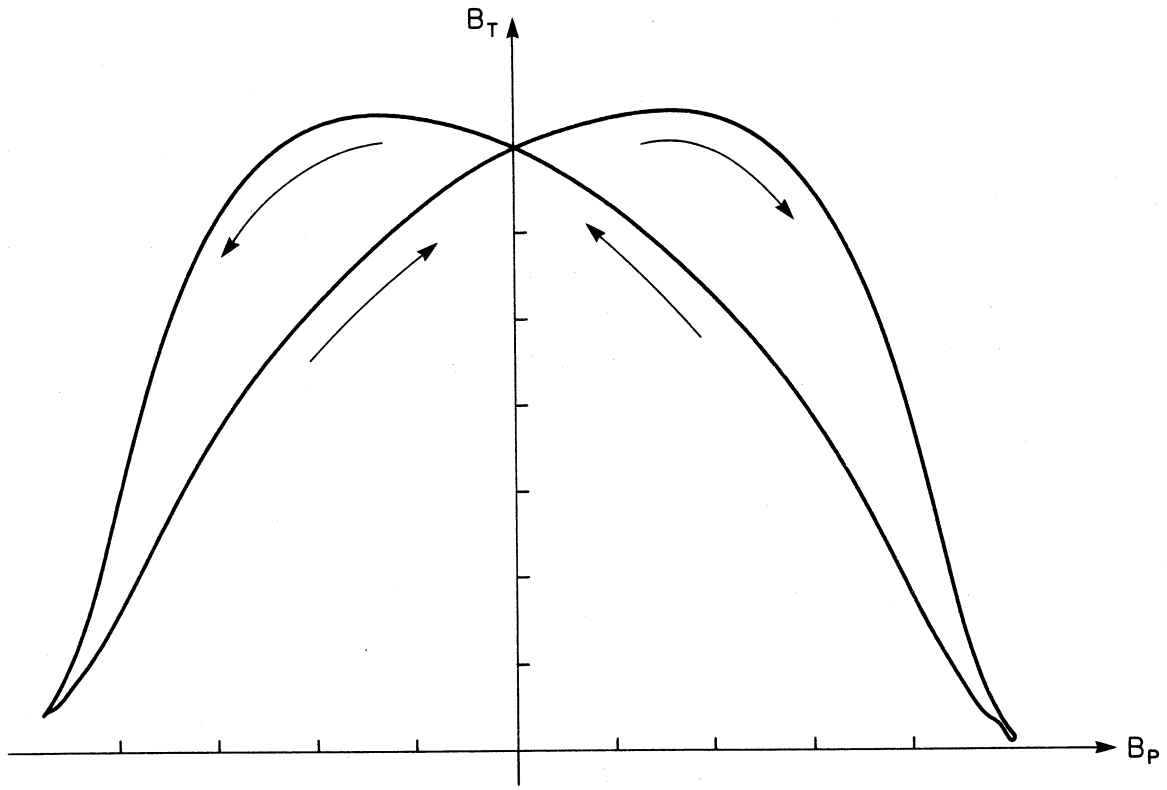

Fig. 8.3 Plot of the transverse flux density B_T versus the principal flux density B_P for the RM10 core of H7C1 material. B_T on the vertical axis is 0.01 tesla per division while B_P is 0.1 tesla per division. The scales are not labeled because it is impossible to determine the true position of the origin from only ac measurements. This clearly shows that, owing to the complex physics of the magnetization process, the way the material leaves a region of saturation is different from the way it approaches saturation.

are only ac measurements, the absolute magnitudes of the flux densities are unknown and no effort has been made to determine them. The axes in Fig. 8.3, however, have been positioned to achieve a qualitative resemblance to the locus of **B** in Fig. 6.1.

A rather subtle feature of Fig. 8.3 is that the curve is not perfectly symmetric with respect to any set of axes. This is caused partly by remanent B-fields and partly by imperfections and asymmetries both in the core and in the driving voltage waveform. Because it is physically impossible to make a structure so that the transverse and principal directions are *exactly* perpendicular everywhere, there will always be some degree of direct coupling between the two windings. Thus a very small signal at the frequency of the principal voltage will be present on the transverse winding even when the transverse current is zero. In other words, one should not expect the fundamental frequency of v_T to be twice that of v_P unless the core and drive waveforms are perfectly symmetrical and B_P has no dc offset.

Hysteresis is responsible for the large change in the slope of the curve of Fig. 8.3 as B_P increases in the positive direction (from $-B_P$ to $+B_P$) or increases in the negative direction (from $+B_P$ to $-B_P$). This effect gives the MTR a greater magnitude in the fourth quadrant than it has in the second quadrant (Fig. 8.2). Since this asymmetry seems to be a natural characteristic of all ferrites, the measured MTR will have its greatest magnitude in only one quadrant, and only that part will be shown in subsequent figures.

An important observation is the change in magnitude of the MTR as a function of transverse current. This is illustrated in Fig. 8.4, which shows the fourth quadrant of several MTRs for this core for different values of transverse current I_T. Note that more transverse current (greater H_T) produces a greater magnitude MTR for the same principal excitation. The trend shown in these curves is consistent with the qualitative predictions given by all the models in Chapter 6 except for the oversimplified piecewise model for hard saturation, which predicts a curve of the same magnitude for all values of H_T.

This chapter has presented a preliminary examination of the characteristics of the Magnetic Transfer Ratio measured on a typical ferrite core. The remarkable similarity of the measurements to the predictions of the earlier analysis demonstrates that often very simple engineering models can be used effectively to understand a problem which at the outset may seem hopelessly complicated. The next chapter will examine in more detail several aspects of the the measured MTR which have great practical importance.

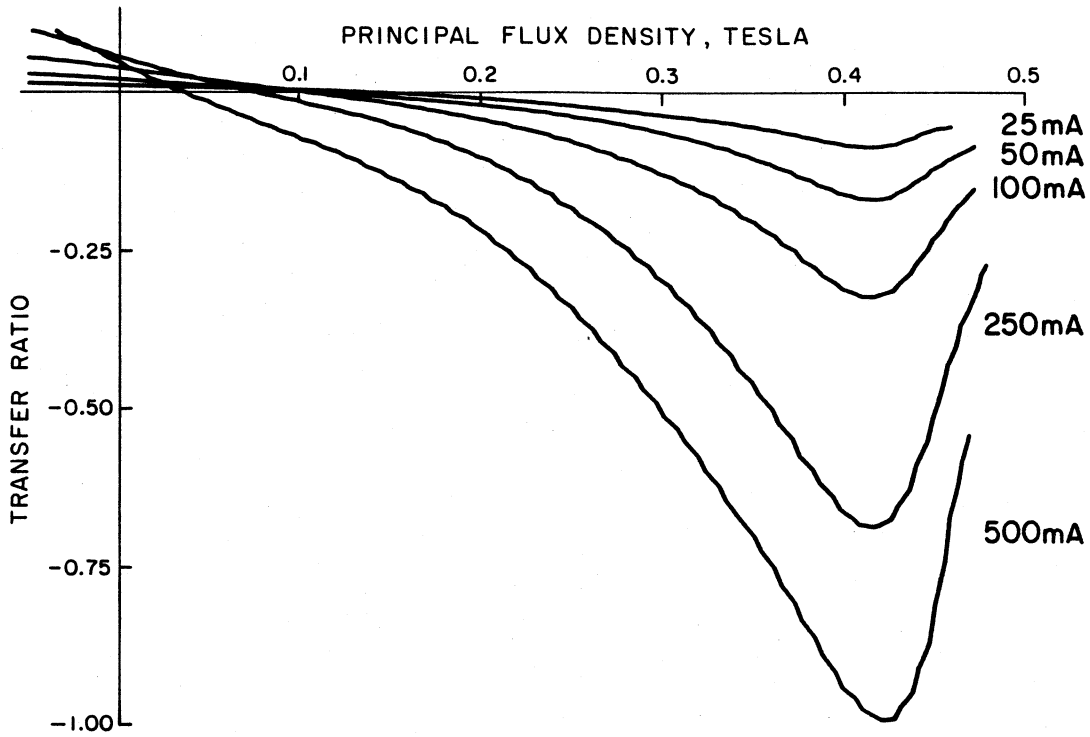

Fig. 8.4 Fourth quadrant plot of the MTR of the RM10 core for different currents in the transverse winding. The increase in magnitude with increasing dc bias current is qualitatively consistent with the predictions of Chapter 6. The artificial waviness of the curves is the result of digital processing and expansion of data points.

CHAPTER 9

EXPERIMENTAL OBSERVATIONS

In the last chapter some measured MTRs were presented and their salient features were compared to the predictions of the analytical models developed earlier. Because the models predict that the magnitude should be a strong function of the transverse field H_T, MTRs for several different bias currents were displayed in Fig. 8.4. The response of the MTR to changes in transverse bias, however, is only a small part of the total picture. The nonlinear characteristics of the particular magnetic material determine the response of the MTR, and these characteristics are strong functions of several variables which the designer cannot always control. This chapter takes a closer empirical look at some of the more important parameters which affect the MTR, and discusses how they influence the engineering applications of this phenomenon.

9.1 Characterization for Design

Because wide variations are possible in the nonlinear characteristics of magnetic materials, it is practically impossible to construct a simple universal model that is very accurate and at the same time useful for design purposes. The most reasonable course for a designer to take is not to attempt to calculate every minute detail of the response, but rather to know the *trends* and the *bounds* of the response as a result of expected changes

in the operating conditions. When this information is reinforced by the understanding which comes from a general analysis, one can produce a sound design. Such is the case in the traditional design of conventional magnetic devices. The properties and performance of the various magnetic materials are not calculated, but are merely measured and cataloged. The designer uses the information provided together with his understanding of the basic principles of operation to arrive at a design which meets the requirements over a range of known operating conditions. For these reasons, the MTR is proposed as a fundamental descriptive characterization of a magnetic material which may rightfully appear on data sheets along with the more traditional B-H characteristics and core-loss information.

The description of this technique to detect impending magnetic saturation by the introduction of a perpendicular field is almost complete. The principles of operation have been established along with practical descriptive expressions which one can use for design. The only step remaining is to characterize the MTR for variations in magnetic materials, physical environment, and different operating conditions.

9.2 Variations with Transverse Bias

According to Eq. (6.21) the general analysis predicts that the magnitude of the MTR should be directly proportional to the transverse current I_T. This is, of course, subject to the satisfaction of the inequalities (6.8) and (6.12). To test the validity of this claim, MTRs for the same core and conditions described previously in Chapter 8 were measured at several

different values of I_T. The peak value of the magnitude of each MTR is plotted against its transverse current in Figs. 9.1 and 9.2. From the figures it is quite clear that the MTR is indeed directly proportional to I_T for small values of transverse bias (Fig. 9.1), but the relationship deviates from that rule, as expected, at high values of I_T (Fig. 9.2). If one uses the actual dimensions of this core, it is easy to compute from these graphs that the relationship begins to deviate from a straight line when the ratio between H_T and H_P is larger than approximately $1/10$. The fact that the deviation does occur, however, is really of no practical consequence as long as the designer knows the true relationship for his particular type of core at a particular set of operating conditions. Moreover, large biases are usually not required; the transverse bias needs to be only large enough to swamp out the effects of noise and parasitic hysteresis on the transverse voltage signal. The currents given in the figures may seem rather large because these data are referred to a single-turn transverse winding. The same magnitude of transverse voltage can be obtained with reduced I_T if N_T is increased. This relationship is shown explicitly in Eq. (6.21).

9.3 Variations with Flux Excursion

The fact that the magnitude of the MTR, and hence the transverse voltage, does not increase indefinitely with flux density may at first appear to be a serious limitation on the utility of this technique. These doubts are quickly put aside, however, when one makes a closer comparison between the MTR and the measured B-H characteristic of the material.

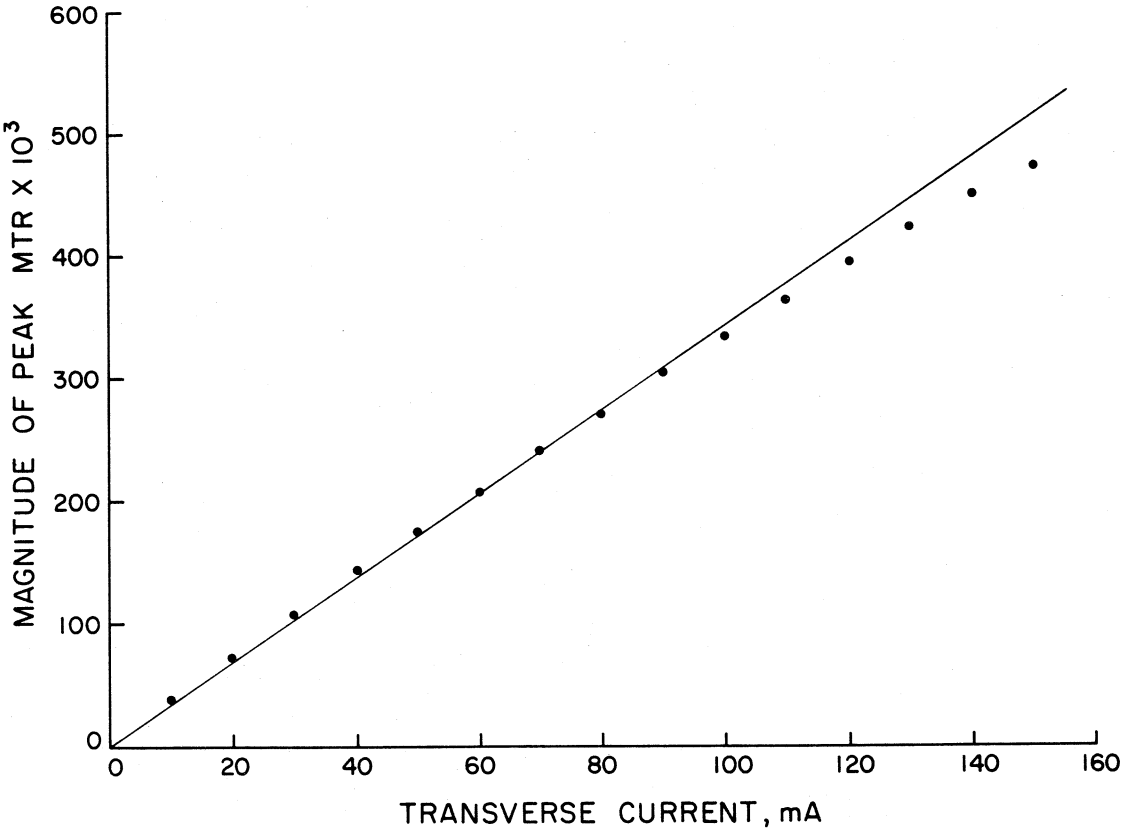

Fig. 9.1 The magnitude of the MTR varies linearly with transverse current for small biases.

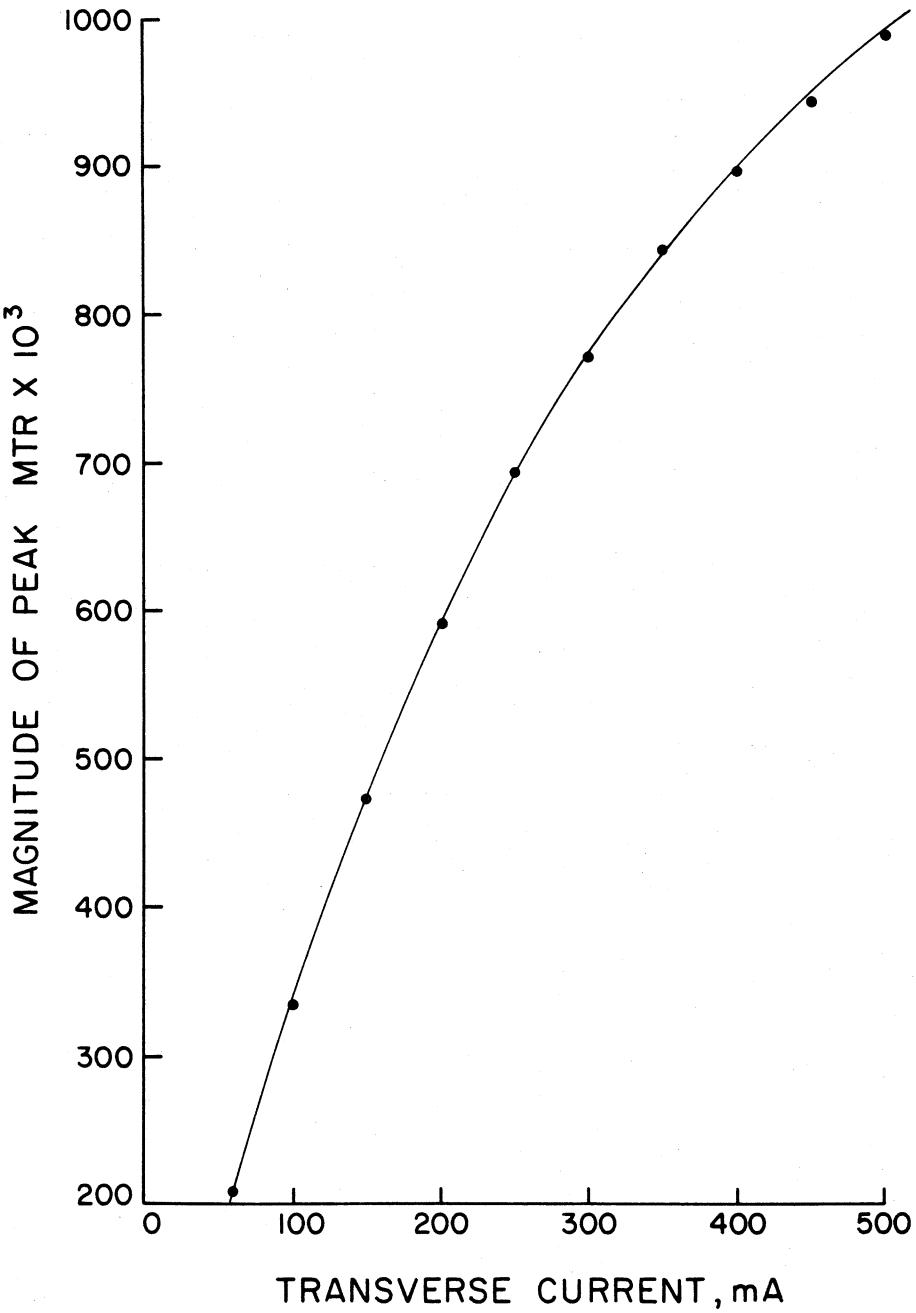

Fig. 9.2 The linear relationship between the magnitude of the MTR and the transverse current breaks down at high transverse biases.

It turns out that in practice a designer would generally not want to permit the flux excursion to come very near to the point of peak MTR, because at that level of excitation the principal current begins to get unreasonably large, and it is desirable to stop the excursion short of this point with some margin to spare. Thus, in practice, the MTR would not usually be measured at the extended excursions demonstrated in the previous sections.

Unfortunately, it is a fact of life that the characteristics of the material generally depend on the characteristics of the excitation: the shape of the B-H characteristic changes according to the magnitude and spectral content of the flux excursion. Since all variations with all possible combinations of these parameters are much too numerous to be given in this presentation, only the variations in MTR with flux excursion for voltage drives of a single waveshape (square wave) at a single frequency (30 kHz) will be shown.

Figure 9.3 gives several MTRs for the same RM10 core for various peak flux densities. There are substantial differences in the magnitudes for different excursions, but luckily the changes occur in a favorable direction. Note that in all the cases of Fig. 9.3, for a given flux density, the magnitude of the MTR gets larger for smaller flux excursions. This means that if a designer were to set a limit on the peak flux density from an MTR measured for an excursion that was larger than he desired, then the flux would be actually limited at a somewhat *lower* level. Thus there would be an extra margin of safety built into the design.

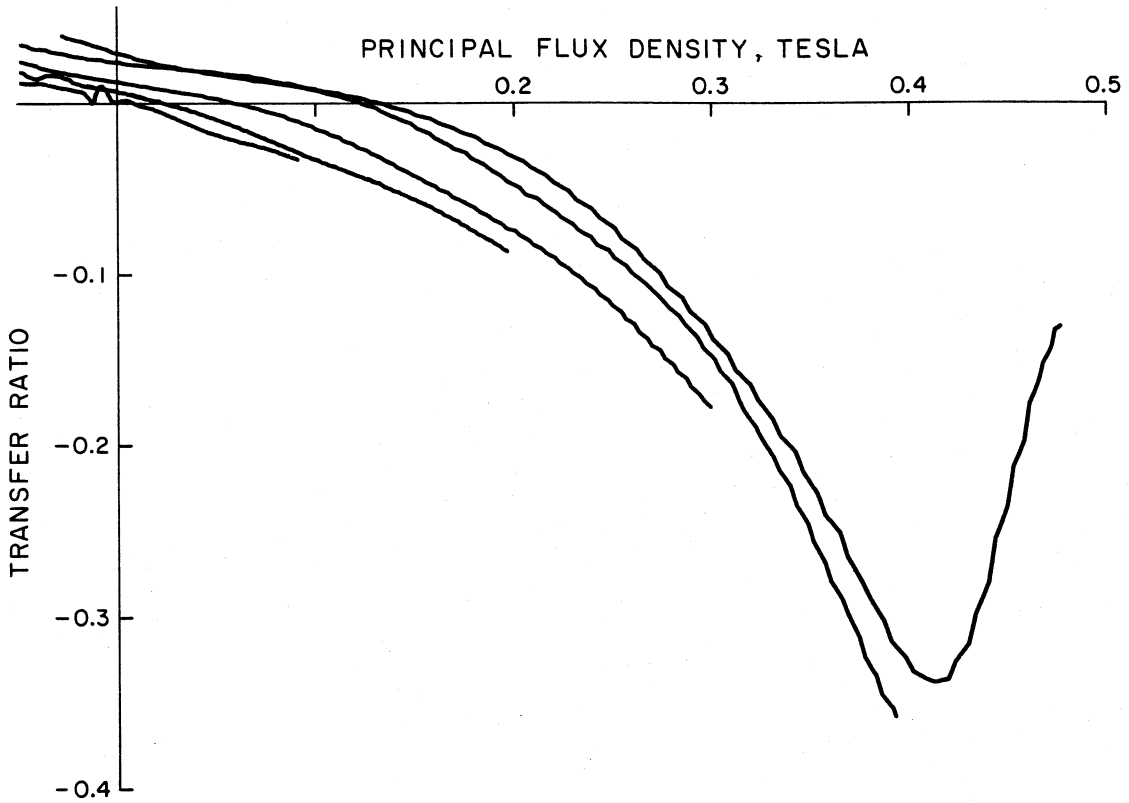

Fig. 9.3 The MTR of an RM10 core of H7C1 material for various excursions of maximum flux density. Transverse current is 100mA in one turn.

9.4 Variations with Material Composition

Ferrite materials are commercially available in many different compositions, and each is distinguished from the others by a unique B-H characteristic. It is only natural, then, to expect that the MTRs of different ferrites should in some way reflect these fundamental differences in the individual materials.

Consider the two measured B-H characteristics in Fig. 9.4, for example. The data for the curve in Fig. 9.4a were obtained from the TDK RM10 core of H7C1 material which has been discussed previously. The curve in Fig. 9.4b was measured on a Ferroxcube 2616 pot core of 3C8 material. Aside from the differences in maximum flux density, the two curves are quite unalike in that they have distinctly different shapes. The H7C1 material of (a) has nearly a straight-line characteristic below the knee of the curve, but it begins to bend rather sharply with increasing H_P. In contrast to this behavior is the 3C8 material in (b), whose characteristic is rather S-shaped below the knee, and then curves gradually as it begins to saturate. From the inductance analogy of Section 7.6 or from an understanding of the general analysis, one would expect a material with a sharper curvature in its B-H characteristic to have a greater MTR. This prediction is indeed correct, as shown by the comparison of the MTRs in Fig. 9.5. The gradual S-shaped bending observed in the B-H characteristic of 3C8 results in an MTR which is quite remarkably different from that of the H7C1 material.

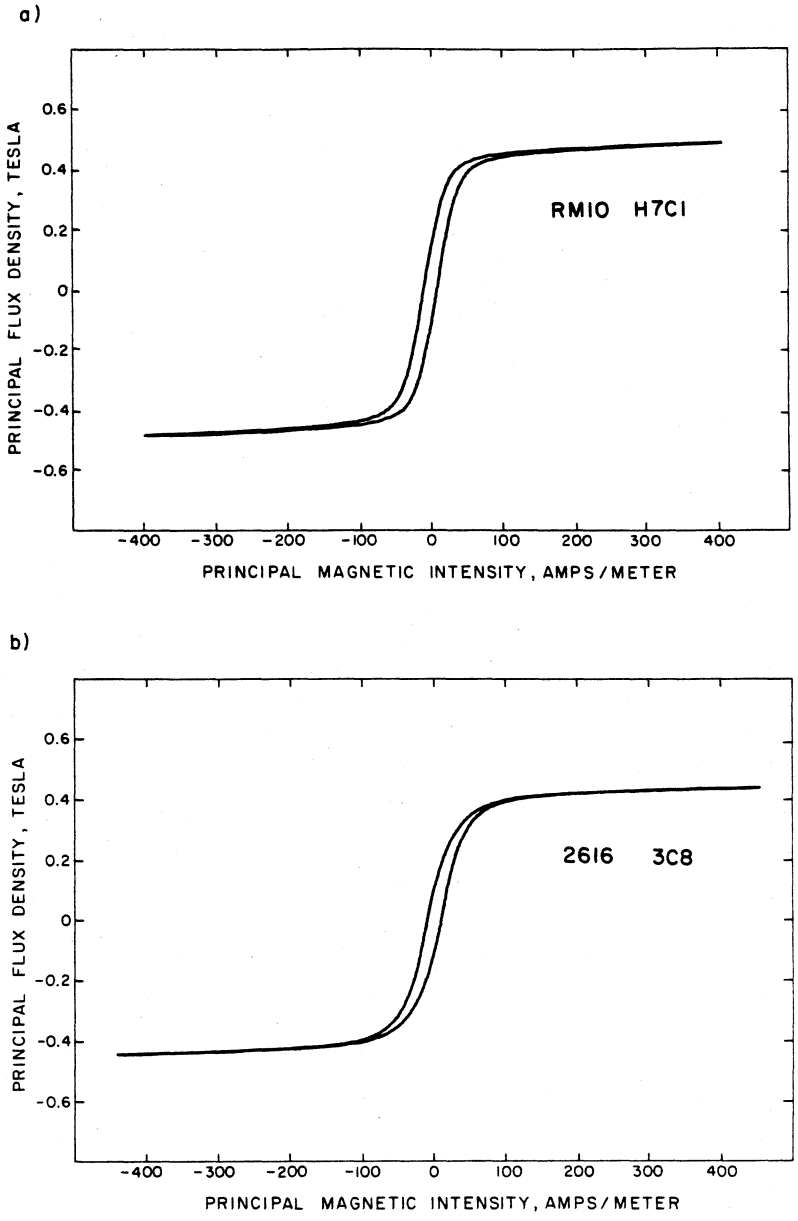

Fig. 9.4 Comparison of the principal B-H characteristics of an RM10 core of H7C1 material, (a), and a 2616 pot core of 3C8 material, (b). Comparison with measurements of these characteristics in the transverse direction and also with manufacturers' data taken on toroids of the same material show that the small geometrical differences in the two cores have an insignificant effect on the general shapes of the curves.

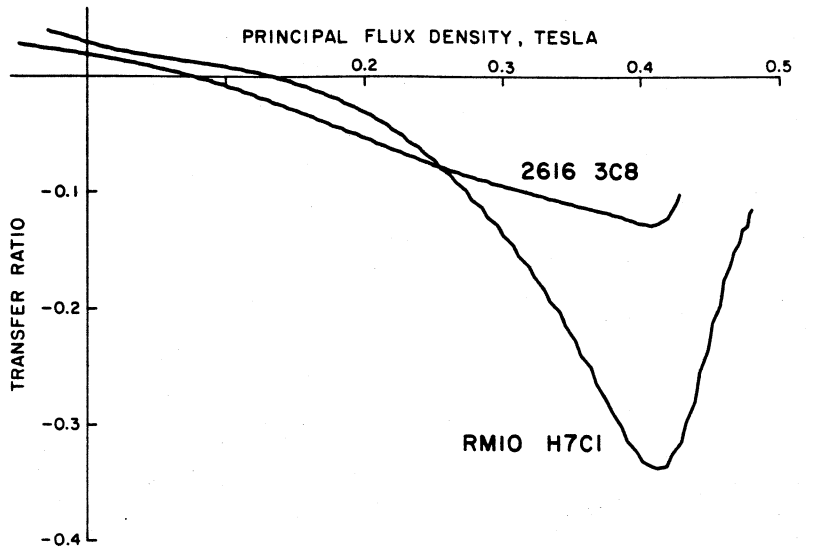

Fig. 9.5 Comparison of the MTRs associated with the B-H characteristics shown in Fig. 9.4. Transverse current is 100mA in one turn. These curves present an indirect comparison of the characteristics of two dissimilar magnetic materials.

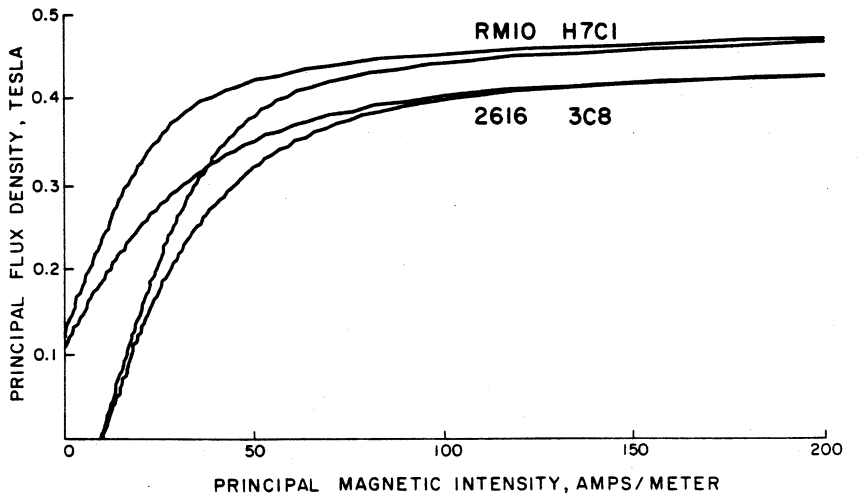

Fig. 9.6 Magnified first quadrant comparison of the two B-H characteristics of Fig. 9.4. Note how the differences in maximum flux density and dissimilar curvatures are reflected in the MTRs of Fig. 9.5. The waviness of the curves is a result of digital processing of the data.

Since the gudermannian function closely resembles the actual B-H characteristic of H7C1 it is able to model the salient features of that MTR quite well. It is not a very good mathematical model for 3C8, however, and thus one should not expect the gudermannian to yield a very good prediction of that MTR. On the other hand, note that the soft-saturation model still accurately predicts that the MTRs tend to zero for large values of B_P. Figure 9.6 shows a magnified detail of a comparison of the two B-H characteristics in the first quadrant. The differences in the curvatures in the vicinity of the knees of the curves are apparent. It is unfortunate that these two materials were not available for testing in exactly the same core geometry, for such a test would leave no doubt that the differences in the MTRs are the result of different materials and not different geometries. However, because the two cores are so similar in structure and have nearly identical critical dimensions, it is most unlikely that the small differences in structure could have more than a second order influence on the dramatic dissimilarities of the two MTRs.

For another comparison, refer to Fig. 9.7, which shows the MTRs for three 2616 pot cores of three different ferrite compositions: Ferroxcube 3C8 and 3B7 and Magnetics F material. One can deduce from the figure that the 3B7 and F materials have B-H characteristics with approximately the same shape with the F material saturating at a higher flux density. Both these materials have characteristics which are more linear below the knee than 3C8, but not nearly as linear as H7C1.

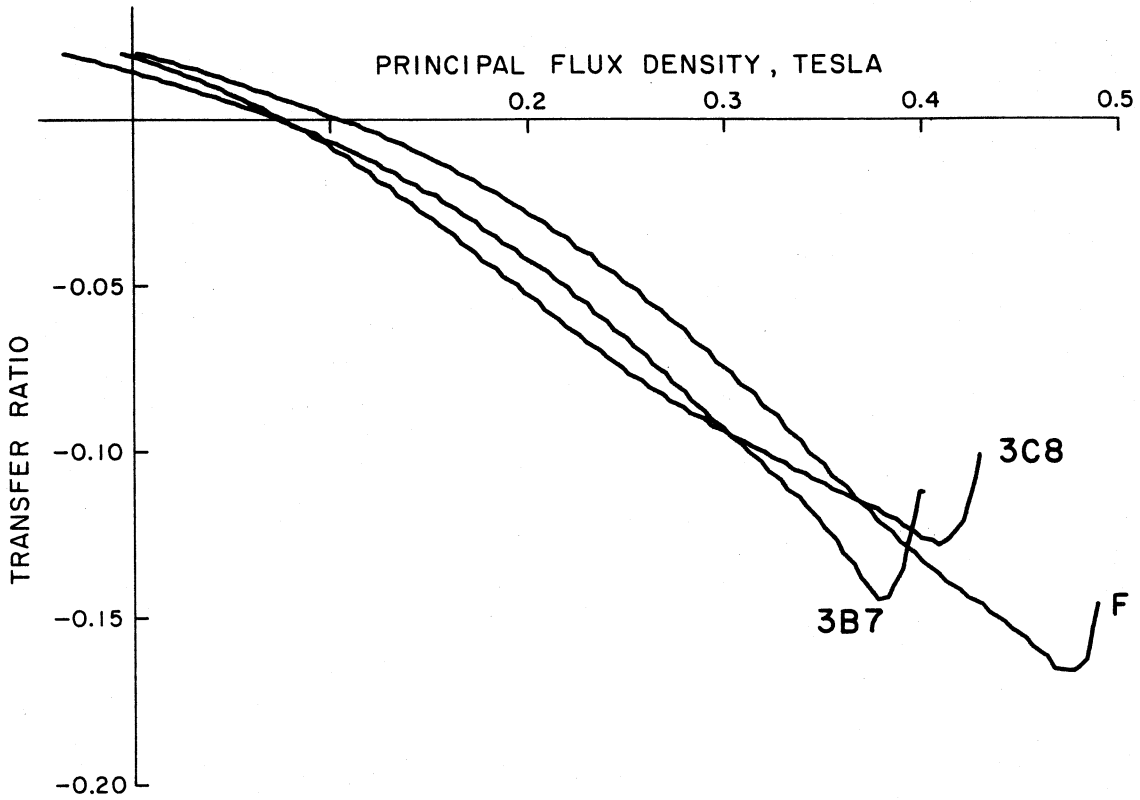

Fig. 9.7 MTRs of three 2616 pot cores of different materials. Transverse current is 100mA on a single turn. This comparison shows that these three materials should have similar B-H characteristics, and this is supported by measurements.

The ability of the MTR to chart the subtle differences in the nonlinearities of magnetic materials suggests that measurement of the MTR may be a means by which materials might be readily identified. This idea has not been thoroughly investigated, and it invites further work to test the reliability of the MTR as a means of "fingerprinting" magnetic materials. One possible application is that it could be the basis of a simple test method for inspection and quality control in the manufacturing process.

9.5 Variations with Temperature

Of all the environmental conditions which affect the characteristics of magnetic materials, changes in temperature are probably the most influential and are therefore of great concern to the designer. Figure 9.8 illustrates the scope of this problem. The B-H characteristics in the figure are of H7C1 material for two extremes in temperature, −55°C and +150°C. The saturation flux density changes by a factor of two over this temperature range, and the width of the loop shows a similar variation.

This observation immediately leads one to question the suitability of this sensing technique for large variations in temperature. The data in Fig. 9.9 were taken in response to these concerns. The figure shows several MTRs of H7C1 material for various temperatures in the range of −55°C to +150°C at a transverse current of 100 mA. As one would expect, the MTR does change substantially with temperature; but, fortunately, it changes in a favorable direction. Note that as the temperature increases and the saturation flux density retreats to lower values, the magnitude of the MTR

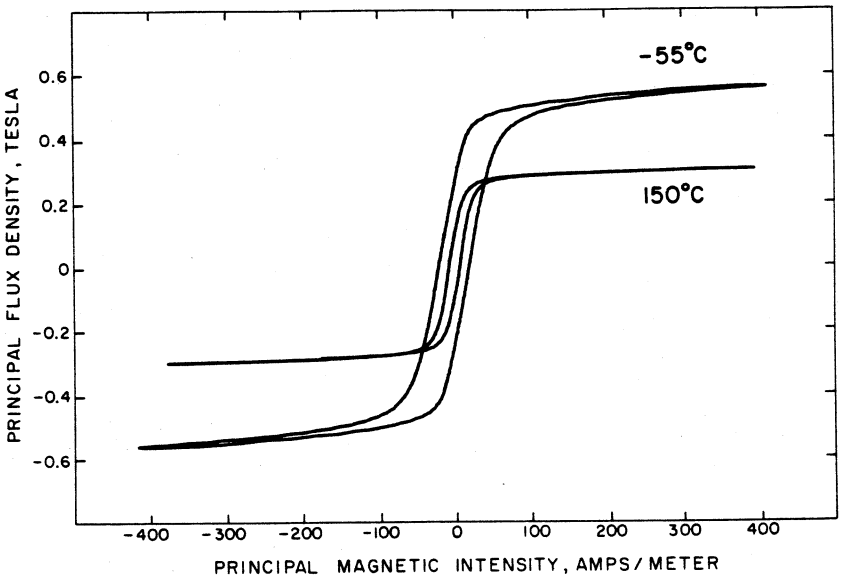

Fig. 9.8 B-H characteristics of an RM10 core of H7C1 material for two extremes of temperature.

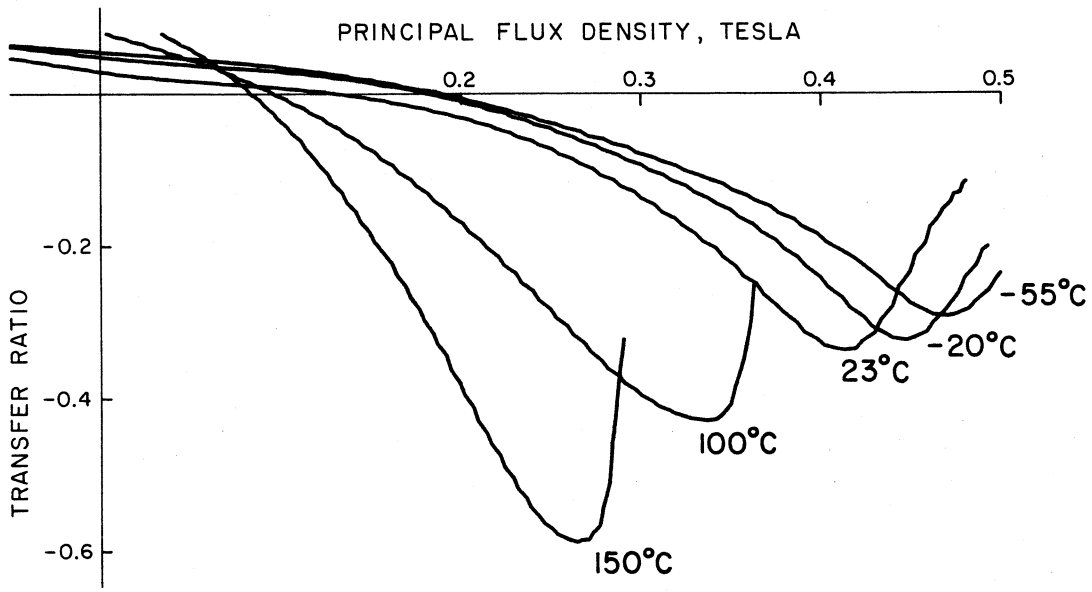

Fig. 9.9 Effects of temperature variations on the MTR of an RM10 core of H7C1 material. All are for 100mA transverse current on a single turn. With no temperature compensation in the sensing circuitry, a low-temperature design has a built-in factor of safety for operation at high temperatures.

increases. This means that if a limit for the peak flux density were set from a low-temperature MTR, then the B_P would be restricted to a *smaller* excursion at higher temperatures. One must be certain, however, to consider the MTR for the lowest temperature expected, for otherwise it is possible to lose protection as a result of reduced transverse voltage when the transformer gets cold.

For H7C1, as can be seen from Figs. 9.8 and 9.9, the MTR is more sensitive to changes in temperature than a designer might desire for optimum performance. To be more specific, if one wanted to use the entire available flux swing at −55°C, say ±0.4 tesla, he would monitor the transverse voltage and cut off the excitation of the transformer when v_T reached a level corresponding to an MTR of about −0.2. But then at +150°C his circuit would limit the flux swing to roughly ±0.15 tesla, or about 75% of what is available at that temperature. This is only a small imperfection, considering the large temperature variation of over 200 degrees, but the performance can be improved if desired.

One can compensate for the non-ideal response to changes in temperature by proper variation of the transverse current. For the case illustrated here, one would want the I_T to *decrease* at higher temperatures. This is not difficult, for as the next chapter will demonstrate, a genuine current source is not required for the generation of I_T -- just a voltage source and a single resistor will suffice. Thus it is a simple matter to make the transverse current temperature-dependent: a thermistor with the proper temperature coefficient is all

that should be required. When one compensates for temperature effects he should remember that since the storage time of power transistors typically increases with temperature, some additional margin in the design is desirable at high temperatures.

CHAPTER 10

PRACTICAL IMPLEMENTATIONS

In this section two practical circuits are shown which use a perpendicular field to sense the level of flux in a power transformer. One circuit is a relatively low power (100W) free-running push-pull converter which depends on the transverse voltage to toggle its two power transistors. This converter, running open loop, illustrates the simplicity of the idea in a straightforward and uncluttered manner. The other circuit is a 4kW push-pull buck converter which uses the transverse voltage signal to keep the power transformer out of saturation. This example shows how the sensing technique can easily be used in a high-power system to maintain high reliability without need for excessive overdesign in the power transformer.

10.1 Low-Power Free-Running Converter

Figure 10.1a is a schematic diagram of the entire power-processing circuitry for this simple converter. The purpose of the converter is to take a dc input, nominally 12 volts from a storage battery or automobile electrical system, and provide positive and negative dc outputs at approximately twice the input voltage for use by an audio power amplifier. The input voltage is "chopped" by the two D44H10 power transistors which alternately switch on and off to deliver a square wave of ±12 volts to the primary of the power transformer. The primary voltage is stepped up by the

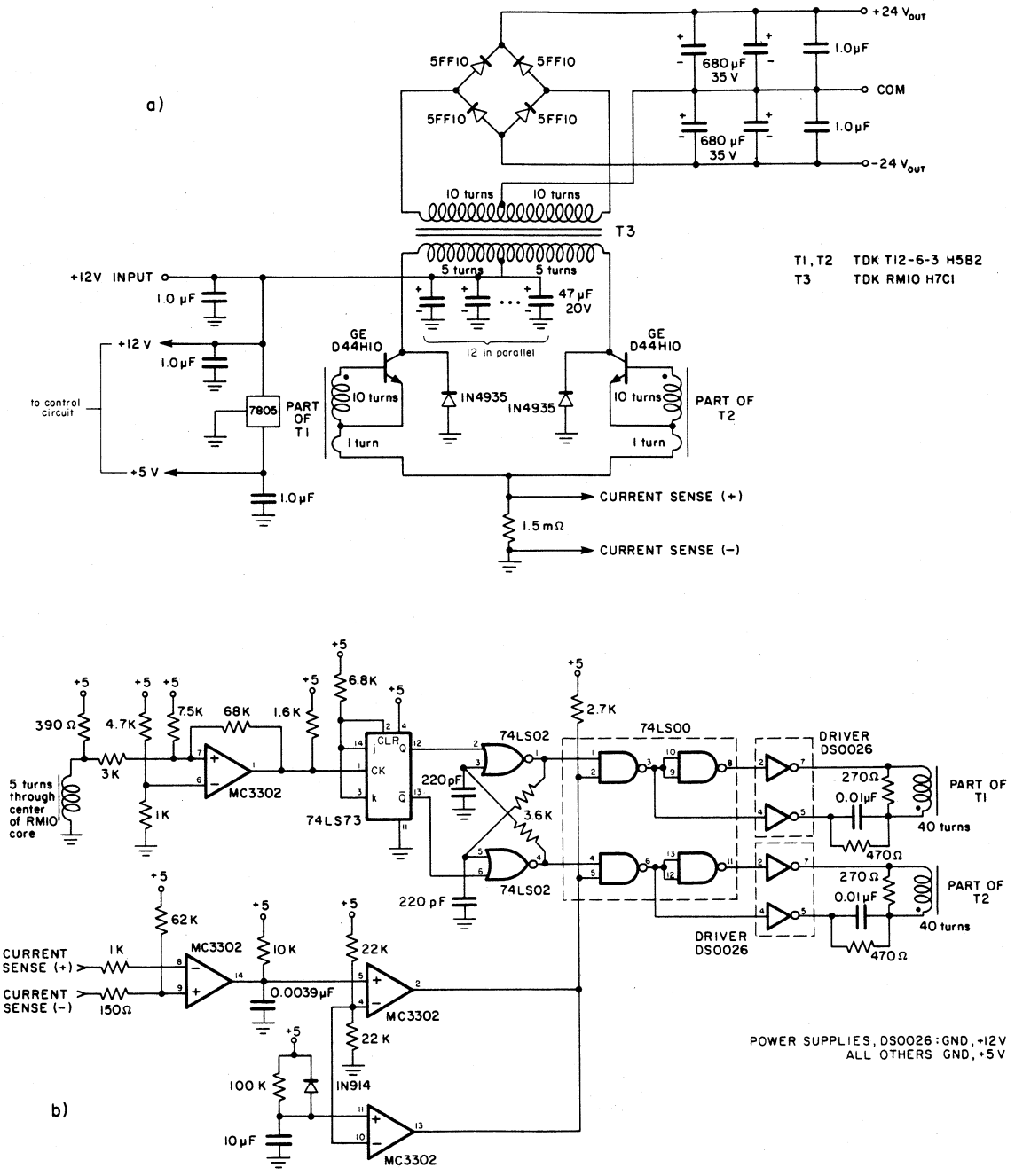

Fig. 10.1 Complete schematic for a 100W free-running power converter using orthogonal flux detection. (a) power circuit; (b) control and protection circuit.

1:2 turns ratio and full-wave rectified by the diode bridge. Since precise regulation of the output voltages is not required for this application, neither inductive energy storage nor pulse-width modulated control is needed. The absence of these requirements permits this extremely simple power supply to be highly efficient and very densely packaged.

The schematic of the control circuitry is shown in Fig. 10.1b. The complete control circuit consists of a comparator, one flip-flop, two drivers for the power transistors, and some nominal protection circuitry. The comparator trips when the transverse voltage reaches approximately -1 volt to toggle the flip-flop and complement the states of the power transistors. At an input voltage of 12 volts, each transistor is on and off for about 16 μs, and thus the transformer sees a square wave at a frequency of about 30kHz.

Figure 10.2 shows some pertinent waveforms from this converter as it runs unloaded. The top trace is one-fifth of the principal voltage, taken from a single-turn sense winding. The scale is 2.5 volts per division. The center trace shows the principal current measured from the collector currents with an ac clip-on current probe. This scale is 500mA per division. The bottom trace is the transverse voltage at one volt per division. Note how this shape resembles the MTRs as discussed previously in Chapter 8. The signal from the transverse winding of 5 turns is quite clean and uncorrupted by noise with a transverse bias of only about 10mA derived from a single resistor and the 5-volt bias supply.

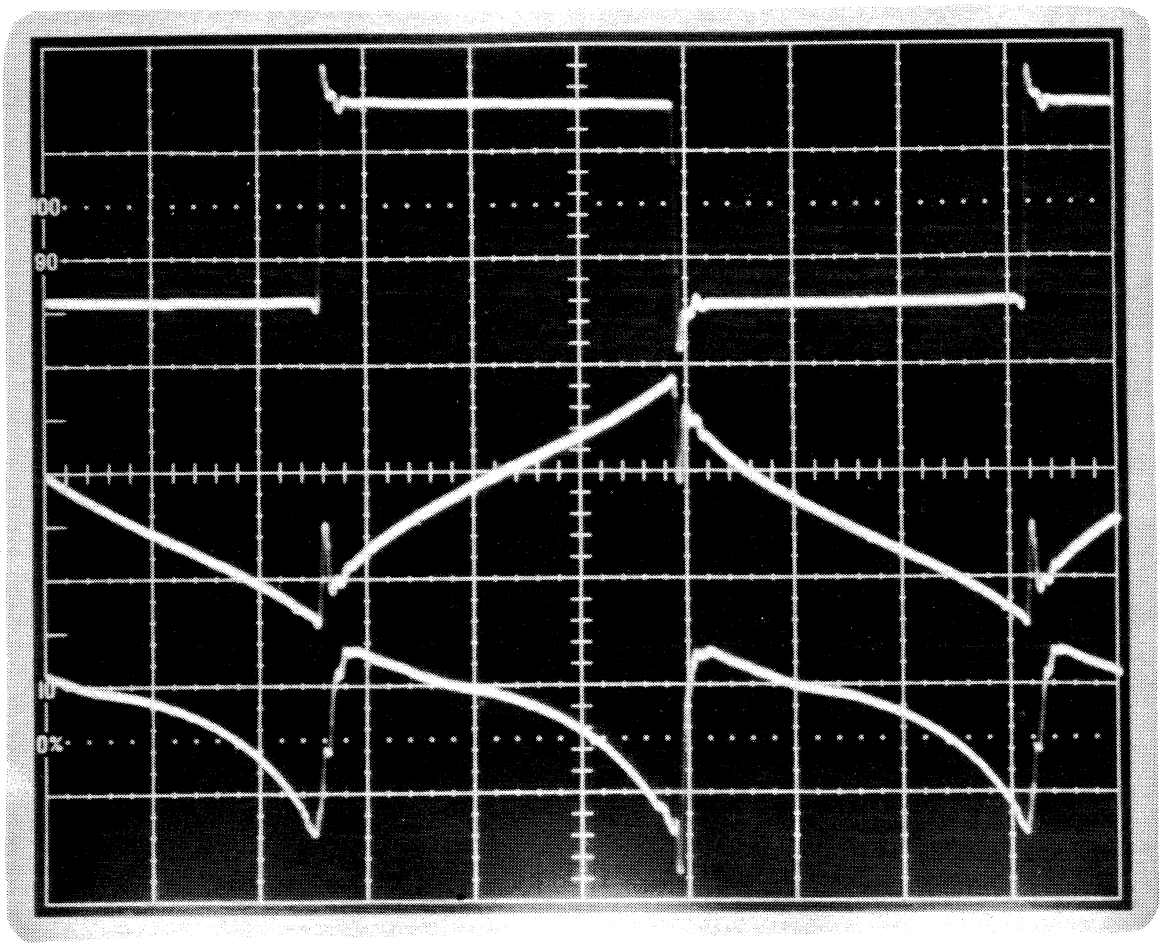

Fig. 10.2 Some relevant waveforms for the 100W free-running push-pull converter with no load. The top trace is the principal voltage, center is the principal current (proportional to H_P), and the bottom is the voltage on the transverse winding. Note how the transverse voltage is the same shape as the MTR. Because the input voltage is dc, the MTR can be easily measured directly from the breadboard with conventional instruments.

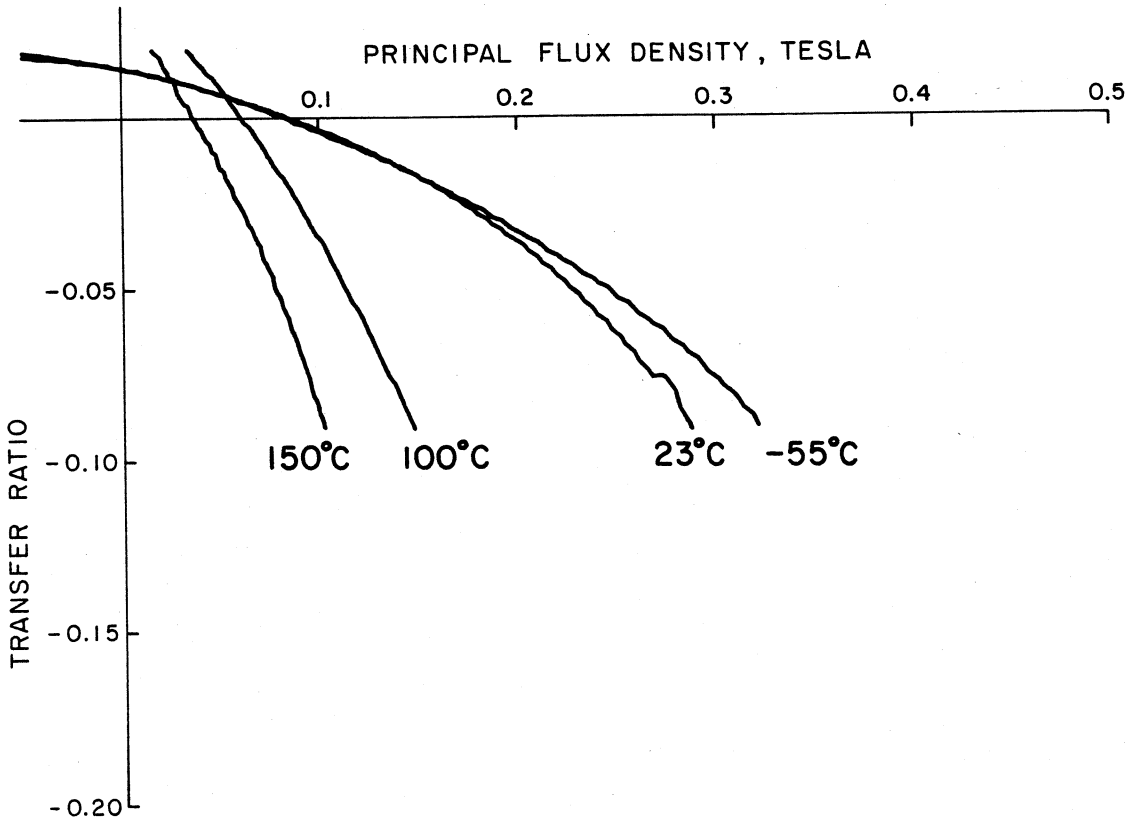

Fig. 10.3 MTRs measured on the working circuit of the free-running converter at different core temperatures. Since no temperature compensation is used, the transformer is limited to smaller flux excursions at high temperatures. Without temperature compensation, however, the transformer is grossly over-designed for high-temperature operation.

To evaluate the performance over temperature of the sensing technique without any thermal compensation, the transformer was detached from the rest of the assembly and was heated and cooled from +150°C to −55°C. Figure 10.3 shows the MTRs measured on the transformer while it was operating over this temperature range. The measurements are not shown in their entirety, but rather are truncated close to the ends of their actual excursions. The last few points on the curves could not be taken as legitimate parts of the MTR owing to the ever-present parasitic voltage spikes at the switching transitions; therefore, to avoid confusion they were not plotted in Fig. 10.3. Note from the maximum flux densities shown in the figure that this design is a rather conservative one, as the room-temperature flux density is limited to less than 0.3 tesla. As the MTR increases in magnitude with increasing temperature, the comparator causes the power transistors to toggle sooner, and, consequently, the converter runs at a higher frequency. At +150°C the comparator's trip-level corresponds to a maximum flux density of about 0.1 tesla, and the converter then operates at a frequency of approximately 70kHz from a 12 volt supply.

10.2 High-Power Constant-Frequency Converter

This section presents an example of the use of the saturation-detector as applied to a 4kW push-pull back converter which switches at a constant frequency of 20kHz. Some simple refinements are made to the detection circuitry of the free-running converter of the previous section to compensate for variations in input voltage and enhance reliability in noisy

environments. Schematic diagrams of the essential circuitry are given and typical waveforms are shown. The latter are especially interesting as they very nicely illustrate the circuit's ability to govern the flux excursion of the transformer.

Power Circuitry

Figure 10.4 is a schematic diagram of the power-processing circuit of this converter, which is part of a prototype inverter designed to interface a solar power system to the 60Hz ac power line [24]. The power transformer is a TDK EIC90 core of H7C1 material with a foil-wound primary and secondary. The two-turn transverse winding is wound with regular insulated wire through a 3.5mm-diameter hole drilled through the center leg. The hole was made with an inexpensive diamond-tipped core-drill. Figure 10.5 is an illustration of the power transformer which shows a single-turn transverse winding.

The transformer was designed to support a maximum magnetization current of about 2A (referred to the primary) while the maximum primary current is 50A. The new sensing technique makes it easy to keep the magnetization current within this limit at any power level or operating condition.

Control Circuitry

The essential parts of the control circuit are detailed in Fig. 10.6. The signal from the transverse winding is used to truncate the on-time of either power transistor as necessary to prevent the flux in the

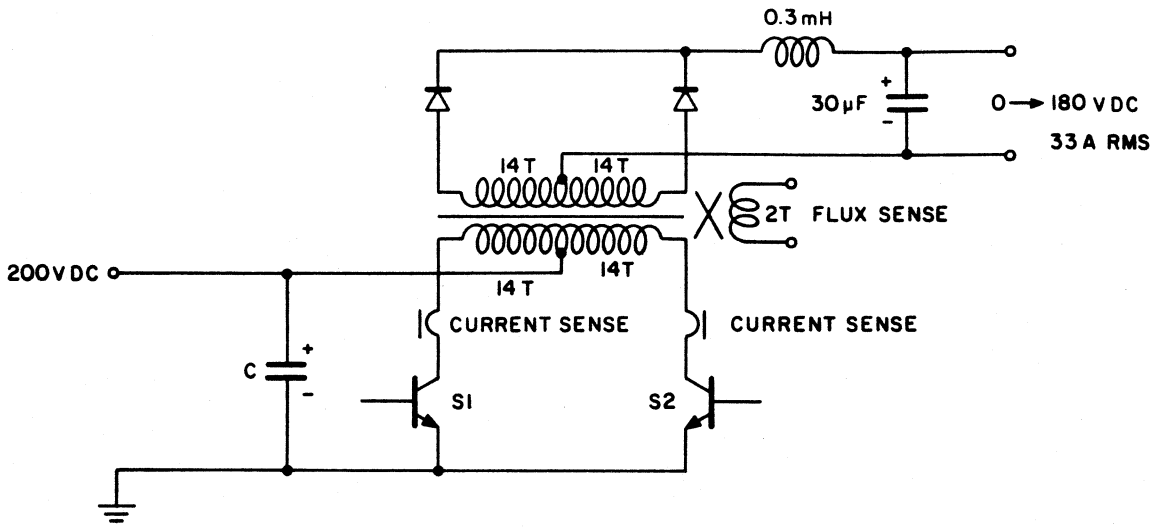

Fig. 10.4 Simplified schematic diagram of the power-processing part of the 4kW (8kW peak) buck converter. The dc output is modulated to produce a full-wave-rectified sinusoid which is later unfolded to deliver 60Hz ac power.

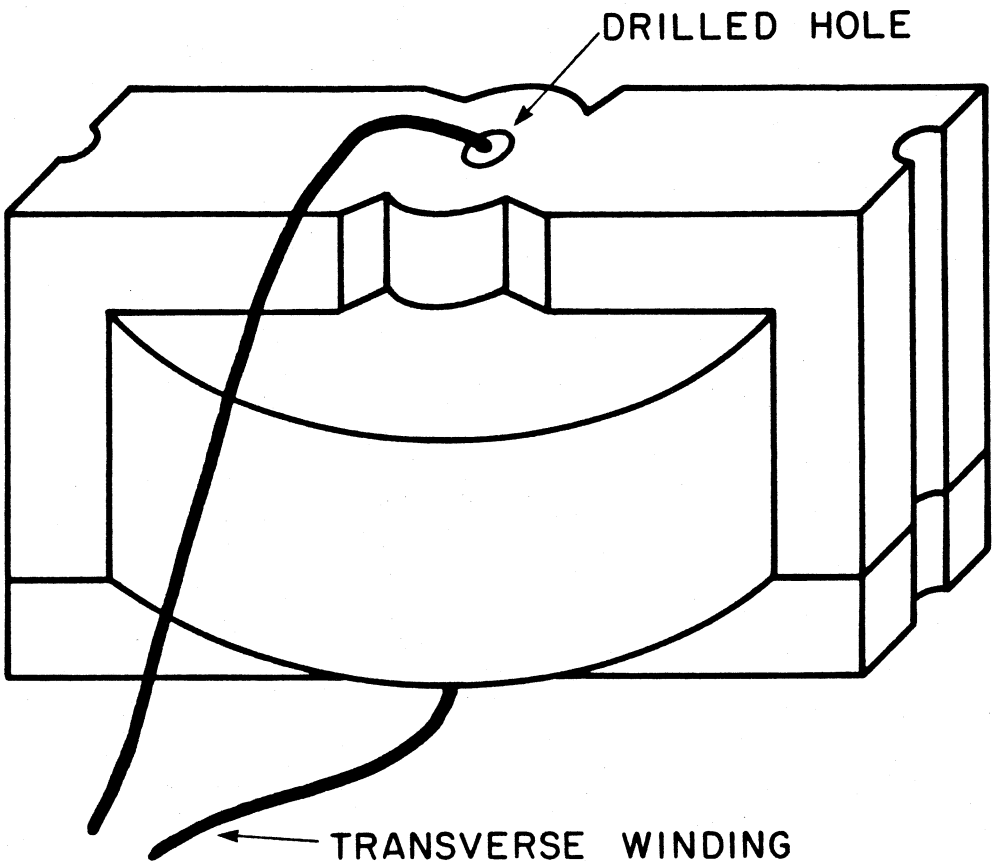

Fig. 10.5 Power transformer for the 4kW converter. The transverse winding is threaded through a hole drilled through both the center leg and I-piece of the TDK EIC90 core of H7C1 material. Primary and secondary are foil-wound. The actual transformer has two turns for the transverse winding. Since most of the transverse flux resides in the cylindrical center post as in the RM10 core, one should expect to measure the same MTRs for the two cores even though their overall geometries are quite different.

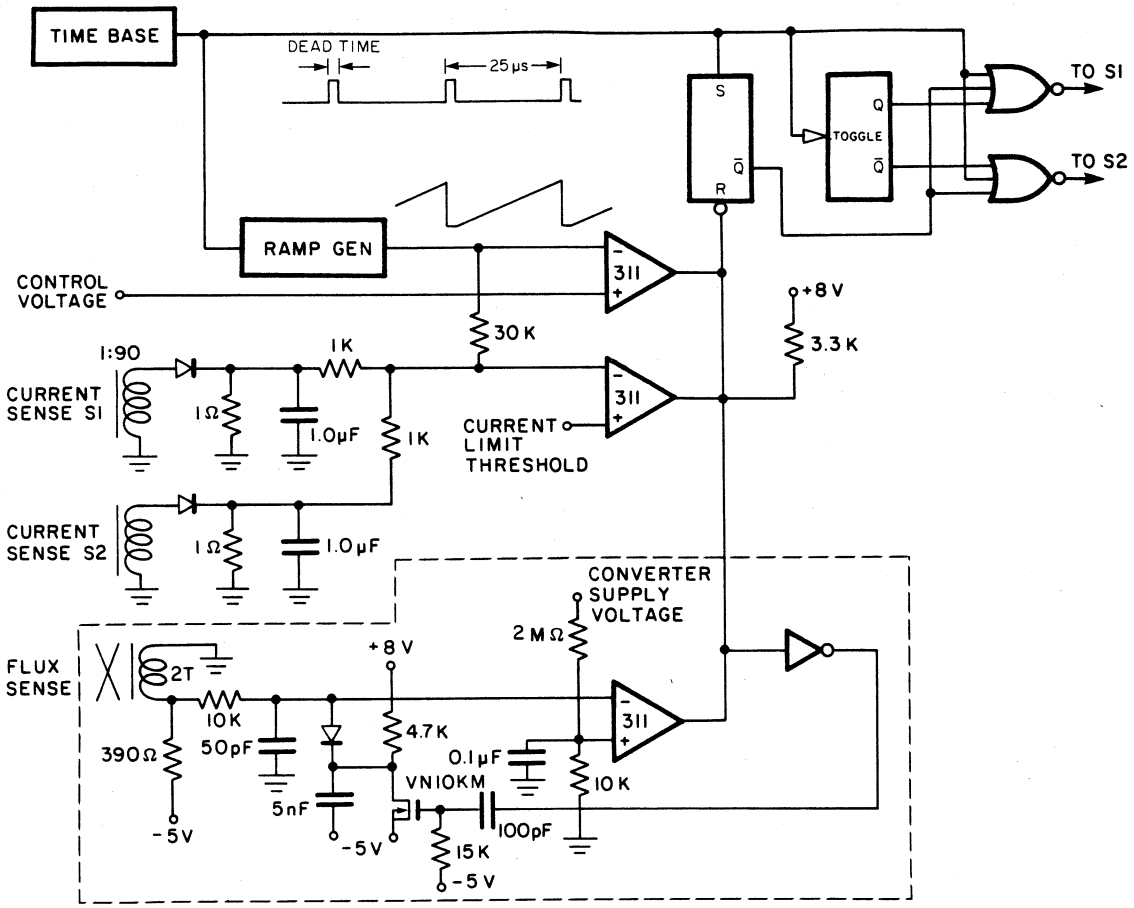

Fig. 10.6 The voltage from a transverse winding on the power transformer is used in the control circuit of the 4kW converter. Note that there is current sensing as well as flux sensing in the control circuit. Although current sensing is necessary to protect the switches from short circuits on the output, that alone is not sufficient to protect the transistors from the much faster-rising currents which can occur when the power transformer saturates.

transformer from exceeding a selected maximum. The circuit terminates the on-time if any one of three events occurs: (1) the ramp voltage exceeds the control voltage; (2) the current in either transistor exceeds the current-limit threshold; (3) the flux density in the transformer exceeds 0.3 tesla.

The transverse winding is biased with -13mA by a resistor connected to -5V, which is a simple but adequate current source. This gives a ***positive*** transverse voltage to indicate the approach to saturation, because the negative transverse current causes the voltage signal to be the ***inverse*** of the waveform shown in the last section. The inversion was done to facilitate a refinement to the detection operation. The threshold of the comparator is no longer constant, but rather is proportional to the converter's input voltage. This feature, which should be standard practice on all designs, makes the saturation detector independent of the converter's input voltage. (Recall that the transverse voltage is directly proportional to the principal voltage.) This addition is an improvement over the simpler constant-threshold design, which dangerously permits a greater maximum flux density at lower imput voltages. The free-running converter described in Section 8.1 does not face this problem because its input voltage is fairly well regulated.

In contrast to the free-running converter, this circuit does not maintain zero flux offset, but merely keeps the maximum flux density between the limits of ±0.3 tesla. Figure 10.7 makes this distinction clear. Figure 10.7a is a typical unrestricted B-H loop. The dashed lines

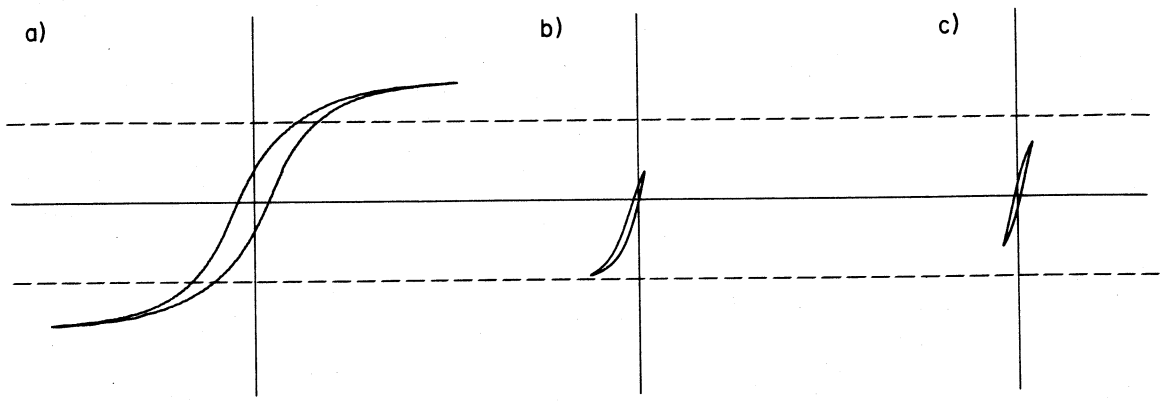

Fig. 10.7 The possible operating range (a) of the transformer is restricted by the control circuit to lie between the dashed lines. For small flux swings the excursion may be limited only at one end (b), or may not require any active limiting (c). One should not expect to see a symmetric transverse voltage at twice the frequency of the principal voltage for the situation in (b).

indicate the boundaries of permissible flux density. Owing to natural asymmetries in the power-processing circuit, a small dc magnetization current will usually build in the transformer such that the flux excursion will not be centered between the two limits, but rather will drift to one end of the permissible operating region, as shown in Fig. 10.7b. Thus the normal mode of operation is that one power transistor is turned off by the ramp comparator while the other is turned off by the saturation-detector. The on-time of the second switch is made shorter than that of the first by typically a few hundred nanoseconds to maintain the volt-second balance. At light loads and at low duty factors, the extremes of the flux excursion may drift away from each limit and become naturally centered as in Fig. 10.7c. In this case the saturation-detector does not truncate the on-times of the switches because the transverse voltage never reaches the threshold of the comparator.

Figure 10.8a shows typical waveforms. The upper trace is the primary voltage measured at the collector of one of the switches, and the lower trace is the transverse voltage. The fact the the flux excursion is being limited at one of the boundaries, as indicated in Fig. 10.7b, is clearly shown by the asymmetry of the transverse voltage signal. Recall that one should expect the frequency of the transverse voltage waveform to be twice that of the principal voltage only under conditions of perfect symmetry.

A further refinement to the detection circuitry is that the transverse signal is low-pass filtered by a 0.5 μs RC before it is fed to

a)

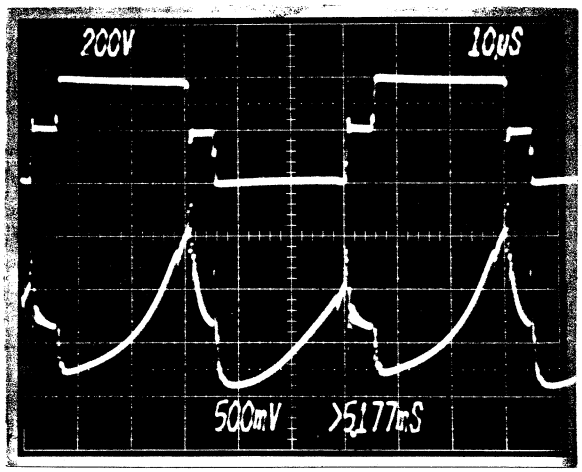

b)

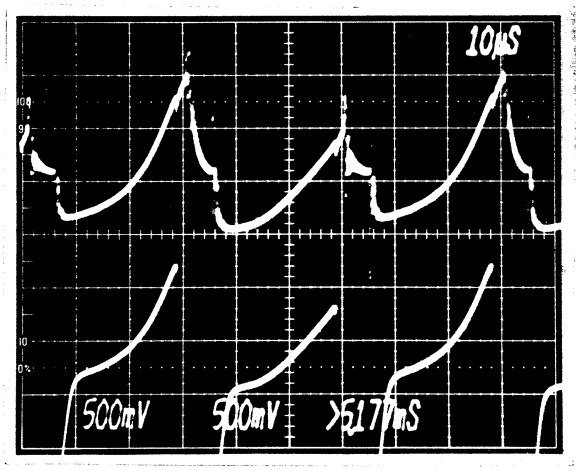

Fig. 10.8 Waveforms from the 4kW converter. In (a) the primary voltage is in the top trace and the unfiltered transverse voltage is at the bottom. The transverse voltage tells that the peak flux is being limited only on one side of the loop. The photograph in (b) shows the pure transverse voltage in the top trace and the filtered and strobed signal which goes to the comparator.

the comparator. The filtering eliminates false triggering from spurious voltage spikes induced by the high electromagnetic fields in the vicinity of the detector. Also, it was necessary to *strobe* the transverse voltage signal to maintain reliable operation at very high duty ratios. Because of transistor storage time, the transverse voltage overshoots the threshold, and, owing to parasitic effects believed to be caused by eddy currents in the core, the voltage remains above the threshold for a few microseconds after the transistor turns off. Without the strobe, this hold-up of the transverse voltage can cause the other transistor to be turned off at the beginning of its on-time. The simple strobe was implemented with a single field-effect transistor and two RC networks which hold the input to the comparator low for 10 μs following the turn-off signal. The filtered and strobed signal is shown in the lower trace of Fig. 10.8b relative to the pure transverse voltage signal in the upper trace.

10.3 Notes on Engineering Applications

In support of the examples presented in the previous sections, and as a general aid to design, this section offers some brief footnotes to facilitate the implementation of this technique to detect impending magnetic saturation.

The first note is concerned with the determination of the cross-sectional areas and lengths of the magnetic paths, which are of interest to the designer for scaling purposes. One can clearly see from Eq. (6.31) that if the behavior of the MTR is known for one core of a particular material, then it can easily be scaled for another core of a different size and geometry

if the appropriate dimensions are known. Unfortunately, the areas and the path lengths for both the principal and transverse directions are usually not given explicitly on manufacturers' data sheets. Therefore, the designer must usually compute these quantities from the mechanical dimensions of the structure.

Special consideration should be given to the principal area, because the correct value for A_P is usually *not* the same as the effective area A_e that is given on the data sheets. For most pot cores and RM cores the A_e on the data sheet is the area enclosed by the circumference of the center post. To obtain the correct principal area from A_e, then, one would have to *subtract the area of the center hole.* Since the area required to determine the flux density in the material is the *actual area of the ferrite* according to the assumptions in Chapter 4, the area not occupied by ferrite must be excluded.

The second note involves the general use of the technique. The practical examples demonstrated in this chapter require a net dc current to flow in the primary of the power transformer to compensate for excessive magnetization current which is supplied from the secondary. Therefore, the method of flux control shown here cannot be used when only the primary is dc blocked, as in the half-bridge converter. This limitation does not depreciate the orthogonal flux-sensing technique, however, because the difficulty is not related to the method by which the flux is *sensed*, but is a consequence of the manner in which the dc flux is *limited.* A study of special circuit techniques to limit flux for this

class of converters is a possible topic for future research.

Finally, because the flux density in practical structures is not uniform throughout, not all parts of a real magnetic device saturate at the same time. Although the MTRs given for different magnetic structures in this presentation are qualitatively very similar, one should not assume that the shapes shown here are representative of *all* structures. Because it is possible that the transverse voltage observed on other transformer structures may be somewhat different from that expected from a more ideal geometry, it is advisable to characterize other geometries to evaluate their suitability to this method of detection before any design is begun.

CHAPTER 11

CONCLUSION

In contrast to other disciplines of modern Electrical Engineering, the emerging field of Power Electronics emphasizes the efficient processing of power rather than the distortionless processing of information. Because dissipative elements are forbidden in circuits which process power, the elements available to the designer of a power-processing system are limited to switches, capacitors, and magnetic devices. The magnetic device has thus been elevated to a position of greater importance and higher visibility, driven by the need for improved performance and greater sophistication in the circuits which process and control electrical energy. One of the basic problems encountered in the use of magnetic devices is the avoidance of undesired saturation of magnetic material, particularly in power transformers.

Part I of this thesis has presented a new active method to detect the impending saturation of power transformers, particularly for use by designers of switched-mode power converters. This technique offers a simple and straightforward solution to the problems of degraded performance and catastrophic failures which can result from saturation of the power transformer.

The method exploits a first-order nonlinear effect, in which two perpendicular magnetic fields interact in the transformer's core to produce a voltage signal which is related to the total flux. This signal can be used directly by the converter's control circuitry to prevent further increase in flux density, and thereby protect the converter from the undesirable effects of saturation. An especially attractive feature of this flux-sensing technique is that it can be implemented directly on many standard, off-the-shelf ferrite cores without any mechanical modifications. In other configurations, only a small modification is required which does not introduce any unwanted air gaps or otherwise affect the length of the magnetic path.

One of the two perpendicular fields in the core is produced by the voltages on the conventional primary and secondary windings. The other field is introduced by an additional winding, transverse to both primary and secondary, which carries a few milliamps of dc current. The voltage which appears across the transverse winding outlines the nonlinearity of the B-H characteristic of the magnetic material, and, in so doing, gives a direct indication of impending saturation.

Since the mechanism of nonlinear interactions is not widely known to engineers in the field of Power Electronics, a simple but complete explanation of the phenomenon has been presented and the explanation has been reinforced through mathematical modelling and analysis. In addition, a simple but useful conceptual model has been developed which relates the transverse voltage to a time-varying

inductance.

Owing to the close relationship between the transverse voltage and the nonlinearity of the material, the voltage signal is a function of several extrinsic and intrinsic parameters: temperature, maximum flux excursion, frequency, and chemical composition are a few. The relationship of the transverse voltage to these and other parameters has been studied, and the information has been presented and discussed as an aid to practical design.

The facility of implementation of the orthogonal flux sensing technique at both high- and low-power levels has been demonstrated in two specific hardware examples: a 100W free-running converter and a 4kW push-pull constant-frequency pulse-width-modulated buck converter. The important specific details of each design have been discussed with the hope that this treatment will contribute another useful tool to the Power Electronics Specialist.

PART II

ANALYSIS OF INTEGRATED MAGNETICS TO ELIMINATE CURRENT RIPPLE IN SWITCHING CONVERTERS

CHAPTER 12

INTRODUCTION

Part I of this thesis discussed the application of a well-known natural phenomenon to the relatively new field of switched-mode power conversion. Although the interaction of orthogonal fields in nonlinear media had been known to physicists and material scientists for nearly a century, its practical application to the modern field of power electronics has just recently come to light. Part II discusses another remarkable phenomenon of certain magnetic devices, which is the extraordinary ability of certain multi-winding structures to exclude ac currents from some of their windings despite their being driven by ac voltages.

In contrast to the interaction of orthogonal fields, this *zero ripple* effect was only recently discovered on a modern switching converter [25]. Unlike earlier discussions of this topic, which were concerned with the performance of power converters which exhibited zero-ripple behavior [26], the treatment given in the following chapters is concerned with the analysis and design of the magnetic device itself. Although the phenomenon had been demonstrated in the laboratory, there was no good analytical basis from which one could properly design the magnetic devices or adequately explain some of the observed phenomena. This general lack of understanding was the chief motivation for this work.

Just as Part I was written to introduce the topic of orthogonal flux to practicing engineers of power conversion equipment, Part II is intended to be a self-contained discussion of the principles of operation and methods of analysis of these rather unusual and still quite unfamiliar magnetic structures.

CHAPTER 13

EVOLUTION OF MAGNETIC INTEGRATION

As explained in Chapter 2, magnetic components play an important role in the lossless conversion of electrical power, and for that reason it should come as no surprise that several inductors and transformers may be found in sophisticated power converters. Until recently these components were treated as separate and individual elements in the design of converters in much the same way as discrete transistors and diodes were used in the design of early signal-processing circuits. However, just as semiconductor devices can be consolidated into an *integrated circuit* and packaged on a single silicon chip, magnetic components often can be integrated into a single magnetic structure to enhance the performance of switched-mode power converters. This chapter gives a short summary of the recent developments which have motivated continued work in *integrated magnetics*, of which this thesis is a part. The review presented here is very brief, for there is an abundance of literature available to describe the details of previous work in the area [27].

13.1 The Basic Ćuk Converter

The pioneers of switched-mode power conversion technology had at their disposal the three basic converter topologies shown in Fig. 13.1, the buck, boost, and buck-boost converters. In addition to their useful properties, each of these circuits has the practical disadvantage of pulsating current at the input or the output, and this undesirable feature impeded the acceptance of switching converters for power supplies in electronic equipment. To reduce the often intolerable electrical noise pollution associated with these pulsating currents, designers resorted to brute-force filtering and heavy shielding which added extra components to the power supply and significantly increased its size and weight. Because such techniques were counterproductive in most applications, a number of new switching configurations were proposed to find a "quiet" converter which possessed all the desirable properties of the original circuits.

A topological simplification of a cascade connection of the boost and buck converters resulted in the basic *Ćuk converter* [28] shown in Fig. 13.2. This circuit was initially called the *optimum topology converter* because as a basic converter it possesses all the desirable properties of a universal switching converter with the minimum number of components. That is, in addition to having an ideal conversion efficiency of 100 per cent, the magnitude of the output voltage can be either greater than, less than, or equal to the source voltage and both input and output currents are non-pulsating. The decision to call the circuit optimum was premature, however, because it was soon discovered that it was possible to make the converter

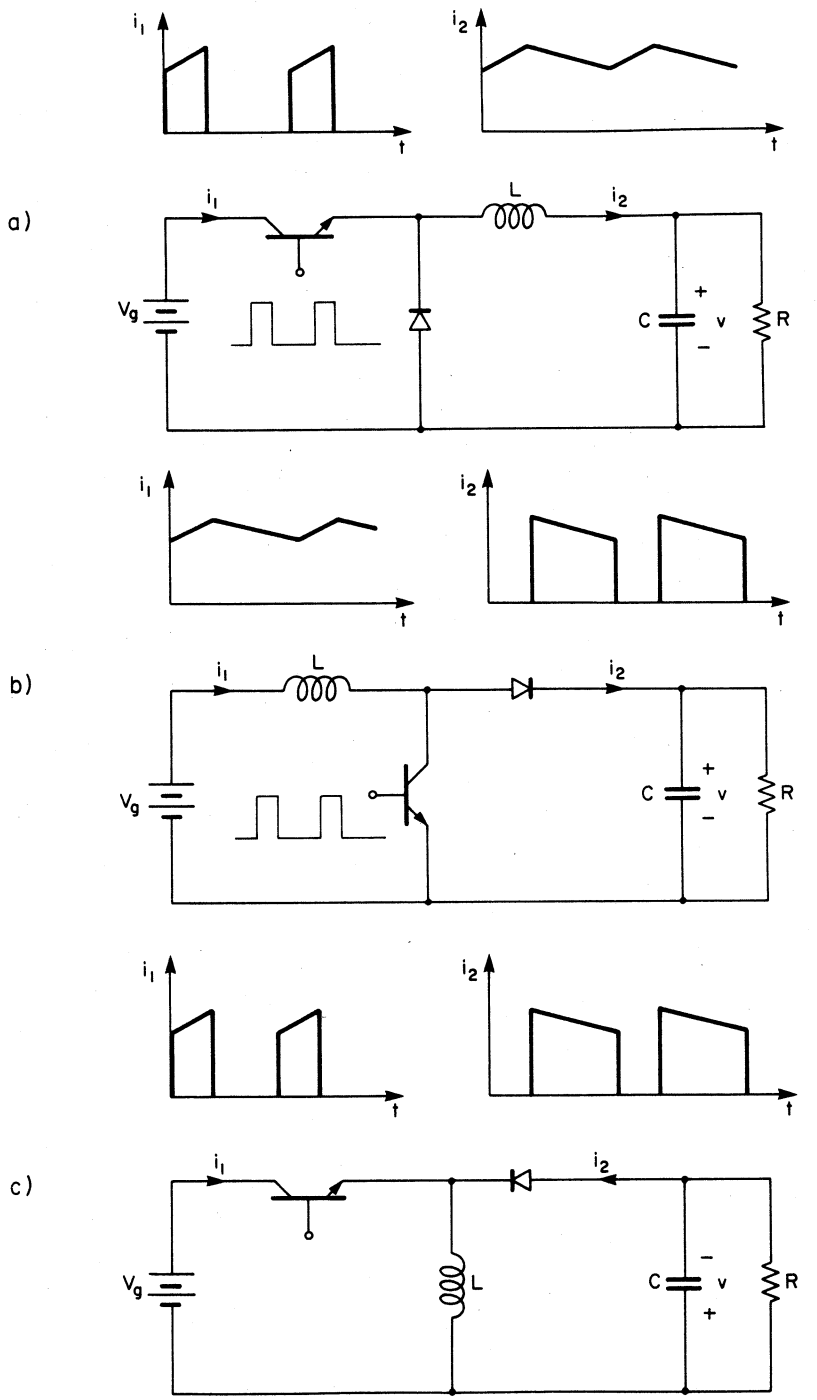

Fig. 13.1 Three basic switching converter topologies which have the undesirable characteristic of pulsating input or output currents. The buck converter (a), has pulsating input current and the boost converter (b), has pulsating output current. In the buck-boost converter of (c), both currents are pulsating.

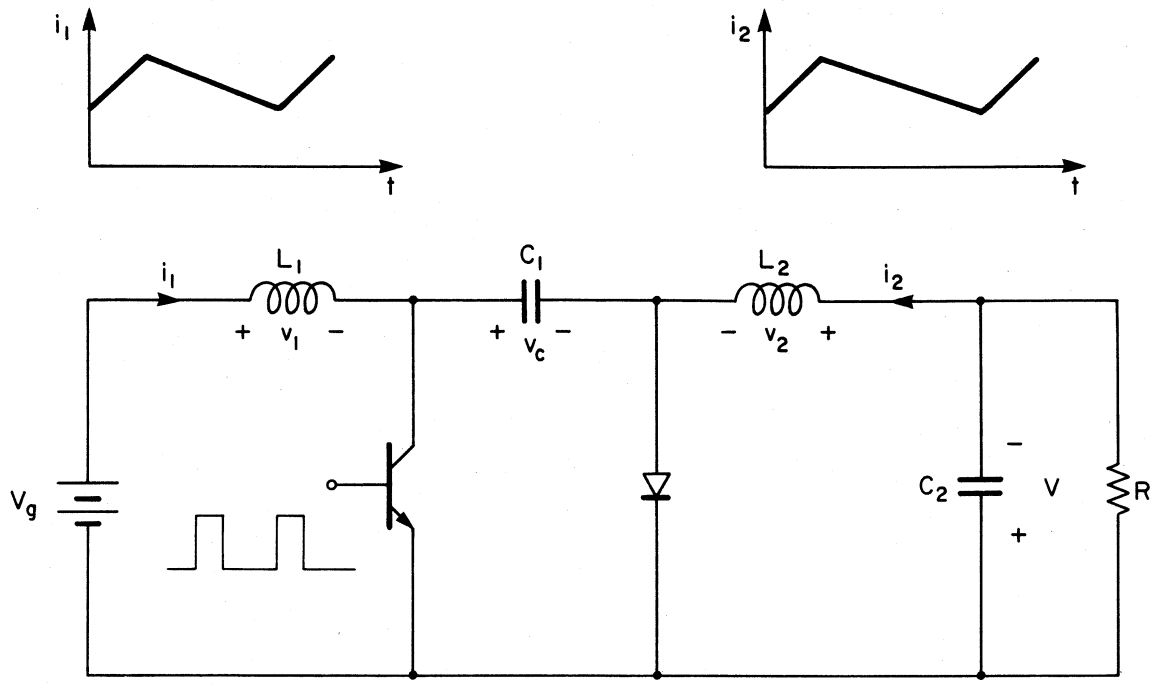

Fig. 13.2 Both input and output currents are non-pulsating in the "optimum topology" Ćuk converter.

even "more optimum."

13.2 Ćuk Converter with Coupled Inductors

Examination of the voltages on the inductors of the basic Ćuk converter of Fig. 13.2 showed that the steady-state waveforms of v_1 and v_2 are identical, and that this feature is independent of the operating point of the converter. If the voltages are always proportional, the inductors can be *coupled* such that both inductors can be wound on the same magnetic core [29]. Besides simplifying the converter by reducing the number of discrete components, the coupled-inductor configuration had the unexpected ability to steer the current ripple from the input to the output and vice versa [25]. While the sum of the input and output ripple magnitudes remained constant, the individual components could be adjusted to virtually any positive or *negative* value. As illustrated in Fig. 13.3, this remarkable discovery meant that the current ripple on the coupled-inductor Ćuk converter could be reduced to *zero* at either the input or the output with real components of finite value. Furthermore, it was found that this new phenomenon is a property not of the converter per se, but a feature of the *magnetics* alone. For example, when the coupled-inductor structure is removed from a converter with zero output ripple and then replaced with the input and output windings interchanged, the *input* becomes the zero-ripple port.

The coupled-inductor extension of the basic Ćuk converter demonstrated for the first time that two magnetic components which were previously considered to be separate entities could be integrated into a single magnetic structure with two windings. Moreover, the integration not

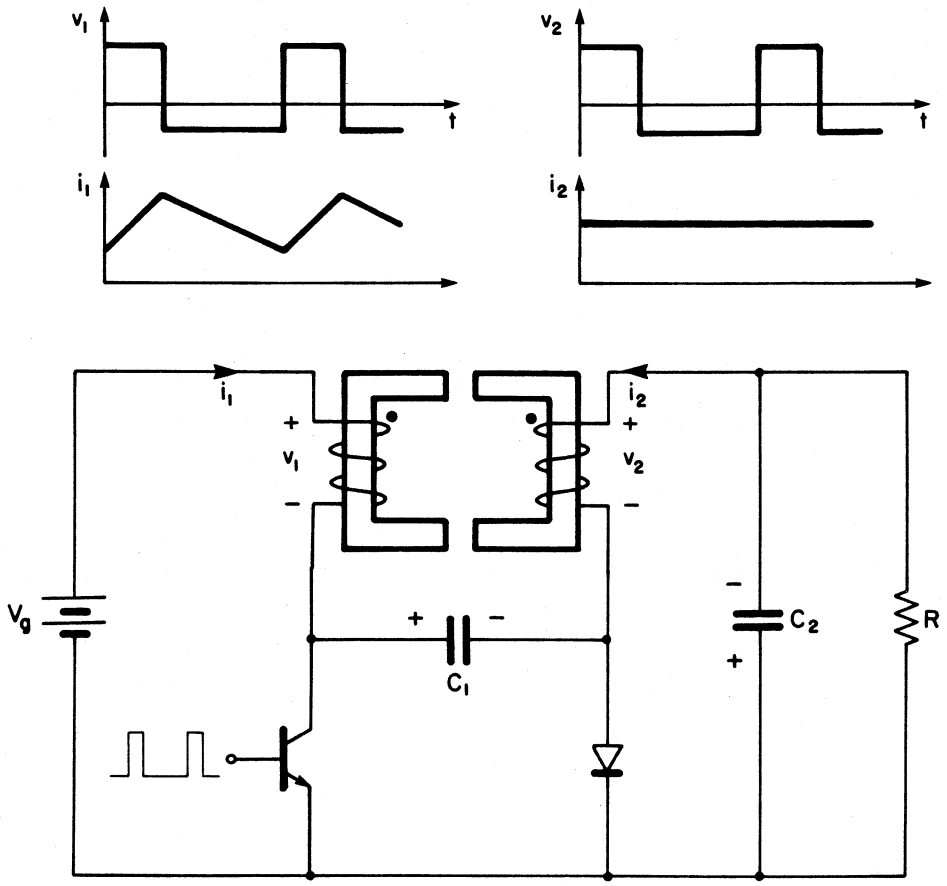

Fig. 13.3 Coupling the inductors of the basic Ćuk converter gives the "more optimum" zero-ripple converter. By proper design of the magnetics, the triangular ripple current on either the input or the output may be reduced to zero.

only preserved the basic functions of the original two separate inductors (energy storage and filtering) but in addition showed a surprising new and useful effect.

With the ability to produce zero current ripple on *one* side of a switching converter comes the unavoidable question of how to get zero current ripple on *both* sides of the converter at the same time. This problem can be solved by brute-force with a cascade connection of two Ćuk converters -- one with zero ripple on the input and the other with zero ripple on the output. There is a more elegant solution, however, and the next section prepares the groundwork for a more enlightened approach to this problem.

13.3 The Isolated Ćuk Converter

The basic Ćuk converter is extended to include electrical isolation between input and output via the steps outlined in Fig. 13.4 [25, 30]. The central energy-transfer capacitor is first split into two capacitors in series as shown in Fig. 13.4a. The dc properties of the converter are unchanged by this modification, but the individual voltages on the two series capacitors are indeterminant. The addition of a third inductor as shown in Fig. 13.4b, however, sets the average voltage at the node between C_A and C_B to zero, which fixes the steady-state voltages on each capacitor without altering any of the dc properties of the original converter. In the third step the new inductor is replaced by two inductors in parallel as illustrated in Fig. 13.4c, which leads to the evolution of the real transformer in the final isolated version of Fig. 13.4d. Because the waveforms of the inductor voltages v_1

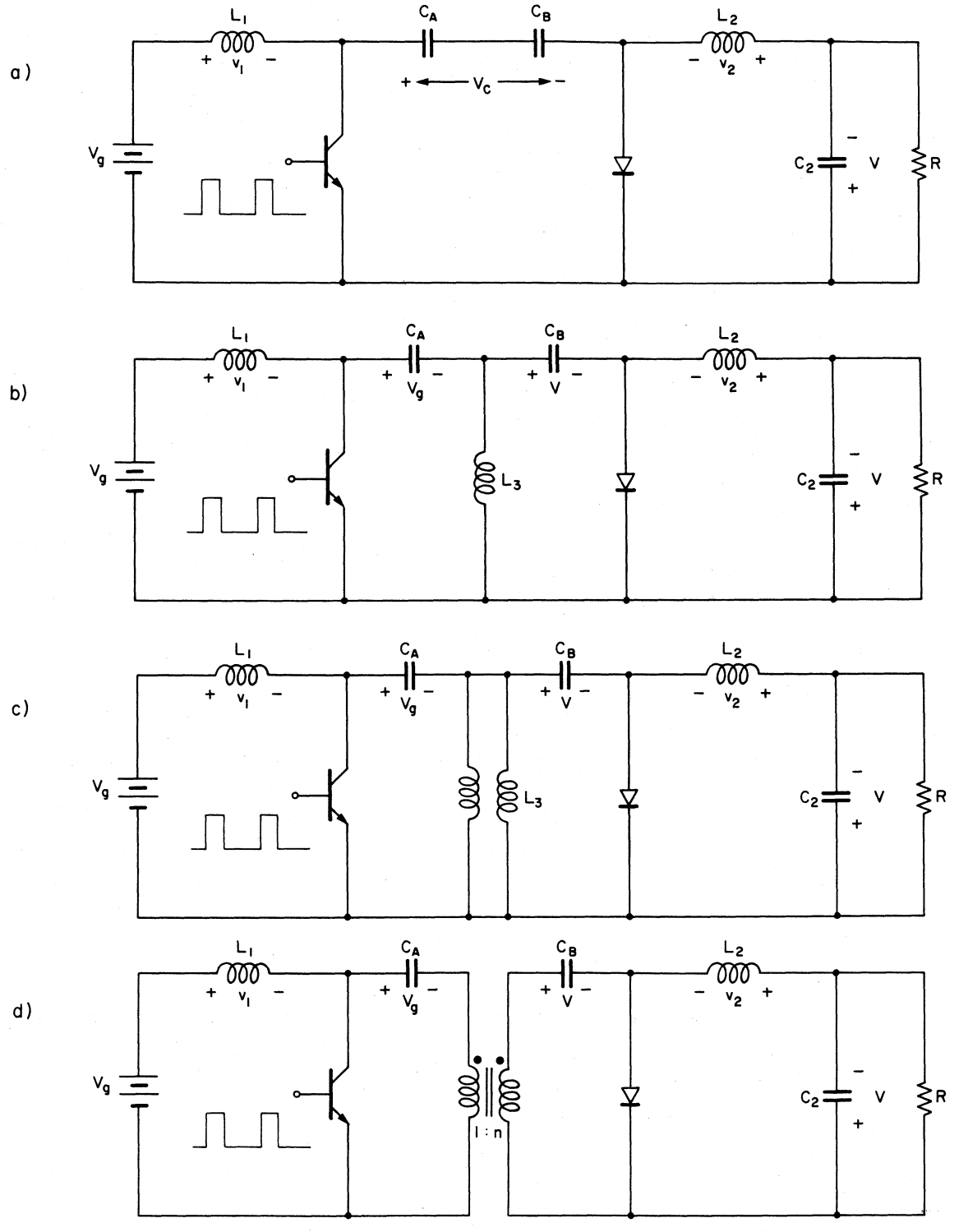

Fig. 13.4 Steps leading to the isolated version of the basic Ćuk converter.

and v_2 are still proportional after each of these transformations, the inductors L_1 and L_2 may be coupled just as in the basic Ćuk converter.

13.4 Converter with Zero Current Ripple on Both Input and Output

The circuit in Fig. 13.4c, which was an intermediate step in the derivation of the isolated version of the basic converter, provides a means for achieving zero current ripple *simultaneously* at both ports of the converter. Analysis of this modified converter reveals that the voltage waveforms on all the inductors are identical. Hence, the inductors may be coupled as shown in Fig. 13.5 to provide separate coupled-inductor structures for the input and output. Because the zero-ripple property observed in the basic Ćuk converter was demonstrated to be a characteristic of the magnetics alone, one should expect to achieve zero current ripple on both the input and the output separately, simultaneously and independently by proper design of the two coupled-inductor structures. It is easily verified that this is indeed true by construction of the circuit as shown in Fig. 13.6, which is drawn to emphasize the hardware implementation of the two coupled inductors.

13.5 Ćuk Converter with Integrated Magnetics

Although it may seem at this point that the ultimate dc-dc converter topology has been found, one can further simplify the circuit of Fig. 13.5 and at the same time introduce isolation while maintaining zero current ripple at both input and output. It is clear that isolation can be achieved by simply dividing the circuit into two parts with a transformer as

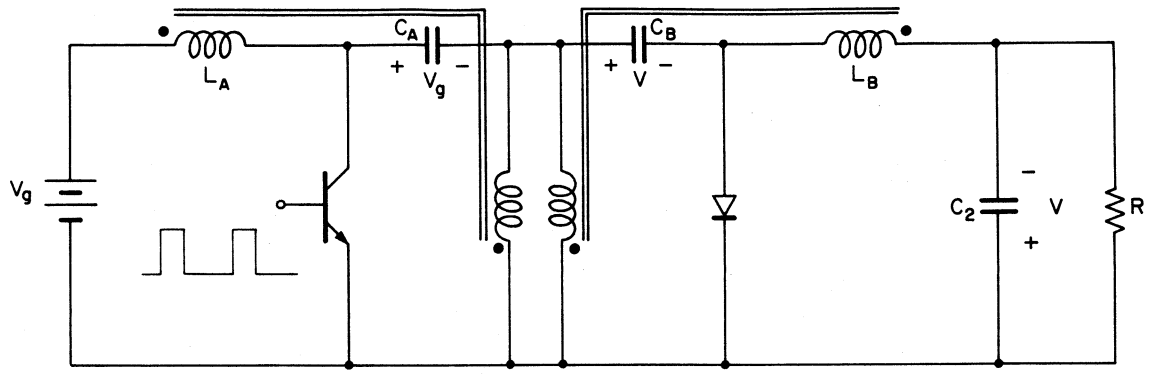

Fig. 13.5 The two central inductors used in the intermediate step of Fig. 13.4c may be coupled to the input and output inductors. This converter with two coupled inductors has an added degree of freedom which permits the converter to have zero current ripple on both the input and the output at the same time.

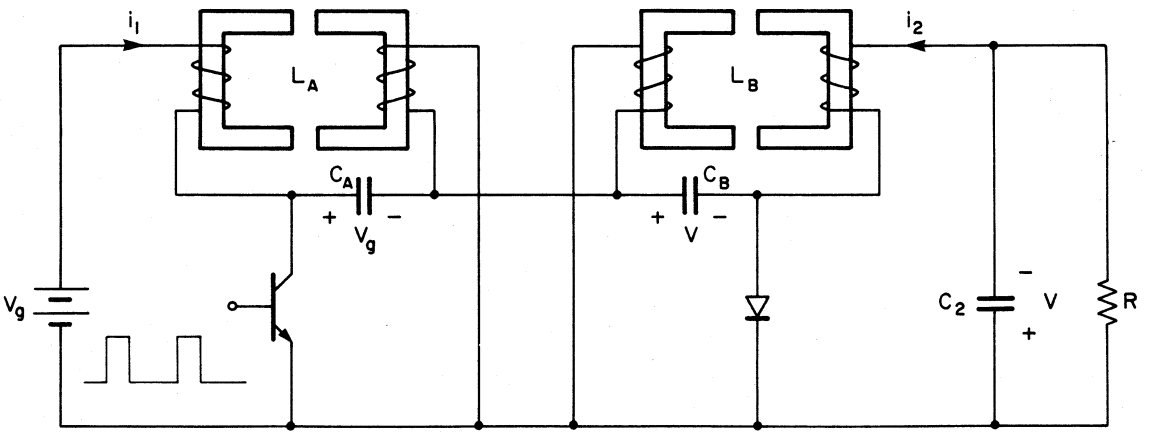

Fig. 13.6 The coupling of the inductors in Fig. 13.5 may be accomplished with two sets of U-cores. By proper design of these two coupled inductor structures one can achieve zero current ripple simultaneously and independently on the input and the output.

shown in Fig. 13.7. The mechanical implementation of this final consolidation of inductive elements is shown in Fig. 13.8, which clearly illustrates the concept of *integrated magnetics* as applied to an isolated single-output Ćuk converter [31]. By adjustment of the air gaps in this single totally integrated magnetic structure, one may control the current ripples on both the input and output to achieve the ideal dc-dc conversion properties not possible with discrete magnetic components.

13.6 Magnetic Integration for other Converters

Although the phenomenon of zero current ripple was first observed on the coupled-inductor Ćuk converter, its use is by no means limited to that topology. As mentioned in Section 13.2, the zero-ripple property is a characteristic of the magnetics -- the converter merely provides the voltage excitations in the proper proportions. To take advantage of this phenomenon, a converter need only provide proportional voltages across two or more independent inductive elements over the entire range of intended operation. Many converters possess this property in their multiple-output extensions [31-33], and therefore have the ability to provide at least one output with zero current ripple [34, 35]. There is no such restriction for *magnetic integration*, however. Even though it may not be possible to achieve zero ripple with a given converter topology, it is often advantageous to integrate the inductive devices to save on magnetic material [31, 36, 37].

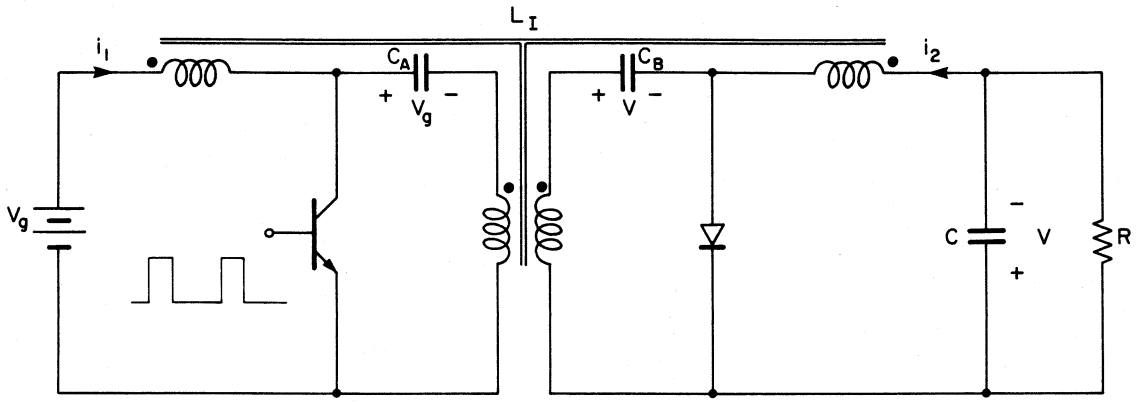

Fig. 13.7 The two central inductors in the circuit of Fig. 13.5 can be separated by an isolation transformer. This modification is portrayed by the unusual transformer symbol in this schematic diagram, where the two central inductors have been incorporated into the magnetization inductance of the transformer.

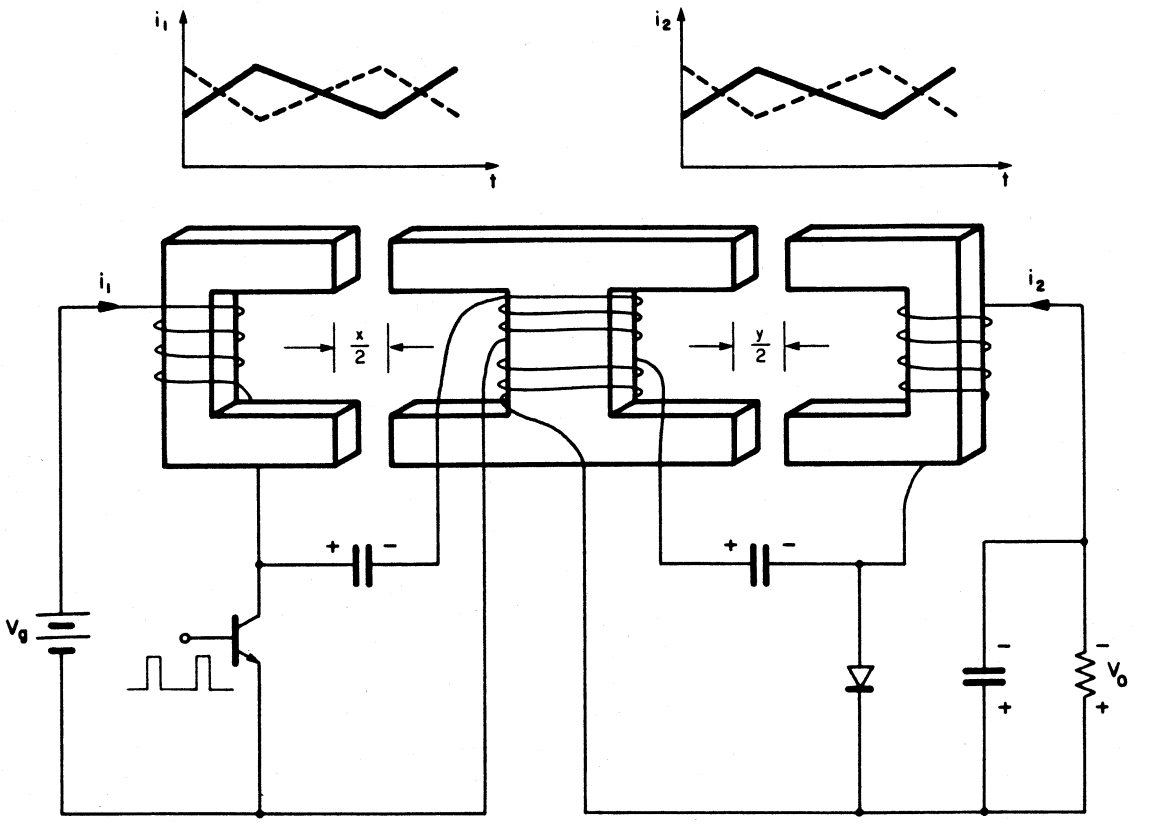

Fig. 13.8 Illustration of how the circuit of Fig. 13.7 may be realized with a magnetic structure. If the windings of the device have the proper number of turns, one can adjust the two air gaps to change the current ripples on both the input and output from positive to negative to zero.

CHAPTER 14

DEFINITION OF THE PROBLEMS

Progress in the field of Power Electronics has been driven jointly by revelations which come from theoretical analyses and by experimental observations of unexpected phenomena. The observation of the ripple-steering capability of the coupled-inductor Ćuk converter of Fig. 13.3 motivated an analysis which predicted the existence of *zero* ripple-current [25, 27]. The analysis also established the necessary electrical characteristics of the coupled-inductor structure which permitted design of two-winding magnetic devices with the zero-ripple property. It was clear that this knowledge could be applied directly to the dual coupled-inductor converter of Fig. 13.6 to obtain zero current ripple simultaneously and independently at both the input and output, and these expectations of the design were verified by experiment.

The converter with totally integrated magnetics of Fig. 13.8 was conceived by simple topological manipulation of the dual coupled-inductor converter. Although hardware implementation of the circuit demonstrated that zero ripple could indeed be achieved by proper adjustment of the two air gaps, no analytical model existed for the integrated structure. The concept of zero ripple by magnetic integration could be demonstrated empirically by trial and error, but no one could design such a structure for that purpose, nor could anyone explain the unexpected phenomena observed

in the adjustment process.

14.1 Adjustments for Zero Ripple

When the integrated structure in the converter of Fig. 13.8 was adjusted for zero ripple, it was observed that the input and output ripples could not be adjusted independently. This was an unexpected result. Figure 14.1 illustrates the observations schematically. Starting with some arbitrary initial combination of the two air gaps, input gap x_0 and output gap y_0, one observes the typical triangular current ripples as shown in Fig. 14.1a. Then, by adjustment of only the input gap from x_0 to x_1, the input current ripple is made to vanish while the output current is still substantial as shown in Fig. 14.1b. Next, the output gap y_0 is adjusted to some value y_1 which gives zero ripple on the output. As seen in Fig. 14.1c, the last adjustment produced zero ripple on the output but caused some ripple to reappear on the input, although at a significantly smaller magnitude than at the original (x_0,y_0) combination. Returning again to the input gap and adjusting it to x_2 nulls the input ripple, but forces a small amount of ripple to reappear on the output. This sequential adjustment in practice converges very quickly to the final solution of air gaps x_s and y_s for which input and output have (to first order) zero current ripple. Oscilloscope photographs of a typical series of adjustments are shown in Fig. 14.2.

If the same experiment were repeated with different initial gap positions, the same solution (x_s,y_s) would be obtained, but the sequence of intermediate gap combinations would be different. Given that it is possible to obtain a solution for simultaneous zero ripple, there appears to be an input

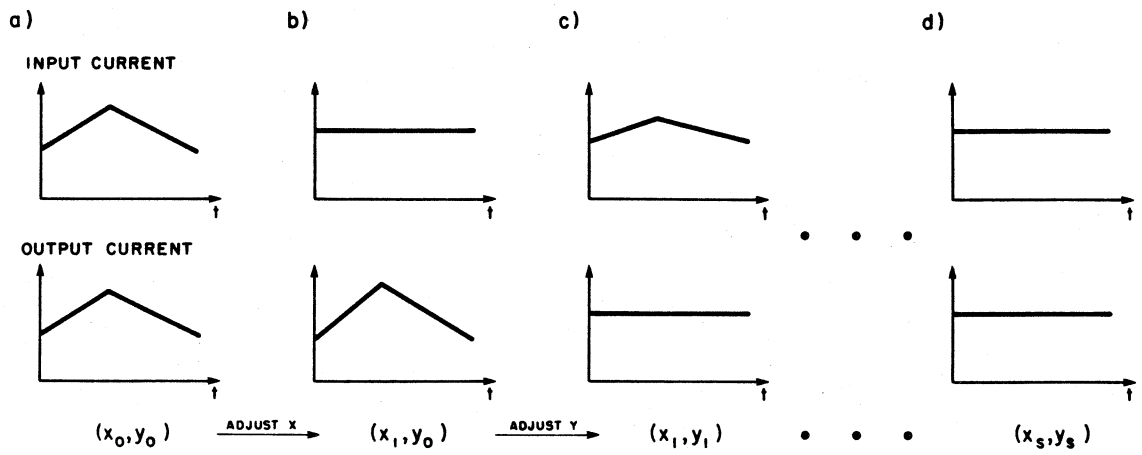

Fig. 14.1 By successive adjustments of the two air gaps, one can adjust both the input and output currents to zero ripple by an iterative procedure.

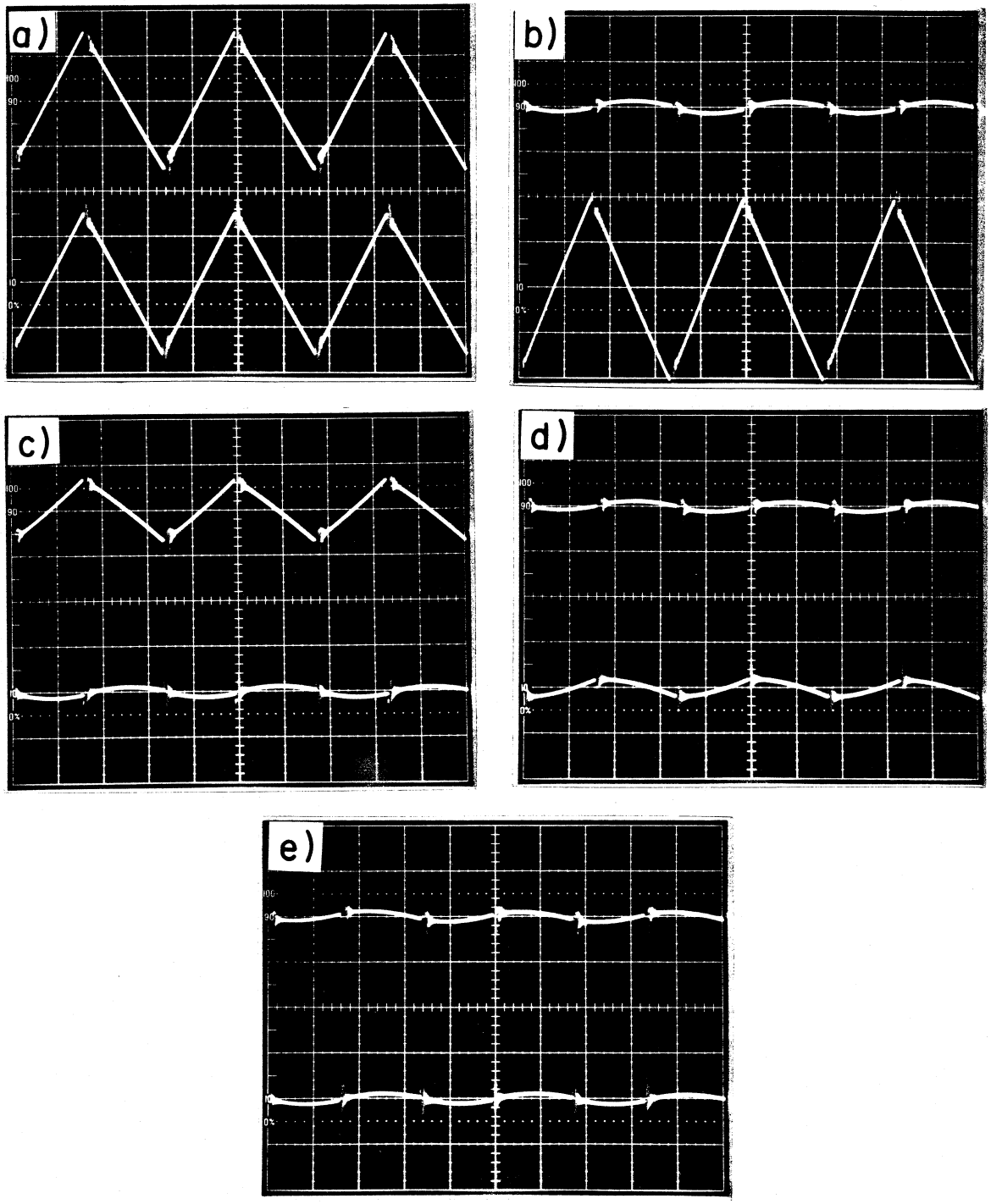

Fig. 14.2 Photographs of the input and output currents for a typical session of adjustments for simultaneous zero ripple. The triangular ripple is nulled out after only a few iterations.

gap x for any output gap y at which only the *input* current has zero ripple. Similarly, for any input gap one finds an output gap which gives zero ripple only on the *output*. Plotting these gap combinations in the y vs. x gap plane results in curves similar to those in the qualitative illustration of Fig. 14.3. The combination which results in zero ripple on both input and output simultaneously is obviously at the intersection of the two curves.

14.2 Zero-Ripple Solution and Models for Design

The above experimental observations demand further analysis of the integrated magnetic structure of Fig. 13.8. First, one would like to know the analytic solution for the combination of gaps which gives zero current ripple simultaneously on both the input and the output. Secondarily, there are several other questions which naturally arise. Is the solution unique? Which physical parameters are most important in the design of such a structure for practical applications and what are the limitations to such a design? What causes the unexpected interactions between the gap adjustments and can they be predicted?

In addition to finding answers to these questions which are related to the design of the *magnetics*, there is a need to provide models which one can use to design the *converter*. The strange integrated magnetic structure in Fig. 13.8 is not compatible with any conventional transformer model. The analysis should provide as a by-product simple *circuit models* which relate the physical parameters of the magnetic structure to electrical elements to aid in the design and dynamic characterization of the power converter.

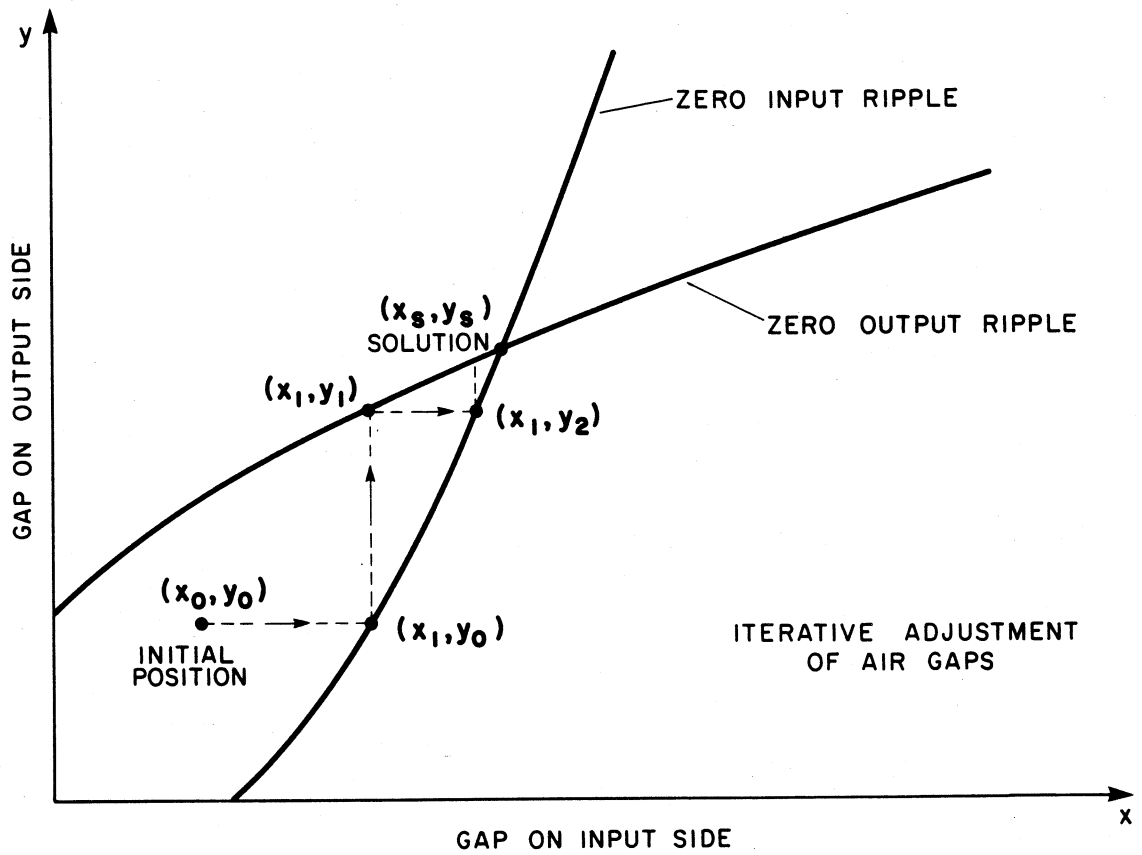

Fig. 14.3 Interpretation of the experimental observations of the interactive gap adjustments. The adjustments seem to suggest the existence of non-orthogonal boundaries of zero current ripple in gap space.

CHAPTER 15

TOOLS FOR ANALYSIS

Although the behavior of the zero-ripple integrated magnetic structure in the circuit of Fig. 13.8 had been demonstrated in the laboratory for several years, no explanation of the observed phenomena was available until now. Analysis of the magnetics had not been enthusiastically pursued simply because everyone believed that it would be too cumbersome and too difficult.

Magnetic structures can be analyzed and characterized in many different ways, and, indeed, if one chooses the wrong approach the situation can quickly become quite hopeless. This chapter reviews some of the basic tools available for the general task of analysis of magnetic structures, and each has its own particular strengths and weaknesses. Subsequent chapters will show how these rather elementary concepts can be applied to obtain good engineering solutions to some very complicated magnetic problems.

15.1 Conventional Coupled Inductor Equations

One way to characterize a static magnetic device is to consider the device to be a black box of linear inductive components, as illustrated by Fig. 15.1. The electrical terminal properties of the device are described in general by a system of linear equations commonly known as the *coupled inductor equations*, which are written below in matrix form.

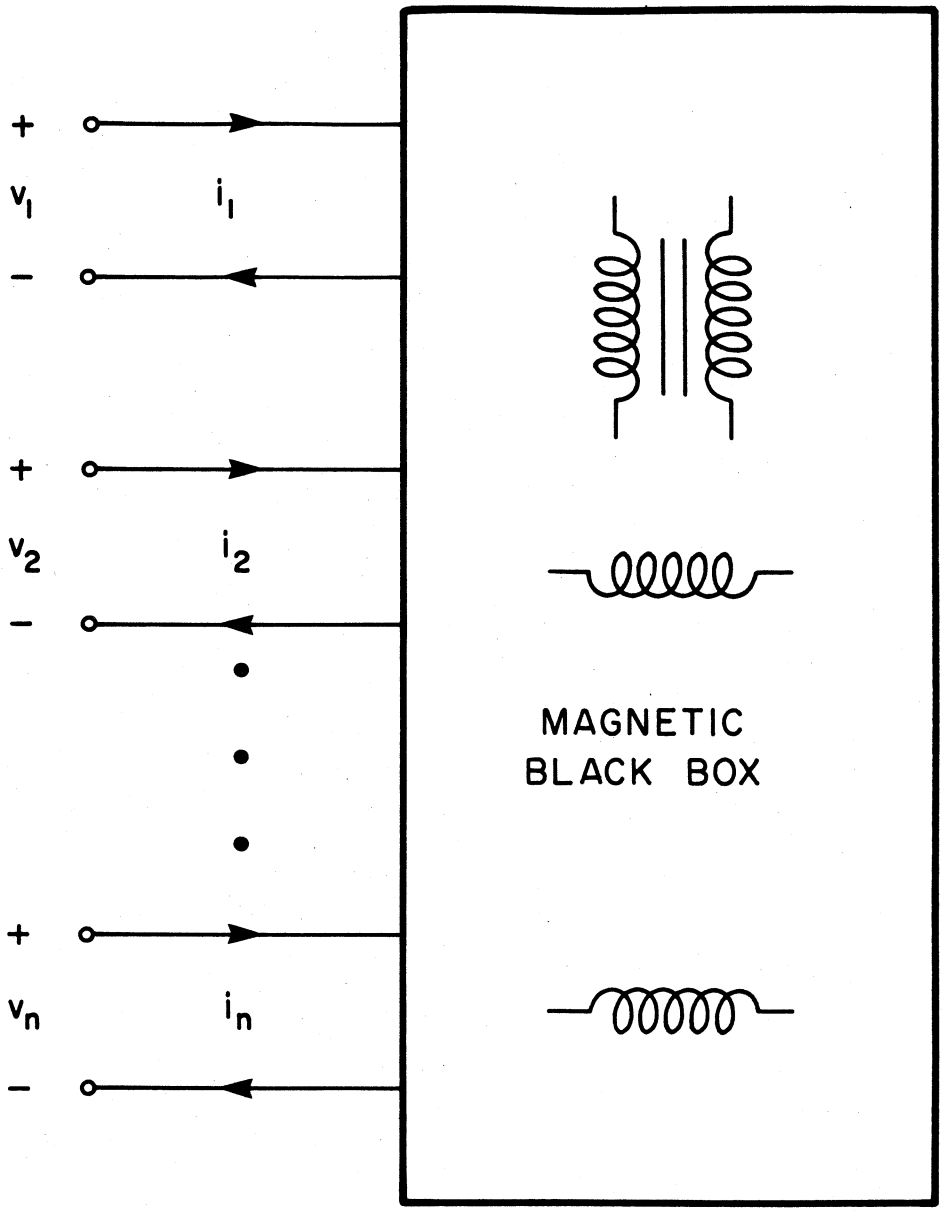

Fig. 15.1 One can model a magnetic device by the coupled inductor equations, which consider only the electrical relationships at the terminals of a magnetic black box without any consideration of the internal structure.

$$\begin{bmatrix} v_1 \\ v_2 \\ \cdot \\ \cdot \\ \cdot \\ v_n \end{bmatrix} = \begin{bmatrix} L_{11} & M_{12} & \cdot & \cdot & \cdot & M_{1n} \\ M_{21} & L_{22} & \cdot & \cdot & \cdot & M_{2n} \\ \cdot & \cdot & & & & \cdot \\ \cdot & \cdot & & & & \cdot \\ \cdot & \cdot & & & & \cdot \\ M_{n1} & \cdot & \cdot & \cdot & \cdot & L_{nn} \end{bmatrix} \begin{bmatrix} \frac{di_1}{dt} \\ \frac{di_2}{dt} \\ \cdot \\ \cdot \\ \cdot \\ \frac{di_n}{dt} \end{bmatrix} \tag{15.1}$$

It can be shown from reciprocity and conservation of energy that $M_{ij} = M_{ji}$, and hence the matrix of inductive elements is symmetric.

This rigorous mathematical representation is useful for linear network analysis, especially when one is interested in a state space description of the circuit. The values of the elements in the matrix can be obtained from direct measurements at the electrical terminals of the physical device without knowledge of the structural details. In addition, the coupled inductor equations can be used in the synthesis problem to define the requirements of the magnetic device for a particular purpose. The major deficiency, however, is that the coupled inductor equations contain no information about the physical description of the magnetic structure, and therefore they are not much use for design purposes. The link between the mathematics of the coupled inductor equations and the hardware of the physical device is easily made through the concept of reluctance and permeance, which follows directly from the idea of the magnetic circuit. These straightforward connections are briefly reviewed in the next section.

15.2 Reluctance, Permeance, and the Magnetic Circuit

The concept of the electric circuit is a simplification of the general field relations which describe electromagnetic phenomena. If one examines these relations in the same light which motivated the idea of the electric circuit, one finds that there is a correspondence between the fundamental equations which describe electric and magnetic fields. This can be seen in the following comparison, in which colinear vectors are assumed.

$$I = \int\int_A J \, dA \qquad \Phi = \int\int_A B \, dA \tag{15.2}$$

$$\text{emf} = V = \int E \, dl \qquad \text{mmf} = NI = \int_{\text{closed}} H \, dl \tag{15.3}$$

$$J = \sigma E \qquad B = \mu H \tag{15.4}$$

The relationships on the left are the basis for the concept of the electric circuit, in which an assumed uniform current density J is totally contained in a material and driven through a resistance by an electromotive force (emf) V. *Magnetic circuits* can be analogously considered as the simplification of the corresponding field equations on the right, in which a uniform flux density B is contained by a high permeability magnetic material and driven through a *reluctance* by a magnetomotive force (mmf) NI.

To elaborate, consider the electric circuit of Fig. 15.2. For a given voltage source V, and under the assumptions of uniform cross section and uniform current density, the current I can be found by sequential solution of the field equations on the left side of (15.2-15.4) as

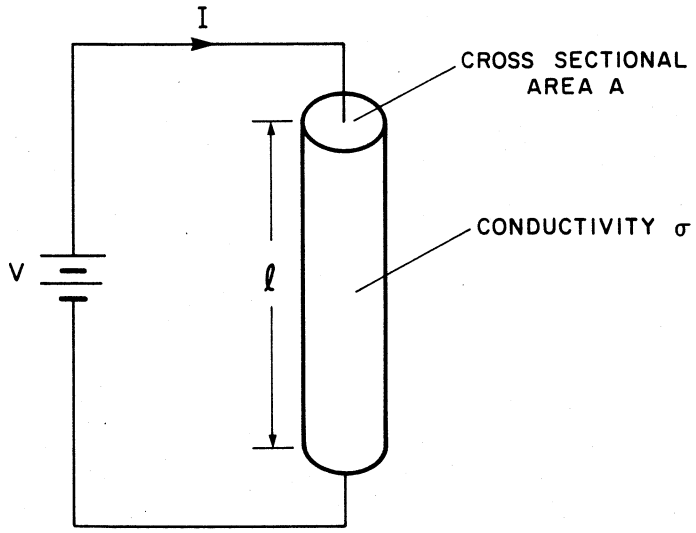

Fig. 15.2 Illustration of how electrical resistance is related to the basic physical parameters of conductivity and geometry.

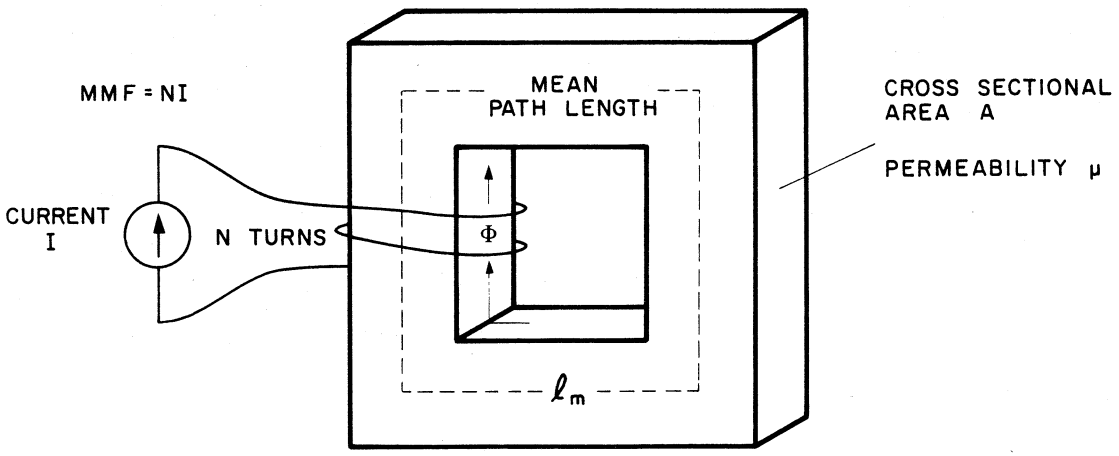

Fig. 15.3 Illustration of how magnetic reluctance is related to the basic physical parameters of permeability and geometry.

$$I = JA = \sigma EA = \frac{\sigma A}{l} V \tag{15.5}$$

Of course, no engineer would actually do this. Instead, he would bypass the field equations completely and find the current directly by using the lumped parameter version of Ohm's Law, $I = \frac{V}{R}$ or $I = VG$ where $R = \frac{l}{\sigma A}$ is the resistance and $G = \frac{1}{R}$ is the conductance.

An analogous procedure may be applied to magnetic circuits under the same assumptions of uniformity. Consider the circuit of Fig. 15.3. To find the flux Φ which results from the magnetomotive force NI, one can use the field equations on the right side of (15.2-15.4) and get

$$\Phi = BA = \mu HA = \mu \frac{NI}{l_m} A \tag{15.6}$$

where l_m is the mean path length along which it is assumed that an average magnetic field intensity H exists. Again, the field equations can be bypassed and the flux can be obtained in a single step as $\Phi = \frac{NI}{R}$, or equivalently $\Phi = NIp$, where $R = \frac{l_m}{\mu A}$ is the *reluctance* and $p = \frac{1}{R}$ is the *permeance* of the magnetic path.

The topology of the reluctance model of the magnetic circuit has a one-to-one correspondence with the physical magnetic structure, as demonstrated in Fig. 15.4 for the case of an air gap in the magnetic path. This correspondence is the forte of the reluctance model for the analysis of magnetic devices. As subsequent chapters of this thesis will

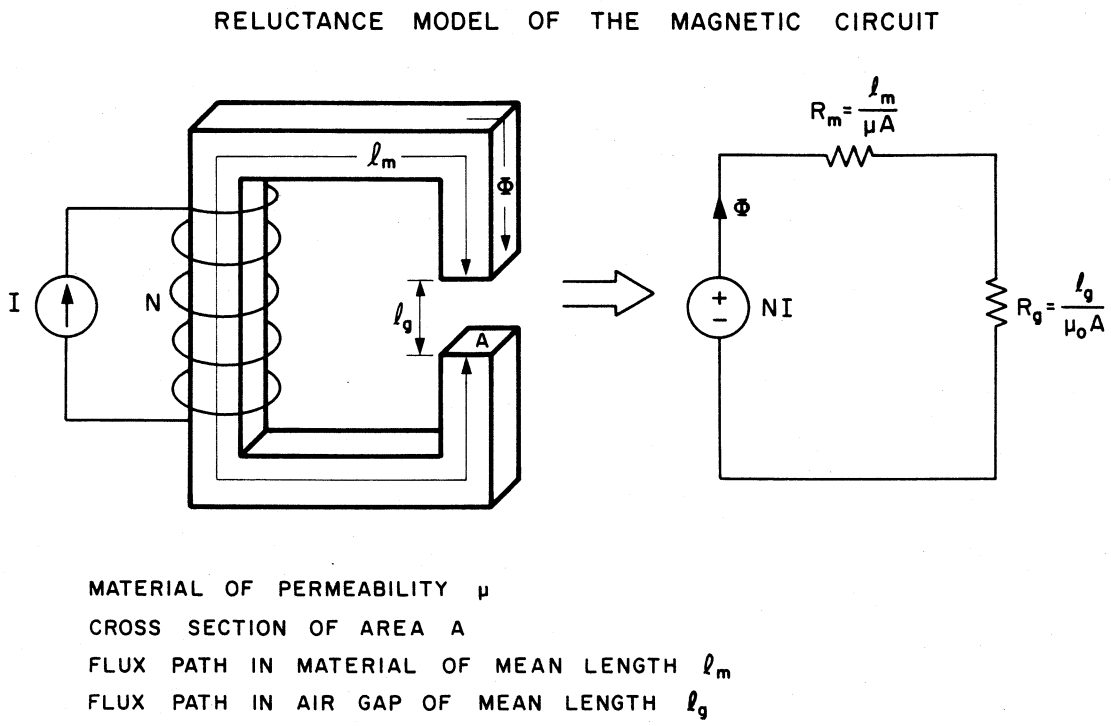

Fig. 15.4 Illustration of the relationship of the reluctance equivalent circuit to the physical magnetic structure.

show, not only is the often-ignored reluctance model valuable as the link between the physical device and the mathematical description of the coupled inductor equations, but it can also be used directly to find simple and accurate answers to aid in the design of complex structures.

CHAPTER 16

EXACT SOLUTIONS VIA THE COUPLED INDUCTOR APPROACH

A natural first approach toward understanding the zero current ripple phenomena is to use the coupled inductor equations. Since the experimental observations do not provide any obvious clues as to which parameters of the magnetic structure dominate the response, it is logical to turn to an exact description of the system for guidance in developing a simple model.

The objective is to find the simplest possible model which satisfactorily explains all the observed phenomena. Rather than starting with an oversimplified model and gradually building toward greater complexity, this treatment will take the opposite approach of starting from the most complete description and working toward greater simplicity. In this way no parameters will be overlooked, and a retrace of the steps of simplification will provide a guide to the other method of analysis, which may then be applied to other problems of this type.

16.1 Review of the Two-Winding Coupled Inductor Structure

The magnetic structure in the circuit of Fig. 13.3 is modelled by the coupled inductor equations as

$$v_1 = L_{11}\frac{di_1}{dt} + M\frac{di_2}{dt} \tag{16.1}$$

$$v_2 = M\frac{di_1}{dt} + L_{22}\frac{di_2}{dt}$$

To find the conditions for zero ripple on the output, one need only find where the time derivative $\frac{di_2}{dt}$ is zero. Since $v_1 = v_2$ Cramer's rule gives

$$\frac{di_2}{dt} = \frac{\det\begin{bmatrix} L_{11} & v \\ M & v \end{bmatrix}}{\det\begin{bmatrix} L_{11} & M \\ M & L_{22} \end{bmatrix}} = 0 \tag{16.2}$$

from which it follows that for zero current ripple on the output it is required that

$$L_{11} = M \qquad\qquad L_{22} \neq M \tag{16.3}$$

Although this condition for zero ripple is simple, rigorous and perfectly correct, it is quite unilluminating and no help at all to an engineer who wishes to build such a device. One significant conclusion can be drawn from this analysis, however, and that is that it is impossible to obtain zero current ripple on both input and output with such a structure. This is clear from symmetry or by direct solution for the conditions for zero ripple on the input.

In an effort to give some physical meaning to the conditions in (16.3), the treatment in [25] introduced the *coupling coefficient*, which is defined in many physics and engineering textbooks as

$$k \equiv \frac{M}{\sqrt{L_{11}L_{22}}} \tag{16.4}$$

Substitution of $L_{11} = M$ into (16.4) yields the "matching condition" given in [25] for zero ripple on the output:

$$k = n \tag{16.5}$$

where n is defined to be the *effective turns ratio*, which for coupling coefficients close to unity is approximately the actual turns ratio.

$$n \equiv \left[\frac{L_{11}}{L_{22}}\right]^{\frac{1}{2}} \approx \frac{N_1}{N_2} \tag{16.6}$$

Measurements of self inductances in [25] resulted in numerical verification of the matching condition of (16.5), but the phenomenon was not well understood in terms of the geometric dimensions and *actual number of turns* on the physical device.

16.2 Exact Solution for the Integrated Magnetic Structure

Because the isolation transformer in the circuit of Fig. 13.8 is required to handle pulsating currents, the primary and secondary must be very tightly coupled. Owing to this practical restriction, the voltages which appear on those two windings can be considered to be exactly in the same

ratio as the physical turns ratio, which can be taken to be unity without loss of generality. This being the case, it is both appropriate and desirable to merge the primary and secondary into a single winding, effectively connecting the two in parallel and removing the isolation property. Although this maneuver is transparent to the other windings on the structure, it has the benefit of eliminating redundant terms in the analysis. Figure 16.1 shows the non-isolated three-winding version of the zero-ripple Ćuk converter with the integrated structure simulated with two sets of U-cores, after the circuit of Fig. 13.6. This configuration was actually one of the intermediate steps used in [31] to arrive at the configuration in Fig. 13.8, and its zero-ripple behavior is indentical to that of the completely integrated isolated converter.

With only a single winding on the center leg of the integrated structure, the coupled inductor equations are

$$\begin{bmatrix} v_1 \\ v_2 \\ v_3 \end{bmatrix} = \begin{bmatrix} L_{11} & M_{12} & M_{13} \\ M_{12} & L_{22} & M_{23} \\ M_{13} & M_{23} & L_{33} \end{bmatrix} \begin{bmatrix} \dot{i}_1 \\ \dot{i}_2 \\ \dot{i}_3 \end{bmatrix} \tag{16.7}$$

where the quantities for the input winding have subscript 1, the output is subscript 2 and the new center winding is designated by subscript 3. Here the time derivatives of the currents are written using the conventional dot notation. As in the previous section, use of Cramer's rule and the fact that $v_1 = v_2 = v_3$ give the conditions for zero ripple:

ZERO INPUT RIPPLE

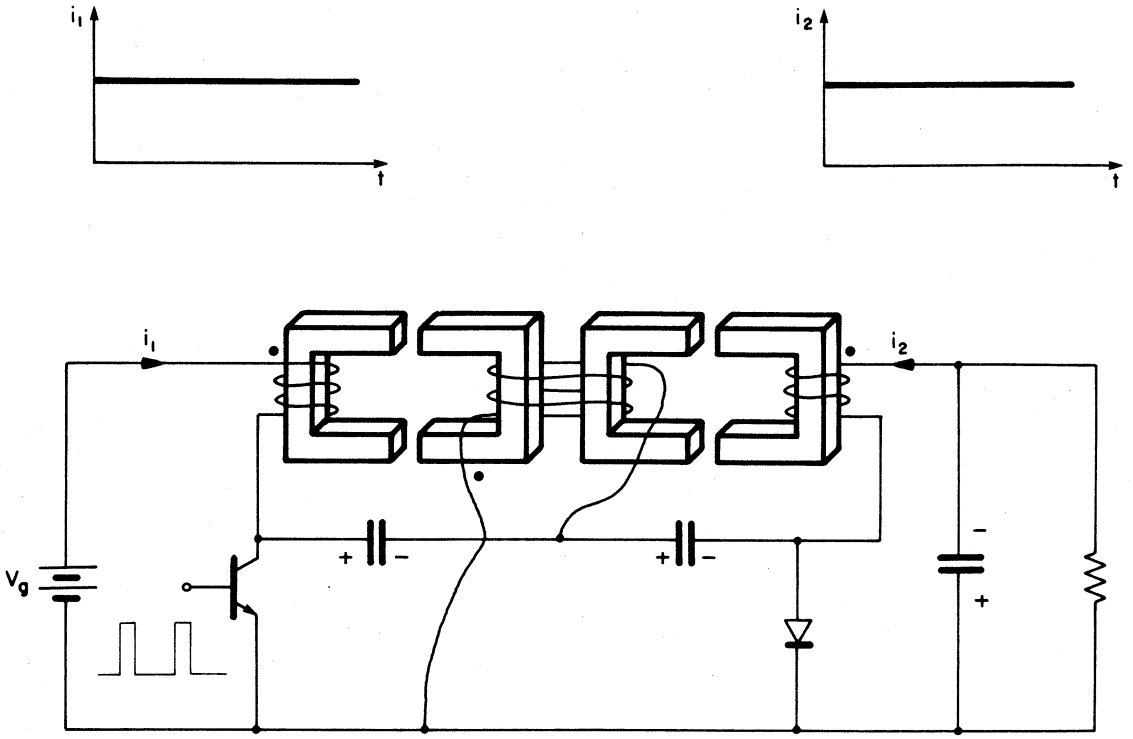

Fig. 16.1 A non-isolated three-winding version of the zero-ripple Ćuk converter. The integrated structure of Fig. 13.8 is simulated with two sets of U-cores. This circuit exhibits the same type of interactive behavior as the more complicated isolated version.

$$L_{22}(L_{33}-M_{13}) + M_{12}(M_{23}-L_{33}) + M_{23}(M_{13}-M_{23}) = 0 \qquad (16.8)$$

ZERO OUTPUT RIPPLE

$$L_{11}(L_{33}-M_{23}) + M_{12}(M_{13}-L_{33}) + M_{13}(M_{23}-M_{13}) = 0 \qquad (16.9)$$

with the restriction that the determinant of the coupled inductor matrix is not zero. That is,

$$\Delta = L_{11}(L_{22}L_{33}-M^2_{23}) - M_{12}(M_{12}L_{33}-M_{13}M_{23}) \qquad (16.10)$$

$$+ M_{13}(M_{12}M_{23}-M_{13}L_{22}) \neq 0$$

It is apparent from these results that the analysis of the three-winding integrated structure is a great deal more complicated than that of the original two-winding case. From the exact analysis of the simpler configuration one could at least obtain a general result regarding simultaneous zero ripple and a "matching condition" for zero ripple based upon the familiar coupling coefficient. An analogous relationship for the integrated structure, however, is certainly not obvious from the above equations, and at this point it is difficult to draw any general conclusions at all. The next chapter will bring the physical parameters into the picture, and, although to do so will not immediately simplify the analysis, it will permit one to gain insight from the exact solutions.

CHAPTER 17

SOLUTION IN TERMS OF PHYSICAL QUANTITIES

It was stated in Chapter 15 that the concept of reluctance and permeance is the bridge between the mathematical abstractions of the coupled inductor equations and the physical reality of the magnetic device. This chapter gives a rigorous presentation of the the relationships required for zero current ripple in terms of the permeances associated with both the two-winding and three-winding structures. It will be seen that the complete analysis of even a three-winding structure is quite formidable, and that the resulting expressions can become impossibly cumbersome and difficult to interpret. Such an analysis, however, has to be done only *once* in order to establish which of the many parameters are important and which can be safely ignored. The results presented here will not have to be repeated, for they will become the source of simple practical models for the solution of similar types of problems.

17.1 The Two-Winding Coupled Inductor Structure

The simple two-winding magnetic structure in the circuit of Fig. 13.3 is illustrated in Fig. 17.1 with the total flux decomposed into four artificial components: (1) the mutual flux φ_m which links both windings through the path defined by the core material and associated air-gap, (2) the flux φ_{12} which links both windings through the air and is independent of the air-gap,

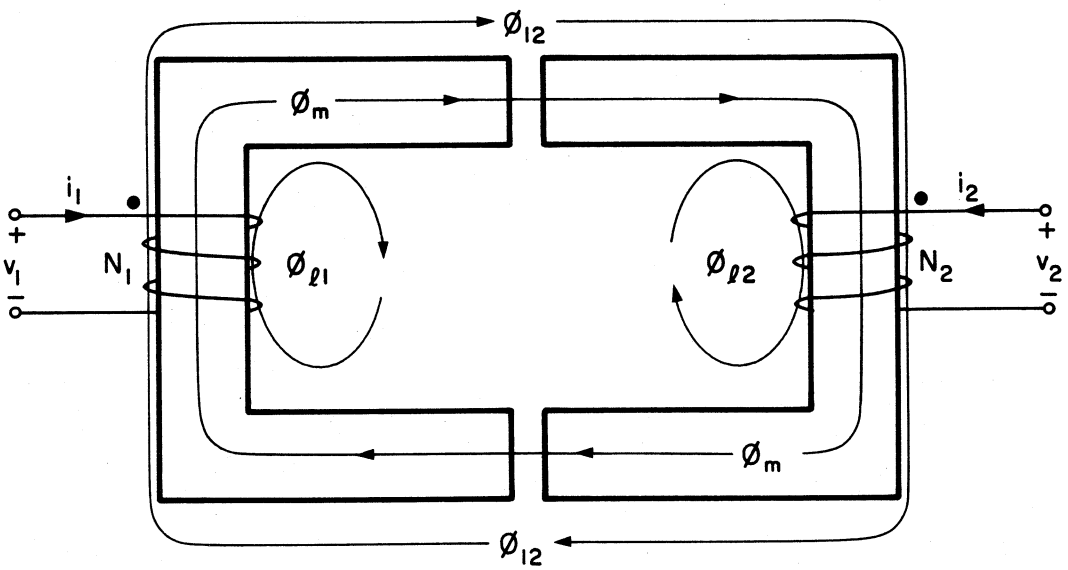

Fig. 17.1 The flux of the two-winding structure in the circuit of Fig. 13.3 can be decomposed into four artificial components.

(3) φ_{l1} which links only the input winding and (4) φ_{l2} which links only the output winding. The fluxes in the air are usually called *leakage* fluxes. In less general treatments the air flux φ_{12} is usually not identified explicitly, but is absorbed into the mutual flux component.

This decomposition is artificial in the sense that the components identified in the figure are chosen to represent the general categories of all possible flux paths as an aid to analysis, and they should not be confused with a flux map of the actual structure when both windings are energized. The actual *resultant* distribution of airborn flux would not necessarily bear any relationship to the leakages as defined here, because the actual flux is a function of the distribution of magnetomotive force between the two windings: Most of the flux lines will link the winding which has the greater instantaneous mmf.

By Faraday's law the voltages on the windings can be written in terms of the time derivatives of the flux components as

$$v_1 = N_1(\dot{\varphi}_m + \dot{\varphi}_{12} + \dot{\varphi}_{l1}) \tag{17.1}$$

$$v_2 = N_2(\dot{\varphi}_m + \dot{\varphi}_{12} + \dot{\varphi}_{l2})$$

Under the assumption of an effective mean path-length through the air, one may define leakage permeances analogous to the core permeance. All the flux components may then be written as functions of the currents which produce them.

$$\varphi_{l1} = p_1 N_1 i_1 \qquad \varphi_{l2} = p_2 N_2 i_2$$

$$\varphi_{12} = p_{12}(N_1 i_1 + N_2 i_2) \tag{17.2}$$

$$\varphi_m = p_m(N_1 i_1 + N_2 i_2)$$

Differentiation of these quantities with respect to time and substitution into (17.1) yields the following description, in which the correspondence to the coupled inductor constants is obvious.

$$\begin{bmatrix} v_1 \\ v_2 \end{bmatrix} = \begin{bmatrix} N_1^2(p_m+p_{12}+p_1) & N_1N_2(p_m+p_{12}) \\ N_1N_2(p_m+p_{12}) & N_2^2(p_m+p_{12}+p_2) \end{bmatrix} \begin{bmatrix} i_1 \\ i_2 \end{bmatrix} \tag{17.3}$$

It follows from (16.2) or (16.3) that the conditions required for zero current ripple on the *output* in terms of the permeances are

$$\frac{N_1}{N_2} = \frac{p_m + p_{12}}{p_m + p_{12} + p_1} \neq 1 + \frac{p_2}{p_m + p_{12}} \tag{17.4}$$

Several conclusions pertaining to the physical realizability of zero current ripple are now apparent. First, for zero ripple on the output there must be a finite leakage on one of the windings. That is, p_1 and p_2 cannot *both* be zero. Some of the flux produced by the mmf on one of the windings must be shunted away from the other. Second, the condition for zero output ripple is *independent* of the leakage on the output -- it doesn't matter how much of the flux generated by winding 2 is shunted away from winding 1. Finally, it is easy to see from symmetry or by comparison with the analogous conditions for zero ripple on the *input*

that, owing to the requirement for nonzero leakage, it is impossible to have zero ripple on both input and output at the same time. Also, it is now clear how the output current ripple in the coupled inductor Ćuk converter of Fig. 13.3 can be adjusted to zero by variation of the air gap. The mutual permeance $\mathcal{P}_m$ is a very strong function of the air gap while the leakages are virtually constant [38, 39]. Zero ripple is achieved when the air gap is adjusted to make the ratio of permeances in (17.4) equal to the turns ratio.

Perhaps the most important fact to be learned, however, is that the zero current-ripple phenomenon depends on the existence of *leakage flux* which is usually ignored in first analyses of magnetic devices. Here is a situation in which quantities that are normally considered to be of second-order are responsible for first-order effects. It is reasonable to expect similar results for the more complicated integrated structure, and because it is not intuitively obvious which second-order quantities will be important, a complete analysis of a multi-winding structure is justified.

One may easily solve (17.4) for $\mathcal{P}_m$ in terms of the leakage permeances and the actual number of turns to determine the required dimensions of the magnetic core and air gap. (Techniques are available to control the leakages by construction.) A similar analysis of multi-winding integrated structures, however, is much more complicated, as the next section will show.

17.2 The Three-Winding Integrated Structure

The flux generated by the windings of the three-winding structure of Fig. 17.2 can be decomposed into eight independent components as indicated by Fig. 17.3. The leakage fluxes can be written in terms of the currents which produce them as

$$\varphi_{l1} = p_1 N_1 i_1 \qquad \varphi_{l2} = p_2 N_2 i_2 \qquad \varphi_{l3} = p_3 N_3 i_3$$

$$\varphi_{12} = p_{12}(N_1 i_1 - N_2 i_2)$$

$$\varphi_{23} = p_{23}(N_2 i_2 + N_3 i_3) \tag{17.5}$$

$$\varphi_{13} = p_{13}(N_1 i_1 + N_3 i_3)$$

The fluxes in the core material can be determined by considering the structure to be composed of three reluctances as indicated in Fig. 17.4a, from which the reluctance equivalent circuit of Fig. 17.4b can be drawn. Solution of the circuit for φ_1 and φ_2 completes the description of the device in terms of flux components. To simplify the notation in the resulting expressions one can define the following structure permeances or "leg permeances" from the reluctances of Fig. 17.4:

$$\frac{1}{R_1} \equiv P_{L1} \qquad \frac{1}{R_2} \equiv P_{L2} \qquad \frac{1}{R_3} \equiv P_{L3} \tag{17.6}$$

from which one can write the core permeances which appear in the equations as

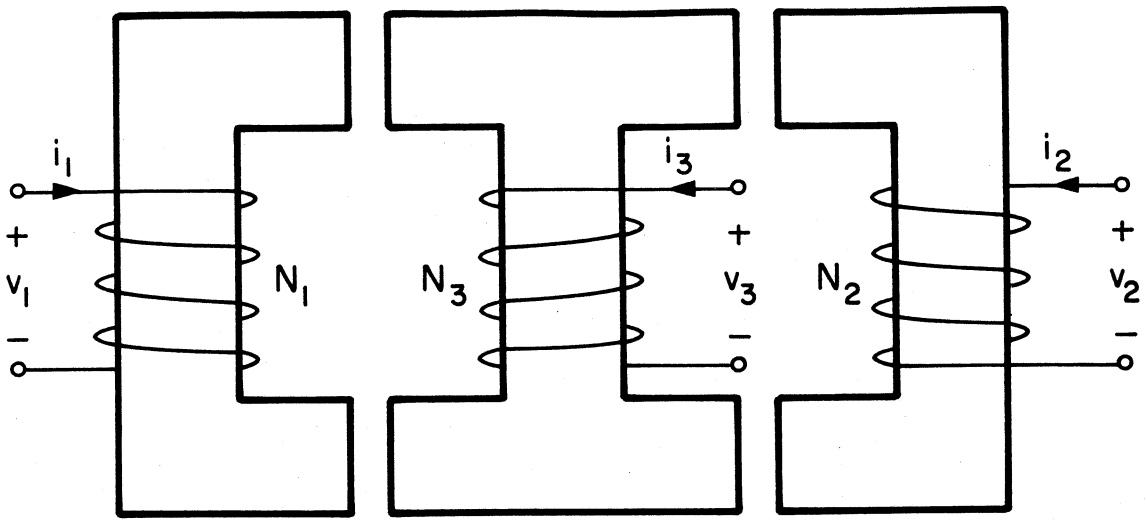

Fig. 17.2 The general three-winding integrated structure chosen for analysis.

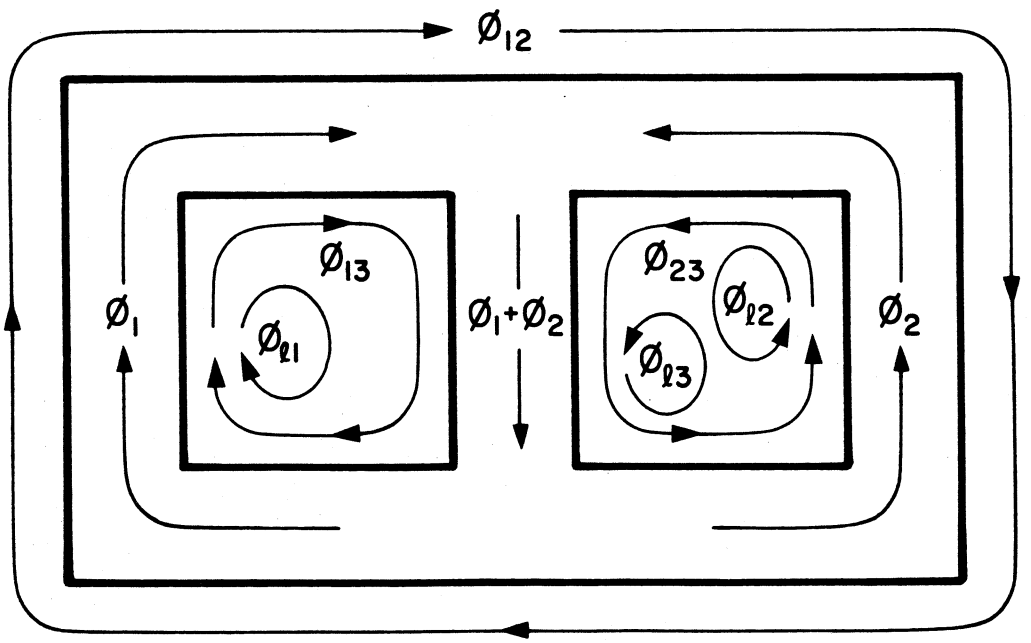

Fig. 17.3 General decomposition of fluxes for the integrated structure of Fig. 17.2.

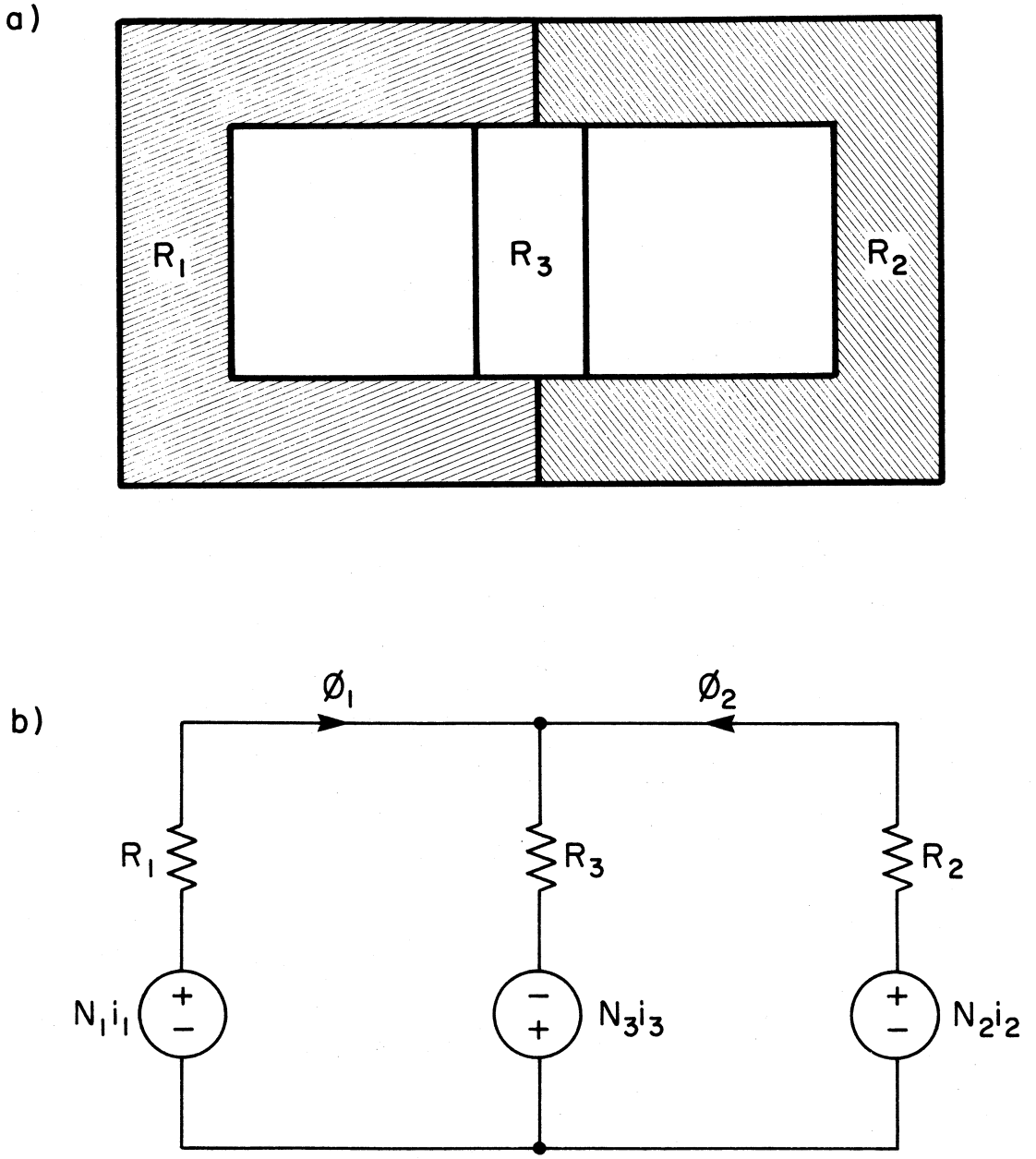

Fig. 17.4 The magnetic paths defined by the core geometry can be conveniently divided into three reluctances (a) which are represented in the reluctance equivalent circuit model (b).

$$P_{C1} \equiv \frac{R_1}{R_1R_2+R_2R_3+R_1R_3} = \frac{P_{L2}P_{L3}}{P_{L1}+P_{L2}+P_{L3}}$$

$$P_{C2} \equiv \frac{R_2}{R_1R_2+R_2R_3+R_1R_3} = \frac{P_{L1}P_{L3}}{P_{L1}+P_{L2}+P_{L3}} \qquad (17.7)$$

$$P_{C3} \equiv \frac{R_3}{R_1R_2+R_2R_3+R_1R_3} = \frac{P_{L1}P_{L2}}{P_{L1}+P_{L2}+P_{L3}}$$

By Faraday's law the voltages on the windings are

$$v_1 = N_1(\dot{\varphi}_1 + \dot{\varphi}_{12} + \dot{\varphi}_{13} + \dot{\varphi}_{l1})$$

$$v_2 = N_2(\dot{\varphi}_2 - \dot{\varphi}_{12} + \dot{\varphi}_{23} + \dot{\varphi}_{l2}) \qquad (17.8)$$

$$v_3 = N_3(\dot{\varphi}_1 + \dot{\varphi}_2 + \dot{\varphi}_{13} + \dot{\varphi}_{23} + \dot{\varphi}_{l3})$$

and the coupled inductor constants may be found from the above equations in exactly the same way as in the two-winding case. If one further defines the following <u>composite permeances</u>

$$P_x \equiv P_{C2} + p_{13} \qquad P_y \equiv P_{C1} + p_{23} \qquad P_z \equiv P_{C3} + p_{12} \qquad (17.9)$$

then the coupled inductor parameters can be written very compactly in terms of permeances as

$$L_{11} = N_1^2(P_x + P_z + p_1)$$

$$L_{22} = N_2^2(P_y + P_z + p_2)$$

$$L_{33} = N_3^2(P_x + P_y + p_3) \tag{17.10}$$

$$M_{12} = -N_1N_2P_z$$

$$M_{13} = N_1N_3P_x$$

$$M_{23} = N_2N_3P_y$$

Note that M_{12} is *negative* for this configuration, which is a departure from what is normally found in the description of conventional structures.

With equal voltages on the three windings, application of Cramer's rule results in the following conditions for zero current-ripple:

ZERO INPUT RIPPLE (WINDING 1)

$$N_2N_3(P_yP_x+P_zP_x+P_zP_y+P_yp_3+P_zp_3+P_xp_2+P_yp_2+p_2p_3)$$

$$+ N_1N_3(P_xP_y+P_zP_x+P_zP_y+P_zp_3) \tag{17.11}$$

$$- N_1N_2(P_xP_y+P_zP_x+P_zP_y+P_xp_2) = 0$$

ZERO OUTPUT RIPPLE (WINDING 2)

$$N_1N_3(P_yP_x+P_zP_x+P_zP_y+P_xp_3+P_zp_3+P_yp_1+P_zp_1+p_1p_3)$$

$$+ N_2N_3(P_xP_y+P_zP_x+P_zP_y+P_zp_3) \tag{17.12}$$

$$- N_1N_2(P_xP_y+P_zP_x+P_zP_y+P_yp_1) = 0$$

with the restriction that the determinant

$$\Delta = N_1^2 N_2^2 N_3^2 \Big[(P_y P_z + P_z P_x + P_x P_y)(p_1 + p_2 + p_3) \tag{17.13}$$

$$+ p_1 p_2 (P_x + P_z) + p_1 p_3 (P_y + P_z) + p_1 p_2 (P_z + P_y) + p_1 p_2 p_3 \Big] \neq 0$$

In contrast to the much simpler two-winding case, few conclusions can be drawn from these results. The increased complexity is compounded when one realizes that many of the terms in the above expressions are themselves composite expressions of the permeances basic to the structure.

The only useful information that is readily available from (17.13) is that at least one of the self-leakages p_1, p_2 or p_3 must be nonzero for the solutions to be defined, for otherwise the determinant of the system would be singular. But is this a sufficient condition for zero current-ripple? How do the second order quantities effect the realizability of the zero ripple solutions? A general analytic solution for zero ripple in terms of the core geometry and all the leakages is certainly out of the question. It is possible to gain insight into the general nature of solutions, however, by making some simplifying assumptions.

17.3 Simplified Expressions for Practical Cases

Because this method of analysis is quite complicated, it is appropriate to introduce some reasonable simplifications of the original problem which will make the algebraic manipulations less cumbersome while maintaining the main qualitative features of the general solution. The first reduction in complexity comes from the supposition of symmetry; i.e., the

case in which the mechanical properties of the input and output windings are the same. This is a natural starting point since the behavior of interactive adjustment for zero ripple was first observed on a symmetrically wound structure. This means that $N_1 = N_2 = \xi N_3$ and $p_1 = p_2 = p_l$.

In addition to the above simplifications, knowledge of the geometry of a real integrated device permits one to make simplifying approximations by comparison of the relative magnitudes of the expected permeances. For example, in the practical structure of Fig. 17.2 the gap-dominated reluctances R_1 and R_2 of Fig. 17.4 are usually very much greater than R_3. Consequently, P_{C3} in (17.7) can be taken to be much greater than P_{C1} and P_{C2}. Furthermore, by virtue of the physical separation of the windings, the mutual leakages p_{13} and p_{23} can be expected to be much less than p_{12}, and these should be small in comparison to the self-leakages p_1, p_2 and p_3. Thus for R_3 and the mutual permeances sufficiently small, P_z can be ignored in comparison with P_x and P_y, and hence one can justify setting $P_z = 0$ in equations (17.11) - (17.13). It is important to note, however, that it is not possible to ignore the self-leakages because the presence of at least one of them is required to keep the determinant nonsingular.

Under the conditions of $N_1 = N_2 = \xi N_3$, $p_1 = p_2 = p_l$, and $P_z = 0$, one can solve analytically for loci of zero current ripple in the two-dimensional permeance space of P_y vs. P_x, and these results are sketched in Fig. 17.5. If the mutual leakages can be ignored, the

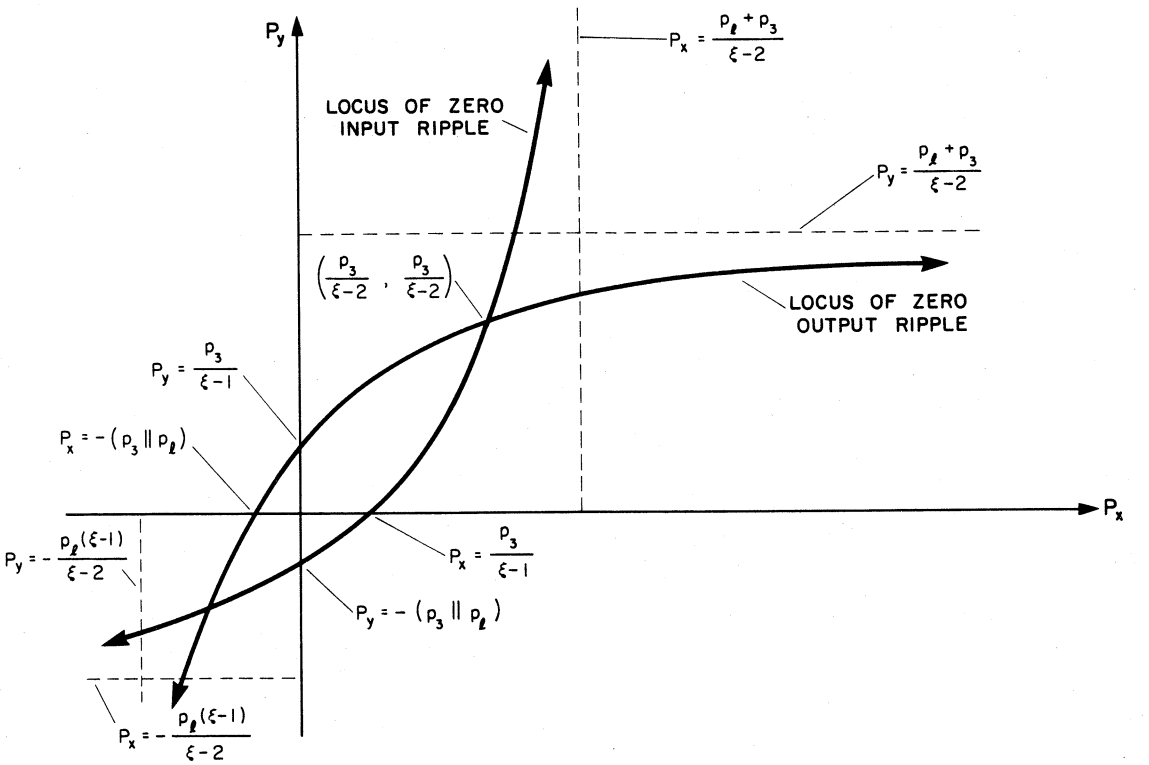

Fig. 17.5 Plot of the loci of zero ripple in permeance space for the symmetric three-winding structure where $N_1 = N_2 = N$ *and* $p_1 = p_2 = p_\ell$. P_z *is assumed to be zero. There is zero ripple on both the input and the output where the two curves intersect. Note that the turns ratio* $\xi \equiv \frac{N}{N_3}$ *must be greater than 2 for physical realizability of simultaneous zero ripple.*

permeances P_x and P_y are proportional, respectively, to the reciprocal gap-lengths $\frac{1}{x}$ and $\frac{1}{y}$ in the integrated structure introduced in Fig 13.8. The loci of $\frac{di_1}{dt}$ and $\frac{di_2}{dt}$ are hyperbolas which intersect at two points that represent the conditions for which zero current ripple may be obtained simultaneously at the input and the output. Because the curves represent the solution to a symmetrical problem, it should come as no surprise that $P_x = P_y$ $(x_s = y_s)$ for zero ripple on both input and output. Only the point of intersection in the first quadrant is physically realizable, however, since permeances can take on only positive values.

Several important observations can be made from the solution of this simplified problem. First of all, the condition for zero ripple on both sides is *independent* of the self-leakages of the input and output windings and depends *only on the leakage of the center winding*. The imperfect coupling of neither the input nor the output windings has any effect on the values of P_x and P_y required for simultaneous zero ripple. This fact is analogous to the result found in the preceding section for zero output ripple with the two-winding structure, in which the leakage on the output was inconsequential.

Second, for N turns on both the input and output windings, the ratio $\xi = \frac{N}{N_3}$ *must be greater than* 2. As ξ approaches 2 from above, the gaps required for simultaneous zero ripple get smaller and smaller until a maximum permeance determined by the core material is reached at zero gap.

Finally, the curvature and orientation of the loci predict *interactive gap adjustments* which converge to the solution of simultaneous zero ripple. One can see from the expressions for the asymptotes that the curvature is a function of the self-leakage permeance of the input and output windings, and that this will affect the degree of interaction observed in adjustment for zero ripple. To see if the simplifications in this analysis have masked any important effects, it is of interest to extend the analysis to include the effects of nonzero P_z and $p_1 \neq p_2$. An expanded analysis has been carried out with the benefit of the simpler solutions as a guide, and the results are sketched in Fig. 17.6.

The extended analysis shows that the solution for simultaneous zero ripple still depends on the leakage of only the third winding and that the turns ratio still has a lower bound of 2. The presence of a nonzero P_z, however, *does* modify the gaps x_s and y_s associated with that solution because now P_x and P_y are rather complicated functions of R_1, R_2, and R_3. Furthermore, since P_x and P_y are no longer proportional to $\frac{1}{x}$ and $\frac{1}{y}$ owing to the intervention of an assumed non-negligible finite P_z, it is very difficult to interpret these curves in terms of actual gap lengths. Explicit expressions for the solutions in terms of the leg permeances P_{L1} and P_{L2} for this case, as well as for the more general case of $N_1 \neq N_2$, are given in the Appendix.

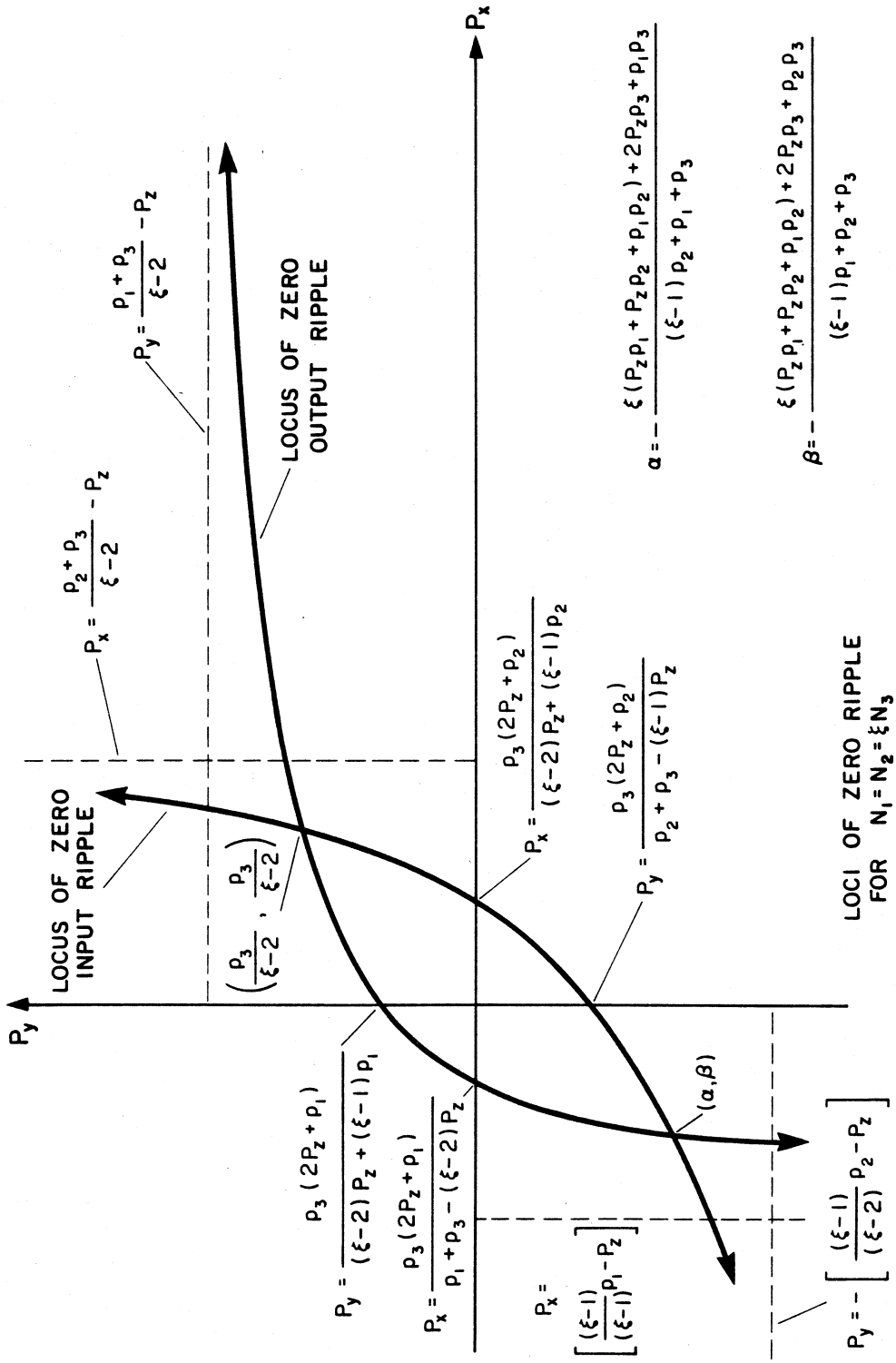

Fig. 17.6 Solutions for zero ripple can quickly become needlessly complicated and very difficult to interpret if one chooses the wrong method for analysis.

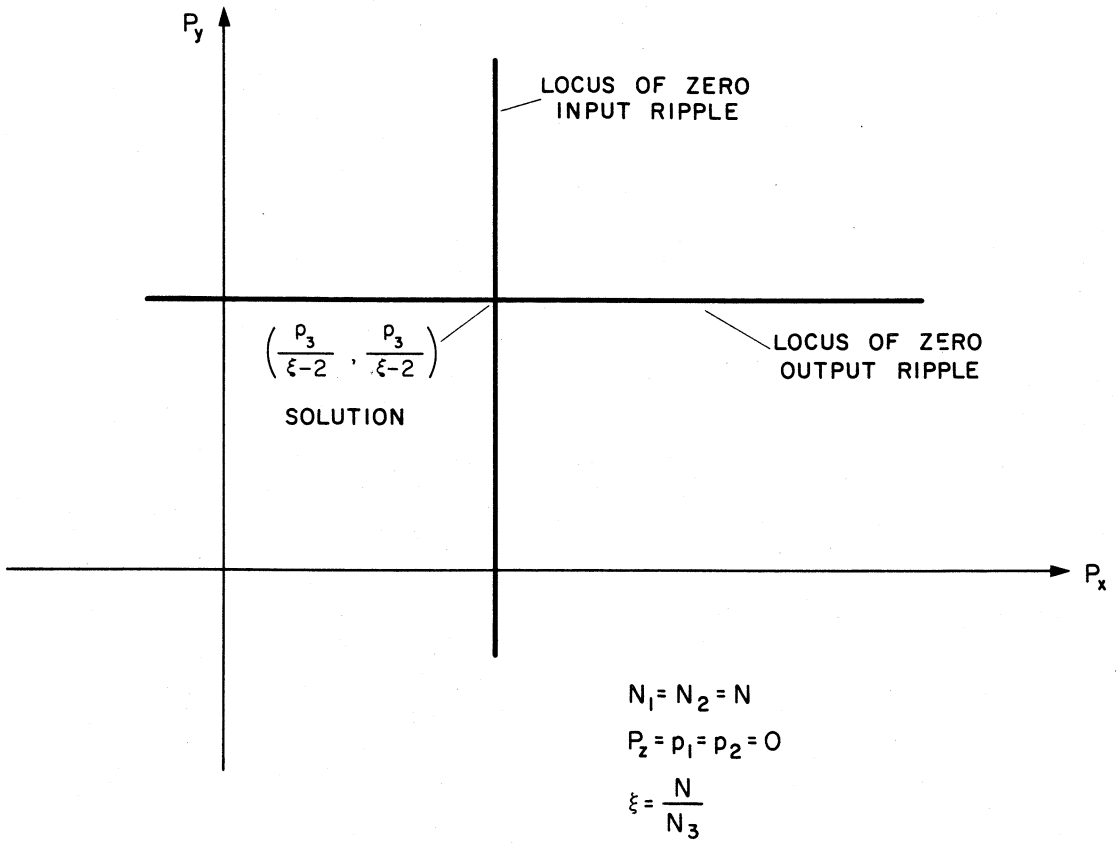

Fig. 17.7 For certain special cases the curves of Figs 17.5 and 17.6 degenerate into straight lines to predict non-interactive adjustments for zero ripple.

A very interesting case is that of $p_1 = p_2 = 0$. Direct solution of (17.11) and (17.12) in terms of the permeances P_{L1} and P_{L2} (which are proportional to the reciprocal gaps) shows that the loci of zero ripple are straight lines parallel to the axes and intersecting in the first quadrant as illustrated in Fig. 17.7. The plot predicts *non-interactive* adjustments of air gaps to obtain simultaneous zero ripple. Although such trial-and-error adjustments are no longer required now that the solutions are known, it is nevertheless interesting to investigate and understand the causes and cures. It turns out that this prediction of non-interactive adjustment is realizable, and will be explored in greater detail and confirmed experimentally in subsequent chapters.

Although the analyses performed here were quite painful to execute, they were successful in providing the answers to the questions of which parameters were important and which could be neglected. This visibility provides the insight necessary for the formulation of the much simpler and more direct method described in the next chapter.

CHAPTER 18

SIMPLE DIRECT SOLUTIONS FROM THE MAGNETIC CIRCUIT IN TERMS OF PHYSICAL QUANTITIES

The preceding chapter served a dual purpose. First, the complete analysis provided a base from which one could make informed decisions regarding which parameters must be included in the model and which can be neglected. Second, the presentation of the resulting equations, even in a somewhat simplified form, illustrated the complexity of the method and made clear the difficulty encountered in interpreting the answers. Although the curves of Fig. 17.6 may be satisfactory solutions for the mathematician, the designer requires simple answers in terms of turns, areas and air gaps. This chapter presents the most direct method by which the solutions may be obtained in the desired form: the reluctance equivalent circuit model. Use of this technique will not only simplify the calculations but will also enhance one's understanding of the physical significance of the results.

Because the magnetic devices discussed here are used in power converters to store energy, some or all of their windings will normally carry dc currents as well as the ac ripple. Since the main objective here is to study the effects of magnetic integration on the ac ripple current, it is appropriate to divide the problem into ac and dc models and study the ac model in greater detail. This separation is valid under the assumption that the devices are operated in the linear region.

18.1 Solutions for the Simplified Two-Winding Model

The reluctance equivalent circuit model for the two-winding structure of Fig. 17.1 under the assumption that $\mathcal{P}_m \gg \mathcal{P}_{12}$ is shown in Fig. 18.1. The reluctances in the circuit are related to the permeances defined in Chapter 17 as follows:

$$R_m \equiv \frac{1}{\mathcal{P}_m} \qquad R_{l1} \equiv \frac{1}{\mathcal{P}_1} \qquad R_{l2} \equiv \frac{1}{\mathcal{P}_2} \tag{18.1}$$

As illustrated in Figure 18.2, the assumption of linearity permits one to decompose the fluxes and currents into dc and ac parts:

$$i = I + \hat{\imath} \tag{18.2}$$

$$\varphi = \Phi + \hat{\varphi}$$

where the ac parts have zero average by definition. Since the dc components (represented by uppercase symbols) are determined by the operation of the converter and its steady-state load, those quantities are not germane to this treatment, and therefore *all subsequent analyses will proceed in terms of ac quantities only.*

From flux summations at the two nodes in the model of Fig. 18.1 one gets

$$\frac{N_1 i_1}{R_{l1}} + \frac{N_1 i_1 + N_2 i_2}{R_m} = \varphi_1 \tag{18.3}$$

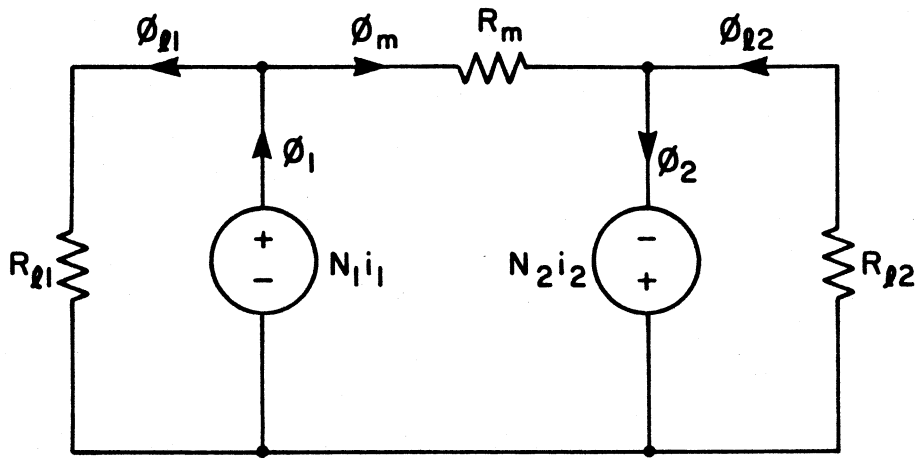

Fig. 18.1 Simplified reluctance equivalent circuit model for the two-winding coupled inductor structure.

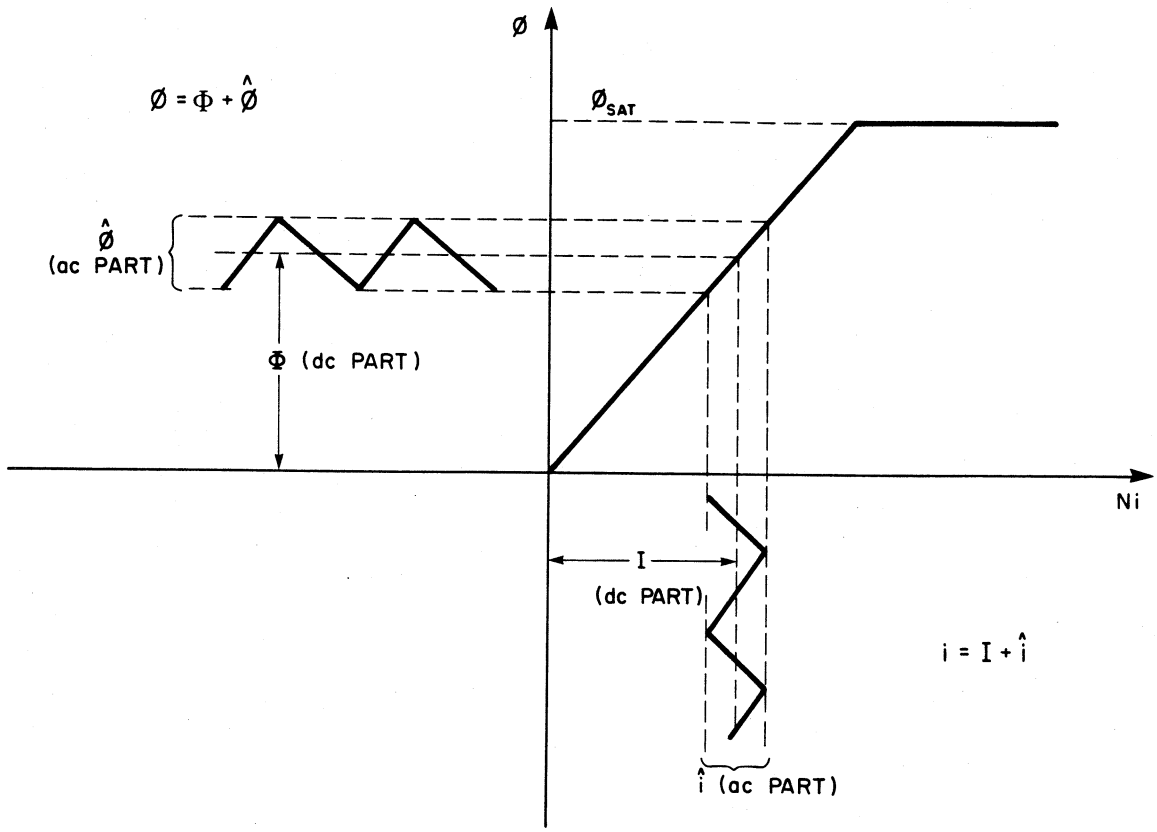

Fig. 18.2 The assumption of linearity permits one to decompose the fluxes and currents into dc and ac parts. This simplifies both the notation and the analysis.

$$\frac{N_2 i_2}{R_{l2}} + \frac{N_1 i_1 + N_2 i_2}{R_m} = \varphi_2 \tag{18.4}$$

From Faraday's law one has the flux constraints

$$\varphi_1 = \frac{1}{N_1}\int v_1 dt \qquad \varphi_2 = \frac{1}{N_2}\int v_2 dt \tag{18.5}$$

where no constant of integration is required since the fluxes by definition have no dc components. Since $v_1 = v_2$, one has $\varphi_1 = \varphi_0/N_1$, $\varphi_2 = \varphi_0/N_2$, and equations (18.3) and (18.4) can be easily solved for the currents:

$$i_1 = \frac{\varphi_0}{\Delta}\left[\frac{N_2}{N_1}\left(\frac{1}{R_m} + \frac{1}{R_{l2}}\right) - \frac{1}{R_m}\right] \tag{18.6}$$

$$i_2 = \frac{\varphi_0}{\Delta}\left[\frac{N_1}{N_2}\left(\frac{1}{R_m} + \frac{1}{R_{l1}}\right) - \frac{1}{R_m}\right] \tag{18.7}$$

where

$$\Delta = N_1 N_2\left(\frac{1}{R_{l1}R_{l2}} + \frac{1}{R_{l2}R_m} + \frac{1}{R_{l1}R_m}\right) \neq 0 \tag{18.8}$$

Thus it is easy to see that the current ripples at either end may be made to vanish provided that:

$$\text{ZERO INPUT RIPPLE} \qquad \frac{N_2}{N_1} = \frac{R_{l2}}{R_{l2} + R_m} \tag{18.9}$$

ZERO OUTPUT RIPPLE

$$\frac{N_1}{N_2} = \frac{R_{l1}}{R_{l1} + R_m} \tag{18.10}$$

From (18.8), (18.9) and (18.10) it follows that both current ripples cannot be set to zero at the same time, in agreement with the previous analyses in Chapters 16 and 17. Note that (18.10) is equivalent to (17.4) under the assumption that $p_m \gg p_{12}$.

If the objective is only to find the zero-ripple conditions (18.9) and (18.10), a shortcut can be made which bypasses the previous lengthy derivations. For example, setting $i_2 = 0$ in the model of Fig. 18.1 produces the simplified ac model of Fig. 18.3. The constraint of zero ripple has automatically shorted the output leakage reluctance R_{l2}, which then obviously has no effect on the condition for zero output ripple, as was predicted by (17.4). Now from Fig. 18.3 one obtains by inspection

$$R_m \varphi_2 = R_{l1} \varphi_1 \tag{18.11}$$

$$\varphi_1 = \varphi_{l1} + \varphi_2 \tag{18.12}$$

where as before, from Faraday's law $\varphi_1 = \frac{\varphi_0}{N_1}$, $\varphi_2 = \frac{\varphi_0}{N_2}$, and $\varphi_0 = \int v dt$. Substitution for φ_1 and φ_2 in (18.11) and (18.12) results after simplification in the familiar expression (18.10).

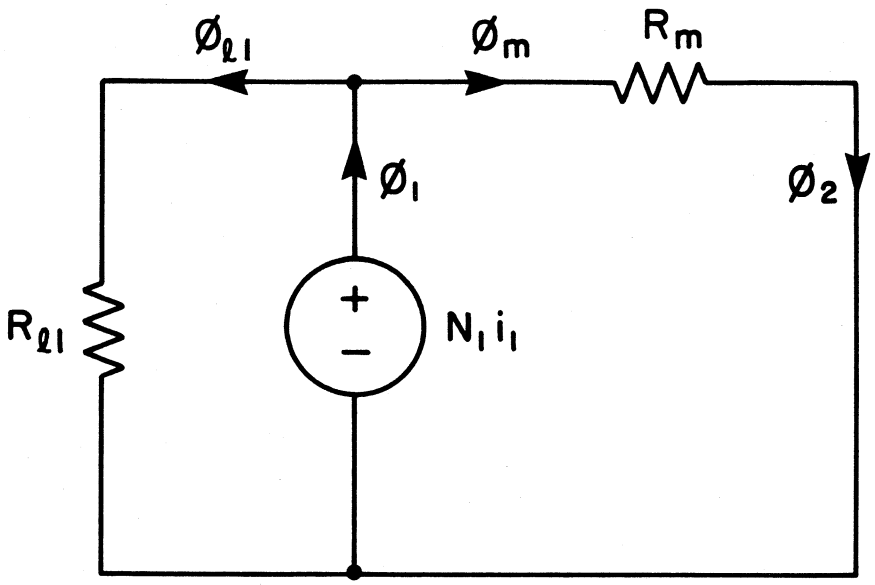

Fig. 18.3 Simplified model of the two-winding device for the case of zero current ripple on the output.

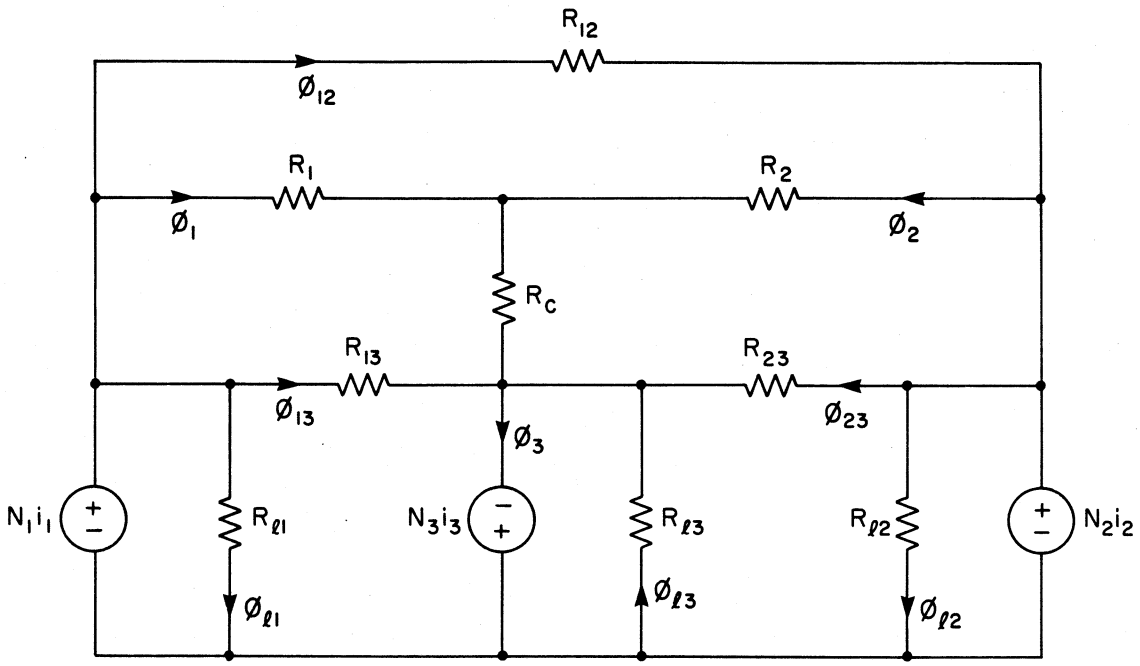

Fig. 18.4 Complete reluctance equivalent circuit model for the three-winding integrated magnetic structure.

18.2 Solutions for the Simplified Three-Winding Model

The complete reluctance equivalent circuit model for the three-winding integrated structure is given in Fig. 18.4, where the reluctances are related to the quantities defined in Chapter 17 as follows:

$$R_x \equiv R_1 \qquad R_y \equiv R_2 \qquad R_c \equiv R_3$$

$$R_{l1} \equiv \frac{1}{\mathcal{P}_1} \qquad R_{l2} \equiv \frac{1}{\mathcal{P}_2} \qquad R_{l3} \equiv \frac{1}{\mathcal{P}_3} \tag{18.13}$$

$$R_{12} \equiv \frac{1}{\mathcal{P}_{12}} \qquad R_{13} \equiv \frac{1}{\mathcal{P}_{13}} \qquad R_{23} \equiv \frac{1}{\mathcal{P}_{23}}$$

Under the realistic approximations discussed in Section 17.3 one may reduce the circuit of Fig. 18.4 to the simplified model of Fig. 18.5. The solution of this model for the conditions of zero ripple on both sides is very simple and straightforward, since with $i_1 = i_2 = 0$ both input and output leakages are shorted as shown in Fig. 18.6. This model for the special case of simultaneous zero ripple reveals that the leakage reluctances R_{l1} and R_{l2} are completely immaterial to the problem.

From the simplified model of Fig. 18.7 one can write two loop equations

$$R_x\varphi_1 = R_{l3}\varphi_{l3} \qquad R_y\varphi_2 = R_{l3}\varphi_{l3} \tag{18.14}$$

and the node equation

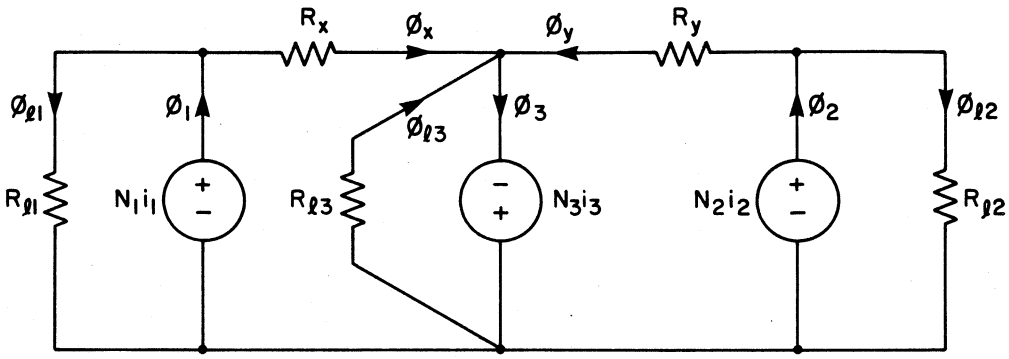

Fig. 18.5 Simplified reluctance equivalent circuit model for the three-winding integrated structure. Numerical values of the reluctances encountered in practical structures justify analytic approximations which lead to the reduction in complexity.

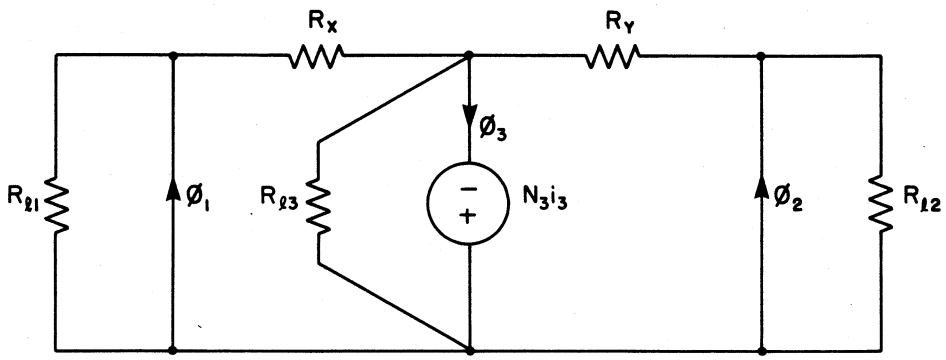

Fig. 18.6 Simplified reluctance model for the three-winding structure when there is zero current ripple on both input and output. Because the outer voltage generators become short circuits when $i_1 = i_2 = 0$, the leakage reluctances R_{l1} and R_{l2} can have no effect on the conditions for zero ripple.

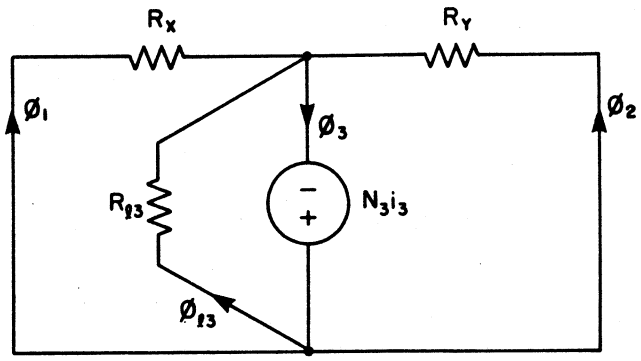

Fig. 18.7 Reluctance model for zero ripple on both ends with the superfluous self leakage reluctances removed.

$$\varphi_{l3} = \varphi_3 - \varphi_1 - \varphi_2 \tag{18.15}$$

For the symmetric case of $N_1 = N_2 = N$ the fluxes are constrained by the following relationships from Faraday's law:

$$\varphi_1 = \frac{\varphi_0}{N} \qquad \varphi_2 = \frac{\varphi_0}{N} \qquad \varphi_3 = \frac{\varphi_0}{N_3} \tag{18.16}$$

where $\varphi_0 = \int v dt$. With (18.16) the node equation simplifies to

$$\varphi_{l3} = \varphi_0 \left(\frac{1}{N_3} - \frac{2}{N} \right) \tag{18.17}$$

Substitution of (18.17) into (18.14) leads to the desired solution:

$$R_{xs} = R_{ys} = \left(\frac{N}{N_3} - 2 \right) R_{l3} \tag{18.18}$$

where the subscript "s" refers to the unique solution for reluctances R_x and R_y. The unsymmetrical case of $N_1 \neq N_2$ is solved just as easily, and the expressions for the solutions are given in the Appendix. Since a designer is ultimately interested in the air gaps x_s and y_s as the solution for zero ripple, it is desired to scale these these reluctance relations to air gap relations. Under the assumption of infinite permeability of the core material these are easily shown to be:

$$x_s = y_s = \left(\frac{N}{N_3} - 2 \right) l \tag{18.19}$$

where l is the equivalent leakage air gap required if the leakage flux

path had the same cross-sectional area as the flux paths of the two main magnetic loops. The gap l is defined by the reluctance relation

$$R_{l3} = \frac{l}{\mu_0 A} \tag{18.20}$$

This definition permits elimination of the cross section A from the reluctance solution of (18.18) to give the simple easy-to-interpret geometric relationships of (18.19).

A physical realization of the simple reluctance model can be constructed with three sets of U-cores as shown in Fig. 18.8, where it is assumed that all the flux is confined to the volume defined by the cores and the gaps. Note that the definition of separate left and right magnetic loops eliminates R_c from the reluctance model, even with finite permeability of the core material.

For the special case of $\frac{N}{N_3} = 3$, illustrated also in Fig 18.8, the zero-ripple solution (18.19) simplifies to $x_s = y_s = l$. Thus for zero ripple with this special turns ratio, the air gaps x and y should be adjusted to the same value as the leakage path air gap l. In practice, of course, the actual magnitudes of the gaps will be determined jointly by the dc currents which will be present in the windings and the dynamic response desired of the power converter. The designer must choose these values to be consistent with the conditions for zero ripple.

To solve for zero current ripple on only the input, one sets $i_1 = 0$ in the model of Fig. 18.5 to get the reduced model of Fig. 18.9.

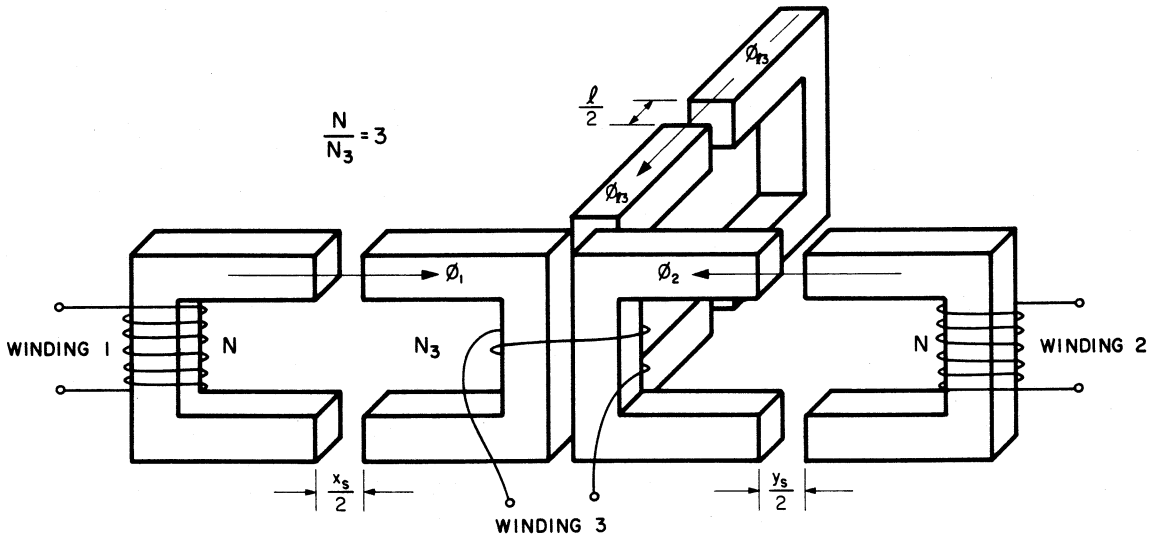

Fig. 18.8 Conceptual realization of the three-winding structure with the self leakage of the center winding defined explicitly by a magnetic core and effective air gap l.

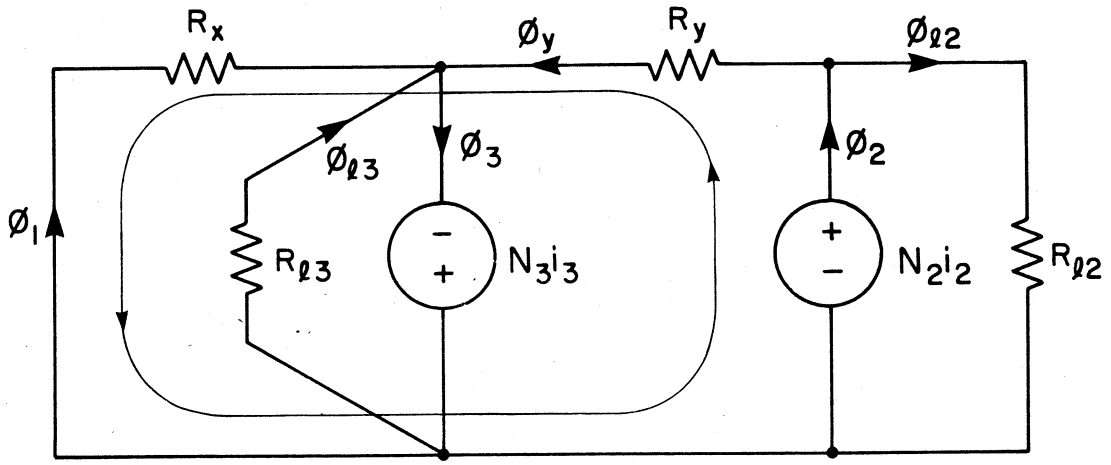

Fig. 18.9 Simple reluctance model of the three-winding structure with zero ripple only on the input.

In addition to the loop and node equations (18.14) and (18.15), another equation from the loop shown in Fig. 18.9 is required to solve the network. For the symmetric case of $N_1 = N_2 = N$ one gets from this loop

$$Ni_2 = \varphi_y R_y - \varphi_1 R_x \tag{18.21}$$

Faraday's law for the three magnetic branches yields

$$\varphi_3 = \frac{\varphi_0}{N_3} \qquad \varphi_1 = \frac{\varphi_0}{N} \qquad \varphi_2 = \frac{\varphi_0}{N} = \varphi_y + \varphi_{l2} \tag{18.22}$$

where $\varphi_{l2} = \dfrac{Ni_2}{R_{l2}}$. Substitution of these flux constraints into the loop and node equations yields the following implicit expression for zero ripple on the *input only*:

$$R_x = \left[\frac{N}{N_3} - 2\right] R_{l3} + \left[\frac{R_y - R_x}{R_y + R_{l2}}\right] R_{l3} \tag{18.23}$$

In a completely analogous manner, either by solving the corresponding reluctance model or by interchanging the subscripts $x \leftrightarrow y$ and $1 \leftrightarrow 2$ in (18.23), one can find the expression for zero ripple on the *output only*:

$$R_y = \left[\frac{N}{N_3} - 2\right] R_{l3} + \left[\frac{R_x - R_y}{R_x + R_{l1}}\right] R_{l3} \tag{18.24}$$

Just as was done previously in (18.20), one can define the equivalent air gaps l_1 and l_2 which refer the leakage reluctances R_{l1} and R_{l2} to the same cross section A as all the other magnetic branches by the equations

$$R_{l1} = \frac{l_1}{\mu_0 A} \qquad R_{l2} = \frac{l_2}{\mu_0 A} \tag{18.25}$$

With (18.25) and (18.20) the dependence on cross section A and permeability μ_0 is eliminated from (18.23) and (18.24) to give expressions in terms of the gaps:

$$x = \left[\frac{N}{N_3} - 2\right] l + \left[\frac{y - x}{y + l_2}\right] l \tag{18.26}$$

$$y = \left[\frac{N}{N_3} - 2\right] l + \left[\frac{x - y}{x + l_1}\right] l \tag{18.27}$$

As an instructive example, consider (18.27) given here explicitly in the form $y = f(x)$.

$$y = \left[\frac{N}{N_3} - 2\right] l + \left[x - \left[\frac{N}{N_3} - 2\right] l\right] \frac{l}{x + l + l_1} \tag{18.28}$$

It is easily seen from (18.28) that variation of l_1 generates a family of curves which pass through the common point

$$x_s = y_s = \left[\frac{N}{N_3} - 2\right] l \tag{18.29}$$

This is illustrated in Fig. 18.10. The intersection point (x_s, y_s) is the

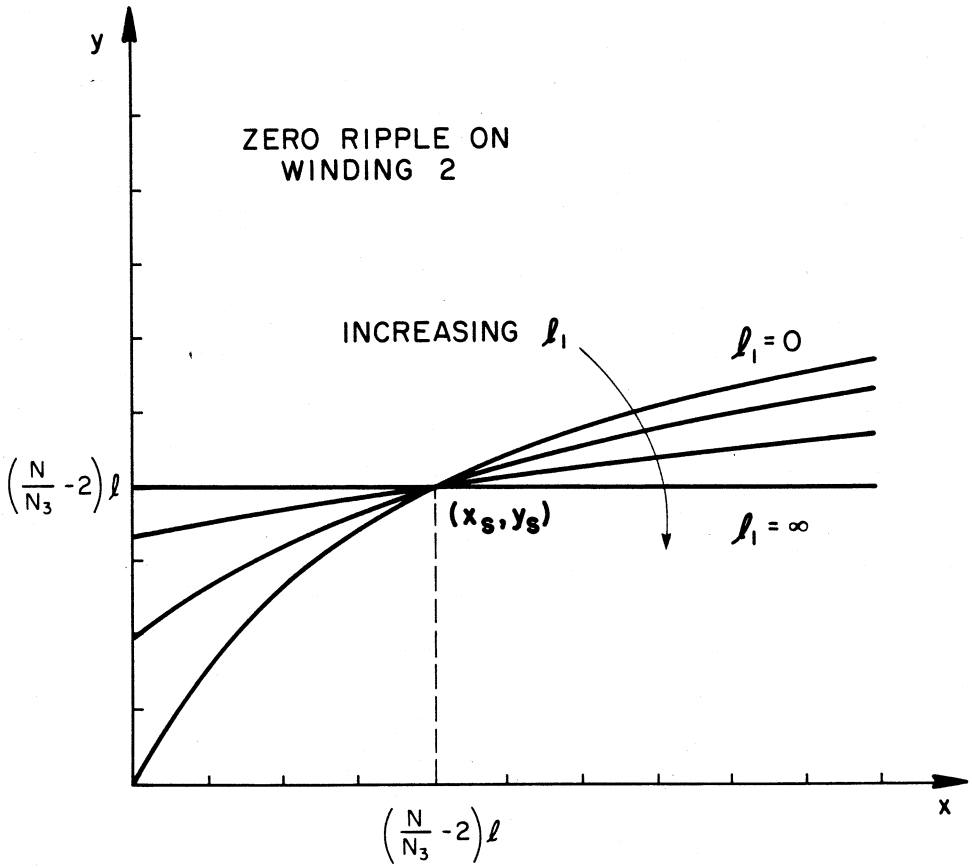

Fig. 18.10 Variation of the self-leakage of the input winding generates a family of curves of zero output ripple which pass through the same point, the zero ripple solution.

solution to zero ripple at both ends simultaneously, and this is in agreement with the previous observation that the solution is independent of the self-leakages of both the input and output windings. This result is of great practical significance. The only leakage that must be well-controlled is that of the center leg of the structure, and this can be accomplished by introduction of an additional magnetic branch as illustrated by the structure in Fig. 18.8. The particular arrangement of input and output windings with their imperfect couplings does not affect the solution for zero ripple in any way.

The salient features of the characteristic curves of (18.26) and (18.27) can be exposed by writing (18.28) as

$$y = f(x) = l\,\frac{\left[\frac{N}{N_3} - 2\right]x + \left[\frac{N}{N_3} - 2\right]l_1}{x + l + l_1} \tag{18.30}$$

and plotting for particular values of leakage gaps l and l_1. Looking at the extremes of $x = 0$ and $x \to \infty$ one gets

$$f(0) = \left[\frac{N}{N_3} - 2\right]\frac{ll_1}{l + l_1} = \left[\frac{N}{N_3} - 2\right] l \| l_1 \tag{18.31a}$$

$$\lim_{x \to \infty} f(x) = \left[\frac{N}{N_3} - 1\right] l \tag{18.31b}$$

Using these results and the analogous expressions for zero input ripple, the two representative curves are sketched in Fig. 18.11 for the case of $l = l_1 = l_2$. Because of the non-orthogonal curvature of the zero

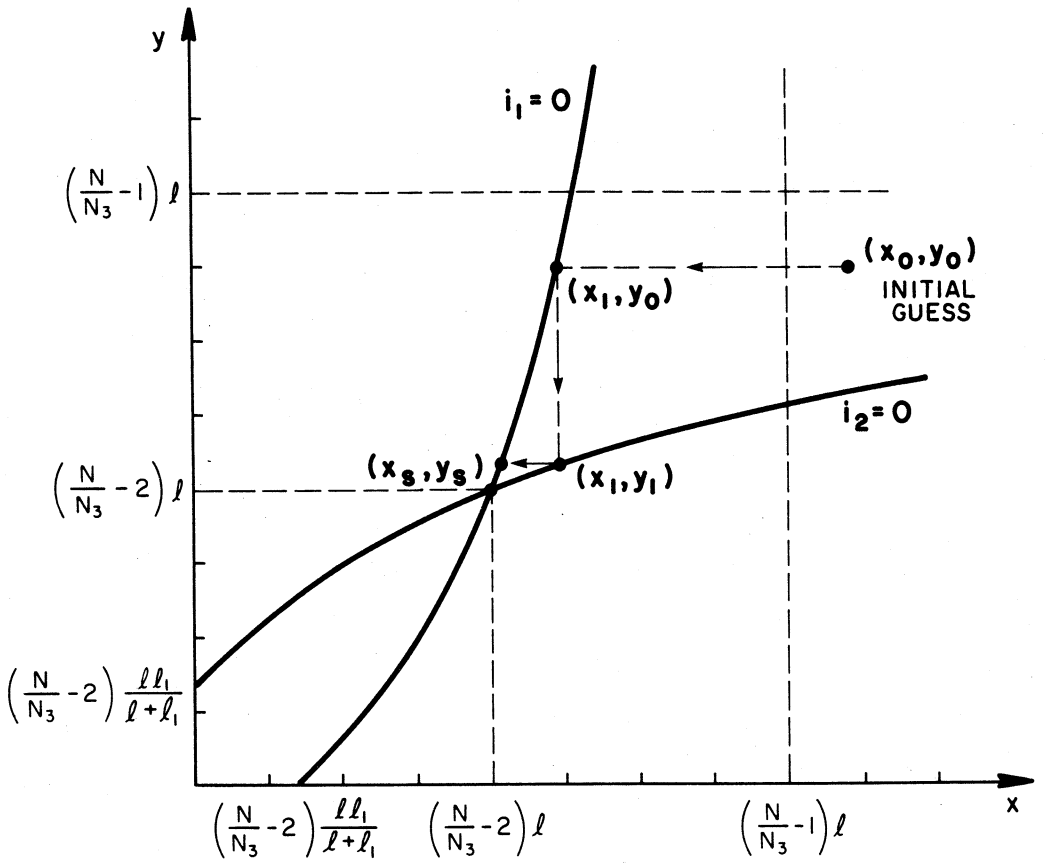

Fig. 18.11 Typical curves of zero current ripple for a symmetric structure showing one possible series of iterative gap adjustments.

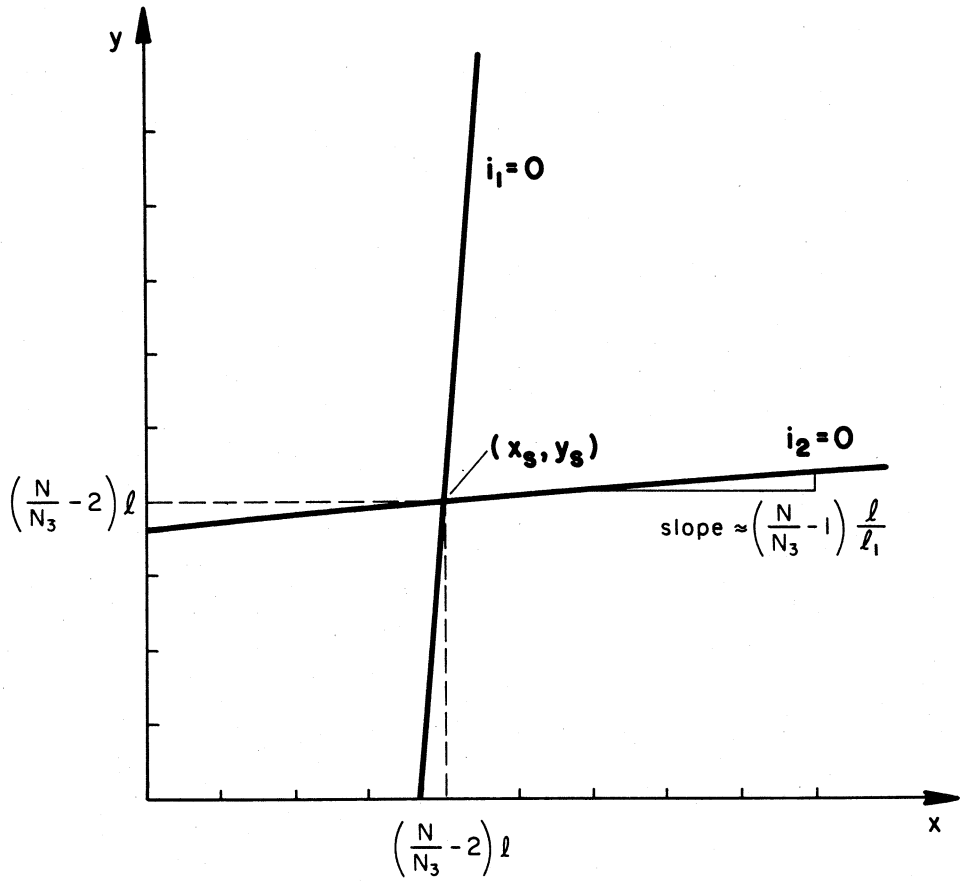

Fig. 18.12 For nearly perfect coupling of the outer windings the curves of zero ripple in gap space approach straight lines with finite slope.

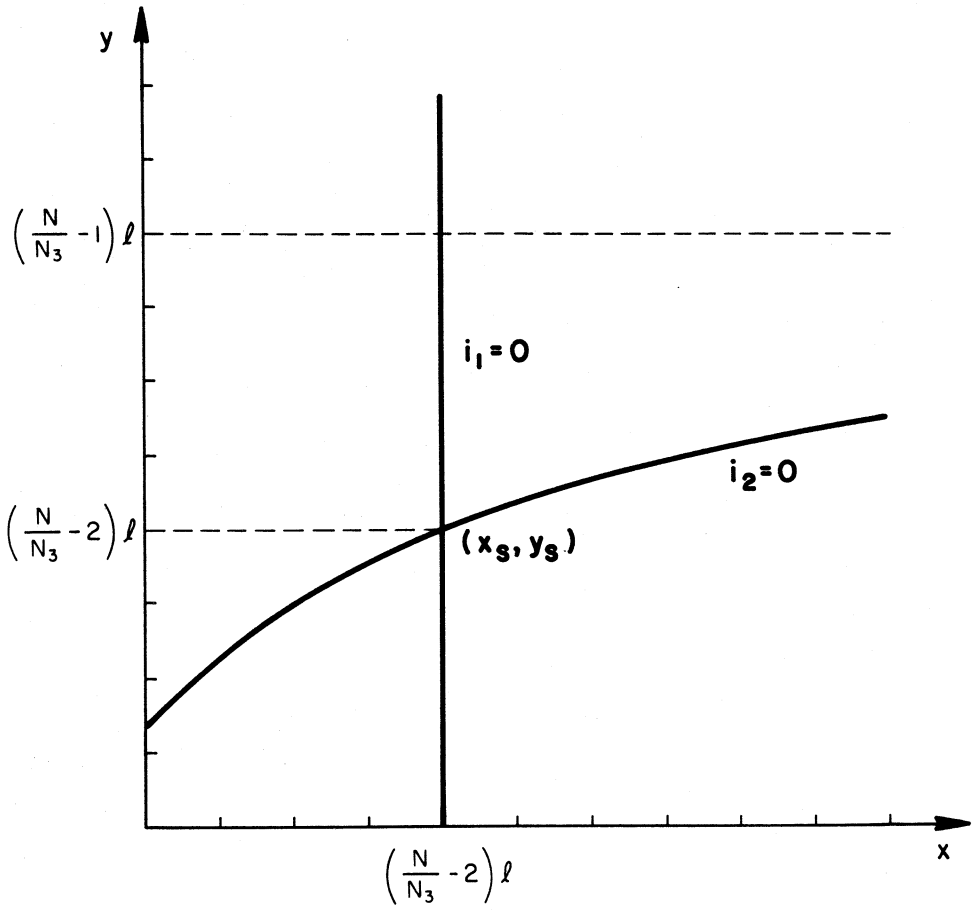

Fig. 18.13 If only one of the outer windings is perfectly coupled to the core, the adjustment of only one of the gaps will show interactive behavior. If the output winding is perfectly coupled as shown here, no adjustment of the gap y will affect zero ripple on the input, but adjustment of the gap x will upset zero ripple on the output.

ripple boundaries, the gap adjustments are not independent, but after several iterations converge to the final solution (x_s, y_s)

Several interesting special cases may be highlighted from the family of curves described by (18.28). For example, for very small self-leakages of the input and output windings (nearly perfect coupling), curves of zero ripple become straight lines with very small slopes as seen in Fig. 18.12. Quantitatively, for $l_1 \gg l$ and $l_1 \gg x$, Eq. (18.30) reduces to a straight line given by

$$y = \left[\frac{N}{N_3} - 2\right] l + \left[\frac{N}{N_3} - 1\right] \frac{l}{l_1} x \tag{18.32}$$

Thus one would expect that fewer adjustments would be required to achieve simultaneous zero ripple if the leakage on the input and output windings is low.

Another interesting example is illustrated in Fig. 18.13 in which the output winding is perfectly coupled to give a vertical line for the locus of zero input ripple. Hence, in this case, once the input current ripple is adjusted to zero, it will remain at zero despite any change of the output gap y. If both input and output windings are perfectly coupled (all the flux linking the center winding) then both boundaries of zero ripple reduce to straight lines as shown in Fig. 18.14, which is analogous to the prediction of the previous analysis shown in Fig. 17.7.

Until now the analysis has treated cases where the reluctance of the center leg of the integrated magnetic structure has been small enough to be negligible, or even non-existent as for the structure of Fig.

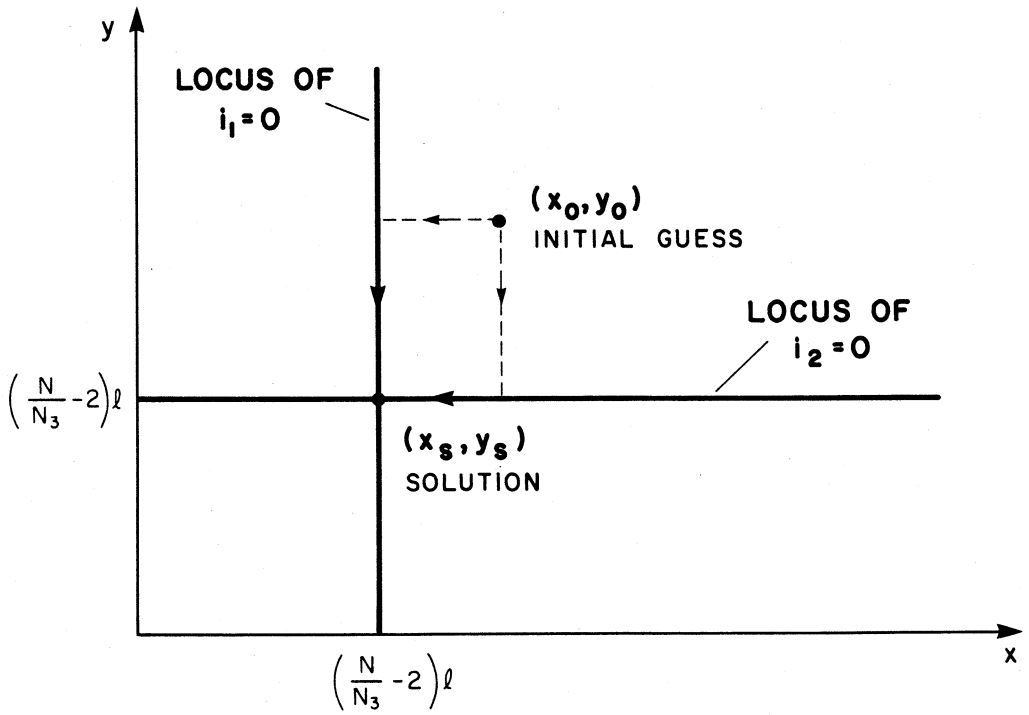

Fig. 18.14 Analysis of the special case of perfect coupling on both outer windings predicts noninteractive adjustments. The zero-ripple solution should be reached in a single step for each winding.

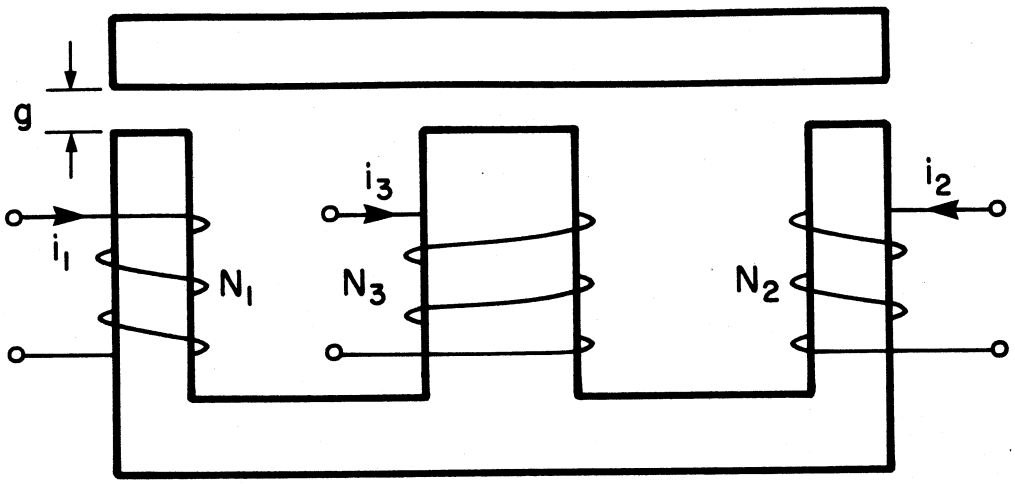

Fig. 18.15 Realization of the three-winding integrated structure with a common E-I core. Each leg has an air gap.

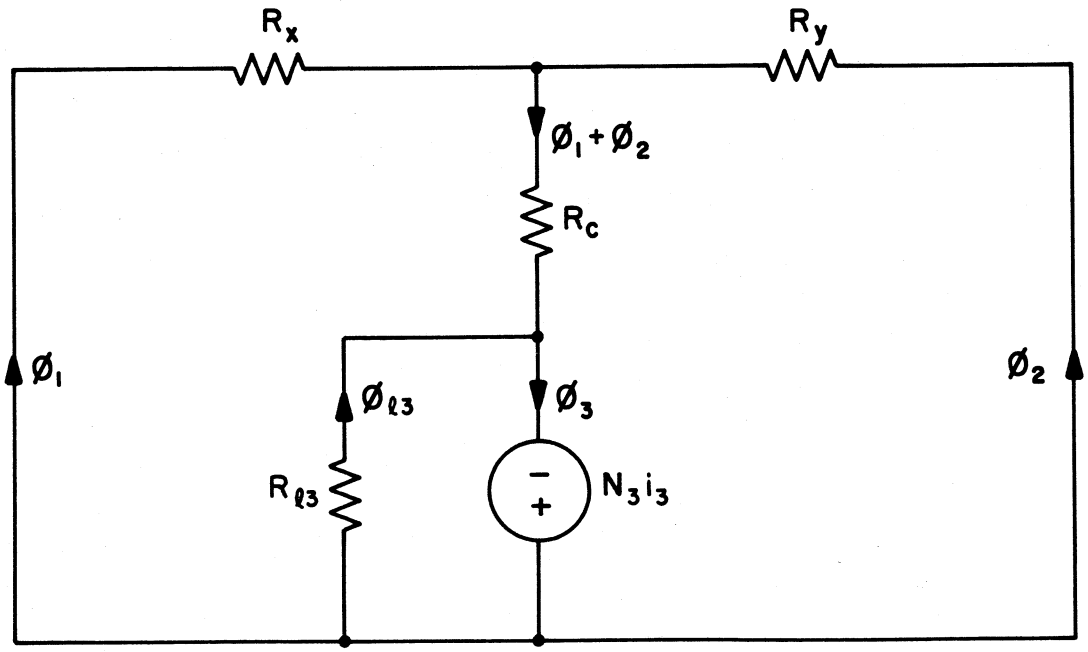

Fig. 18.16 Simple reluctance model for the zero-ripple E-I structure of Fig. 18.15. The air gap in the center leg raises the value of the reluctance of R_c such that it can no longer be ignored in the model.

18.8. Often it may be necessary to consider the effects of this reluctance, however, as in the practical structure of Fig. 18.15, which is made from a conventional E-I core combination. The zero-ripple solution for this configuration can be found from the reluctance equivalent circuit model of Fig. 18.16, from which one obtains for the the symmetrical case

$$R_{xs} = R_{ys} = \left(\frac{N}{N_3} - 2\right)R_{l3} - 2R_c \tag{18.33}$$

Thus the effect of the finite reluctance of the center leg is to reduce the previous solutions (18.19) by $2R_c$. If there were no center gap and one were concerned only with the reluctance of the core material in the center leg, the expression in terms of gaps would be

$$x_s = y_s = \left(\frac{N}{N_3} - 2\right)l - \frac{c}{\mu_r} \tag{18.34}$$

where c is the length of the center leg and μ_r is the relative permeability of the material with respect to μ_0. The fact that the center leg has twice the cross-sectional area of the outer legs has been taken into account in (18.34). This result is identical to (18.19) except for the correction term $\frac{c}{\mu_r}$. For a relative permeability of 2000 for a typical ferrite and for a center length of $c \approx 1$ cm, the correction term is approximately 0.005 mm. In most cases this will be truly negligible in comparison with the equivalent l of the center winding leakage, which is on the order of 1 mm or higher. For the structure illustrated in Fig. 18.15, where the gap in the center is the same as in the outer legs, it is

easy to show the common gap is

$$g_s = \left[\frac{N}{N_3} - 2\right]\frac{l}{2} \tag{18.35}$$

This chapter has shown how one may use the simple reluctance equivalent circuit model to quickly solve for the zero-ripple conditions in terms of geometric quantities. The key to the rapid solution is the realization that the problem can be separated into an ac part and a dc part. Since only the ac problem need be addressed to find the zero-ripple conditions, one may use a short-cut procedure in which the mmf generators that represent the windings with zero ripple are replaced by short circuits in the equivalent circuit model.

The next chapter introduces alternative winding configurations for the three-winding integrated structure. One new configuration will permit experimental verification of the characteristics predicted here, and the other is a proposal by which one may reduce the amount or magnetic material required for the zero-ripple structure.

CHAPTER 19

ALTERNATIVE WINDING CONFIGURATIONS FOR THE INTEGRATED STRUCTURE

It has been determined analytically that the interactive behavior observed in adjusting the two air gaps in the integrated structure for zero ripple is caused by the self-leakages of the input and output windings. In addition, the only leakage which determines the gaps at which zero ripple occurs (to first order) is the self-leakage of the third or non-zero ripple winding. The surprising prediction that perfect coupling on the input and output windings would result in independent gap adjustments demands further attention. With this as the motivation, the zero-ripple structure is examined to find a way to verify this unusual result.

19.1 The Non-Interactive Configuration

According to the analyses, if one is able to eliminate the self-leakages of the input and output windings of the integrated structure while maintaining the self-leakage of the third winding, he can fabricate a structure for which the gap adjustments are independent. The physical meaning of self-leakage is that some of the flux generated by one winding does not link any other winding. One should expect that the windings of the standard zero-ripple configuration would have a great deal of self-leakage simply because they are so widely separated. One way to reduce or

eliminate the self-leakages is to put the windings closer together so that all the flux generated by a winding links at least one other winding. This can be accomplished by a simple topological manipulation of the third winding, as illustrated in Fig. 19.1.

Figure 19.1a shows the usual configuration with a single turn for the center winding. Figures 19.1b and 19.1c clearly illustrate how the wire of the center winding can be stretched and maneuvered to the same locations as the input and output windings, whose self-leakages diminish as the windings get closer together. If the turns of the former center winding are tightly woven among those of the others, all the flux generated by the input and output windings will be coupled to at least one other winding, and there will be no self-leakage at the input or output. The converse is not true, however, since some of the flux generated by the third winding will not link any other, as illustrated by the leakage flux φ_{l3} in Fig. 19.1c.

Figure 19.2 illustrates how the non-interactive configuration may be constructed with two sets of U-cores plus an auxiliary U-I core to control the leakage of the third winding. Note that the auxiliary magnetic pieces are drawn with a different cross-sectional area than the main pieces, and the auxiliary turns are designated as N_{l3}. This is to emphasize that in general the particular combination of turns, area and air gap of this piece is not important to the operation of the device, but it is only the flux φ_{l3} which matters. The notation in this thesis is based on the assumption that $N_{l3} \equiv N_3$ and all pieces have the same

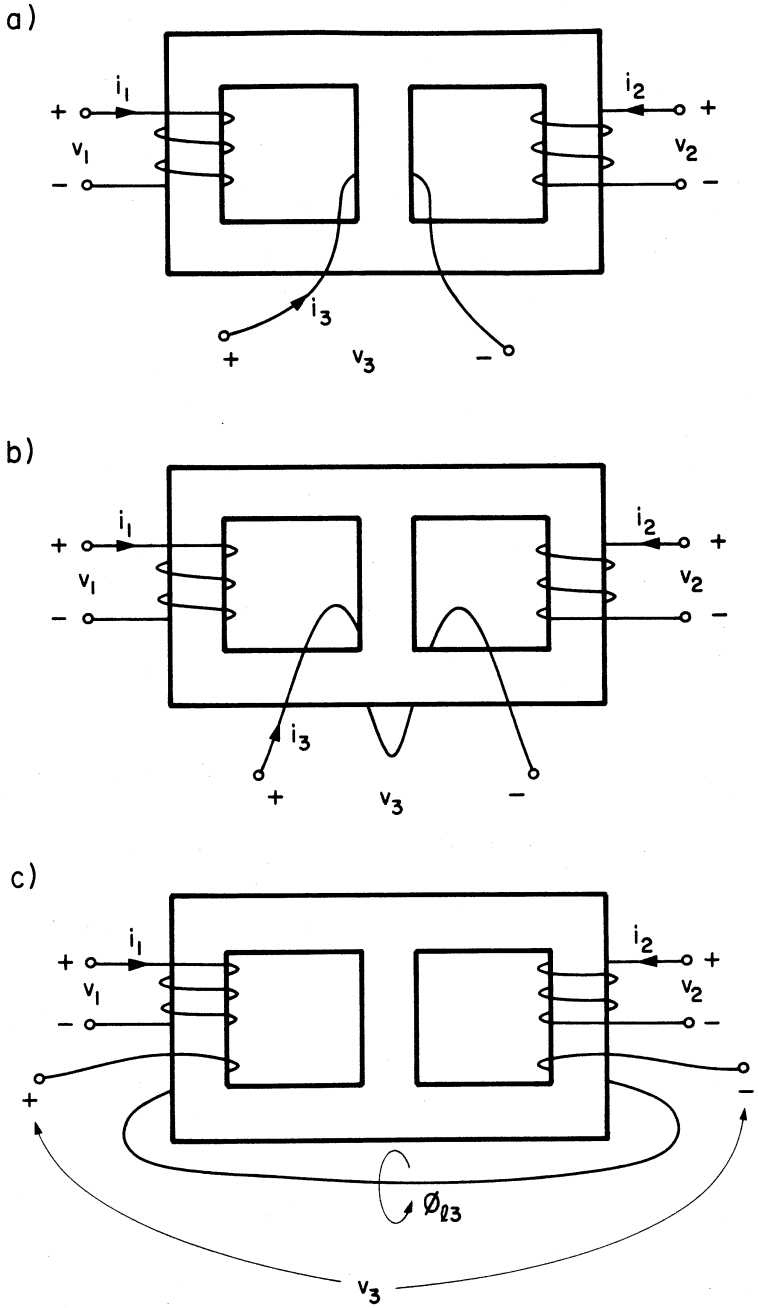

Fig. 19.1 The center winding can be topologically manipulated to reduce the self-leakages of the outer windings. The sequence shows how a single turn is removed from the center leg and maneuvered to the outer legs without changing the fundamental topology of the magnetic circuit.

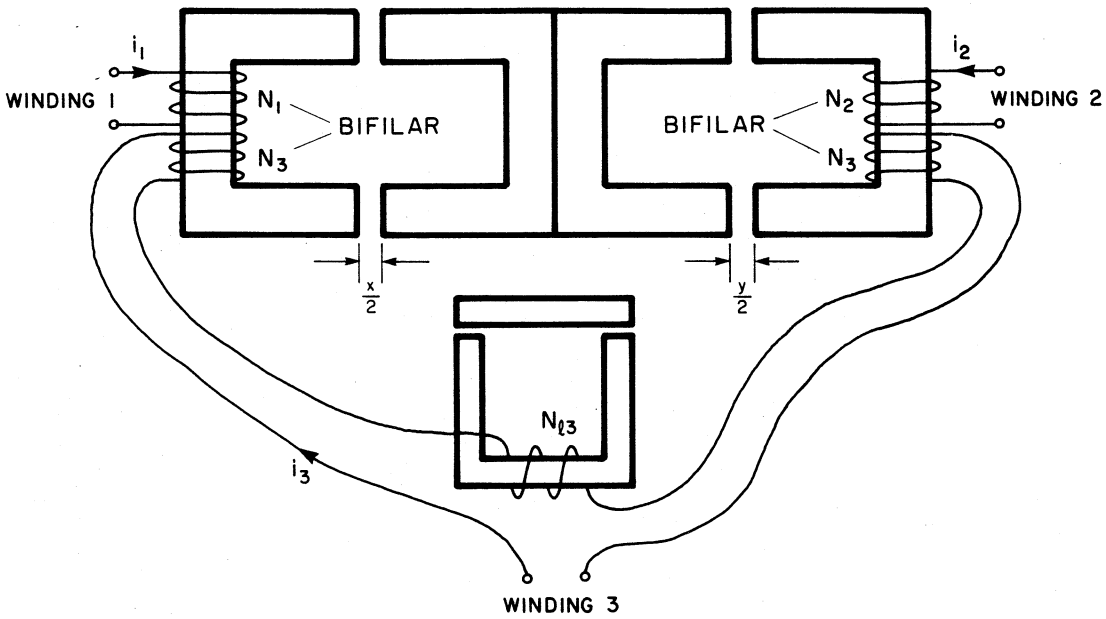

Fig. 19.2 Hardware realization of the zero-ripple structure with virtually zero self-leakage on the input and output windings. The necessary self-leakage of the third winding is controlled by a separate auxiliary core and air gap.

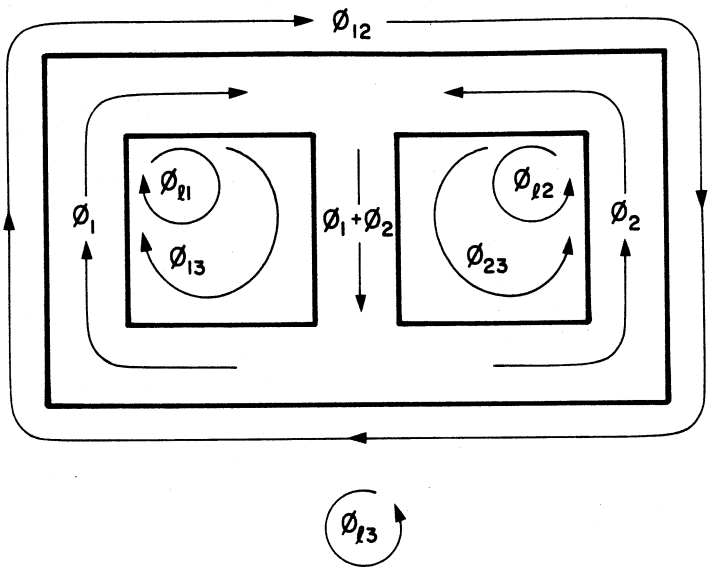

Fig. 19.3 General decomposition of fluxes for the modified winding configuration of Fig. 19.1.

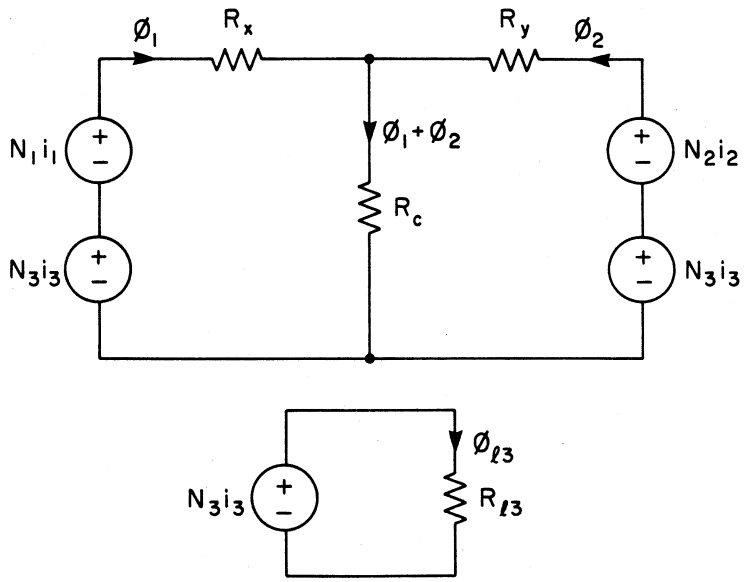

$$\emptyset_3 = \emptyset_1 + \emptyset_2 + \emptyset_{\ell 3}$$

Fig. 19.4 Simple reluctance model for the non-interactive configuration. This model can be easily obtained from the model of the standard configuration of Fig. 18.5 for the case of no self-leakage on the input and output windings.

area, but it is a simple matter to rescale the parameters used here to suit the dimensions of other configurations.

Although the flux patterns for the non-interactive configuraton are different from those of the original structure, the flux still may be decomposed into the same components as in the original analysis, and thus the same reluctances and permeances may be defined. Figure 19.3 shows the general decomposition of fluxes for the winding arrangement of Fig. 19.1. The self-leakages of the the input and output windings are shown for the general case of non-bifilar windings.

The same approximations which were used in the analysis of the original structure are valid here, and thus the simple reluctance equivalent circuit model for the non-interactive (bifilar winding) configuration can be easily shown to be that of Fig. 19.4. It is also easily shown that if the input and output windings are assumed to have no leakage flux ($R_{l1} = R_{l2} = \infty$), then the model of Fig 19.4 can be obtained from the equivalent original reluctance model of Fig. 18.5 via simple network transformations. Thus *all the results of the previous analyses are valid for this configuraton as well.*

19.2 The Minimum-Material Configuration

Just as in the standard configuration, the center leg of the non-interactive structure must contain the *sum* of the fluxes of the outer legs. If the directions of the windings on either the left or right legs were reversed as illustrated by Fig. 19.5, the flux in the center leg would then be the *difference* between the outer fluxes rather than the sum, and this is true

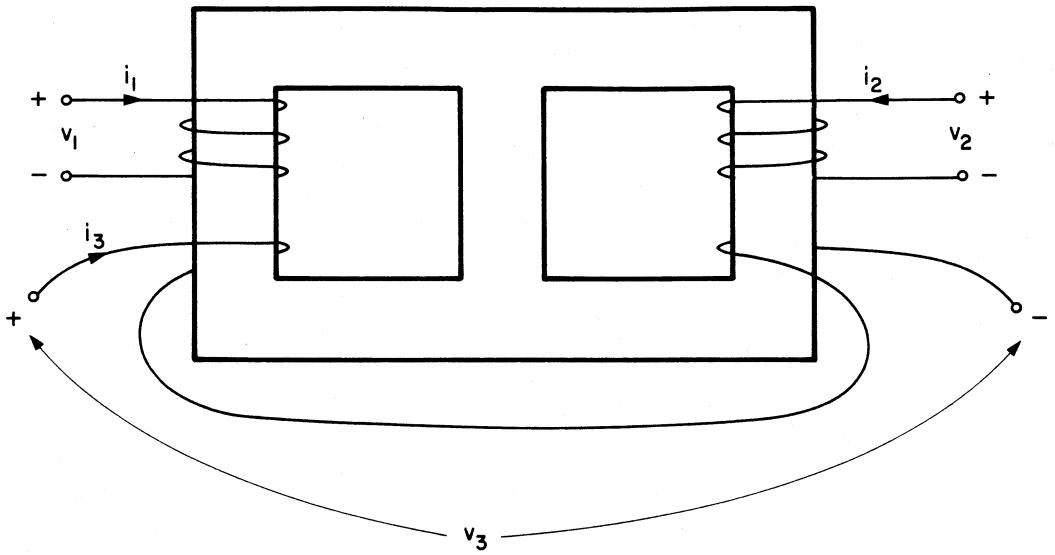

Fig. 19.5 When the wires on the right leg of the non-interactive configuration are wound in the opposite sense, the fluxes in the center leg subtract instead of add. Since less core material is then required in the center leg, this is called the minimum-material configuration.

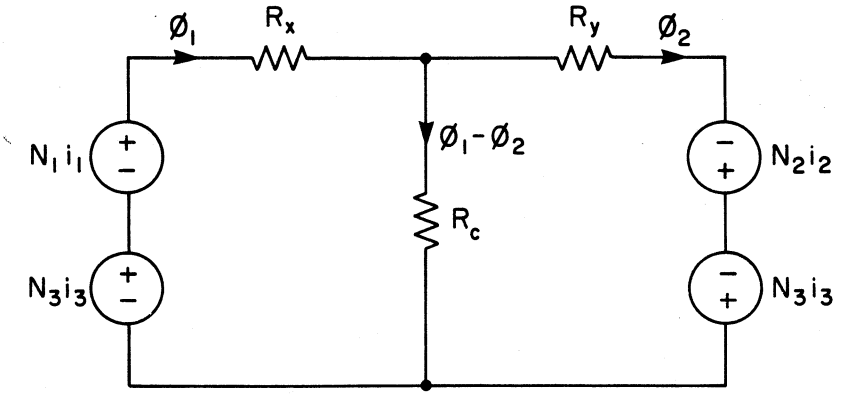

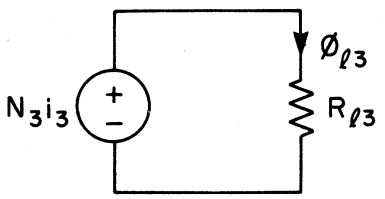

$$Ø_3 = Ø_1 + Ø_2 + Ø_{\ell 3}$$

Fig. 19.6 Reluctance equivalent circuit model for the minimum-material configuration.

for both the ac and dc fluxes. Figure 19.6 shows the simplified reluctance equivalent circuit model for this configuration. Note that the polarities of the sources $N_2 i_2$ and $N_3 i_3$ and the direction of φ_2 in the rightmost branch are the the reverse of those in Fig. 19.4. Because the center leg does not have to support as much total flux as in the original configuration, less cross-sectional area is required to maintain the flux density below the level of saturation. Owing to the saving of magnetic material in the center leg, this modification is called the minimum-material configuration.

Can the minimum-material configuration give zero ripple? Application of the techniques described in Chapter 17 quickly shows that for the special symmetric case of $N_1 = N_2 = N$, zero-ripple solutions do exist and are *exactly the same* as for the standard configuration with $R_c \equiv 0$, namely Eq. (18.18). Moreover, it can be shown by the same method that for the symmetric case the solutions are *independent* of the reluctance of the center leg R_c. This does not mean that the center leg can be removed, however. An exact analysis will show that with no self-leakages the determinant of the system is singular if $R_c \to \infty$. The solutions for the case of $N_1 \neq N_2$ are given in the Appendix.

Several methods have been described in the preceding chapters by which one may design magnetic components for ripple-free power conversion. In addition to the switching characteristics, however, the designer must be concerned with the overall dynamic response of the system in order that it be properly controlled for the intended

application. To this end it is desirable to have *electric circuit models* for each component of the system so that the entire converter can be modelled for frequency domain analysis by familiar techniques. The next chapter presents some electrical equivalent circuit models of the magnetic devices discussed thus far and relates the electrical elements in the models to the geometry of the magnetic structures.

CHAPTER 20

ELECTRIC CIRCUIT MODELS

Two methods to model magnetic devices have been discussed thus far. The coupled inductor equations provided a complete but rather cumbersome and non-physical description while the physically oriented magnetic circuit model permitted quick and simple solutions for the zero-ripple conditions. As a bonus, the magnetic circuit description gave physical insight which suggested a material-saving improvement to the original design. This chapter presents another type of circuit model in which the physical parameters of the magnetic device are related to ideal electrical elements connected in a physically meaningful topology. These *electric circuit models* are valuable not only because they permit a relatively unfamiliar magnetic device to be viewed in a more illuminating form, but also because they permit a designer to quickly assess the device's performance in the operating environment of an electronic circuit.

20.1 Application of Duality to Magnetic Circuits

In deriving an electric circuit model for a magnetic device, one hopes to describe the electrical terminal properties of the device by means of an interconnection of inductors and ideal transformers. Since the topology of an electrical network is not determined by its terminal properties, many different circuits are possible.

There are two principal routes by which one may obtain suitable models. The traditional course, which was used very successfully to model transformers in [38], is first to hypothesize a general circuit topology which contains a sufficient number of variables to describe all possible terminal relationships. After the voltage and current relationships are found in terms of the parameters of the model, the resulting equations are solved to determine the unknown parameters in terms of either the coupled inductor constants or the permeances. The main disadvantage of this method is that for unconventional structures a good choice of topology is not always obvious, and, consequently, the elements of the model may turn out to be quite complicated and unilluminating functions of the basic magnetic properties of the device. Unfortunately, the electric circuit model is not much help unless the electrical elements can be readily identified with the important individual parameters of the magnetic structure.

The other method derives an electric circuit model directly from the reluctance equivalent circuit model by application of the principles of *duality*. The greatest advantage of this straightforward method is that the elements of the resulting electric circuit have a one-to-one correspondence with the reluctances of the magnetic device. Moreover, even if the complete electric circuit is more complicated than one would like, its basic structure serves as a guide to the selection of a simpler topology to which the first method may be applied.

The concept of duality as applied to graphs and electric networks is well-known, and detailed treatments can be found in many standard textbooks [40, 41]. Although the analogous application to magnetic circuits is not as common, the technique has been well established [42]. The duality method consists of four steps [23]. First, one draws the reluctance equivalent circuit which has the same topology as the magnetic device to be modelled. Then a dual of the reluctance circuit is drawn (as shown by an example in the Appendix) in which the elements of the dual circuit become permeances. The permeances are then scaled by the appropriate number of turns to relate the fluxes in the network to the terminal voltages. Finally, all N^2p's are replaced by L's to put all the relationships in terms of voltages and currents. Ideal transformers may then be added as desired for cosmetic scaling purposes.

The following sections show how these two methods may be used jointly to derive simple and illuminating electric circuit models of the rather unusual magnetic devices studied in the previous chapters.

20.2 Electric Circuit Model for the Two-Winding Structure

Figure 20.1 shows an appropriate electric circuit model for the two-winding coupled inductor structure, which may be readily identified as the π-model that has been used for decades to model transformers. From the model one can see that for zero output ripple no voltage will appear across the output leakage inductance L_{l2} because $\frac{di_2}{dt} = 0$, and therefore $v_s = v_2$.

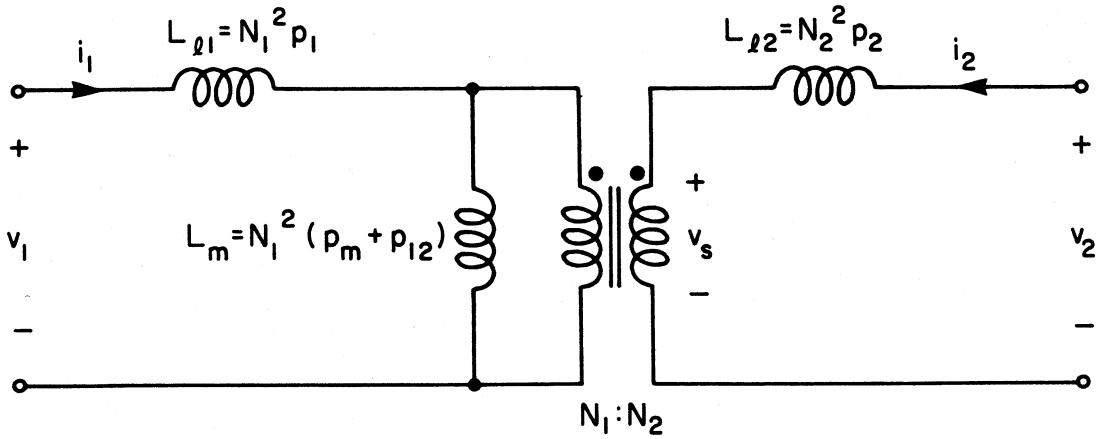

Fig. 20.1 Electric circuit model for the two-winding coupled inductor structure.

The condition for zero ripple is then by simple impedance division

$$\frac{N_2}{N_1}\,\frac{L_m}{L_m + L_{l1}}\,v_1 = v_2 \tag{20.1}$$

or equivalently

$$\frac{N_2}{N_1}\,\frac{p_m + p_{12}}{p_m + p_{12} + p_1}\,v_1 = v_2 \tag{20.2}$$

from which we get

$$\frac{N_1}{N_2} = \frac{v_1}{v_2}\,\frac{p_m + p_{12}}{p_m + p_{12} + p_1} \tag{20.3}$$

which reduces to (17.4) for the special case of $v_1 = v_2$. Thus from the electric circuit model it is easy to see why the conditions for zero output ripple must be independent of the self-leakage of the output winding. It should be noted for state variable analysis that, although this model portrays three explicit inductances, the circuit has *only two states* because the currents in only two of the inductances are independent.

Equation (20.3) emphasizes the fact that to obtain zero ripple the voltages which appear on the windings of the coupled inductor *do not have to be equal* but *only proportional*. The fact that those voltages were equal in the original Ćuk converter not only motivated the idea of coupling the inductors, but also unintentionally promoted the common misconception that the voltages and the turns must be equal.

An added advantage of having the circuit model is that it is easy to compute the amount of ripple current which would appear at the input and output if the conditions for zero ripple were not met. This

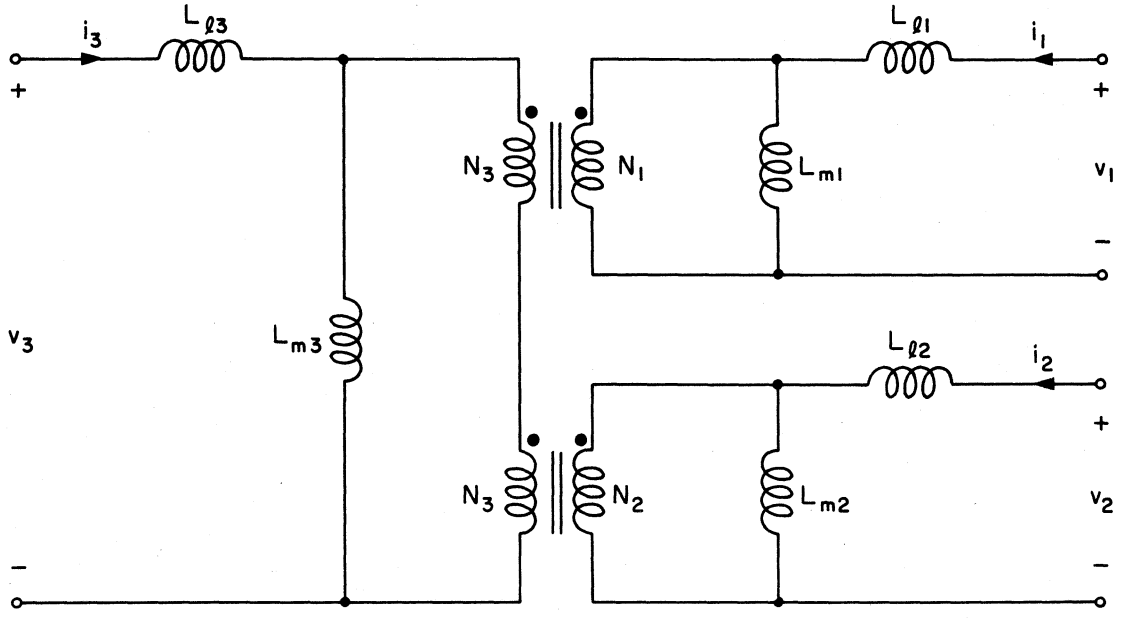

Fig. 20.2 Electric circuit model for the conventional three-winding integrated structure.

information is important to a designer, who must be aware of the sensitivity of his circuit to component tolerances and natural variations of parameters.

20.3 Model for the Conventional Three-Winding Integrated Structure

In [38] the π-model was shown to be uniquely determined for three-winding transformers, and the utility of that model in the design and understanding of such devices was demonstrated in an impressive and elegant manner. However, since the integrated structure is not a three-winding transformer, one finds that attempts to use a similar π-model result in non-physical parameters (like negative inductances) and complicated non-illuminating expressions. As shown in the Appendix, however, straightforward application of the principles of duality to a simplified reluctance equivalent circuit model of the conventional integrated structure yields the more appropriate topology of Fig. 20.2. It is obvious from the equivalent topology of Fig. 19.2 that this model bears a proper physical relationship to the original device. It is easy to see that even the coupled inductor constant M_{12} is negative for this circuit.

Solution of this model in terms of the permeances defined in Chapter 17 gives the exact expressions

$$L_{l1} = N_1^2 p_1 \qquad L_{l2} = N_2^2 p_2 \qquad L_{l3} = N_3^2 p_3 \tag{20.4}$$

$$L_{m1} = N_1^2 \frac{P_y P_x + P_y P_z + P_x P_z}{P_x} \tag{20.5}$$

$$L_{m2} = N_2^2 \frac{P_y P_x + P_y P_z + P_x P_z}{P_y} \tag{20.6}$$

$$L_{m3} = N_3^2 \frac{P_y P_x + P_y P_z + P_x P_z}{P_z} \tag{20.7}$$

It is easy to show that under the realistic approximations discussed in Section 17.3 the permeances in the last three expressions simplify to yield the reduced expressions given below in terms of the reluctances defined in (18.13).

$$L_{l1} = \frac{N_1^2}{R_{l1}} \qquad L_{l2} = \frac{N_2^2}{R_{l2}} \qquad L_{l3} = \frac{N_3^2}{R_{l3}} \tag{20.8}$$

$$L_{m1} = \frac{N_1^2}{R_x} \qquad L_{m2} = \frac{N_2^2}{R_y} \qquad L_{m3} = \frac{N_3^2}{R_c} \tag{20.9}$$

The reduced expressions for the elements in the model are directly related to the explicit reluctances of the physical structure. Note that, if the reluctance of the center leg R_c is zero, the inductance L_{m3} vanishes from the circuit model, because an infinite inductance can have no current if its energy is to remain finite. Also, since there are only three independent inductor currents the circuit has only three state variables.

Aside from being able to determine the general conditions for simultaneous zero ripple on windings 1 and 2, one can find the magnitude of the ripple appearing on winding 3 by simple inspection of the circuit model. Since under zero-ripple conditions no voltage is

developed across the leakage inductances L_{l1} and L_{l2}, it is easy to see that

$$\frac{di_3}{dt} = \frac{v_3 - \left[\frac{N_3}{N_1} v_1 + \frac{N_3}{N_2} v_2\right]}{L_{l3}} \tag{20.10}$$

which one can show must be greater than zero. Without the benefit of the circuit model such computations would be a great deal more difficult. It is now also easy to see why the gap adjustments are non-interactive when the self-leakages L_{l1} and L_{l2} are zero. Under these conditions the voltages on the two ideal transformers in the model are fixed and independent of the adjusted values of L_{m1} and L_{m2}. Hence, variation of L_{m1} will change only i_1 and adjustment of L_{m2} will affect only i_2. Note that the ripple on the third winding will not change when L_{m1} and L_{m2} are adjusted.

20.4 Model for the Minimum-Material Configuration

The electric circuit model for the minimum-material configuration of Fig. 19.5 is similar to that of the conventional integrated structure, but not as easy to use except in certain special cases. As above, application of duality to a simplified reluctance equivalent circuit model of the minimum-material configuration leads to the electric circuit model of Fig. 20.3. The anti-parallel orientation of windings 1 and 2 causes the mutual inductance M_{12} to be positive for this configuration, and hence the modified topology. Solution for the elements of the model in terms of the reluctances gives

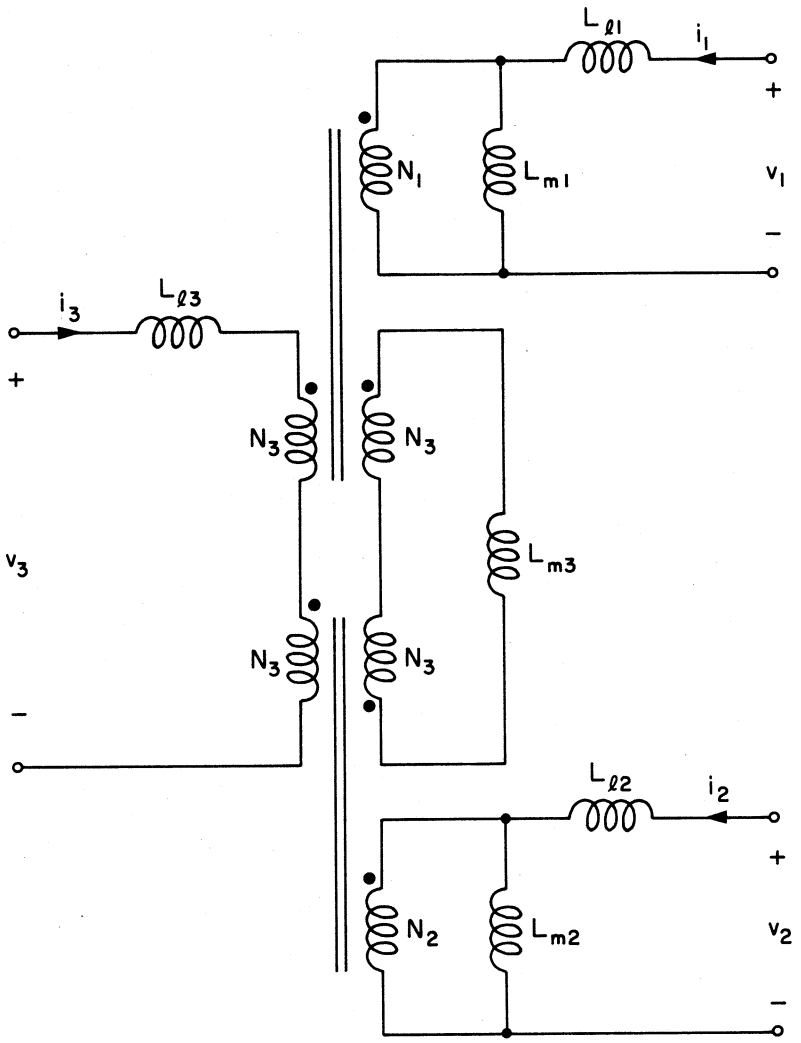

Fig. 20.3 Electric circuit model for the minimum-material configuration of the integrated structure.

exact expressions which are too complicated to be useful for design purposes, but under the realistic restriction that the mutual air leakages can be ignored they reduce to (20.8) and (20.9). It is comforting to note that for the case of $R_c = 0$ the two models reduce to the same topology. This outcome should be expected, because with $R_c = 0$ the structure in Fig. 19.2 is effectively reduced to two separate magnetic loops whose characteristics should be independent of the relative orientation of the core pieces which contain the windings as long as the air gaps remain the same. Since the material in the center of the device is a magnetic short circuit when $R_c = 0$ it is immaterial whether the fluxes there add or subtract.

This chapter has demonstrated that the development of electric circuit models for magnetic structures can be very beneficial to the design of specific devices as well as to one's understanding of their peculiar properties. Another important application of these models is in the understanding of the effects of parasitic quantities, which will be addressed next.

CHAPTER 21

EFFECTS OF PARASITIC QUANTITIES

The previous chapters have discussed the phenomenon of zero ripple in terms of the magnetic properties of an ideal device, and that treatment has been quite successful in explaining the observed first-order effects. As one experiments with these devices, however, it becomes clear that there are some rather obvious second-order effects which have not been addressed. Looking at the sequence of photographs of the zero-ripple adjustments of Fig. 14.2, for example, one can see that the "zero-ripple" currents are not really zero. When the currents are studied in greater detail by increasing the sensitivity of the current probe, one finds that despite the most painstaking adjustments it is impossible to make the current pure dc. In addition, it is observed that the conditions for zero ripple (actually *minimum* ripple) are somewhat dependent on the frequency of excitation.

Since earlier observations of these phenomena were made on power converters, it was easy to blame this non-ideal behavior on the known and accepted non-idealities of the converter. As will be shown in the next chapter, however, the same effects are observed when the converter is eliminated and the device is driven with ideal voltage waveforms. Therefore, the observed second-order effects cannot be caused entirely by the non-idealities of the converter, but must be attributed to some property of the device itself. This chapter will show that these effects can be explained by

the presence of natural losses in the real device, and, consequently, that true zero ripple may be achieved only under some very special circumstances. This treatment will be concerned with only the two-winding structure, as that will adequately illustrate how the techniques and concepts apply directly to more complicated devices.

21.1 Winding Resistance

One unavoidable parasitic quantity in practical magnetic devices is the finite electrical resistance of the windings. If each of the two windings (1 and 2) has a respective series resistance r_1 and r_2, then the coupled inductor equations (16.1) will be modified as follows:

$$v_1' = r_1 i_1 + v_1 \qquad v_2' = r_2 i_2 + v_2$$

so that

$$v_1' = r_1 i_1 + L_{11}\frac{di_1}{dt} + M\frac{di_2}{dt} \tag{21.1}$$

$$v_2' = r_2 i_2 + M\frac{di_1}{dt} + L_{22}\frac{di_2}{dt}$$

where v_1' and v_2' are the voltages applied to the terminals of the device and v_1 and v_2 are the voltages which generate the fluxes. It is clear that now the dc component of the current cannot be easily dismissed as it was in Section 18.1, for the presence of a dc current will change the voltages which actually produce the fluxes. The imposition of equal terminal voltages does not necessarily mean that $v_1 = v_2$, and thus the conditions for zero ripple

can change with the operating point of a power converter.

Consider that there is no dc current present in the windings. Taking the Laplace transform and writing the equations in matrix form gives

$$\begin{bmatrix} v_1'(s) \\ v_2'(s) \end{bmatrix} = \begin{bmatrix} r_1 + sL_{11} & sM \\ sM & r_2 + sL_{22} \end{bmatrix} \begin{bmatrix} i_1(s) \\ i_2(s) \end{bmatrix} \tag{21.2}$$

Solution for $i_2(s)$ and $i_1(s)$ shows after a few lines of algebra that it is *impossible* to make either current identically zero for any physically realizable condition. Furthermore, although it is possible to adjust either current for a *minimum ripple*, that condition is *frequency-dependent*. The solutions show that the current has both a real and imaginary part, and, although it is possible adjust either part to zero separately, both cannot be made zero at the same time. The frequency dependence of the solutions indicates that the current ripple which results from a rectangular voltage drive will no longer be purely triangular. In a lossless device all Fourier components of a rectangular voltage drive would be phase-shifted by 90 degrees and attenuated by the amount necessary to produce a triangular current waveform, and all components could be nulled by proper adjustment of the reluctances. With losses, however, the nulling property of the magnetic device is frequency selective, and therefore all frequency components cannot be nulled at the same time. In the adjustments of Fig. 14.2 only one frequency component is completely removed from the current ripple and the others

are reduced by lesser amounts. This accounts for the unusual ripple waveforms which remain after the ripple is adjusted to a minimum.

One easy way to see the impossibility of zero ripple is to use the electric circuit model. Figure 21.1 shows how the electric circuit model of the two-winding coupled inductor structure is augmented to include the resistances of the windings. Under the assumption of zero dc current, zero output ripple necessarily means that $i_2 \equiv 0$, and thus v_2' appears across the ideal transformer. By simple impedance division this requires that

$$v_1'(s) \frac{sL_m}{r_1 + s(L_{l1} + L_m)} \frac{N_2}{N_1} = v_2'(s) \tag{21.3}$$

Owing to the phase shift caused by the presence of r_1, there is no way this equation can be satisfied if v_1' and v_2' are in phase. The impossibility of the satisfaction of (21.3) for the special case of $v_1' = v_2'$ is obvious.

The electric circuit models and the coupled inductor equations for the three-winding integrated structures are modified to include the effects of winding resistances in exactly the same way as shown above for the two-winding case, and analysis of these models for conditions of zero ripple results in similar conclusions. Although the presence of winding resistance alone is sufficient to qualitatively explain the observed second-order effects, there is another loss mechanism which can produce similar results.

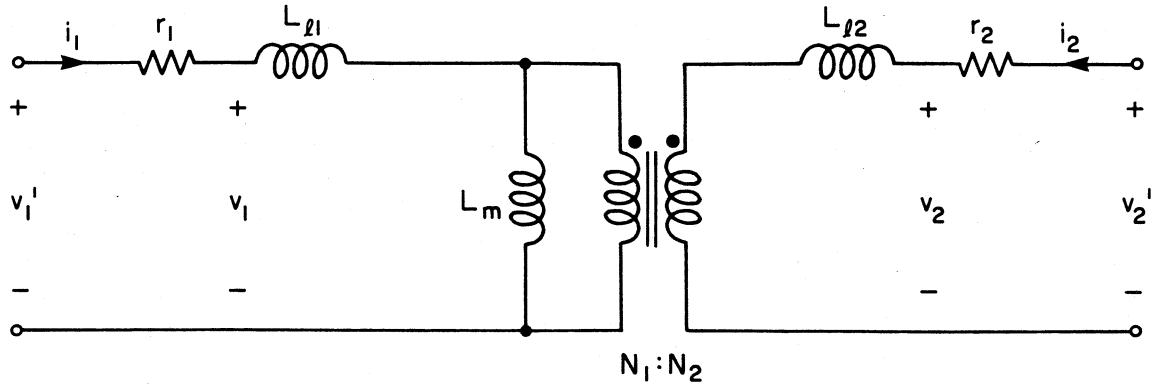

Fig. 21.1 From the electric circuit model of the two-winding coupled inductor structure it is easy to see how the resistance of the windings will change the zero-ripple conditions computed for an ideal device. If identical voltages are applied to the input and output ports it is impossible to make the current ripple exactly zero. At best, only a minimum ripple can be obtained.

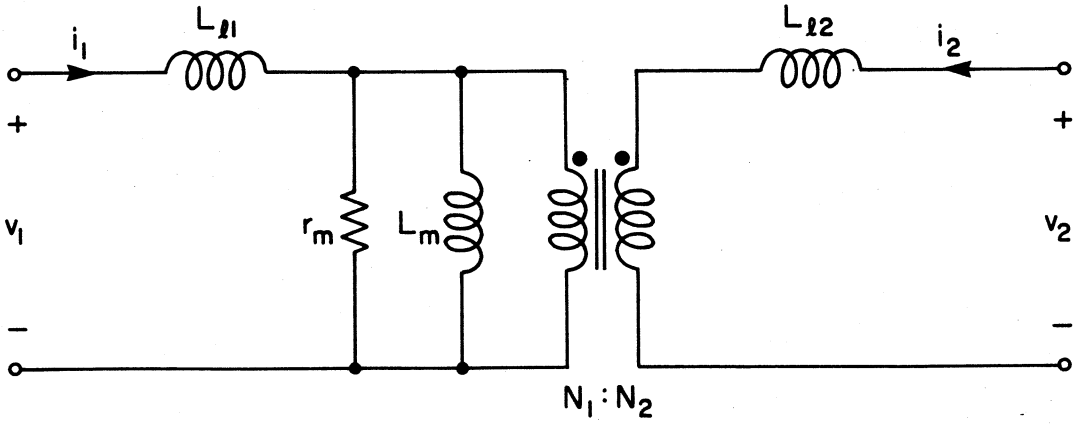

Fig. 21.2 The electric circuit model can be used to model the effects of core losses as well as copper losses. A parallel resistance is put across those inductive elements which are identified with flux contained in magnetic material. In this model the leakage fluxes are assumed to be entirely in the air, but the leakage inductances would not be lossless if they were controlled by auxiliary loops of magnetic material.

21.2 Core Losses

The dynamic losses which result from hysteresis and eddy currents are conveniently modelled by a resistance in parallel with the inductive element which models the reluctance of the magnetic material. In the electric circuit model of Fig. 21.2 this is shown by the resistor r_m in parallel with the inductance L_m. Here it is assumed that the leakages L_{l1} and L_{l2} have their fluxes entirely in the air, which is lossless. If these leakages are added externally or are controlled by means of extra magnetic loops, then they too would exhibit losses which would be modelled as parallel resistances. It is easy to see that the core losses can also produce a phase shift and a corresponding frequency dependence which will prevent the attainment of true zero ripple.

In real devices both the winding resistances and core losses can contribute to a second-order residual ripple which normally cannot be adjusted to zero. The effects of these parasitic quantities are nearly always negligible in practice, however, and consideration of the structure as ideal does indeed lead to excellent results, as will be seen from the experimental verifications described in the next chapter.

CHAPTER 22

EXPERIMENTAL VERIFICATIONS

This chapter describes several interesting experiments which were carried out to verify the results obtained from the previous analysis of integrated magnetic structures. A great deal of comprehensive testing has been done on many different structural arrangements, and, although all the results cannot be reported here in their entirety, several of the basic experiments which confirm key analytic results have been selected to be discussed in detail.

22.1 Hardware, Excitations, and Instrumentation

Although the Ćuk switching converter may be used to study zero-ripple phenomena, these experiments were conducted to evaluate the properties of the magnetic structure rather than the performance of the converter. Therefore, in order to maintain better control over the experiments and to provide for greater flexibility in the driving waveforms, a power oscillator was used instead of a converter to supply the desired voltage waveforms to excite the windings of the magnetic device. An ac sinusoidal source was chosen for all the experiments discussed in this chapter with the exception of the last section which addresses parasitic effects. The sinusoidal drive has the particular advantage of eliminating the high-frequency ringing which occurs when a fast-switching square wave

excites the parasitic LC resonances of the windings.

The salient features of a typical experimental set-up are shown in Fig. 22.1. Because a truly integrated magnetic structure as illustrated in Fig. 13.8 is not commercially available, equivalent variable-gap devices have been fabricated from ferrite U-cores. The basic structure is wound symmetrically with $N_1 = N_2 = N$ and all three windings are driven in parallel by the same voltage source. This configuration was chosen for these discussions not only for its simplicity, but also because it represents a typical device which would be used in a practical power converter. Several more complicated variations of this construction were made to emphasize and control specific variables of interest, and these will be described in detail in the following sections. A two-trace oscilloscope and two ac current probes are the only instrumentation required.

The structures to be studied are mounted on a specially built test bed which permits one to adjust and measure accurately the two variable air gaps x and y. The left and right U-cores are mounted on movable stages whose distances from the fixed center pieces may be changed independently with the precision of the two metric micrometer adjustments. The test fixture is shown in Fig. 22.2 with one of the more complex structures to be described in the next section.

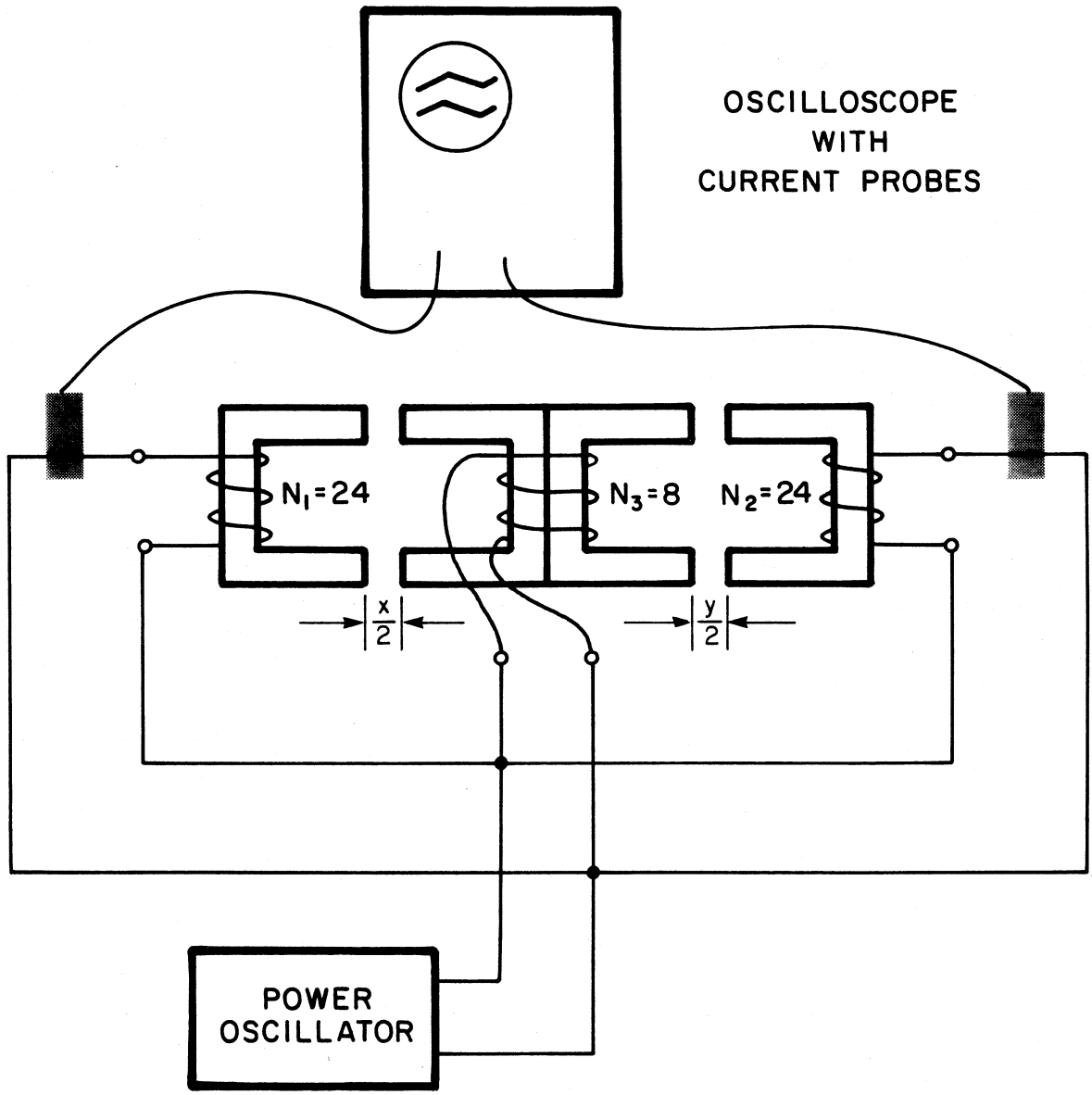

Fig. 22.1 The experimental set-up for the study of zero current ripple consists of a power oscillator, oscilloscope, two current probes and a variable-gap magnetic structure. For more precise measurements the magnetic device is excited with sine waves instead of rectangular voltage waveforms.

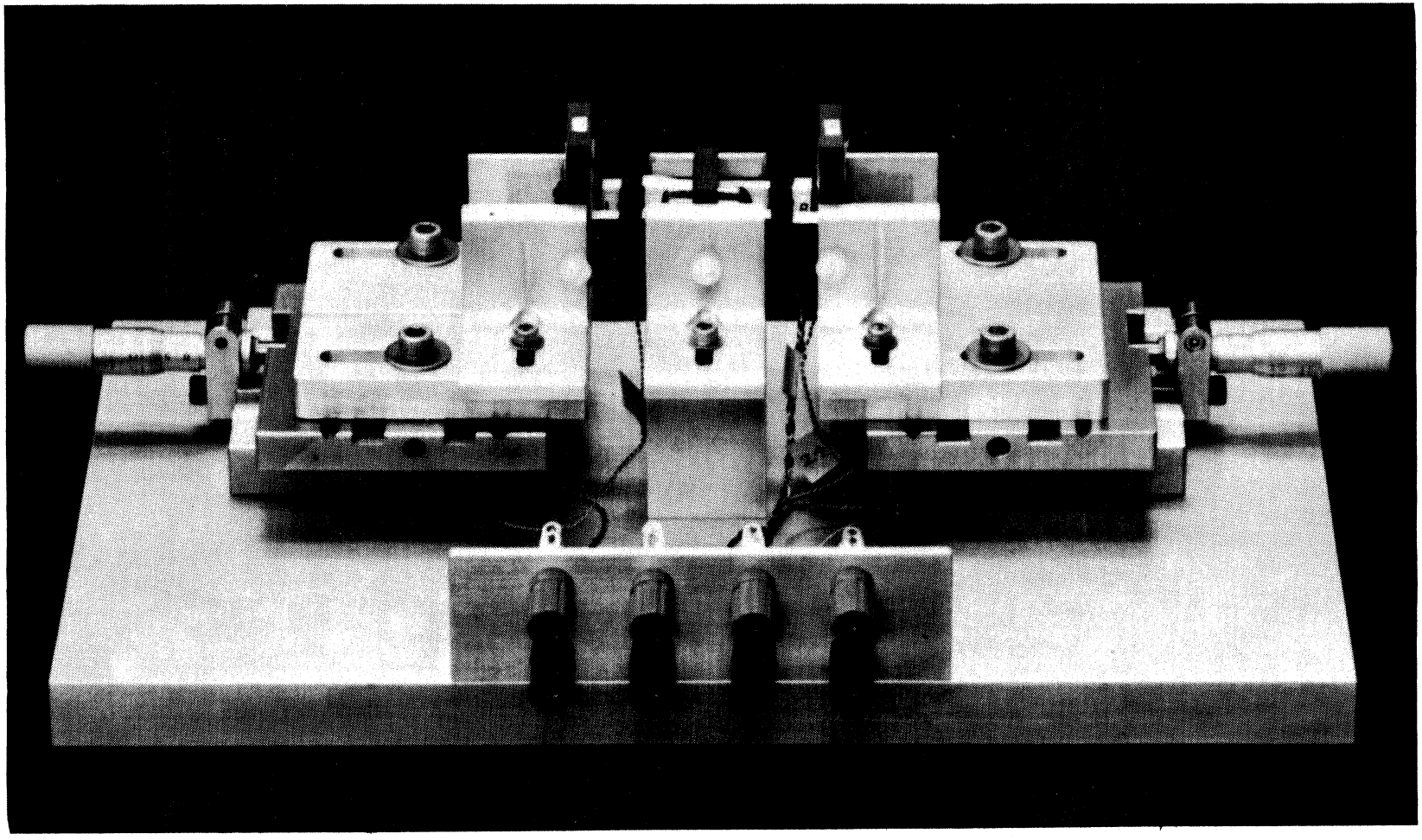

Fig. 22.2 The special test fixture permits accurate adjustment and measurement of air gaps. The left and right magnetic pieces are mounted on precision single-axis variable platforms which are positioned by micrometer adjustments.

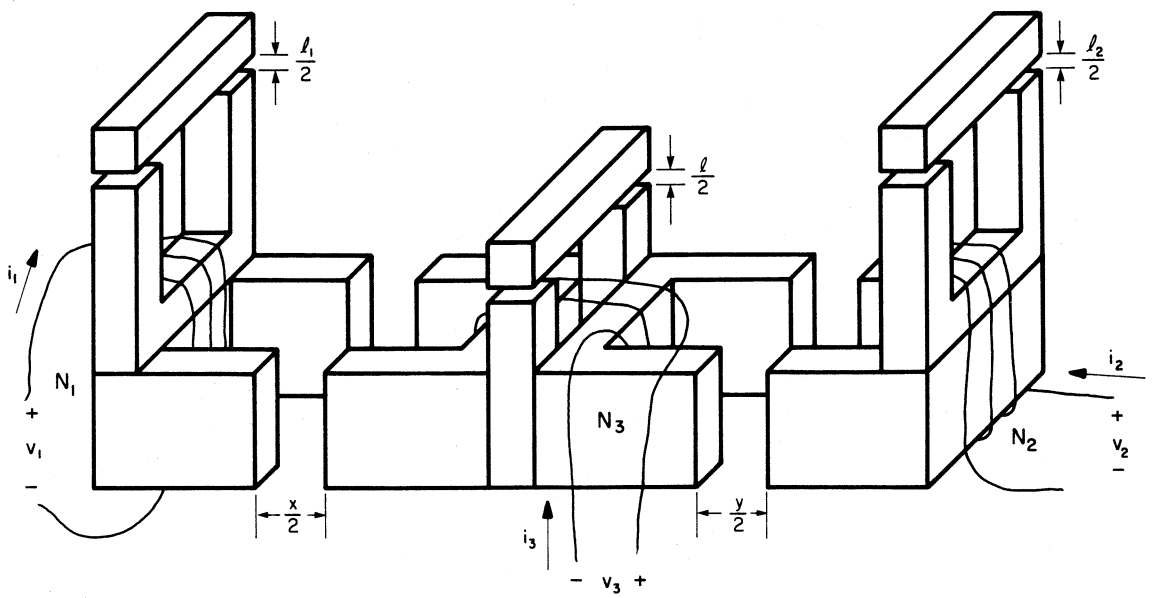

Fig. 22.3 Sketch of a three-winding structure in which the self-leakages of all three windings may be varied by changing the air gaps in the auxiliary magnetic loops.

22.2 Verification of Solutions for the Interactive Case

The analysis has shown that the most interesting characteristics of these devices are determined by the leakage fluxes of the windings. Because these leakage paths are not precisely known, it is practically impossible to design an experimental structure for a particular value of leakage flux. Although it is extremely difficult to design for a specific leakage, it is very easy to *change* the leakage by simply adding to the inherent leakage of the particular winding arrangement.

Figure 22.3 illustrates how the basic structure is modified by the addition of magnetic shunt branches to enhance and control the leakage fluxes of the three windings. The base structure is made from two sets of Magnetics, Inc. F-42530-UC cores and the leakage enhancement is done with F-42515-UC cores which are closed by I-pieces with paper spacers. The outer windings are 24 turns of #24 magnet wire and the center winding consists of 8 turns of three parallel strands of the same wire. This particular arrangement was chosen so that all the windings would cover the same linear distance and occupy the entire channel of the U-piece, with the hope that the commonality would help to maintain the symmetry of the structure and make the results more reproducible.

In the first experiment a sinusoidal voltage of 1.6 V peak to peak at 100 kHz was applied to all three windings. Keeping the center leakage fixed, the micrometers were then adjusted to find the gaps at which zero ripple was measured on windings 1 and 2 for several values of leakage reluctance in the outer windings. Examples are shown in Fig. 22.4 for the cases of two

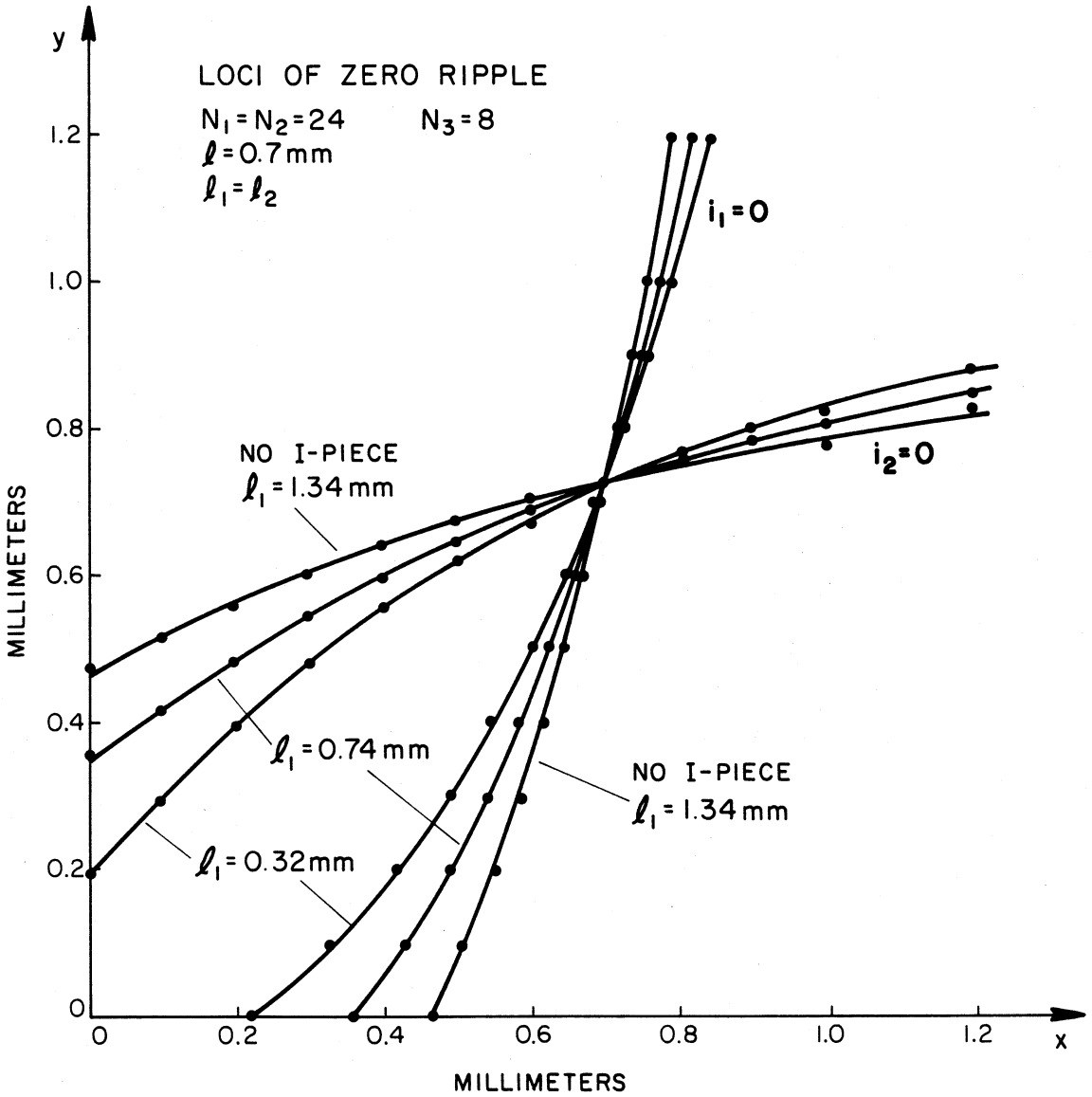

Fig. 22.4 Measurements of zero ripple for three different values of self leakage in the outer legs of a symmetric device. Note that all three curves intersect at the same point, corresponding to zero ripple on both input and output.

different spacers in the outer leakage loops and also for the case of maximum reluctance with no I-pieces. It can be seen that the curves have the same general shape as those originally predicted in Fig. 18.11.

Since the actual air gaps in the leakage loops are by no means the effective gaps discussed in the analysis, it may not be obvious at this point how one can correlate the experimental data in Fig. 22.4 with the theoretical predictions. How, for example, can one find an equivalent air gap for the case when there are no I-pieces in the leakage loops? One could first measure the voltages and currents for each of the data points, use the information to compute the coupled inductor constants, and then work backwards to find the reluctances. Fortunately, there is a much easier way to obtain the information.

Note that in the theoretical expression of (18.30) one can easily find the intersection of the locus of zero current ripple ($i_2 = 0$) with the y-axis by setting $x = 0$ to get

$$y(0) = \frac{l_1}{l+l_1}\left[\frac{N}{N_3} - 2\right]l \tag{22.1}$$

$$y(0) = \frac{l_1}{l+l_1}\, y_s$$

From the experimental curve for $i_2 = 0$ one can find the gap $y(0)$ at which the locus meets the y-axis. Also, the zero-ripple solution (x_s, y_s) can be easily determined experimentally, which can be used to calculate the value of the effective gap l from (18.29). Then by use of the measured $y(0)$ and the calculated l one can compute an equivalent gap

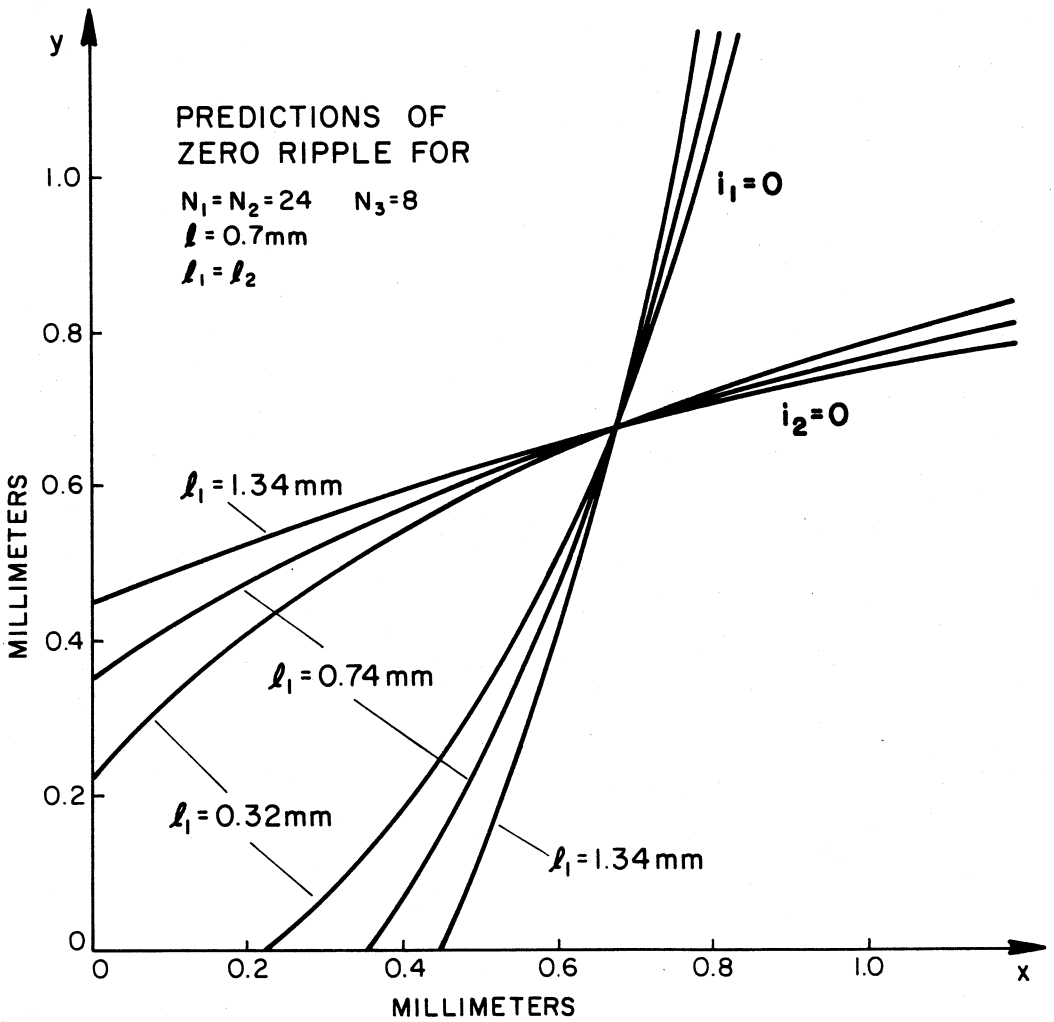

Fig. 22.5 Theoretical predictions corresponding to the measurements of Fig. 22.4.

l_1 from (22.1). This method was used to compute the equivalent air gaps for l_1 and l_2 which are labeled in Fig. 22.4 and to generate the corresponding theoretical curves of $y = f(x)$ from (18.30). These curves, plotted in Fig. 22.5, show very good agreement with the experimental data. Similar curves for other turns ratios and gap combinations can be found in the same way, with slightly more algebra required to compute the effective gaps for non-symmetrical structures.

To illustrate the special case of very small leakages on the input and output windings (nearly perfect coupling), the configuration of Fig. 22.6 was used. Here the air-leakages of the outer windings provided the less than perfect coupling while the leakage of the center winding was controlled by an extra magnetic path. Figure 22.7 shows that the experimental curves obtained for zero input and output ripple approach the straight lines predicted by (18.32).

22.3 Verification of Solutions for the Non-Interactive Configuration

The realizability of non-interactive adjustments is verified with a structure similar to that already proposed in Fig. 19.2. In this experiment the windings on the left and right U-cores are wound *quadrafilar* with $N_1 = N_2 = 24$ and $N_3 = 8$. Eight turns of a cable made from 4 strands of magnet wire twisted tightly together were wound on the core. Then 3 of the strands were connected in series to make the 24 turns of N_1 and N_2, and the remaining conductor made the 8 turns of N_3. Here again the main structure is made from F42530-UC cores and the leakage path of winding 3 is an F24515-UC core with an I-piece and paper spacer.

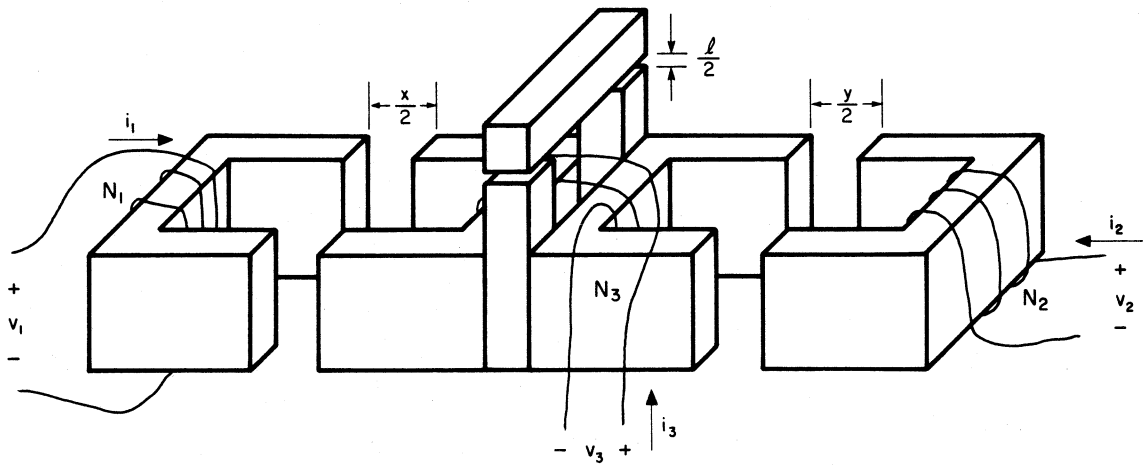

Fig. 22.6 The auxiliary magnetic loops are removed from the input and output windings to verify the analysis for the case of nearly perfect coupling on the outer windings.

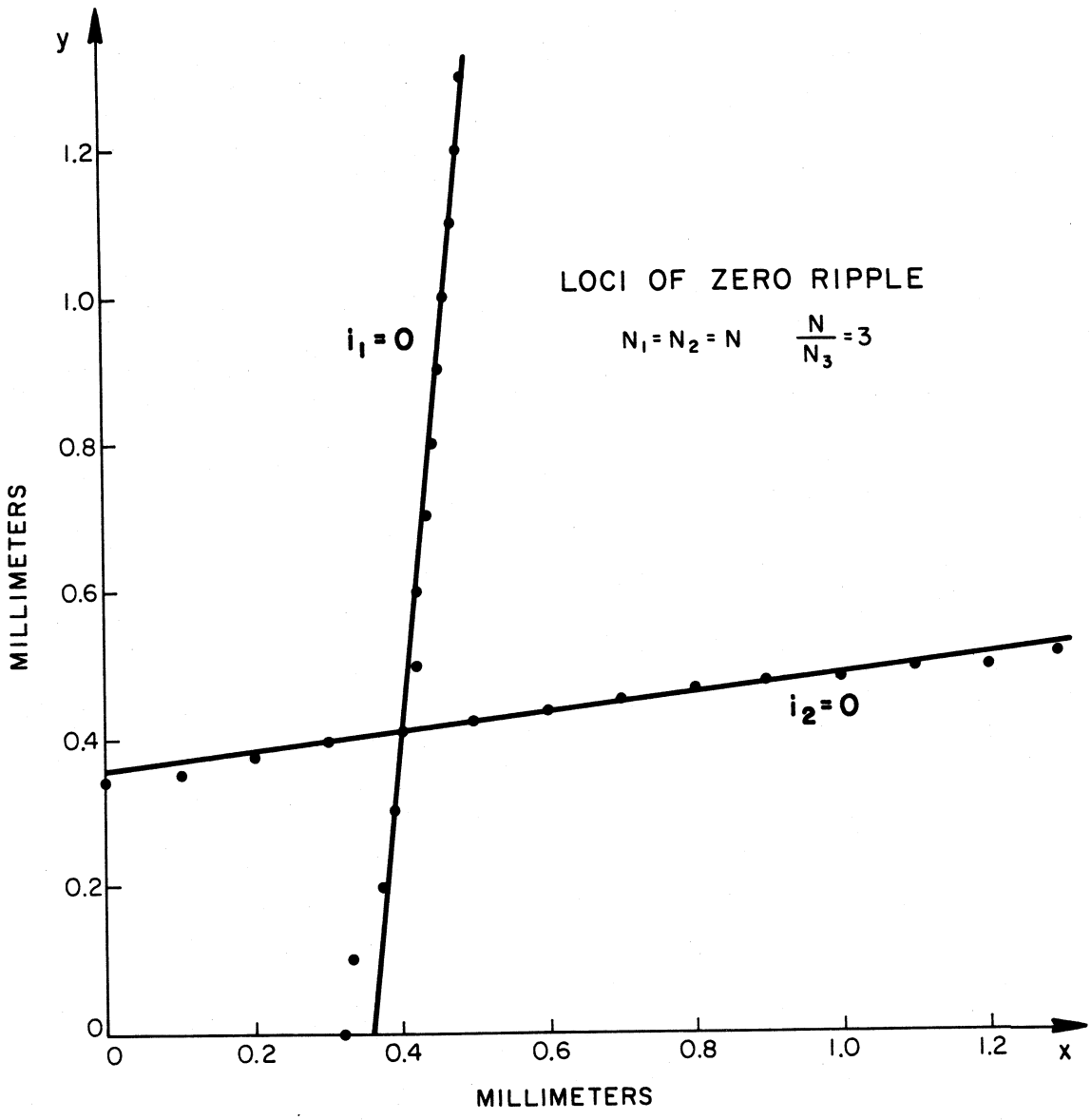

Fig. 22.7 Curves of zero ripple for nearly perfect coupling on the outer windings are approximately straight lines. This corresponds to the theoretical predictions of Fig. 18.12.

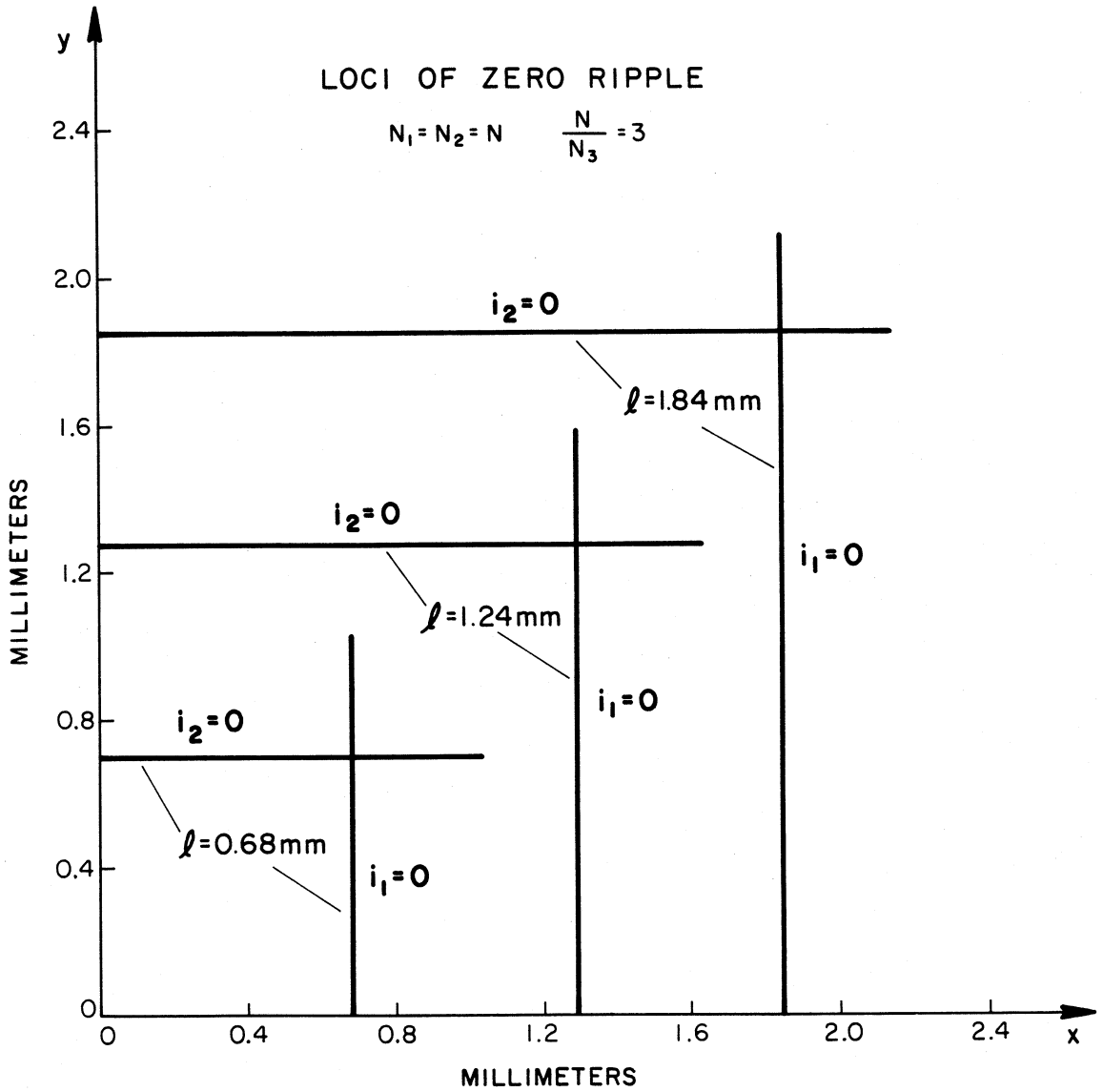

Fig. 22.8 Experimental curves for the non-interactive configuration for three different self-leakages of the center winding. Data points are not explicitly labeled to emphasize the experimental observation that there is no discernible interaction in the adjustments. Every point on the lines qualifies as a valid data point.

Figure 22.8 shows the experimental results obtained for three different gaps in the leakage path of the center winding. The actual spacers used were, of course, different from the effective values of l given in the figure, not only because of the existence of the natural air leakage described above, but also because the spacer is half the total air gap and the area of the external leakage core is half that of the other U-cores. The remarkably straight lines in the figure are actually experimental data. There are no data points explicitly marked on the plot because there is virtually no variation in the observed ripple over an enormous range of adjustment. Thus the entire continuum of gap adjustments qualifies as valid data. These results are in very good agreement with the predictions of Chapters 17 and 19. The zero-ripple solution can indeed be obtained after only a single adjustment of each gap.

The minimum-material structure can be configured very easily from the above structure by merely reversing the sense of one of the outer U-cores. In this way one is able to verify quickly that the predictions of zero ripple are valid for this case as well.

Finally, any combination of the three cases discussed above may be easily constructed and verified. For example, an experiment was set up in which the output winding had zero self-leakage while the input and center windings were imperfectly coupled. As expected, the zero-ripple curves closely followed the trajectories given by the theoretical predictions described previously in Fig. 18.13.

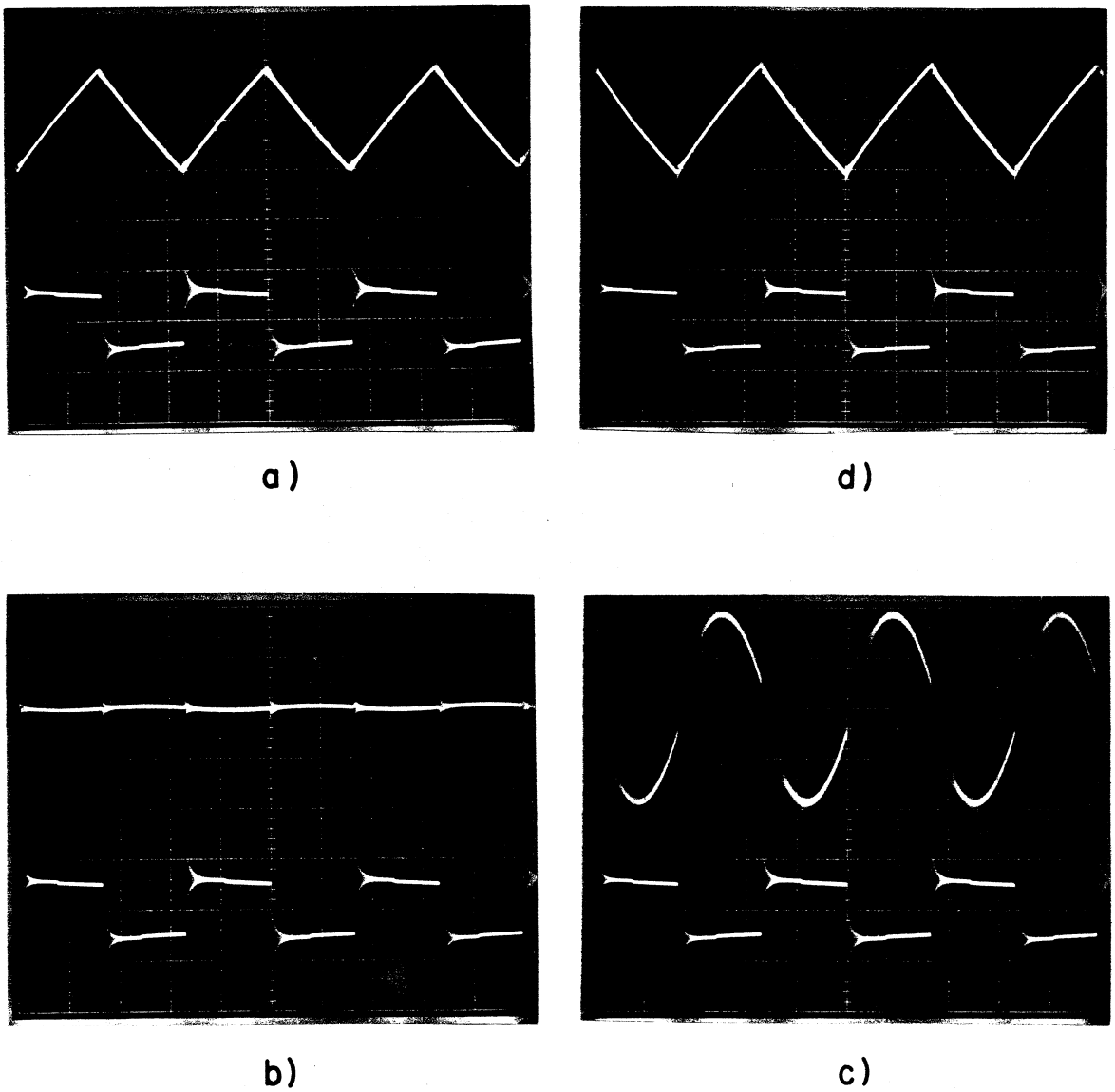

Fig. 22.9 Illustration of parasitic effects on reduction of current ripple. In each photograph the top trace is the current and the bottom trace is the voltage drive. Although the current ripple may be adjusted from positive (a) to negative (d), the magnitude does not pass through zero. The accepted zero-ripple current seen in the top trace of (b) is not really zero, but only a minimum, as can be seen in (c) where the current scale is expanded 50 times.

22.4 Demonstration of Parasitic Effects

It has often been stated [25] that if the slope of a triangular current ripple can be adjusted from positive to negative it must pass through zero, thereby verifying the existence of true zero ripple. This section presents an interesting demonstration showing that this is not completely true.

Figure 22.9 shows several photographs of current and voltage waveforms from the non-interactive structure described in the last section with the windings excited by a square-wave voltage source. In each of the pictures the top trace is the current in the input winding and the bottom trace is the voltage applied to the three windings. Figure 22.9a shows the waveforms before the adjustments, with 22.9b showing zero ripple and 22.9d negative ripple, all on the same scale. In Fig. 22.9c the zero-ripple current waveform of Fig. 22.9b is magnified fifty times. Note that the residual ripple is not triangular in shape, but rather is some combination of square wave and paraboloid. This is a manifestation of the frequency dependence of zero ripple described in Chapter 21. Although the triangular component of the ripple current has been for the most part nulled out, some components of the square-wave source remain, including one which is exactly 180 degrees out of phase with the voltage.

One can get a better understanding of what is happening if the square-wave source is replaced with a sinusoidal drive, as shown in Fig. 22.10. Note that, before the adjustments, Fig. 22.10a shows that the current in the upper trace lags the voltage by 90 degrees, as one would expect with

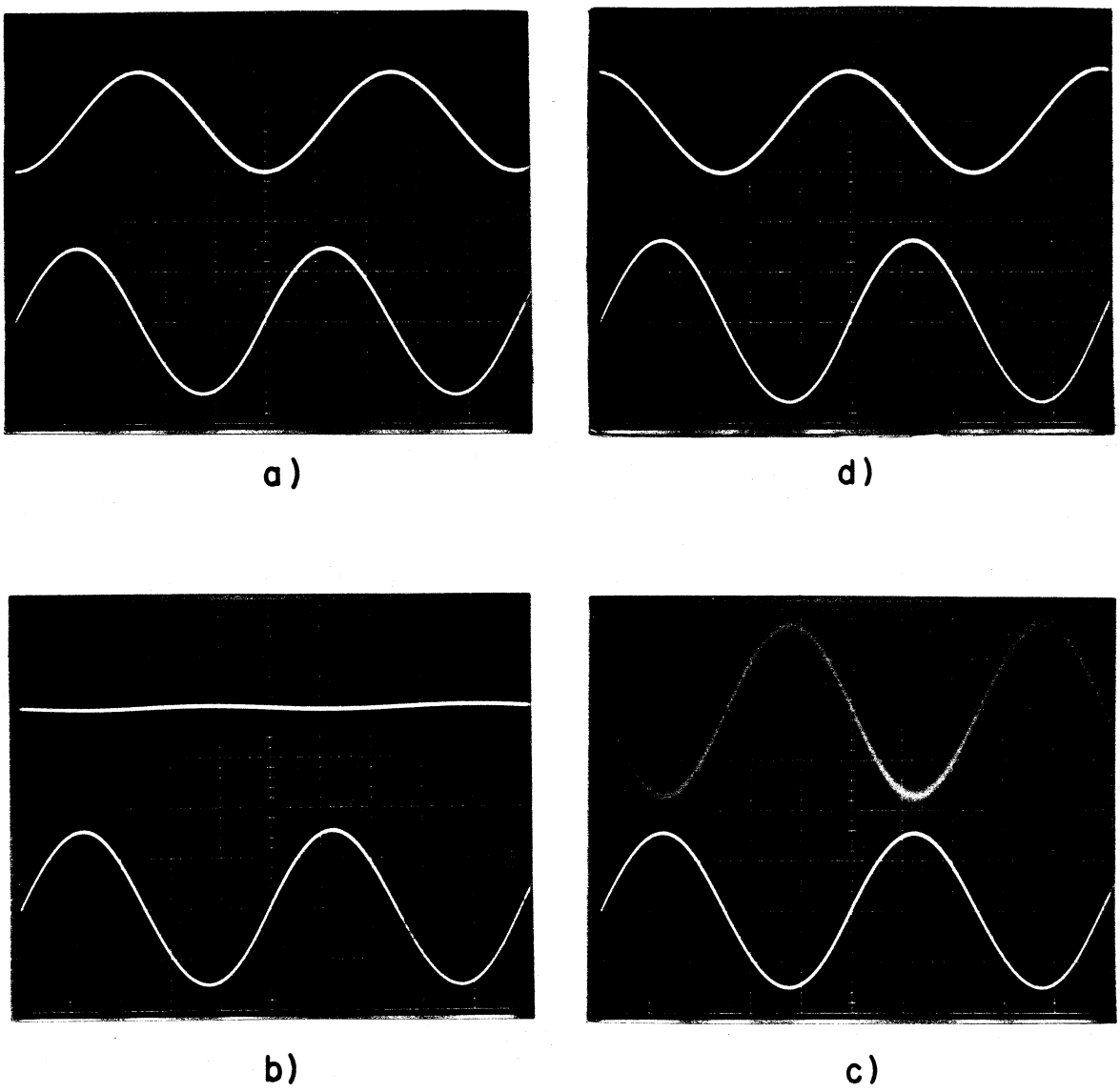

Fig. 22.10 Repeat of the adjustments of Fig. 22.9 but with a sinusoidal drive. Top traces are currents and bottom traces are voltages. As the ripple is adjusted from positive (a) to negative (d) it does not pass through zero as it seems to in (b), but only reaches a minimum as shown by the expanded scale in (c).

an element which is mostly inductive. The negative ripple in Fig. 22.10d appears as a *leading* 90 degree phase shift. The "zero-ripple" current of Fig. 22.10b is magnified as before by 50 times in Fig. 22.10c. Note that the ripple never really goes to zero, even though there is an overall change in phase which corresponds to a transition from positive to negative ripple. Instead, the ripple only reaches a *minimum* at which point the current is exactly 180 degrees out of phase with the voltage, after which the magnitude grows and the phase continues to shift as the ripple becomes negative. When adjusted for minimum ripple, the imaginary (90-degree-shifted) part of the current is nulled out to leave only the real part, which may be positive or negative depending on the values of the various loss mechanisms at that particular frequency.

CHAPTER 23

CONCLUSION

Recent developments in the field of Power Electronics have raised the complexity of inductive components used in switching converters from the level of the common *magnetic device* to the more sophisticated *integrated magnetic circuit*, in which the functions formerly performed by individual inductors and transformers have been merged into a single magnetic structure with multiple windings and non-parallel flux paths. Although these integrated magnetic structures offer a number of advantages to electrical power conversion, their use was chiefly limited to laboratory demonstrations owing to a lack of an analytic base from which one could understand their operation and develop models for design.

The greatest obstacle to the undertaking of this analysis was the *apparent* insurmountable complexity of the problem. The source of the difficulty is that the desired operation of the device is controlled by a number of second-order parameters which are normally ignored in the analysis of conventional magnetic devices. Indeed, one can quickly become discouraged if he attempts to find an *exact* model of an integrated magnetic structure. The key to finding a simple and useful solution to the problem is in the recognition that not *all* the characteristic parameters of the structure are required to model the magnetic device adequately. One of the major contributions of the treatment given here is the determination of the

most relevant parameters which control the zero-ripple performance of these structures.

Although several methods are available for the general analysis of magnetic devices, some are a great deal more useful than others, and the utility depends largely on the desired form of the results. This presentation has demonstrated that the simple *reluctance equivalent circuit model* can be used to determine quickly the necessary conditions for a zero-ripple structure. Apart from solving some particular practical problems, the greatest contribution of the analysis presented here is that it offers a methodology of solution for similar structures of much greater complexity. Moreover, it has been shown how these reluctance models can be transformed into more illuminating *electric circuit models* which bear a topological resemblance to the geometry of the original physical structure.

Despite the presentation of long-awaited solutions for some particularly interesting magnetic devices, the single most important result of this analysis is that it has established a physically oriented method by which power-processing engineers may easily model and understand the operation of complex integrated magnetic structures to design high-performance power conversion equipment.

REFERENCES

[1] A. Cocconi, "Transformer with Orthogonal Fields to Detect Impending Saturation," Patent applied for, California Institute of Technology.

[2] Daniel S. Shull, Jr., "Investigation of Cross-Magnetization in Ferrite Structures," Ph.D. Thesis, Carnegie Institute of Technology, Department of Electrical Engineering, Pittsburgh, Pennsylvania, September 24, 1964.

[3] R. D. Middlebrook, "Power Electronics: An Emerging Discipline," IEEE International Symposium on Circuits and Systems 1981 Record, Chicago, April 1981.

[4] Kevan O'Meara, "Passive Balancing of Transformer Flux in Power Converters," Proc. Tenth International Solid-State Power Electronics Conference (Powercon 9), pp. A2.1-A2.11, March 1983.

[5] Richard Redl, Moshe Domb, and Nathan O. Sokal, "How to Predict and Limit Volt-Second Unbalance in Voltage-Fed Push-Pull Power Converters," Proc. Sixth International PCI '83 Conference, pp. 314-330, April 1983.

[6] F. C. Schwarz, "An Unorthodox Transformer for Free Running Parallel Inverters," IEEE Transactions on Magnetics, vol. MAG-5, No. 4, December

1969, pp. 908-912.

[7] F. C. Schwarz, "95 per cent Efficient Regulating 500 Watt Full Bridge Parallel Inverter-Converter Module with an Internal Frequency of 20kHz," IEEE Power Electronics Specialists Conference, 1978 Record, pp. 331-343 (IEEE Publication 78CH1337-5 AES).

[8] W. J. Hirschberg, "A New PWM Control Technique that Eliminates Transformer Unbalance Problems in Power Converters," Proc. Sixth National Solid-State Power Conversion Conference (Powercon 6), pp. F2.1-F2.4, May 1979.

[9] R. Patel, "Detecting Impending Core Saturation in Switched-Mode Power Converters," Proc. Seventh National Solid-State Power Conversion Conference (Powercon 7), pp. B3.1-B3.11, March 1980.

[10] R. Kuttner, "Circuit Techniques for Eliminating Primary Current Unbalance in Push-Pull Power Converters," Proc, Seventh National Solid-State Power Conversion Conference (Powercon 7), pp. F2.1-F2.9, March 1980.

[11] D. Wilson, "A New Pulsewidth Modulation Method Inherently Maintains Output Transformer Flux Balance," Proc. Eighth International Solid-State Power Electronics Conference (Powercon 8), pp. D1.1-D1.15, April 1981.

[12] C. W. Diesch, "Simple Switching Control Method Changes Power Converter into a Current Source," IEEE Power Electronics Specialists Conference, 1978 Record, pp. 300-306 (IEEE Publication 78CH1337-5 AES).

[13] A. Capel, G. Ferrante, D. O'Sullivan, and A. Weinberg, "Application of the Injected Current Model for the Dynamic Analysis of Switching Regulators with the New Concept of LC^3 Modulator," IEEE Power Electronics Specialists Conference, 1978 Record, pp. 135-147 (IEEE Publication 78CH1337-5 AES).

[14] S. Hsu, A. Brown, L. Rensink, and R. D. Middlebrook, "Modelling and Analysis of Switching Dc-to-Dc Converters in Constant-Frequency Current-Programmed Mode," IEEE Power Electronics Specialists Conference, 1979 Record, pp. 284-301 (IEEE Publication 79CH1461-3 AES).

[15] R. A. Heartz and H. Buelteman, Jr., "The Application of Perpendicularly Superposed Magnetic Fields," AIEE Transactions, Part 1, vol. 74, November 1955, pp. 655-660.

[16] W. McMurray, "Analog Division Circuit," AIEE Transactions, Part 1, vol. 78, November 1959, pp. 606-612.

[17] Dudley A. Buck and Werner I. Frank, "Nondestructive Sensing of Magnetic Cores," AIEE Transactions, vol. 72, Part 1, 1953 (January 1954 Section), pp. 822-830.

[18] J. K. Watson, "On the Nonlinearities of Inductance Using Linear Ferrite Toroidal Cores," IEEE Transactions on Magnetics, vol. MAG-17, No. 3, May 1981, pp. 1320-1325.

[19] S. L. Gokhale, "Law of Magnetization," AIEE Transactions, vol. 45, June 1926, pp. 1013-1031.

[20] J. D. Ryder, "Ferroinductance as a Variable Electric-Circuit Element," AIEE Transactions, vol. 64, October 1945, pp. 671-678.

[21] W. H. Beyer, Editor, *CRC Standard Math Tables*, 25th Edition, CRC Press, Inc., 1978, p. 262.

[22] L. T. Rader and E. C. Litscher, "Some Aspects of Inductance When Iron is Present," AIEE Transactions, vol. 63, March 1944, pp. 133-139.

[23] J. K. Watson, *Applications of Magnetism*, John Wiley & Sons, 1980.

[24] Alan Cocconi, Slobodan Ćuk, and R. D. Middlebrook, "High-Frequency Isolated 4kW Photovoltaic Inverter for Utility Interface," Proc. Seventh International PCI '83 Conference, pp. 39-59, September 1983.

[25] Slobodan Ćuk, "Switching Dc-to-Dc Converter with Zero Input or Output Current Ripple," IEEE Industry Applications Society Annual Meeting, 1978 Record, pp. 1131-1146 (IEEE Publication 78CH1346-6 IA).

[26] Loman Rensink, "Switching Regulator Configurations and Circuit Realizations," Ph.D. Thesis, California Institute of Technology, Department of Electrical Engineering, Pasadena, California, December 3, 1979.

[27] R. D. Middlebrook and Slobodan Ćuk, *Advances in Switched-Mode Power Conversion*, vols. I, II & III, Published by Teslaco, Pasadena, California, 1981 & 1983.

[28] Slobodan Ćuk and R. D. Middlebrook, "A New Optimum Topology Switching Dc-to-Dc Converter," IEEE Power Electronics Specialists Conference, 1977 Record, pp. 160-179 (IEEE Publication 77CH1213-8 AES).

[29] Slobodan Ćuk and R. D. Middlebrook, "Coupled-Inductor and Other Extensions of a New Optimum Topology Switching Dc-to-Dc Converter," IEEE Industry Applications Society Annual Meeting, 1977 Record, pp. 1110-1126 (IEEE Publication 77CH1246-8-IA).

[30] R. D. Middlebrook and Slobodan Ćuk, "Isolation and Multiple Output Extensions of a New Optimum Topology Switching Dc-to-Dc Converter," IEEE Power Electronics Specialists Conference, 1978 Record, pp. 256-264 (IEEE Publication 78CH1337-5 AES).

[31] Slobodan Ćuk, "A New Zero-Ripple Switching Dc-to-Dc Converter and Integrated Magnetics," IEEE Power Electronics Specialists Conference, 1980 Record, pp. 12-32 (IEEE Publication 80CH1529-7

AES).

[32] Walter J. Hirschberg, "Improving Multiple Output Converter Performance with Coupled Output Inductors," Proc. Ninth International Solid-State Power Electronics Conference (Powercon 9), pp. G4.1-G4.5, July 13-15, 1982.

[33] David I. Sheppard and Brian E. Taylor, "A New Converter Topology Imparts Non-Pulsating Currents to Input and Output Lines," Proc. PCI/MOTORCON, pp. 60-73, September 1983.

[34] G. E. Bloom and A. Eris, "Practical Design Considerations of a Multi-Output Ćuk Converter," IEEE Power Electronics Specialists Conference, 1979 Record pp. 133-146 (IEEE Publication 79CH1461-3 AES).

[35] G. E. Bloom, A. Eris, and R. Ruble, "Modeling and Analysis of a Multi-Output Ćuk Converter," IEEE Power Electronics Specialists Conference, 1980 Record pp. 33-47 (IEEE Publication 80CH1528-7 AES).

[36] Slobodan Ćuk, "New Magnetic Structures for Switching Converters." Presented at PCI '81, Munich, W. Germany, Sept. 16-17, 1981.

[37] R. Mahadevan, S. El-Hamamsy, W. M. Polivka, and S. Ćuk, "A Converter with Three Switched-Networks Improves Regulation, Dynamics and Control," Proc. Tenth International Solid-State Power

Electronics Conference (Powercon 10), pp. E1.1-E1.19, March 22-24, 1983.

[38] Shi-Ping Hsu, "Problems in Analysis and Design of Switching Regulators," Ph.D. Thesis, California Institute of Technology, Department of Electrical Engineering, Pasadena, California, September 13, 1979.

[39] Shi-Ping Hsu, R. D. Middlebrook, and Slobodan Ćuk, "Transformer Modelling and Design for Leakage Control," Power Conversion International, February 1982, p.68.

[40] Charles A. Desoer and Ernest S. Kuh, *Basic Circuit Theory*, McGraw Hill, 1969.

[41] Balabanian and Bickart, *Electrical Network Theory*, John Wiley & Sons, 1969.

[42] E. Colin Cherry, "The Duality Between Electric and Magnetic Circuits and the Formation of Transformer Equivalent Circuits," Proc. Phys. Soc., 62B, pp. 101-111, February 1949.

APPENDIX

A.1 Expressions for Zero-Ripple Solutions

In support of the discussion of Section 17.3, explicit expressions are given below for the zero-ripple solutions in terms of the leg permeances P_{L1} and P_{L2} when $N_1 = N_2 = N$ and $\xi = \frac{N}{N_3}$.

$$P_{L1} = \frac{P_{L3}(p_3 - p_{13})}{(\xi - 2)[P_{L3} + p_{23} + p_{13}] - 2p_3} \tag{A.1}$$

$$P_{L2} = \frac{P_{L3}(p_3 - p_{23})}{(\xi - 2)[P_{L3} + p_{23} + p_{13}] - 2p_3} \tag{A.2}$$

Note that although $N_1 = N_2 = N$, this does not guarantee that $P_{L1} = P_{L2}$ unless $p_{13} = p_{23}$. However, if the mutual leakage permeances can be ignored in comparison to larger quantities, one obtains

$$P_{L1} = P_{L2} = \frac{p_3}{(\xi - 2) - 2\frac{p_3}{P_{L3}}} \tag{A.3}$$

which is equivalent to the reluctance expression of Eq. (18.33).

For the case of $N_1 \neq N_2$ under normal conditions where the mutual permeances may be ignored in comparison to larger terms, one obtains the solutions

$$P_{L1} = \frac{2N_2}{N_1+N_2} \frac{p_3}{(\xi_p - 2) - \frac{p_3}{P_{L3}}} \tag{A.4}$$

$$P_{L2} = \frac{2N_1}{N_1+N_2} \frac{p_3}{(\xi_p - 2) - \frac{p_3}{P_{L3}}} \tag{A.5}$$

where

$$\xi_p \equiv 2\frac{N_1 \| N_2}{N_3} \tag{A.6}$$

Note that (A.4) and (A.5) reduce to (A.1) and (A.2) when $N_1 = N_2 = N$. In terms of reluctances the solutions are

$$R_{xs} = \frac{1}{2}\left(1 + \frac{N_1}{N_2}\right)\left[(\xi_p - 2)R_{l3} - 2R_c\right] \tag{A.7}$$

$$R_{ys} = \frac{1}{2}\left(1 + \frac{N_1}{N_2}\right)\left[(\xi_p - 2)R_{l3} - 2R_c\right] \tag{A.8}$$

which reduce to Eq. (18.33) for $N_1 = N_2 = N$.

For the minimum-material configuration (Section 19.2) the solutions are

$$R_{xs} = \frac{1}{2}\left(1 + \frac{N_1}{N_2}\right)\left[(\xi_p - 2)R_{l3} - 2\left[\frac{N_2 - N_1}{N_1 + N_2}\right]R_c\right] \tag{A.9}$$

$$R_{ys} = \frac{1}{2}\left(1 + \frac{N_2}{N_1}\right)\left[(\xi_p - 2)R_{l3} - 2\left[\frac{N_1 - N_2}{N_1 + N_2}\right]R_c\right] \tag{A.10}$$

A.2 Derivation of Electric Circuit Models by Duality

This section shows the derivation of the electric circuit model of the conventional three-winding integrated structure of Section 20.3 to illustrate the application of duality to the modelling of magnetic devices.

The procedure, taken from [23], begins with the reluctance equivalent circuit of the device. A reference dot, designated in Fig. A.1 by a circle surrounding an uppercase letter, is placed inside each loop of the planar network and a reference dot is placed outside the network. These points will become the nodes of the dual circuit. The nodes of the original circuit, labeled with triangles in Fig. A.1, will correspond to the loops of the dual circuit, Fig. A.2.

Next, a line is drawn between any two nodes of the original circuit to pass through one and only one circuit element. The corresponding dual element is then constructed between the same two nodes of the dual circuit, as shown in Fig. A.2. For example, the line drawn from loop A to loop B in the original circuit passes through the voltage source $N_1 i_1$, which corresponds to the *current source* $N_1 i_1$ between the *nodes* A and B in the dual circuit of Fig. A.2. The orientation of the corresponding dual branches is obtained by *counterclockwise* rotation of the original branches until they coincide with their dual branch directions. That is, when the voltage source in the original circuit is rotated counterclockwise so that it coincides with the line drawn from A to B, a positive voltage is encountered in going from A to B. Thus, in the dual circuit a positive current must go from node A to node B. This procedure is repeated for each element of the original

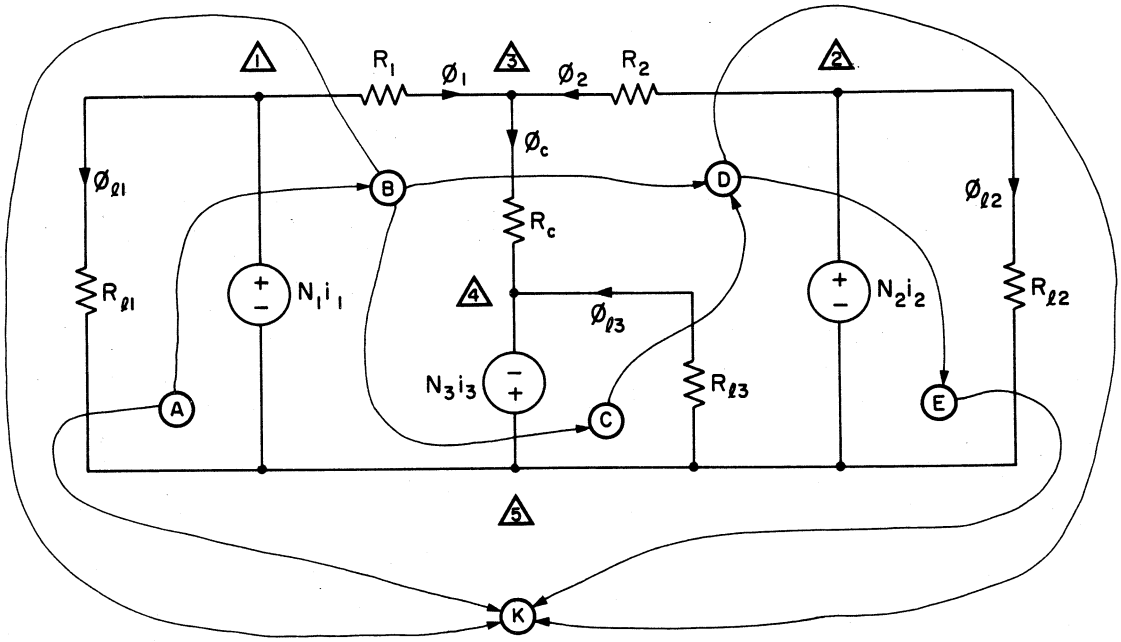

Fig. A.1 The loops of the reluctance equivalent circuit are connected by drawing lines which pass through one and only one circuit element.

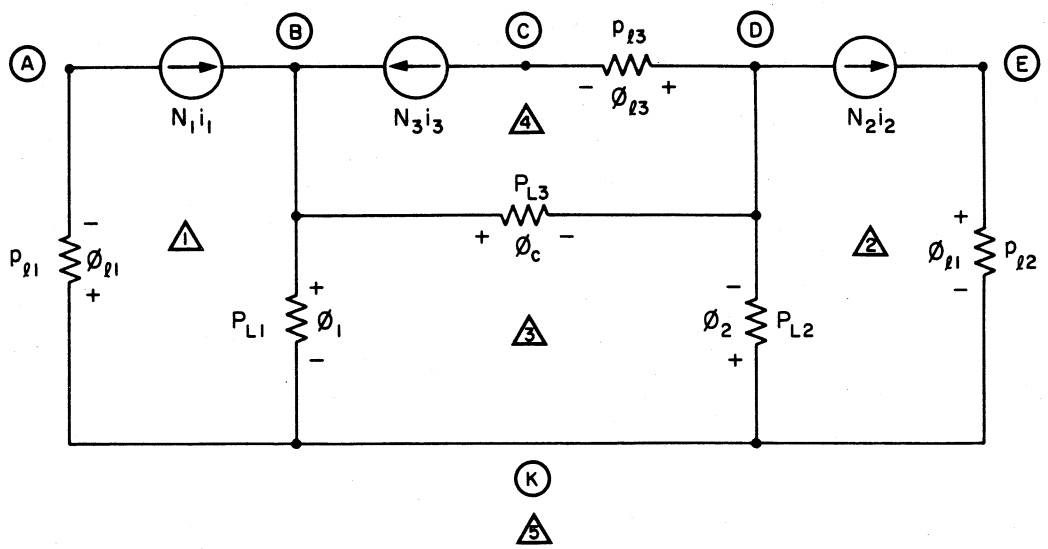

Fig. A.2 The loops of the original reluctance equivalent circuit correspond to nodes in the dual circuit. Voltage sources are transformed to current sources and reluctances become permeances in the dual circuit.

circuit.

The dual network is scaled by appropriate turns ratios such that the permeances are multiplied by turns squared. In Fig. A.3 the permeances were multiplied by N_3^2. Care should be taken in the choice of the multiplier, for, although multiplication by N_1 or N_2 would be a valid operation, the resulting circuit would be more difficult to simplify in the remaining steps.

Recognition that the time derivative of $N\varphi$ is voltage permits one to redraw the dual circuit in the more familiar electrical form of Fig. A.4., in which the N^2p's have been replaced by L's to put the circuit into a v vs. i relationship.

Finally, ideal transformers have been added in Fig. A.5 for cosmetic scaling purposes to produce the same circuit of Fig. 20.2.

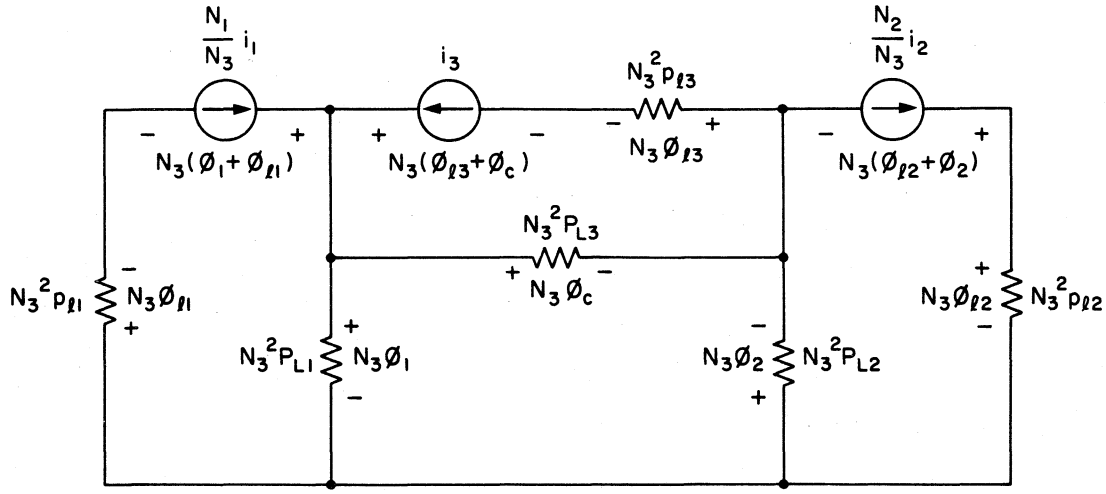

Fig. A.3 The dual circuit is scaled to put the permeances in the form of N^2p.

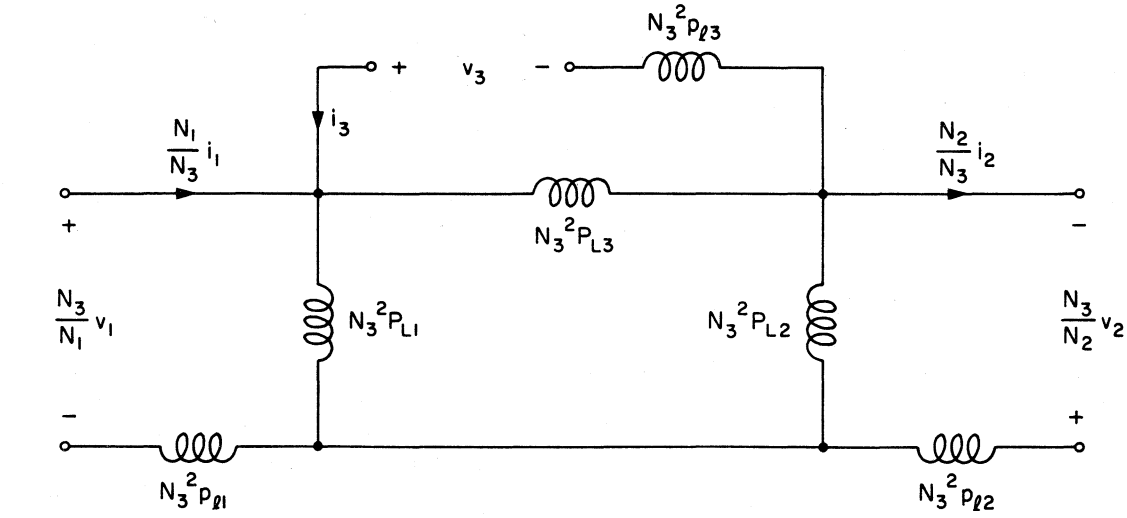

Fig. A.4 Consideration of the time derivatives of the fluxes and currents leads to a circuit in terms of voltages, currents and inductances.

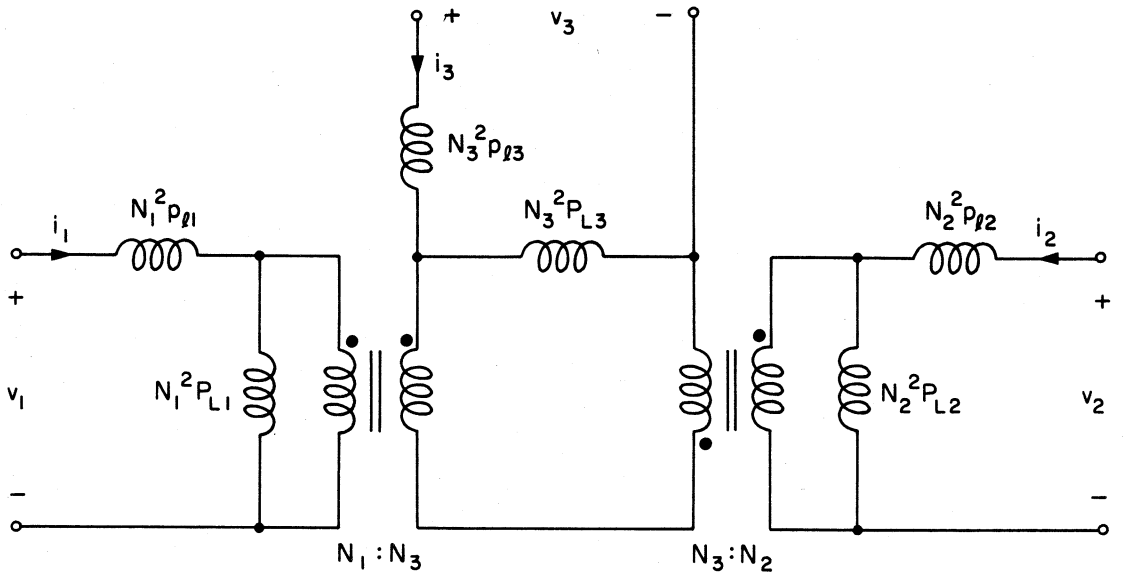

Fig. A.5 Ideal transformers can be added to match the ports of the model to the inputs and outputs of the original magnetic device.